Armands Rudušs

JAUNAS IZSTAROTĀJU STRUKTURĀLĀS PIEEJAS *OLED* IEKĀRTU RAŽOŠANAS IZMAKSU SAMAZINĀŠANAI

Promocijas darbs

DEVELOPMENT OF NOVEL STRUCTURAL APPROACHES FOR COST-EFFECTIVE OLED EMITTERS

Doctoral Thesis

RĪGAS TEHNISKĀ UNIVERSITĀTE
Materiālzinātnes un lietišķās ķīmijas fakultāte
Lietišķās ķīmijas institūts

RIGA TECHNICAL UNIVERSITY
Faculty of Materials Science and Applied Chemistry
Institute of Applied Chemistry

Armands Rudušs
Doktora studiju programmas "Ķīmija" doktorants
Doctoral Student of the Study Programme "Chemistry"

JAUNAS IZSTAROTĀJU STRUKTURĀLĀS PIEEJAS *OLED* IEKĀRTU RAŽOŠANAS IZMAKSU SAMAZINĀŠANAI
Promocijas darbs

DEVELOPMENT OF NOVEL STRUCTURAL APPROACHES FOR COST-EFFECTIVE OLED EMITTERS
Doctoral Thesis

Zinātniskie vadītāji / Scientific supervisors
asociētais profesors *Dr. chem.* / Associate Professor Dr. chem.
KASPARS TRASKOVSKIS,
profesors *Dr. chem.* / Professor Dr. chem.
VALDIS KOKARS

RTU Izdevniecība / RTU Press
Rīga 2022 / Riga 2022

NATIONAL DEVELOPMENT PLAN 2020

EUROPEAN UNION
European Social Fund

INVESTING IN YOUR FUTURE

PROMOCIJAS DARBS IZVIRZĪTS ZINĀTNES DOKTORA GRĀDA IEGŪŠANAI RĪGAS TEHNISKAJĀ UNIVERSITĀTĒ

Promocijas darbs zinātnes doktora (*Ph. D.*) grāda iegūšanai tiek publiski aizstāvēts 2022. gada 15. decembrī plkst. 14 Rīgas Tehniskās universitātes Materiālzinātnes un lietišķās ķīmijas fakultātē, Paula Valdena ielā 3, 272. auditorijā.

OFICIĀLIE RECENZENTI

Vadošais pētnieks *Dr. chem.* Pāvels Arsenjans,
Latvijas Organiskās sintēzes institūts, Latvija

Vadošais pētnieks *Dr. phys.* Mārtiņš Rutkis,
Latvijas Universitātes Cietvielu fizikas institūts, Latvija

Profesors *Dr. habil.* Jozs Vids Gražulevičs,
Kauņas Tehnoloģiju universitāte, Lietuva

APSTIPRINĀJUMS

Apstiprinu, ka esmu izstrādājis šo promocijas darbu, kas iesniegts izskatīšanai Rīgas Tehniskajā universitātē zinātnes doktora (*Ph. D.*) grāda iegūšanai. Promocijas darbs zinātniskā grāda iegūšanai nav iesniegts nevienā citā universitātē.

Armands Rudušs ………………………….
                    (*paraksts*)

Datums: ....

Promocijas darbs ir sagatavots kā tematiski vienotu zinātnisko publikāciju kopa ar kopsavilkumu latviešu un angļu valodā. Promocijas darbs ietver četrus rakstus, kas publicēti zinātniskajos žurnālos, un divas publikācijas konferenču ziņojumu izdevumos (*proceedings*). Raksti zinātniskajos žurnālos, kā arī publikācijas konferenču ziņojumu izdevumos ir angļu valodā, to kopējais apjoms, ieskaitot pielikumus, ir 215 lpp.

SATURS

LIETOTIE SAĪSINĀJUMI

A	akceptors
BPhen	4,7-difenil-1,10-fenantrolīns
CBP	4,4′-di(9*H*-karbazol-9-il)-1,1′-difenils
Cbz	karbazols
CMA	karbēns–metāls–amīds
CT	lādiņa pārnese
CzSi	9-(4-*terc*-butilfenil)-3,6-di(trifenilsilil)-9*H*-karbazols
D	donors
DCC	dicikloheksilkarbodiimīds
DCM	dihlormetāns
DFT	blīvuma funkcionālā teorija
Dipp	2,6-diizopropilfenilgrupa
DMAP	4-dimetilaminopiridīns
DMF	dimetilformamīds
DMSO	dimetilsulfoksīds
DPEPO	di[2-(difenilfosfīno)fenil]ētera oksīds
DSC	diferenciālā skenējošā kalorimetrija
HOMO	augstākā aizņemtā molekulārā orbitāle
ISC	starpsistēmu pāreja
ITO	indija alvas oksīds
LCD	šķidro kristālu ekrāns
LE	lokālā ierosināšana
LLCT	ligands-ligands lādiņa pārnese
LUMO	zemākā neaizņemtā molekulārā orbitāle
mCBP	3,3′-di(9*H*-karbazol-9-il)-1,1′-difenils
mCP	3,5-di(9*H*-karbazol-9-il)benzols
Me	metilgrupa
MLCT	metāls-ligands lādiņa pārnese
NHC	*N*-heterocikliskais karbēns
OLED	organiskā gaismu izstarojošā diode
OXD-7	1,3-di[2-(4-*terc*-butilfenil)-1,3,4-oksadiazo-5-il]benzols
PEDOT:PSS	poli(3,4-etilēndioksitiofēn)-polistirolsulfonāts
Ph	fenilgrupa
PL	fotoluminiscence
PMMA	polimetilmetakrilāts
PolyTPD	poli(4-butiltrifenilamīns)
ppy	2-fenilpiridīns
PVK	polivinilkarbazols
RISC	atgriezeniskā starpsistēmu pāreja
S	singleta stāvoklis

SOC	spina-orbītas mijiedarbība
T	tripleta stāvoklis
TADF	termiski aktivētā aizkavētā fluorescence
TAPC	1,1-di[(di-4-tolilamino)fenil]cikloheksāns
TCTA	tri(4-karbazol-9-ilfenil)amīns
TD-DFT	no laika atkarīgā blīvuma funkcionālā teorija
THF	tetrahidrofurāns
TmPyPB	1,3,5-tri(3-piridil-3-fenil)benzols
TPBi	1,3,5-tri(1-fenil-1*H*benzimidazol-2-il)benzols
UV	ultravioletā gaisma
Vis	redzamā gaisma

PROMOCIJAS DARBA VISPĀRĒJS RAKSTUROJUMS

Tēmas aktualitāte

Organiskā gaismu izstarojošā diode (*OLED*) ir ierīce, ko var izmantot gan ekrānu, gan apgaismes iekārtu izgatavošanā. *OLED* tehnoloģija sniedz iespējas izstrādāt ekrānus, kas dažādos veiktspējas un estētiskajos aspektos pārspēj šobrīd plaši izmantoto šķidro kristālu ekrānu (*LCD*) analogus.[1] Savukārt iespēja izgatavot plānus, lokanus, liela laukuma *OLED* paneļus paver jaunas iespējas dekoratīvu apgaismes elementu dizainā.[2] Lai gan šobrīd *OLED* ekrāni tiek plaši lietoti viedierīču izgatavošanā, lielāka laukuma televizoru un datoru ekrāni, kā arī apgaismes paneļi plašākam patērētāju lokam nav pieejami to dārdzības dēļ. Kā galvenie potenciālie virzieni izmaksu samazināšanai literatūrā minēti *OLED* izgatavošanas procesa optimizācija un lētāku materiālu izmantošana.[3]

Galvenais process *OLED* izgatavošanā ir iekārtas struktūru veidojošo plāno materiāla kārtiņu uzklāšana. Visplašāk lietotā pieeja šādu struktūru veidošanai šobrīd ir vakuuma uzklāšanas tehnoloģija. Metodes ietvaros uznesamais cietvielas materiāls vakuuma un siltuma avota ietekmē pāriet gāzes fāzē. Gāzveida stāvoklī esošās molekulas pārvietojas uz substrāta virsmu un uz tās, lēnām kondensējoties, veido plāno kārtiņu.[4] Nepieciešamība nodrošināt augstu vakuumu, atsevišķiem materiāliem piemītošā augstā iztvaikošanas temperatūra, materiāla zudumi vakuuma kamerā, kā arī tehniskās grūtības, kas saistītas ar liela virsmas laukuma pārklājumu izgatavošanu, sadārdzina šo tehnoloģisko procesu.[5] Kā izmaksu ziņā lētāka alternatīva tiek piedāvāta plāno kārtiņu pagatavošana no šķīdumiem (rotācijas uzklāšana, drukāšana u. c.). Tomēr organiskie izstarotāji, kas izmantojami vakuuma uzklāšanai, vairumā gadījumu nav piemēroti šķīdumu uzklāšanas metodēm. Galvenās problēmas saistītas ne tikai ar dažreiz nepietiekamo materiālu šķīdību organiskajos šķīdinātājos, bet arī ar savienojumu nepietiekamo spēju veidot viendabīgu amorfo fāzi, kurai būtu augsta morfoloģiskā un termiskā stabilitāte.[6]

Promocijas darba pirmajā daļā pētītas iespējas modificēt *OLED* plaši lietotos fosforescentos irīdija(III) kompleksus, lai iegūtu izstarotājus, kas būtu uznesami ar šķīdumu metodēm. Irīdija(III) kompleksi tika funkcionalizēti ar tritilgrupām (-CPh$_3$), kas palielina savienojumu šķīdību organiskajos šķīdinātājos un uzlabo izgatavoto plāno amorfo kārtiņu optisko kvalitāti un morfoloģisko stabilitāti. Iegūtajiem izstarotājiem veikts fotofizikālo īpašību raksturojums, kā arī noteikti to veiktspējas parametri ar šķīdumu metodēm pagatavotās *OLED* iekārtas.

OLED izmaksas palielina ne tikai sarežģītais ražošanas process, bet arī izmantoto materiālu dārdzība, ko lielā mērā nosaka tieši izmantotie izstarotāji. Šobrīd nozīmīgākā izstarotāju klase ar praktisku pielietojumu komercializētās *OLED* iekārtās ir fosforescentie irīdija metālorganiskie kompleksi.[7] Reto pārejas metālu dārdzības, kā arī potenciālo vides piesārņojuma risku dēļ tiek meklēti risinājumi fosforescento materiālu aizstāšanai, piemēram, ar termiski aktivētās aizkavētās fluorescences (*TADF*) izstarotājiem.[8]

Promocijas darba otrajā daļā aprakstīta karbēna–metāla–amīda (*CMA*) tipa *TADF* izstarotāju sintēze, kuros kā kompleksveidojošais elements izmantots varš. Jaunisgūtajiem savienojumiem veikts struktūras un fotofizikālo īpašību raksturojums, kā arī izpētīts

luminiscences mehānisms. Uz 1,3-tiazol-2-ilidēna karbēna fragmenta bāzētajiem *CMA* atvasinājumiem demonstrēts praktiskais lietojums efektīvās baltās gaismas *OLED* iekārtās.

Pētījuma mērķis un uzdevumi

Promocijas darba mērķis ir tādu organisku mazmolekulāru izstarotāju sintēze, kas samazinātu *OLED* iekārtu ražošanas izmaksas. Darba mērķa īstenošanai definēti vairāki uzdevumi.

1. Sintezēt ar tritilgrupām funkcionalizētus fosforescentos irīdija(III) metālorganiskos kompleksus. Raksturot iegūto savienojumu fotofizikālās un morfoloģiskās īpašības plānajās amorfajās kārtiņās.
2. Novērtēt ar tritilgrupām funkcionalizēto irīdija(III) kompleksu piemērotību augstas efektivitātes *OLED* izveidē.
3. Sintezēt luminiscentus karbēna–metāla–amīda (*CMA*) tipa vara(I) metālorganiskos kompleksus. Raksturot iegūto savienojumu struktūru un izpētīt to *TADF* īpašības.
4. Novērtēt jaunieūgto *CMA* atvasinājumu piemērotību augstas efektivitātes *OLED* izveidē.

Zinātniskā novitāte un galvenie rezultāti

Promocijas darba pirmajā daļā sintezētas ar tritilgrupām funkcionalizētu heteroleptisku 2-arilbenzo[d]tiazola ligandus saturošu, kā arī homoleptisku 2-fenilpiridīna ligandus saturošu fosforescento irīdija(III) kompleksu sērijas. Savienojumu fotofizikālās un morfoloģiskās īpašības plānajās amorfajās kārtiņās ir atbilstošas, lai iegūtos irīdija kompleksus izmantotu ar šķīdumu metodēm izgatavotās *OLED* iekārtās. Tomēr, veicot sistemātisku pētījumu par tritilgrupu ietekmi uz *OLED* veiktspējas parametriem, tika konstatēts, ka tritilgrupas negatīvi ietekmē lādiņnesēju transportu aktīvajā izstarojošajā slānī, kas samazina *OLED* izstarošanas efektivitāti. Lai gan iegūtie dati liecina par tritilgrupu ierobežotu lietojumu efektīvos *OLED* izstarotājos, tomēr rezultāti dod paplašinātu ieskatu par priekšnoteikumiem, kas būtu jāņem vērā ar šķīdumu metodēm uzklājamu irīdija(III) kompleksu molekulārajā dizainā.

Promocijas darba otrajā daļā sintezētas divas jaunu *CMA* tipa *TADF* izstarotāju sērijas. Pirmajā kā karbēna fragmenti izmantoti imidazola tipa *NHC* atvasinājumi, kam pie perifērajiem stēriskajiem fragmentiem pievienotas akceptorās fenilsulfonilgrupas. Otrajā kā karbēna fragmenti kalpo 1,3-tiazol-2-ilidēna tipa *NHC* atvasinājumi. Ar fenilsulfonilgrupām funkcionalizētajiem kompleksiem aprakstīts *CMA* savienojumu klasei līdz šim nezināms *TADF* īstenošanās mehānisms. Savukārt 1,3-tiazol-2-ilidēna atvasinājumiem izpētīta stērisko efektu ietekme uz savienojumu luminiscences īpašībām. Demonstrēts 1,3-tiazol-2-ilidēna *CMA* atvasinājumu potenciālais pielietojums augstas efektivitātes *OLED* iekārtu izstrādē.

Darba struktūra un apjoms

Promocijas darbs sagatavots kā tematiski vienota zinātnisko publikāciju kopa, kas veltīta luminiscentu ar tritilgrupām funkcionalizētu irīdija(III), kā arī *CMA* tipa vara(I) metālorganisko

kompleksu sintēzei, fotofizikālo īpašību raksturošanai un iegūto izstarotāju piemērotības noteikšanai zemu izmaksu *OLED* izstrādei.

Darba aprobācija un publikācijas

Promocijas darba galvenie rezultāti apkopoti četros rakstos zinātniskajos žurnālos, kā arī divās publikācijās konferenču ziņojumu izdevumos (*proceedings*). Pētījumu rezultāti atspoguļoti septiņos ziņojumos, kas prezentēti piecās konferencēs.

Raksti zinātniskajos žurnālos

1. **Ruduss, A.**; Turovska, B.; Belyakov, S.; Stucere, K. A.; Vembris, A.; Baryshnikov, G.; Ågren, H.; Lu, J.; Lin, W.; Chang, C.; Traskovskis, K. Thiazoline Carbene–Cu(I)–Amide Complexes: Efficient White Electroluminescence from Combined Monomer and Excimer Emission. *ACS Appl. Mater. Interfaces.* **2022**, *14* (13), 15478–15493. doi: 10.1021/acsami.2c00847. Žurnāla ietekmes faktors (2021): 10,383.

2. **Ruduss, A.**; Turovska, B.; Belyakov, S.; Stucere, K. A.; Vembris, A.; Traskovskis, K. Carbene–Metal Complexes As Molecular Scaffolds for Construction of Through-Space Thermally Activated Delayed Fluorescence Emitters. *Inorg. Chem.* **2022**, *61* (4), 2174–2185. doi: 10.1021/acs.inorgchem.1c03371. Žurnāla ietekmes faktors (2021): 5,436.

3. **Ruduss, A.**; Kokars, V.; Tetervenoka, N.; Vembris, A.; Traskovskis, K. Effects of Steric Encumbrance of Iridium(iii) Complex Core on Performance of Solution-Processed Organic Light Emitting Diodes. *RSC Adv.* **2020**, *10* (46), 27552–27559. doi: 10.1039/D0RA04652C. Žurnāla ietekmes faktors (2021): 4,036.

4. Traskovskis, K.; **Ruduss, A.**; Kokars, V.; Mihailovs, I.; Lesina, N.; Vembris, A. Thiphenylmethane Based Structural Fragments as Building Blocks Towards Solution-Processable Heteroleptic Iridium(iii) Complexes for OLED Use. *New J. Chem.* **2019**, *43* (1), 37–47. doi: 10.1039/C8NJ04484H. Žurnāla ietekmes faktors: 3,925.

Publikācijās konferenču ziņojumu izdevumos (*proceedings*)

1. Jece, A.; **Ruduss, A.**; Štucere, K. A.; Vembris, A.; Traskovskis, K. TADF Active Carbene-Metal-Amide Complexes Exhibiting Through-Space Charge Transfer: An Impact of Metal Atom. *Organic Electronics and Photonics: Fundamentals and Devices III.* **2022**, 1214909. doi: 10.1117/12.2621156.

2. **Ruduss, A.**; Sisojevs, Ž.; Vembris, A.; Štucere, K. A.; Traskovskis, K. Symmetrical versus Asymmetrical Molecular Configuration in Metal-Assisted-Through-Space Charge Transfer TADF Emitters. *Organic Electronics and Photonics: Fundamentals and Devices III*. **2022**, 1214908. doi: 10.1117/12.2620983.

Ziņojumi zinātniskajās konferencēs:

1. **Ruduss, A.**; Sisojevs, Z.; Vembris, A.; Stucere, K.; Traskovskis, K. Symmetrical Versus Asymmetrical Molecular Configuration in Metal Assisted-Through-Space Charge Transfer TADF Emitters. *SPIE Photonics Europe, Conference 12149, Organic Electronics and Photonics:Fundamentals and Devices III*, Strasbourg, France, April 4–6, **2022**.

2. Jece, A.; **Ruduss, A.**; Vembris, A.; Stucere, K.; Traskovskis, K. TADF active carbene-metal-amide complexes exhibiting through-space charge transfer: an impact of metal atom. *SPIE Photonics Europe, Conference 12149, Organic Electronics and Photonics:Fundamentals and Devices III*, Strasbourg, France, April 4–6, **2022**.

3. **Ruduss, A.**; Sisojevs, Z.; Jece, A. Thiazoline Carbene-Cu(I)-Carbazolide Complexes as Luminescent TADF Materials. *80th International Scientific Conference of the University of Latvia 2022. Chemistry Section*, Riga, Latvia, February 11, **2022**.

4. **Ruduss, A.**; Jece, A.; Balodis, K.; Traskovskis, K. The Use of Thiazoline-Based Carbenes for a Development of Metalorganic Thermally Activated Delayed Fluorescence Emitters. *Riga Technical University 62nd International Scientific Conference "Materials Science and Applied Chemistry"*, Riga, Latvia, October 22, **2021**.

5. Sisojevs, Z.; **Ruduss, A.**; Balodis, K.; Traskovskis, K. Synthesis and photophysical properties of metal-amide complexes of *N*-heterocyclic carbenes containing peripheral acceptor groups. *Riga Technical University 62nd International Scientific Conference "Materials Science and Applied Chemistry"*, Riga, Latvia, October 22, **2021**.

6. **Ruduss, A.**; Traskovskis, K.; Kokars, V. Photophysical Properties of 9,9'-Bis-Methoxypenyl Substituted 3,3'-Bicarbazoles. *13th International Conference on Optical Probes of Organic and Hybrid Optoelectronic Materials and Applications 2019*, Vilnius, Lithuania, July 7–13, **2019**.

7. **Ruduss, A.**; Traskovskis, K.; Otikova, E.; Vembris, A.; Grzibovskis, R.; Kokars, V. 3,3'-Bicarbazole Structural Derivatives as Charge Transporting Materials for Use in OLED Devices. *SPIE Photonics Europe, Conference 10687, Organic Electronics and Photonics:Fundamentals and Devices III*, Strasbourg, France, April 24–26, **2018**.

PROMOCIJAS DARBA GALVENIE REZULTĀTI

1. *OLED* uzbūves un darbības pamatprincipi

Organiskajā gaismu izstarojošajā diodē (*OLED*) gaismas izstarošana elektriskās strāvas ietekmē īstenojas no organiska elektroluminiscenta materiāla.[9] Vienkāršots *OLED* uzbūves princips redzams 1.1. attēlā.[10] Tipiska *OLED* iekārta sastāv no vairākām plānām kārtiņām, kas secīgi uzklātas viena uz otras, kā pamatni izmantojot stiklu vai kādu citu caurspīdīgu materiālu. Plānās kārtiņas var tikt uzklātas, izmantojot vakuuma vai šķīdumu uzklāšanas metodes. Izmantotajam materiālam jābūt piemērotam attiecīgajam apstrādes paņēmienam. Materiāliem jābūt ne tikai ar augstu ķīmisko un fotoķīmisko izturību, lai novērstu degradāciju ierīces darbības laikā, bet arī ar augstu morfoloģisko stabilitāti.[11]

Iekārtas darbības nodrošināšanai ir nepieciešams ārējs elektriskās strāvas avots. Pieliekot spriegumu, caurumi (pozitīvi lādēti lādiņnesēji) un elektroni (negatīvi lādēti lādiņnesēji) pārvietojas attiecīgi no anoda un katoda uz izstarojošo slāni. Lai nodrošinātu zemu ievades barjeru, kā arī līdzsvarotu un efektīvu lādiņnesēju transportu, starp elektrodiem un izstarojošo slāni var tikt izvietoti lādiņnesēju ievades (nav parādīti 1.1. att.), lādiņnesējus vadošie un lādiņnesējus bloķējošie slāņi.[12] Izstarojošajā slānī, caurumiem un elektroniem rekombinējoties organiskas molekulas ietvaros, tā tiek ierosināta. Šādi ierosinātu molekulu atgriešanās pamatstāvoklī ar gaismas izstarošanu tiek saukta par elektroluminiscenci. Izstarojošajā slānī esošā luminofora koncentrācija parasti ir zema, un izstarotājs ir iejaukts (dopēts) īpašā lādiņus vadošā matricā. Šādu maisījumu sauc par "viesis-saimnieks" (*guest-host*) sistēmu. Pateicoties tam, izstarotāja molekulas tiek telpiski attālinātas cita no citas, samazinot starpmolekulāro mijiedarbību un ierosināto stāvokļu dzēšanos.[13]
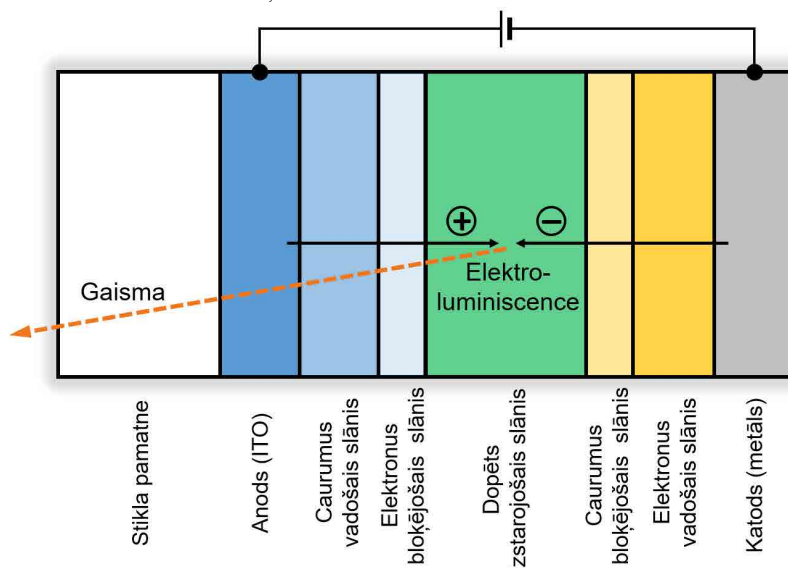
1.1. att. *OLED* principiālā uzbūves shēma.

Lādiņnesēju rekombinācijas rezultātā izstarojošajā slānī veidojas cieši saistītu elektronu un caurumu pāri jeb eksitoni. Tālāka eksitona relaksācija no ierosinātā stāvokļa uz pamatstāvokli var novest pie fotona izstarošanas. Šī iemesla dēļ efektīvai eksitonu enerģijas pārnesei uz izstarotāja molekulām ir būtiska nozīme elektroluminiscences nodrošināšanā. Jāņem vērā, ka, rekombinējoties lādiņnesējiem, rodas divu veidu – singleta (S) un tripleta (T) – eksitoni (1.2. att.). Spinu statistika nosaka, ka radušos singleta un tripleta eksitonu skaita attiecība ir 1 : 3.[14]
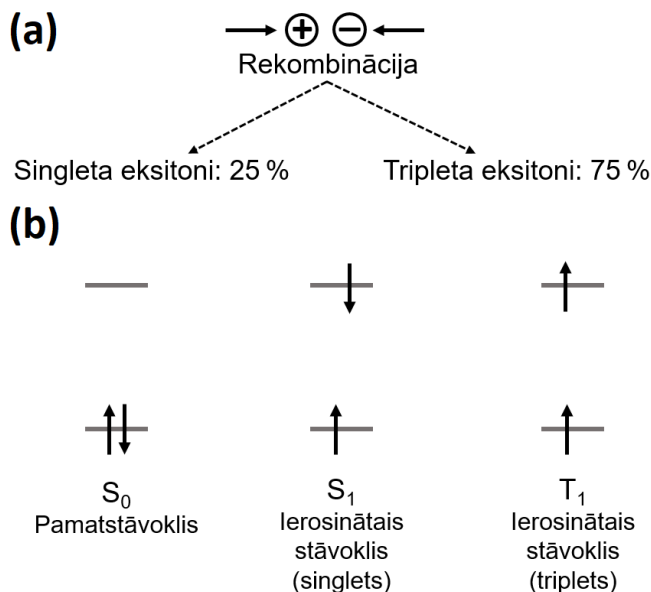
1.2. att. (a) Singleta un tripleta eksitonu veidošanās attiecība; (b) elektronu spina konfigurācija pamatstāvoklī (S$_0$), kā arī S$_1$ un T$_1$ ierosinātajos stāvokļos.

Lai raksturotu luminiscentu materiālu izstarošanas efektivitāti, izmanto kvantitatīvu lielumu – luminiscences kvantu iznākumu (Φ).[15] Kvantu iznākums tiek definēts kā ierosināto stāvokļu īpatsvars, kas relaksācijas rezultātā izstaro fotonu:

$$\Phi = \frac{k_\mathrm{r}}{k_\mathrm{r} + k_\mathrm{nr}}, \tag{1.1}$$

kur: Φ – kvantu iznākums;

k_r – radiatīvo procesu ātruma konstante;

k_nr – neradiatīvo procesu ātruma konstante.

Praktiskos mērījumos samērā vienkārši ir eksperimentāli noteikt materiālu fotoluminiscences kvantu iznākumu (Φ_PL).[15] Fotoluminiscences kvantu iznākums ir materiāla izstaroto fotonu daudzuma attiecība pret materiāla absorbēto fotonu daudzumu:

$$\Phi_\mathrm{PL} = \frac{N_\mathrm{em}}{N_\mathrm{abs}}, \tag{1.2}$$

kur: Φ_PL – fotoluminiscences kvantu iznākums;

N_em – izstaroto fotonu daudzums;

N_abs – absorbēto fotonu daudzums.

Radiatīvās relaksācijas ātruma konstantes[16] noteikšanai nepieciešams noskaidrot fotoluminiscences kvantu iznākumu un fotoluminiscences dzīves laiku:

$$k_\mathrm{r} = \frac{\Phi_\mathrm{PL}}{\tau_\mathrm{PL}}, \qquad (1.3)$$

kur τ_PL – fotoluminiscences dzīves laiks.

Fluorescentu izstarotāju gadījumā tikai singleta eksitoni (S_1) ir spējīgi relaksēties ar fotona izstarošanu (1.3. att., a). Tripleta ierosinātā stāvokļa (T_1) relaksācija uz pamatstāvokli (S_0) ir spina–aizliegta pāreja, tādēļ šim procesam (fosforescencei) ir raksturīgs ļoti ilgs dzīves laiks. Līdz ar to izstarošanu no T_1 stāvokļa gandrīz pilnībā nomāc dažādi neradiatīvās relaksācijas procesi. Šī iemesla dēļ fluorescento *OLED* maksimālā sasniedzamā iekšējā kvantu efektivitāte ir 25 %.[17]

Kā viens no risinājumiem, lai maksimālo teorētisko iekšējo kvantu efektivitāti palielinātu no 25 % līdz 100 %, ir fluorescentu izstarotāju aizstāšana ar fosforescentiem analogiem (1.3. att., b). Fosforescentie materiāli parasti ir smago pārejas metālu (Ir, Pt, Os, Ru u. c.) kompleksie savienojumi, kas satur dažādus organiskos ligandus. Smagie atomi nodrošina efektīvu spina-orbītas mijiedarbību (*SOC*). *SOC* ir process, kas sekmē spina inversiju, līdz ar to tiek veicināta starpsistēmu pāreja (*ISC*), kā arī T_1 stāvokļa fosforescentā relaksācija.[18]

Kā alternatīvu smagos pārejas metālus saturošajiem fosforescentajiem materiāliem iespējams lietot izstarotājus ar termiski aktivētās aizkavētās fluorescences (*TADF*) īpašībām (1.3. att., c). *TADF* materiālos enerģijas starpība starp S_1 un T_1 (ΔE_ST) stāvokļiem ir zemāka par 0,1 eV. Šādi tiek veicināta atgriezeniskā starpsistēmu pāreja (*RISC*). Tādējādi neradiatīvie tripleta stāvokļi tiek pārvērsti par radiatīvajiem singletiem, no kuriem iespējama t. s. aizkavētā fluorescence. Gan fosforescences, gan *TADF* mehānisms nodrošina pilnīgu singleta un tripleta eksitonu izmantošanu radiatīvajos procesos, tādējādi sasniedzot maksimālo teorētiski iespējamo iekšējo kvantu efektivitāti (100 %).[19]
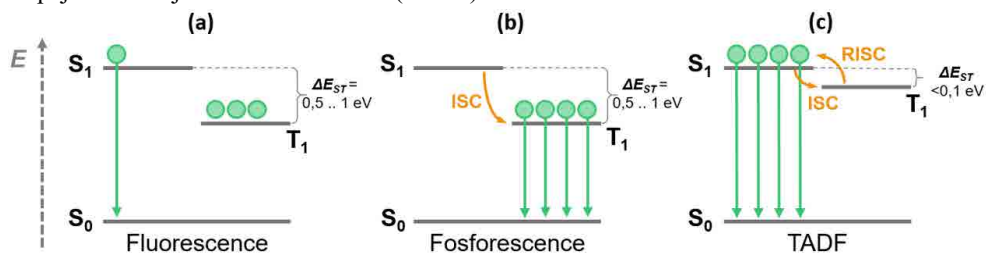
1.3. att. Shematisks fluorescences, fosforescences un *TADF* attēlojums.

2. Ar tritilgrupām funkcionalizētu Ir(III) kompleksu sintēze un fosforescences īpašības

Par vienu no galvenajām problēmām, kas ievērojami sadārdzina *OLED* izgatavošanas izmaksas, uzskatāma energoietilpīgā aktīvo slāņu vakuuma uzklāšanas tehnoloģija. *OLED* izstarojošā slāņa vakuuma uzklāšanu papildus apgrūtina nepieciešamība kopā ar izstarojošo vielu uznest matricas materiālu (viesis-saimnieks sistēma). Alternatīva metode ir plāno kārtiņu uzklāšana no šķīdumiem, izmantojot, piemēram, rotācijas uzklāšanas metodi no koncentrēta

vielas šķīduma.[20] Lai vielu varētu izmantot šķīdumu uzklāšanas tehnoloģijā, tai jābūt ne tikai labi šķīstošai viegli gaistošos organiskajos šķīdinātājos, bet arī jāveido stabila amorfā fāze ar augstu stiklošanās temperatūru un optisko kvalitāti. Mūsu grupas iepriekšējos pētījumos tika konstatēts, ka dažādu mazmolekulāru savienojumu funkcionalizēšana ar tritilgrupām (-CPh₃) veicina šo materiālu spēju veidot stabilu amorfo fāzi.[21–23]

Lai iegūtu efektīvus, ar šķīdumu metodēm apstrādājamus amorfu fāzi veidojošus *OLED* izstarotājus, par pamatu tika izmantoti literatūrā aprakstīti fosforescenti 2-arilbenzo[d]tiazola ligandus saturoši irīdija(III) kompleksi.[24–26] Šo kompleksu sintēzei vispirms tika iegūti ar tritilgrupām funkcionalizēti 2-arilbenzo[d]tiazola ligandi **2**, **5** un **8** (2.1. shēma). Ligandi tika izmantoti tālākai sintēzei, vispirms sagatavojot di-μ-hloro irīdija(III) kompleksu dimērus un pēc tam pievienojot attiecīgi pikolīnskābes (kompleksi **3a**, **6a** un **9a**) vai acetilacetona (kompleksi **3b**, **6b** un **9b**) palīgligandus.

Iegūtajiem savienojumiem ir ļoti laba šķīdība dažādos viegli gaistošos organiskajos šķīdinātājos, piemēram, DCM, hloroformā un THF. Izmantojot rotācijas uzklāšanas metodi, no vielu šķīdumiem ir iespējams pagatavot amorfas plānās kārtiņas. Ar diferenciālās skenējošās kalorimetrijas (*DSC*) metodi noteiktās sintezēto materiālu stiklošanās temperatūras ir robežās no 124 °C līdz 188 °C. Vairāku karsēšanas-dzesēšanas ciklu laikā netika novērotas fāžu pārejas, kas varētu liecināt par materiālu kristalizēšanos.
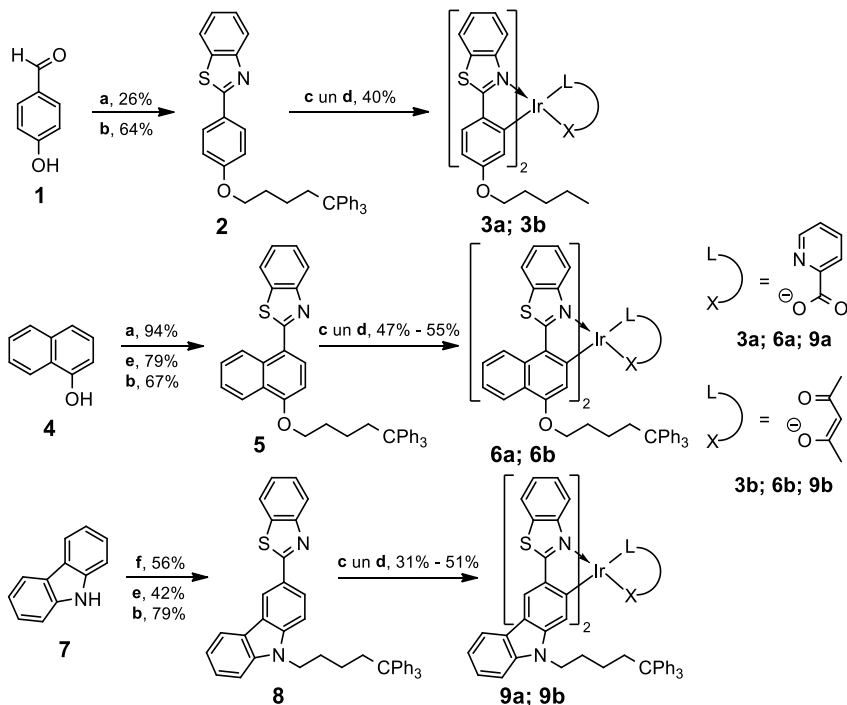
2.1. shēma. 2-Arilbenzo[d]tiazola ligandus saturošo irīdija(III) kompleksu sintēze.
(**a**) 1,1,1-Trifenil-5-jodpentāns, K₂CO₃, DMSO; (**b**) 2-aminotiofenols, DMSO; (**c**) IrCl₃·3H₂O, 2-etoksietanols/H₂O; (**d**) acetilacetons vai 2-pikolīnskābe, 2-etoksietanols, K₂CO₃; (**e**) POCl₃, DMF; (**f**) 1,1,1-trifenil-5-jodpentāns, NaH, THF.

14

Ar tritilgrupām funkcionalizēto irīdija(III) kompleksu un literatūrā aprakstīto[24–26] nefunkcionalizēto struktūras analogu *UV-Vis* absorbcijas ainas ir līdzīgas. Zemākās enerģijas *UV-Vis* absorbcijas joslas šajos savienojumos ir saistītas ar metāls–ligands lādiņa pārnesi (*MLCT*; 2.1. tab.). Savienojumu sērijā vislielākā absorbcijas joslu batohromā nobīde novērojama 2-(naftalīn-1-il)benzo[d]tiazola ligandu saturošajiem kompleksiem **6a** un **6b**. Visiem savienojumiem ir novērojama intensīva fosforescence ar izteiktu vibracionālo sīkstruktūru. Tas liecina par izstarošanas saistību ar ligandu lokālajām $^3\pi{\rightarrow}\pi^*$ pārejām. Arī fosforescences gadījumā vislielākā batohromā nobīde ir kompleksiem **6a** un **6b**, kam novērojama oranžīgi sarkana fosforescence, savukārt kompleksu **3a**, **3b**, **9a** un **9b** fosforescence ir spektra dzeltenajā daļā.

Nosakot gan fosforescentu materiālu, gan *TADF* materiālu Φ_{PL}, mērījumi jāveic degazētos bezskābekļa apstākļos, jo skābeklis dzēš ierosinātos tripleta stāvokļus, tādējādi pazeminot noteikto Φ_{PL} vērtību.[27, 28] Savienojumiem ir samērā augsts Φ_{PL} atšķaidītos šķīdumos (no 0,64 līdz 0,90 THF šķīdumā). Savukārt tīrām izstarotāju (bez matricas) amorfajām plānajām kārtiņām Φ_{PL} nokrīt robežās no 0,02 līdz 0,10. Šajā gadījumā, neņemot vērā inertās 5,5,5-trifenilpentilgrupas, aktīvā izstarotāja masas koncentrācija plānajās amorfajās kārtiņās ir aptuveni 50 %, kas izraisa ievērojamu agregācijas ierosinātu izstarošanas dzēšanos. Izgatavojot *OLED* aktīvo slāni, praktiski vienmēr izstarotājs tiek iejaukts matricā, kurā izstarotāja masas koncentrācija ir zemāka par 10 %, tāpēc tika nolemts noteikt plāno amorfo kārtiņu Φ_{PL} arī viesis-saimnieks sistēmām ar *CBP* un *PVK*. Ņemot vērā, ka inertās 5,5,5-trifenilpentilgrupas veido aptuveni pusi no savienojumu molmasas, kompleksi tika iejaukti matricā 20 % masas koncentrācijā, nodrošinot aptuveni 10 % aktīvā izstarotāja masas koncentrāciju. *CBP* matricā Φ_{PL} vērtības sasniedz 0,50. Savukārt *PVK* matricā Φ_{PL} ir vērtības ir zemas un būtiski neatšķiras no tīru amorfo plāno kārtiņu Φ_{PL}, kas varētu būt saistīts ar pastiprinātu izstarotāja agregāciju polimēra tipa *PVK* matricā. Papildus tam novērojama tendence, ka pikolīnskābes palīgligandu saturošajiem kompleksiem galvenokārt ir augstāks Φ_{PL} nekā acetilacetona palīgligandu saturošajiem kompleksiem.

2.1. tabula

2-Arilbenzo[d]tiazola ligandus saturošo irīdija(III) kompleksu fotofizikālās īpašības

Savien.	$\lambda_{\text{max abs}}$[a], nm (lg ε)	$\lambda_{\text{max em}}$[b], nm	Φ_{PL}[c]	τ[d], µs	k_r[d], ×10^5 s^{-1}	k_{nr}[d], ×10^5 s^{-1}
3a	433 (3,7)	537, 576 (544, 576)	0,87/0,10/0,06/0,39	4,48	1,78	1,44
3b	464 (3,8)	552, 588 (553, 591)	0,78/0,02/0,15/0,31	3,32	1,56	0,45
6a	485 (4,3)	591, 641 (598, 644)	0,64/0,04/0,08/0,50	5,63	1,10	0,68
6b	496 (4,1)	595, 648 (604, 651)	0,64/0,03/0,06/0,27	3,75	1,15	2,49
9a	456 (4,0)	549, 588 (556, 587)	0,90/0,05/0,02/0,50	3,65	2,05	0,67
9b	464 (3,9)	568, 603 (568, 603)	0,69/0,02/0,02/0,12	2,61	1,34	1,52

[a] Zemākās enerģijas absorbcijas joslas maksimums, THF šķīdums. [b] Fosforescence, THF šķīdums (*CBP* filma, 20 % masas koncentrācija). [c] THF šķīdums/tīra amorfā kārtiņa/*PVK* filma (20 % masas koncentrācija)/*CBP* filma (20 % masas koncentrācija). [d] *PMMA* filma (1 % masas koncentrācija).

OLED izgatavošanā tika izmantoti karbazola fragmentu saturošie kompleksi **9a** un **9b** (*Dr. phys.* A. Vembris). *OLED* tika izgatavotas, izmantojot šādu struktūru: *ITO/PEDOT:PSS* (40 nm)/izstarojošais slānis (60 nm)/*BPhen* vai *TPBi* (20 nm)/LiF (1 nm)/Al, kur caurumus vadošais *PEDOT:PSS* un izstarojošais slānis tika izgatavots no vielu šķīdumiem ar rotācijas uzklāšanas metodi, savukārt elektronus vadošais *BPhen*/*TPBi* un elektronu ievades LiF slānis, kā arī alumīnija elektrods tika izgatavoti ar vakuuma uzklāšanas metodi. Augstākus veiktspējas parametrus uzrāda ierīce, kurā izmantots kompleksa **9a** un *CBP* matricas izstarojošais slānis, sasniedzot 7,9 % ārējo kvantu efektivitāti, 12,4 cd·A^{-1} strāvas efektivitāti un 7,8 lm·W^{-1} jaudas efektivitāti pie 6000 cd·m^{-2} spilgtuma, maksimālais spilgtums – 17451 cd·m^{-2} (2.2. tab.). Līdzīgi kā Φ_{PL} mērījumu gadījumā, zemāki veiktspējas parametri novērojami ierīcēm, kurās izmantota *PVK* matrica un acetilacetona palīgligandu saturošais komplekss **9b**.

2.2. tabula

Kompleksu **9a**–**b** *OLED* raksturlielumi

Izstarojošais slānis[a]	V_{on}[b], V	L_{max}, cd·m^{-2}	η_{ext}[c], %	η_c[d], cd·A^{-1}	η_p[e], lm·W^{-1}	λ_{max}, nm
9a:*PVK*	6,5	3229	4,8/4,8[f]	7,2/7,2[f]	4,5/4,5[f]	553
9a:*CBP*	5,5	17451	7,9/5,1	12,4/8,0	7,8/5,6	554
9b:*PVK*	7,0	1708	2,1/1,7	3,1/2,4	1,9/1,3	561
9b:*CBP*	6,5	7295	5,2/5,1	7,3/7,1	4,9/4,7	563

[a] Irīdija(III) kompleksu masas koncentrācija izstarojošā slānī ir 20 %. [b] Spriegums, pie kura iekārtas spilgtums ir 1 cd·m^{-2}. [c] *OLED* ārējā kvantu efektivitāte. [d] Strāvas efektivitāte. [e] Jaudas efektivitāte. [f] Maksimālās sasniegtās vērtības un vērtības noteiktas pie 1000 cd·m^{-2}.

Ar tritilgrupām funkcionalizēto irīdija(III) kompleksu *OLED* veiktspēju raksturojošie parametri ir augstāki, salīdzinot ar citiem literatūrā aprakstītiem strukturāli līdzīgiem dzeltenajiem izstarotājiem, kur izstarojošais slānis uzklāts ar rotācijas uzklāšanas metodi.[29, 30] Tomēr iegūtie dati un literatūras avotu analīze liecina, ka ar šķīdumu metodēm izgatavotās *OLED* veiktspējas ziņā atpaliek no tām, kas izgatavotas ar vakuuma metodēm.[31, 32] Turklāt ne vienmēr inertu izolējošo grupu, piemēram, garu alkilķēžu ieviešana, kam vajadzētu samazināt agregācijas izraisītu ierosināto stāvokļu dzēšanos, izraisa *OLED* veiktspējas uzlabošanos.[33] Šie rezultāti pamudināja veikt sistemātisku pētījumu, lai varētu noteikt tritilgrupu ietekmi uz *OLED* veiktspēju.

Lai sasniegtu šo uzdevumu, uz plaši *OLED* izmantotā savienojuma **Ir(ppy)₃**[34] bāzes tika sintezēti savienojumi **15a**, **15b** un **15c**, kur **Ir(ppy)₃** izstarotāja kodolam pievienotas attiecīgi viena, divas un trīs tritilgrupas (2.2. shēma). Šim nolūkam di-μ-hlor- dimēri **13a** un **13b** tika kompleksēti ar trešo ciklametalējošo ligandu, izmantojot *Colombo*[35] izstrādāto metodi, kas ļauj iegūt oktaedrālos irīdija(III) kompleksus *fac* konfigurācijā. Mērķsavienojumi tika sintezēti, reducējot ar NaBH₄ attiecīgi vienu, divas vai trīs aldehīdgrupas saturošos kompleksus **14a**, **14b** un **14c** un iegūtos spirtus esterificējot ar 3,3,3-trifenilpropānskābi.

Ar tritilgrupām funkcionalizētie savienojumi ir šķīstoši viegli gaistošos organiskajos šķīdinātājos, un rotācijas uzklāšanas metode ir izmantojama, lai no šķīdumiem pagatavotu

kvalitatīvas šo materiālu plānās amorfās kārtiņas. Savienojumu **15a**, **15b** un **15c** stiklošanās temperatūras ir attiecīgi 158 °C, 142 °C un 131 °C. Stiklošanās temperatūras samazinājums savienojumu sērijā varētu būt saistīts ar konformacionālās brīvības palielināšanos, pieaugot tritilgrupu skaitam molekulās.
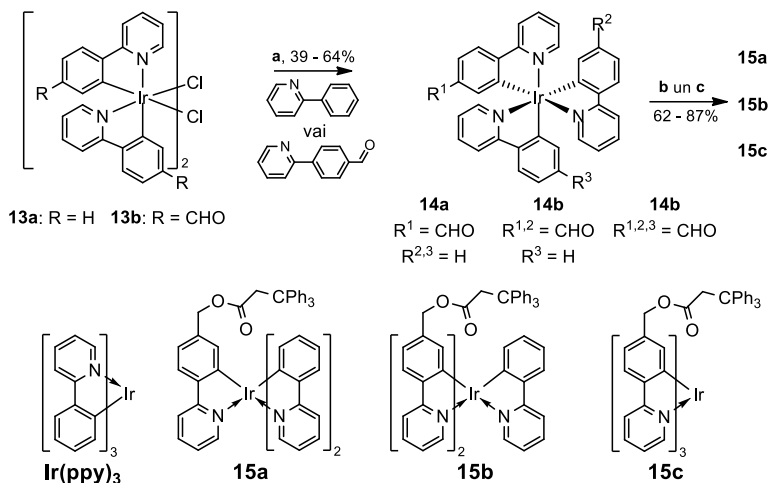
2.2. shēma. Ar tritilgrupām funkcionalizēto **Ir(ppy)₃** atvasinājumu sintēze.
(**a**) AgOTf, diglīms; (**b**) NaBH₄, CH₂Cl₂/MeOH; (**c**) CPh₃CH₂COOH, *DCC, DMAP*, CH₂Cl₂.

Savienojumu sērijā netika novērota būtiska tritilgrupu ietekme uz savienojumu absorbcijas un izstarošanas īpašībām šķīdumā (2.3. tab.). Φ_{PL} THF šķīdumos ir augsts, sasniedzot vērtības no 0,90 līdz 0,94. Tīriem izstarotājiem amorfajās kārtiņās Φ_{PL} nokrītas robežās no 0,01 līdz 0,08, kas liecina par intensīvu savienojumu agregāciju cietajā fāzē. Lai gan savienojumam **15c** ir funkcionalizēts ar trīs tritilgrupām, *fac* ligandu konfigurācijas dēļ tās telpiski ir vērstas vienā virzienā, nosedzot tikai vienu molekulas pusi. Tas ļauj izvirzīt hipotēzi, ka šajā gadījumā agregācijas rezultātā veidojas vāji izstarojoši kompleksa molekulu dimēri.

2.3. tabula

Ar tritilgrupām funkcionalizēto **Ir(ppy)₃** atvasinājumu fotofizikālās īpašības

Savien.	$\lambda_{\text{max abs}}$[a], nm	$\lambda_{\text{max em}}$[b], nm	Φ_{PL}[c]	τ[d], µs	k_r[d], $\times 10^5$ s^{-1}	k_{nr}[d], $\times 10^5$ s^{-1}
Ir(ppy)₃	379	522	0,94/-	1,7	5,5	0,35
15a	380	525	0,91/0,01	1,8	5,1	0,50
15b	379	525	0,90/0,03	1,7	5,3	0,58
15c	379	525	0,93/0,08	1,8	5,2	0,38

[a] Absorbcija, THF šķīdums. [b] Fosforescence, THF šķīdums. [c] THF šķīdums/tīra amorfā kārtiņa. [d] THF šķīdums.

Jauniegūto kompleksu elektroluminiscences īpašības tika pētītas (*Dr. phys.* A. Vembris), izmantojot šādu *OLED* struktūru: *ITO/PEDOT:PSS* (40 nm)/izstarojošais slānis (50 nm)/*TPBi*

(20 nm)/LiF (1 nm)/Al. Trīs veidu "saimnieks" (*host*) matricas tika izmantotas izstarojošā slāņa izveidei – pirmkārt, tīra pārsvarā caurumus transportējošā *PVK* matrica, otrkārt, *PVK* un pārsvarā elektronus transportējošā *OXD-7* maisījums 7 : 3 masu attiecībā, treškārt, *PVK* un *OXD-7* maisījums 3 : 7 masu attiecībā. Irīdija(III) kompleksi matricā tika iejaukti konstantā 7 % masas koncentrācijā, inertās tritilgrupas pieskaitot matricas masai. Izstarojošais slānis tika pagatavots no šķīduma ar rotācijas uzklāšanas metodi. Iegūtie rezultāti (2.4. tab.) liecina, ka nemodificētais **Ir(ppy)₃** pārspēj ar tritilgrupām funkcionalizētos savienojumus *OLED* veiktspējas parametros. Turklāt, palielinoties tritilgrupu skaitam molekulā, novērojama tendence veiktspējas parametriem samazināties. Tika izvirzīta hipotēze, ka šo savienojumu gadījumā inertās tritilgrupas traucē lādiņnesēju pārnesi uz izstarotāja molekulām, tādā veidā samazinot elektroluminiscenci. Šī iemesla dēļ savienojums **Ir(ppy)₃**, kura mijiedarbību ar lādiņnesējmatricu nekavē stēriski apjomīgas inertās grupas, uzrāda visefektīvāko elektroluminiscenci. Ņemot vērā šos rezultātus, var secināt, ka ar šķīdumu metodēm izgatavojamu *OLED* izstarotājos agregācijas novēršanai nevajadzētu izmantot pasīvas izolējošās grupas. Kā labāku alternatīvu varētu piedāvāt perifērās grupas ar labām lādiņu transporta īpašībām un pielāgotiem enerģētiskajiem līmeņiem.

2.4. tabula

Ar tritilgrupām funkcionalizēto **Ir(ppy)₃** atvasinājumu *OLED* raksturlielumi

Izstarojošais slānis[a]	V_{on}[b], V	L_{max}, cd·m⁻²	η_c[c], cd·A⁻¹	η_p[d], lm·W⁻¹	*Efekt. samaz.*[e], %
PVK					
Ir(ppy)₃	4,5	2446	6,8	3,9	44
15a	4,5	844	4,8	2,4	71
15b	6	127	1,6	0,6	–
15c	7	136	1,0	0,3	–
PVK:OXD-7 (7:3)					
Ir(ppy)₃	3,5	2983	7,8	4,4	6
15a	4	3308	6,9	3,7	10
15b	4	2692	7,3	3,9	27
15c	3,5	1794	6,6	3,8	10
PVK:OXD-7 (3:7)					
Ir(ppy)₃	3,5	1048	2,2	1,1	27
15a	3,5	638	2,0	1,0	23
15b	3,5	680	2,4	1,3	28
15c	4	560	2,2	1,3	25

[a] Irīdija (III) kompleksu masas koncentrācija izstarojošā slānī ir 7 % (inertās tritilgrupas pieskaitot matricas masai). [b] Spriegums, pie kura iekārtas spilgtums ir 1 cd·m⁻². [c] Strāvas efektivitāte. [d] Jaudas efektivitāte. [e] Strāvas efektivitātes samazinājums intervālā no maksimālās vērtības līdz vērtībai pie maksimālā spilgtuma.

Oriģinālpublikācijas par šajā nodaļā aprakstītajiem pētījumiem – promocijas darba 1. un 2. pielikumā.

3. Karbēna-metāla-amīda kompleksu sintēze un *TADF* īpašības

Reto pārejas metālu (Ir, Pt u. c.) dārdzības, kā arī vides faktoru dēļ pēdējos gados tiek meklētas iespējas aizstāt fosforescentos izstarotājus ar *TADF* materiāliem. Lai nodrošinātu iespējami zemu ΔE_{ST}, kas veicinātu *RISC*, visbiežāk lietotā *TADF* molekulārā dizaina stratēģija ietver donora (D) un akceptora (A) molekulas fragmentu telpisku atdalīšanu, samazinot *HOMO* un *LUMO* pārklāšanos.[36] Tomēr vāja spina-orbītas mijiedarbība noved pie lēnas *RISC* un zema radiatīvo procesu ātruma.[37] Karbēna-metāla-amīda (*CMA*) kompleksi uzskatāmi par jaunu *TADF* materiālu klasi, kurā d^{10} metāla (Cu, Ag vai Au) atoms veido lineāras ģeometrijas kompleksu ar elektronakceptoro *N*-heterociklisko karbēna (*NHC*) ligandu un elektrondonoro amīda ligandu. Šāda ligandu konfigurācija nodrošina efektīvu frontālo molekulāro orbitāļu telpisko atdalīšanu, samazinot ΔE_{ST}. Savukārt metāla atoms veicina spina-orbītas mijiedarbību, kas nepieciešama ātrai *RISC*. Tādēļ iespējams īstenot *TADF* ar augstu Φ_{PL} un fotoluminiscences dzīves laiku zem 1 µs. Šo iemeslu dēļ *CMA* izstarotāji *OLED* iekārtās uzrāda veiktspējas parametrus, kas ir salīdzināmi ar fosforescentajiem izstarotājiem.[38–41]
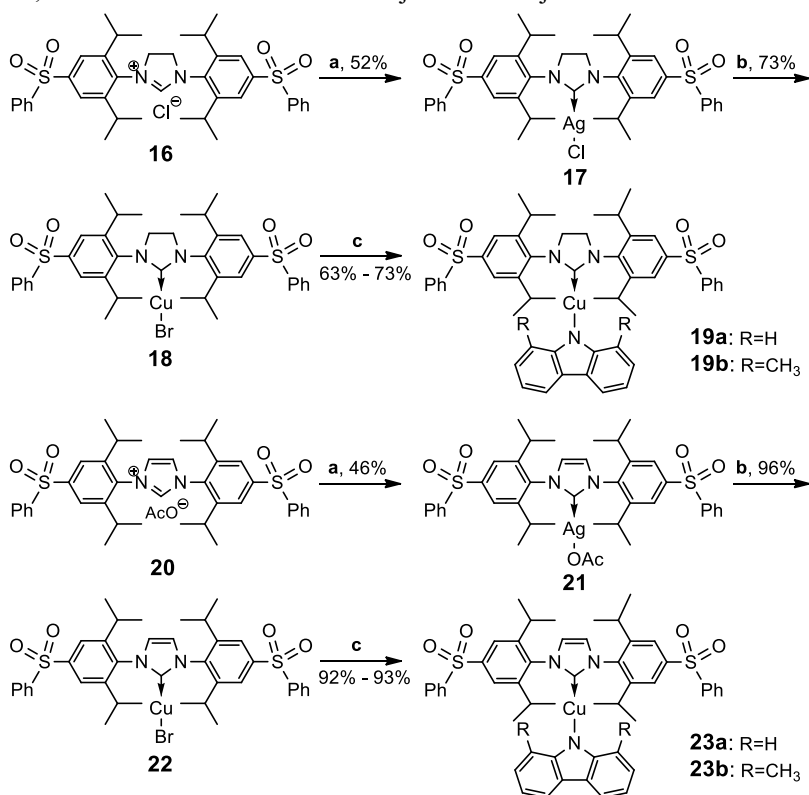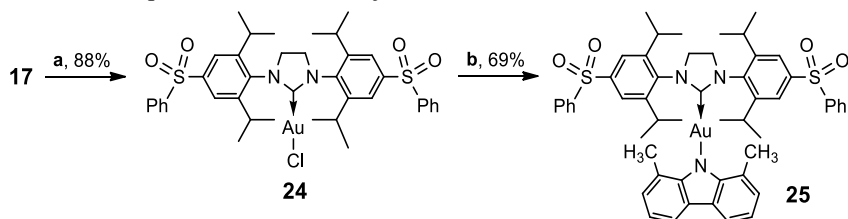

3.1. shēma. Ar fenilsulfonilgrupām funkcionalizētu Cu(I) *CMA* atvasinājumu sintēze.
(**a**) Ag₂O, MeCN; (**b**) CuBr, CH₂Cl₂; (**c**) Karbazola atvasinājums, KO*t*Bu, THF.

Promocijas darba ietvaros tika sintezēta *CMA* savienojumu sērija, kurā imidazola tipa *NHC* atvasinājuma 2,6-diizopropilfenilgrupām (*Dipp*) 4-pozīcijā pievienotas akceptorās

fenilsulfonilgrupas. *NHC* atvasinājumu sintēzei nepieciešamie 4,5-dihidro-1*H*-imidazolija un 1*H*-imidazolija sāļi **16** un **20** tika iegūti, modificējot literatūrā aprakstītu metodi.[42] Savienojumu **16** un **20** reakcijā ar Ag₂O tika iegūti sudraba(I) kompleksi **17** un **21**, no kuriem transmetalēšanas reakcijā ar CuBr sudrabs tika nomainīts ar varu, iegūstot vara(I) kompleksus **18** un **22**. Reakcijā ar deprotonētu karbazolu (*Cbz*) vai arī 1,8-dimetilkarbazolu (Me*Cbz*) tika iegūti *CMA* kompleksi **19a**, **19b**, **23a** un **23b** (3.1. shēma).

Lai noteiktu metāla atoma ietekmi uz ar fenilsulfongrupām funkcionalizēto *CMA* izstarotāju luminiscences īpašībām, tika iegūts kompleksa **19a** analogs **25**, kurā vara atoms nomainīts ar zelta atomu (3.2. shēma). Savienojuma **25** iegūšanai nepieciešamā izejviela **24** tika iegūta, sudraba kompleksu **17** transmetalējot ar AuCl·Me₂S.

3.2. shēma. Ar fenilsulfongrupām funkcionalizēta Au(I) *CMA* atvasinājuma **25** sintēze. (**a**) AuCl·Me₂S, DCM; (**b**) Karbazola atvasinājums, KO*t*Bu, THF.

Savienojumu sērija tika paplašināta tālāk, iegūstot nesimetriskus kompleksus **28a** un **28b**, kuros tikai vienai no *Dipp* grupām ir fenilsulfonilaizvietotājs (3.3. shēma). Šajā gadījumā vara(I) komplekss **27** no 4,5-dihidro-1*H*-imidazolija hlorīda **26** tika iegūts vienā stadijā, izmantojot *Santoro* izstrādāto procedūru.[43] Izmantojot šo metodi, nav nepieciešams vispirms iegūt sudraba kompleksu, ko tālāk izmanto transmetalēšanas reakcijā.
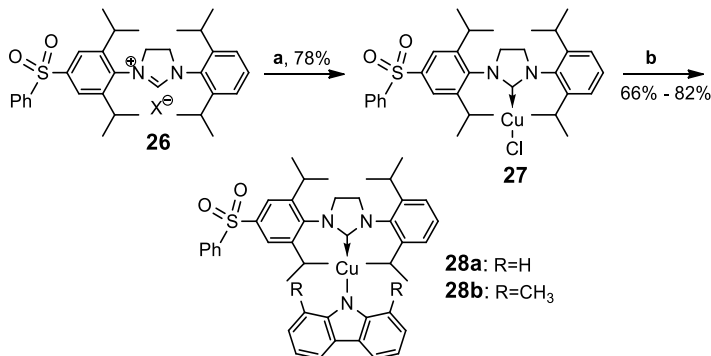
3.3. shēma. Nesimetrisku ar fenilsulfongrupu funkcionalizētu Cu(I) *CMA* atvasinājumu sintēze. (**a**) CuCl, K₂CO₃, acetons; (**b**) karbazola atvasinājums, KO*t*Bu, THF.

Iegūtie kompleksi ir baltas vai vāji iedzeltenas kristāliskas vielas. Cietā stāvoklī savienojumi ir stabili gaisā un neuzrāda sadalīšanās pazīmes pēc vairāku mēnešu glabāšanas. Vielām ir tendence sadalīties šķīdinātājos protonu avotu (H₂O, HCl u. c.) klātienē.

Nesimetriskajiem vienu fenilsulfonilgrupu saturošajiem kompleksiem **28a** un **28b** piemīt labāka šķīdība mazpolāros šķīdinātājos nekā simetriskajiem kompleksiem. Savienojumiem **19a**, **23b** un **28a** struktūras kristāliskā stāvoklī izdevās raksturot ar rentgenstruktūranalīzes palīdzību (3.1. att.). Nozīmīgākās savienojumu struktūras variācijas ir novērojamas amīda liganda ietekmē. Savienojumiem **19a** un **28a** (ar *Cbz* ligandu) Cu(I) metāla koordinācijai ir lineāra ģeometrija ar nelielu izliekumu pie metāla centra (∢α) un nelielu nobīdi no planārās sp^2 ģeometrijas (∢β) pie karbazolīda N atoma. *Cbz* un imidazolidīna plaknes šajos savienojumos ir novietotas praktiski koplanāri. Savienojumā **23b** Me*Cbz* liganda metilgrupu stēriskā efekta dēļ novērojamas ievērojamas nobīdes no lineārās kompleksa ģeometrijas, kas galvenokārt izpaužas kā ievērojama karbazolīda N atoma piramidalizācija (∢β = 147,3°). Tā rezultātā Me*Cbz* liganda un *Dipp* cikla plakņu novietojums tuvojas koplanāram (∢γ = 43,4°).
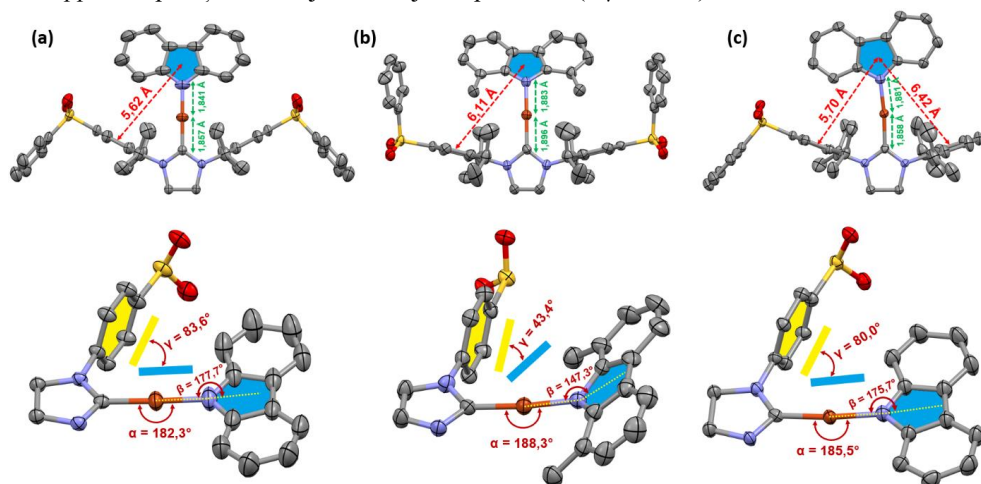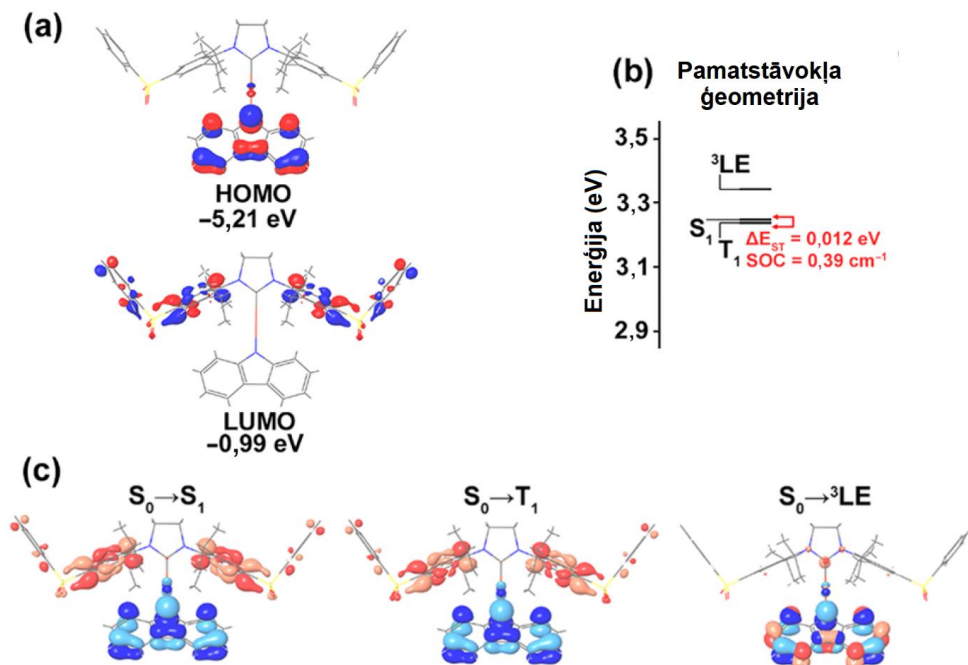

3.1. att. Savienojumu **19a** (a) **23b** (b) un **28a** (c) rentgenstruktūras un galvenie struktūru raksturojošie parametri.

Izmantojot no laika atkarīgos *DFT* (*TD-DFT*) aprēķinus, tika noskaidrots, ka visiem sērijas savienojumiem *HOMO* pamatā atrodas uz karbazolīda liganda un tai ir neliels metāla atoma ieguldījums (3.2. att., a). *LUMO* ir novietota uz difenilsulfongrupas bez centrālā karbēna cikla un metāla atoma ieguldījuma šajā orbitālē, kas ir būtiska atšķirība no literatūrā aprakstītajiem *CMA* izstarotājiem.[44–46] Šāds ortogonāls frontālo molekulāro orbitāļu novietojums noved pie ļoti mazas *HOMO* un *LUMO* pārklāšanās.

Zemākās enerģijas singleta pāreja (S$_0$→S$_1$) norisinās ar caurtelpas (*through-space*) ligands-ligands lādiņa pārneses (*LLCT*) mehānismu (3.2. att., c). Visiem sērijas savienojumiem S$_0$→S$_1$ pārejas paredzamais oscilatora spēks ir zems (robežās no 0,0021 līdz 0,0069). Kompleksiem ar Me*Cbz* ligandu S$_0$→S$_1$ pārejai ir paredzams lielāks oscilatora spēks nekā kompleksiem ar *Cbz* ligandu, kas saistīts ar leņķa γ samazināšanos (3.1. att.) starp donora karbazola un akceptora *Dipp* plaknēm. Frontālās molekulārās orbitāles ir telpiski atdalītas, tāpēc paredzamā enerģijas starpība starp S$_1$ un T$_1$ stāvokļiem ir zema (ΔE_{ST} = 0,007–0,021 eV). Niecīgā metāla atoma ieguldījuma *LUMO* orbitālē dēļ *SOC* starp S$_1$ un T$_1$ stāvokļiem ir zemāka nekā citiem *CMA*

kompleksiem (3.2. att., b).[47] Tomēr arī neliela *SOC* var nodrošināt ātru *RISC*, ņemot vērā zemās ΔE_{ST} vērtības.[48]

(a)

HOMO
−5,21 eV

LUMO
−0,99 eV

(b) **Pamatstāvokļa ģeometrija**

Enerģija (eV)

^{3}LE

S_1
T_1 ΔE_{ST} = 0,012 eV
SOC = 0,39 cm^{-1}

(c)

$S_0 \rightarrow S_1$

$S_0 \rightarrow T_1$

$S_0 \rightarrow {}^3LE$

3.2. att. (a) *HOMO* un *LUMO* orbitāles savienojumam **19a**. (b) Zemākās enerģijas ierosināto stāvokļu enerģētiskā diagramma. (c) Naturālās pārejas (*natural transition*) orbitāles.

Visiem savienojumiem sērijā piemīt praktiski identiska *UV-Vis* absorbcijas aina. 300–380 nm apgabalā novērojamas vairākas strukturētas absorbcijas joslas, kuru novietojums un forma dažādas polaritātes šķīdinātājos mainās maz (3.3. att., a). Šīs absorbcijas joslas ir attiecināmas uz karbazolīda liganda lokālajām π–π* pārejām. *CT* pārejai šajos savienojumos atbilst plata vājas intensitātes absorbcijas josla, kas mazpolāros šķīdinātājos turpinās līdz aptuveni 450 nm. Šīs absorbcijas joslas *LLCT* raksturu apstiprina hipsohromā nobīde, kas novērojama, palielinoties šķīdinātāja polaritātei.[40] Pārklāšanās ar karbazolīda liganda π–π* absorbcijas joslām dēļ *CT* joslas intensitātes precīza noteikšana ir apgrūtināta. Toluola šķīdumos *CT* absorbcijas joslas ekstinkcijas koeficientu var aptuveni novērtēt robežās no 1000 M^{-1}cm^{-1} līdz 3000 M^{-1}cm^{-1}. Turklāt savienojumu sērijas ietvaros savienojumiem ar Me*Cbz* ligandu novērojama intensīvāka *CT* absorbcija nekā savienojumiem ar *Cbz* ligandu, apstiprinot *TD-DFT* aprēķinu rezultātus.
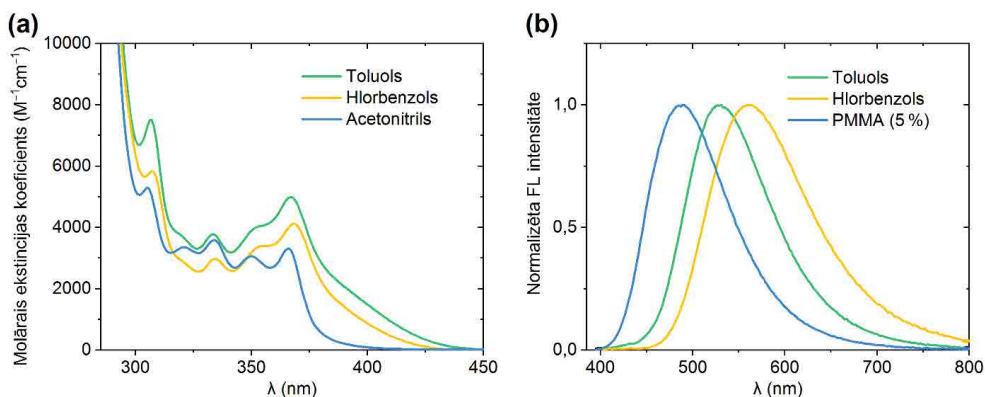
3.3. att. (a) Savienojuma **19b** *UV-Vis* absorbcija dažādos šķīdinātājos (10^{-5} M);
(b) savienojuma **19b** fotoluminiscence toluolā, hlorbenzolā (10^{-5} M) un *PMMA* (5 % masas koncentrācija).

Savienojumiem raksturīgas līdzīgas luminiscentās īpašības toluola šķīdumos (3.1. tab.). Kompleksiem toluola šķīdumā novērojama izstarošana no *CT* ierosinātā stāvokļa ar maksimumu pie 519–547 nm. Palielinoties šķīdinātāja polaritātei, *CT* izstarošanas joslai novērojama batohroma nobīde (3.3. att., b). Dažādu iespējamo vibracionālās relaksācijas procesu dēļ toluola šķīdumā kompleksu Φ_{PL} nepārsniedz 0,39. Turklāt, līdzīgi kā fosforescento irīdija kompleksu gadījumā, skābekļa klātienē *CMA* kompleksu Φ_{PL} samazinās, netieši liecinot par tripleta ierosināto stāvokļu iesaisti izstarošanas mehānismā.

3.1. tabula

Ar fenilsulfonilgrupām funkcionalizēto *CMA* atvasinājumu luminiscences raksturlielumi

Savien.	$\lambda_{\max em}{}^{a}$, nm	$\Phi_{PL}{}^{a}$	$\lambda_{\max em}{}^{b}$, nm	$\Phi_{PL}{}^{b}$	$\tau_{prompt}{}^{b}$, ns	$\tau_1{}^{b}$, µs	$\tau_2{}^{b}$, µs	$k_r{}^{b}$, $\times 10^5$ s^{-1}	$k_{nr}{}^{b}$, $\times 10^5$ s^{-1}
19a	523	0,31	472	0,86	6 (0,2 %)	2,5 (45,4 %)	10,6 (54,4 %)	1,25	0,20
19b	521	0,25	482	0,84	12 (0,4 %)	1,5 (61,6 %)	5,2 (38,0 %)	2,89	0,55
23a	547	0,21	488	0,90	10 (0,4 %)	2,0 (46,6 %)	8,3 (53,0 %)	1,68	0,19
23b	541	0,28	492	0,84	19 (0,8 %)	1,4 (59,8 %)	4,3 (39,4 %)	3,32	0,63
25	521	0,27	502	0,69	1 (0,2 %)	1,4 (31,8 %)	4,7 (68,0 %)	1,89	0,85
28a	519	0,38	464	0,80	19,4	2,3	9,9	–	–
28b	521	0,39	476	0,79	37,2 (0,7 %)	1,4 (44,3 %)	5,4 (55,0 %)	2,21	0,59

[a] Luminiscence, toluola šķīdums. [b] Luminiscence, *PMMA* filma (5 % masas koncentrācija).

Cietajā fāzē samazinās molekulārās kustības iespējas, tādēļ, salīdzinot ar šķīdumiem, plānajās amorfajās kārtiņās (*PMMA*, 5 % izstarotāja masas koncentrācija) kompleksu Φ_{PL} ievērojami pieaug, sasniedzot maksimālo vērtību 0,90 savienojumam **23a**. Salīdzinot ar šķīdumiem, *PMMA* filmām novērojama izstarošanas hipsohroma nobīde (rigidohromisms[49]). Kompleksu *PMMA* filmām raksturīgs samērā sarežģīts *TADF* mehānisms ar dažādām variācijām savienojumu sērijas ietvaros. Visiem savienojumiem raksturīga trieksponenciāla fotoluminiscences dzīveslaika kinētika (3.4. att., a). Lēnas *ISC* dēļ savienojumiem novērojama *TADF* tūlītējā (*prompt*) fluorescence (τ_{prompt} = 6 – 37 ns), tās ieguldījums kopējā fotoluminiscences intensitātē nepārsniedz 1 %. Starpsistēmu pārejas ātrumu šajā gadījumā samazina zemā *SOC* starp S_1 un T_1 līmeņiem. Savienojumiem novērojamas divas *TADF* aizkavētās fluorescences komponentes: pirmā ar dzīves laiku (τ_1) robežās no 1,36 μs līdz 2,50 μs un otrā ar dzīves laiku (τ_2) robežās no 4,25 μs līdz 10,59 μs. Abu aizkavēto fluorescences komponenšu ieguldījums kopējā fotoluminiscences intensitātē ir samērojams. Aizkavēto fluorescences komponenšu *TADF* daba tika pierādīta, dzēsējot paraugus un novērojot pakāpenisku radiatīvo procesu ātrumu konstantes (k_r) samazināšanos. Eksperimentāli noteiktā *TADF* aktivācijas enerģija (ΔE_{ST}) savienojumu sērijā mainās robežās no 0,0068 eV līdz 0,0110 eV, kas sakrīt ar *TD-DFT* aprēķinos paredzētājām vērtībām. Duālā *TADF* šajā gadījumā ir izskaidrojama ar izstarošanu no divām dažādām molekulas konformācijām. Kā izņēmums jāmin Au(I) komplekss **25**, kam ātrākā komponente (τ_1) ir *TADF* izstarošana, savukārt lēnākā komponente (τ_2) saistīta ar fosforescenci no S_1 enerģētiski tuvā T_2 stāvokļa. Kopējā radiatīvo procesu ātrumu konstante savienojumu sērijā mainās robežās no $1{,}25\cdot10^5$ līdz $3{,}32\cdot10^5$ s^{-1}. Kompleksiem ar Me*Cbz* ligandu k_r vērtības ir lielākas nekā kompleksiem ar *Cbz* ligandu, kas saistīts ar lielāku oscilatora spēku zemākās enerģijas *CT* pārejām šajos savienojumos.
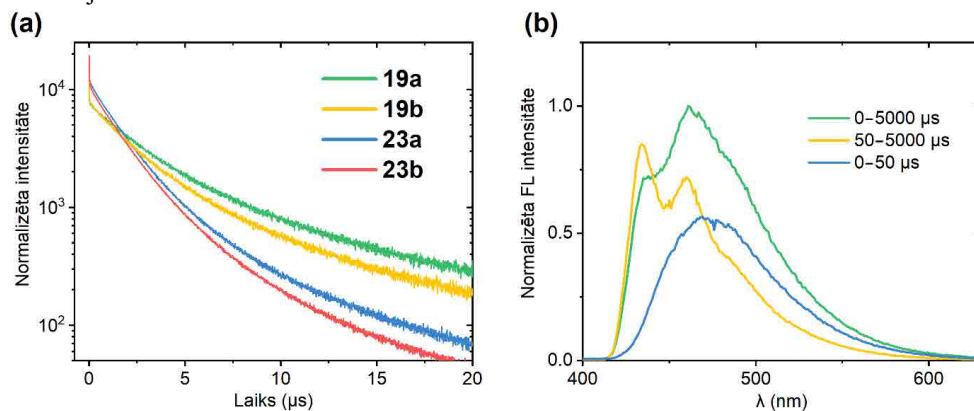
3.4. att. (a) Savienojumu **19a–b** un **23a–b** fotoluminiscences kinētika *PMMA*;
(b) savienojuma **19b** laikā atkarīgā fotoluminiscence, *PMMA* filma (5 % masas konc.) 77 K temperatūrā.

Bez *TADF* un iespējamās fosforescences no T_2 stāvokļa (savienojums **25**) jāņem vērā arī izstarošana no karbazolīda lokālā tripleta ierosinātā stāvokļa (^3LE). Salīdzinot ar *TADF*, šai

izstarošanai ir ļoti ilgs dzīves laiks (vairāki simti līdz tūkstoši μs), tādēļ laikā atkarīgā (*time resolved*) emisijas spektroskopija ir izmantojama, lai izšķirtu šo luminiscences komponenti (3.4. att., b). Izstarošanai no ^3LE ir novērojama karbazola atvasinājumu fosforescencei raksturīga sīkstruktūra.[41] Savienojuma **23a** (*PMMA* filma) gadījumā karbazolīda lokālā tripleta izstarošana novērojama istabas temperatūrā, pārējiem savienojumiem tā parādās, paraugus dzesējot. Saskaņā ar *TD-DFT* aprēķiniem ^3LE līmenis pēc enerģijas ir samērā tuvs S_1 līmenim. Atdzesējot paraugus, notiek *PMMA* rigidifikācija, kas destabilizē ar *LLCT* procesu saistīto S_1 līmeni. Tā rezultātā S_1 pēc enerģijas var tuvināties ^3LE līmenim vai pat pārsniegt to, padarot iespējamu fosforescenci no ^3LE ierosinātā stāvokļa.

Lai gan jauniegūto savienojumu sērijas savienojumi pēc struktūras atbilst *CMA* izstarotāju klasei, luminiscences mehānismi būtiski atšķiras. Šajā gadījumā *TADF* tiek īstenota ar caurtelpas (*through-space*) *CT* mehānismu. Tādēļ izstarotājiem ir ļoti zemas ΔE_{ST} vērtības. Savukārt nelielā *SOC*, ko nodrošina kompleksa metāla atoms, veicina *RISC*. Tādējādi sasniegtās Φ_{PL} un k_r vērtības ir salīdzināmas ar šobrīd labākajiem *CMA* klases izstarotājiem.[50] Karbēna cikls jaunajos savienojumos no fotofizikālo īpašību skatpunkta ir inerts savienojošais struktūrelements starp donora un akceptora fragmentiem.

Lai izvērtētu savienojumu elektroluminiscences īpašības, komplekss **23b** tika izmantots, lai izgatavotu *OLED* (*Dr. phys.* A. Vembris) ar šādu struktūru: *ITO/PEDOT:PSS* (40 nm)/*PolyTPD* (30 nm)/**23b** (20 masas %):*CzSi* (40 nm)/*TPBi* (40 nm)/LiF (1 nm)/Al (100 nm). Izstarojošais slānis tika pagatavots no vielu šķīduma, izmantojot rotācijas uzklāšanas metodi. Iekārta uzrādīja 6 V ieslēgšanās spriegumu, 1,7 cd/A strāvas efektivitāti, 0,6 lm/W jaudas efektivitāti un 0,8 % ārējo kvantu efektivitāti. Iekārtas elektroluminiscences spektrs liecina par izstarošanu no kompleksa *CT* stāvokļa. Iegūtie rezultāti demonstrē savienojumu piemērotību elektroluminiscento ierīču izveidei, tomēr ierīču veiktspējas uzlabošanai nepieciešama tālāka optimizācija.

Promocijas darba turpinājumā tika pētītas uz 1,3-tiazol-2-ilidēna karbēna fragmenta bāzētu *CMA* atvasinājumu fotofizikālās īpašības un elektroluminiscences pielietojuma iespējas. Mērķsavienojumu sintēzei kā izejvielas tika izmantoti literatūrā aprakstītie 1,3-tiazolija perhlorāta sāļi **29–31** (3.4. shēma).[51] No perhlorāta sāļiem CuCl klātbūtnē *in situ* iegūstot brīvus karbēnus, vispirms tika sintezēti karbēna–Cu–Cl kompleksi, kas tālāk tika izmantoti *CMA* atvasinājumu sintēzē. Izmantojot dažādus karbazola atvasinājumu ligandus, tika iegūta astoņu savienojumu sērija: **32a**, **33a** un **34a** ar karbazola (*Cbz*) ligandu, **32b**, **33b** un **34b** ar 1,8-dimetilkarbazola (Me*Cbz*) ligandu, **34c** ar 3,6-di-*terc*-butilkarbazola (*t*Bu*Cbz*) un **34d** ar 3,6-di-*terc*-butil-1,8-dimetilkarbazola (Me*t*Bu*Cbz*) ligandu. Savienojumi cietajā fāzē ir stabili, uzglabājot gaisā, un ar vidēji labu šķīdību organiskajos šķīdinātājos, piemēram, toluolā, hlorbenzolā, dihlormetānā un THF. Savienojumu šķīdību ievērojami uzlabo *terc*-butilgrupas. Kā interesants izņēmums jānosauc savienojums **34b**, kuram istabas temperatūrā ir ļoti zema šķīdība organiskajos šķīdinātājos.
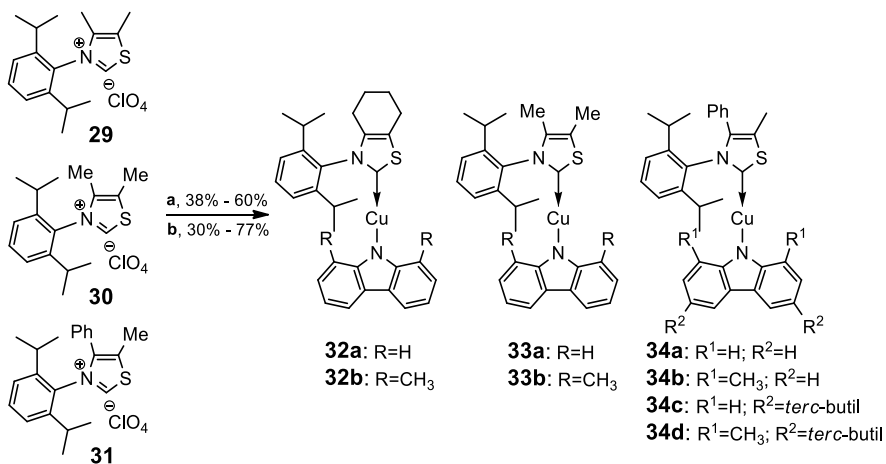
3.4. shēma. Uz 1,3-tiazol-2-ilidēna karbēna fragmenta bāzēto Cu(I) *CMA* atvasinājumu
sintēze.
(**a**) CuCl, NaO*t*Bu, THF; (**b**) karbazola atvasinājums, KO*t*Bu, THF.

Savienojumiem raksturīga praktiski lineāra ģeometrija pie kompleksveidotāja metāla atoma
un koplanārs karbazolīda un karbēna ciklu novietojums (3.5. att.). Dažādas strukturālās
deformācijas ievieš aizvietotāji pie karbazolīda liganda (1,8-dimetilgrupas), kā arī pie
1,3-tiazol-2-ilidēna cikla (4-fenilgrupa). 1,8-Dimetilgrupas pie karbazolīda liganda izraisa
atgrūšanos no *Dipp* grupas, pagriežot ∡α stēriski neaizsegtā sēra atoma virzienā, kā arī
pagarinot Cu-N un Cu-C$_{karbēns}$ saišu garumus. Savukārt 4-fenilgrupa pie karbēna cikla izraisa
Dipp (∡γ) un karbazolīda (∡β) plakņu pagriešanos attiecībā pret karbēna cikla plakni.
Attiecīgās grupas ievieš ne tikai struktūras deformācijas, bet arī samazina molekulas
konformacionālo brīvību, ierobežojot *Dipp*, 4-fenilgrupas un karbazolīda liganda rotācijas
iespējas. Savienojuma **34b** zemā šķīdība varētu būt tieši saistīta ar rigīdo molekulāro struktūru,
kas paaugstina molekulas tendenci veidot vāji šķīstošus kristālus.
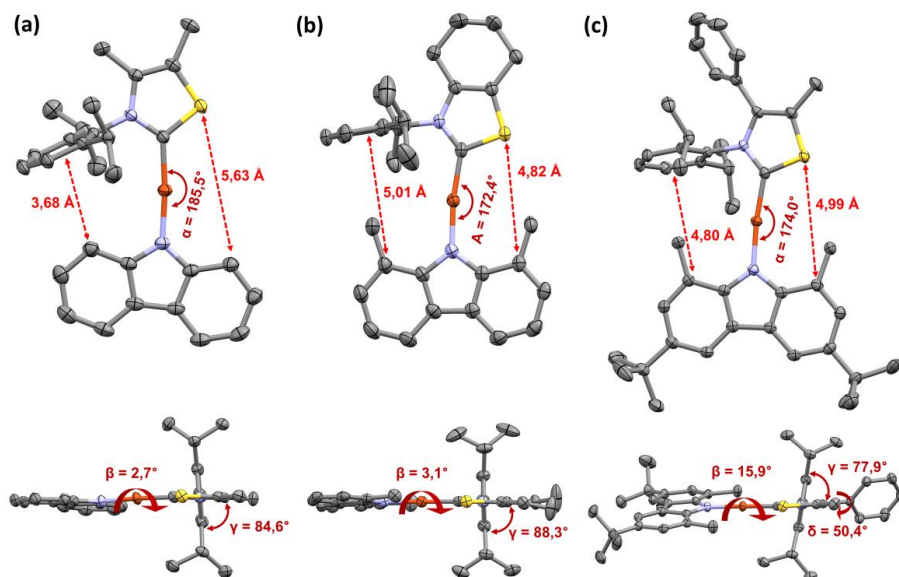
3.5. att. Savienojumu **33a** (a), **32b** (b) un **34d** (c) rentgenstruktūras un galvenie struktūru raksturojošie parametri.

Līdzīgi kā ar fenilsulfonilgrupām funkcionalizēto *CMA* gadījumā, arī 1,3-tiazol-2-ilidēna atvasinājumiem toluola šķīdumā apgabalā no 300 nm līdz 380 nm novērojamas karbazolīda liganda lokālo π–π* pāreju *UV-Vis* absorbcijas joslas (3.6. att., a). Savukārt kompleksu zemākās enerģijas absorbcijas joslas ir atbilstošas *CT* pārejai, kuras intensitāte ir ievērojami lielāka nekā fenilsulfonilfunkcionalizētajiem *CMA* atvasinājumiem, sasniedzot molārās ekstincijas koeficientu $8,0 \cdot 10^3$ M^{-1} cm^{-1} savienojuma **34c** gadījumā. *CT* absorbcijas maksimuma novietojums ir atkarīgs no aizvietotājiem pie karbazolīda liganda. Pievienojot karbazolīda ligandam vāji elektrondonorās metil- vai *terc*-butilgrupas, novērojama neliela absorbcijas maksimuma batohroma nobīde. Raksturīgi *CMA* tipa savienojumiem, kompleksu *CT* absorbcijas joslas, palielinoties šķīdinātāja polaritātei, nobīdās hipsohromi.[40]
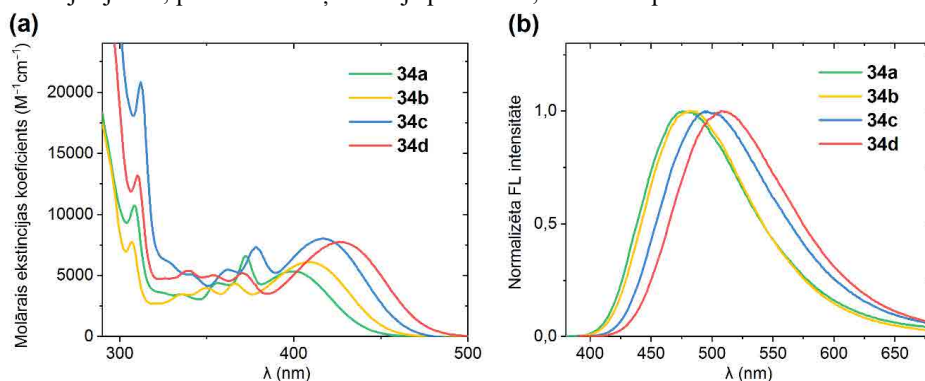
3.6. att. (a) Savienojumu **34a–d** *UV-Vis* absorbcija toluolā (10^{-5} M); (b) savienojumu **34a–d** fotoluminiscence *PMMA* filmā (5 % masas koncentrācija).

Savienojumu toluola šķīdumu un plāno amorfo kārtiņu (*PMMA*, 5 % izstarotāja masas koncentrācija) luminiscences raksturlielumi apkopoti 3.2. tabulā. Izstarošana norisinās no *CT* ierosinātā stāvokļa. Līdzīgi kā *UV-Vis* absorbcijas gadījumā, luminiscences maksimuma novietojums ir atkarīgs no aizvietotājiem pie karbazolīda liganda (3.6. att., b). Salīdzinot ar kompleksu šķīdumiem, cietajā fāzē novērojama Φ_{PL} palielināšanās un luminiscences maksimuma hipsohroma nobīde. Cietajā fāzē novērojama korelācija starp kompleksu struktūru un k_r. Kompleksiem ar 1,8-dimetilaizvietotu karbazolīda ligandu k_r ir 1,1–1,6 reizes lielāka nekā struktūras analogiem ar 1,8 pozīcijās neaizvietotu karbazolīdu. Turklāt vislielākās k_r vērtības ir kompleksiem **34b** un **34d**, kuriem bez 1,8-dimetilaizvietota karbazolīda ir 4-fenilaizvietots 1,3-tiazol-2-ilidēna cikls. Tādēļ var secināt, ka karbazolīda liganda rotācijas ierobežošana palielina k_r vērtības.

3.2. tabula

1,3-Tiazol-2-ilidēna karbēna Cu(I) *CMA* atvasinājumu luminiscences raksturlielumi

Savien.	$\lambda_{\max em}{}^a$, nm	$\Phi_{PL}{}^a$	$\lambda_{\max em}{}^b$, nm	$\Phi_{PL}{}^b$	τ^b, μs	$k_r{}^b$, ×10^5 s^{-1}	$k_{nr}{}^b$, ×10^5 s^{-1}
32a	511	0,37	471	0,74	2,6	2,8	1,0
32b	517	0,42	478	0,82	1,9	4,3	0,9
33a	507	0,41	467	0,68	1,9	3,6	1,6
33b	513	0,79	474	0,84	2,1	4,0	0,8
34a	521	0,39	479	0,71	2,1	3,4	1,4
34b	527	0,23	484	0,78	1,6	4,9	1,4
34c	549	0,73	499	0,73	1,6	4,6	1,7
34d	554	0,76	509	0,86	1,2	7,2	1,2

[a] Luminiscence, toluola šķīdums. [b] Luminiscence, *PMMA* filma (5 % masas koncentrācija).

Savienojumiem *PMMA* filmās novērojama monoeksponenciāla fotoluminiscences dzīveslaika kinētika ar τ_{PL} robežās no 1,2 μs līdz 2,6 μs (3.7. att., a). Visiem sērijas savienojumiem, izņemot **34d**, dzesējot paraugu, parādās izstarošana no karbazolīda lokālā tripleta ierosinātā stāvokļa (^3LE). Līdzīgi kā ar fenilsulfonilgrupām funkcionalizēto *CMA* gadījumā, luminiscence no ^3LE ir izskaidrojama ar *PMMA* matricas rigidifikāciju un tās izraisītu *CT* līmeņu destabilizāciju. Savienojums **34d** šajā gadījumā ir izņēmums, jo tā *CT* līmenis pēc enerģijas ir nobīdīts pārāk tālu no ^3LE līmeņa. Tādēļ savienojumam **34d** visā temperatūru apgabalā no T_{ist} līdz 10 K ir raksturīga tikai *CT* izstarošanas josla, kuras maksimumam pie pakāpeniskas dzesēšanas novērojama hipsohromā nobīde. Paraugu dzesējot, novērojams arī τ_{PL} pieaugums līdz 140 μs pie 10 K (3.7. att., b), kas liecina par *CT* izstarošanas *TADF* dabu. Ja istabas temperatūrā ir novērojama *TADF* no S$_1$ līmeņa, tad, pakāpeniski atdzesējot paraugu, pieaug fosforescences intensitāte no T$_1$ līmeņa, līdz 50 K temperatūrā izstarošana notiek praktiski tikai no T$_1$ līmeņa. Attiecinot τ_{PL} atkarību no temperatūras pret pārveidotu Bolcmana vienādojumu[52] (3.7. att., b), tika noteikta ΔE_{ST}, kas savienojumam **34d** ir 0,044 eV.
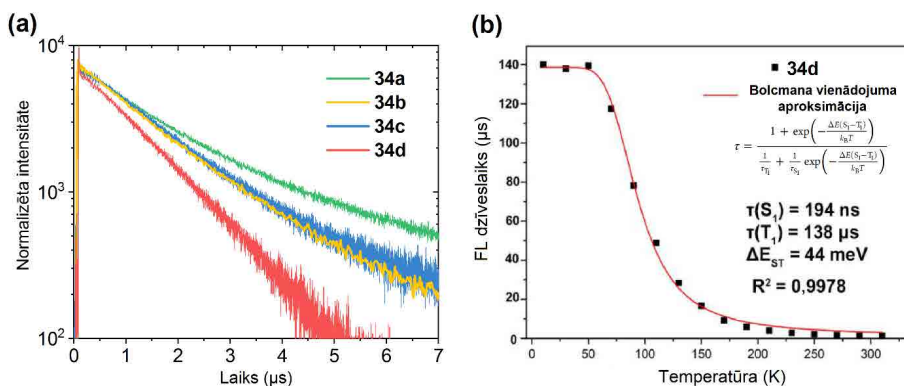
3.7. att. (a) Savienojumu **34a–d** fotoluminiscences kinētika, *PMMA* filma (5 % masas koncentrācija); (b) savienojuma **34d** fotoluminiscences dzīves laika atkarības no temperatūras attiecināšana pret pārveidotu Bolcmana vienādojumu, *PMMA* filma (5 % masas koncentrācija).

Lai izpētītu luminiscences mehānismu un izprastu stērisko efektu ietekmi uz luminiscences īpašībām, kompleksiem **34a** un **34b** tika veikti *TD-DFT* aprēķini (*Dr. chem. G. Baryshnikov*). Aprēķinu rezultātā tika noskaidrots, ka savienojumiem *HOMO* atrodas uz karbazolīda liganda, savukārt *LUMO* – uz 1,3-tiazol-2-ilidēna fragmenta (3.8. att., a). Tādēļ pārejai uz S_1 ierosināto stāvokli ir *LLCT* daba. Gan *HOMO*, gan *LUMO* ir neliels metāla atoma ieguldījums, tāpēc palielinās gan $S_0 \rightarrow S_1$ pārejas oscilatora spēks, gan ΔE_{ST}.

Saskaņā ar *TD-DFT* aprēķiniem, 1,3-tiazol-2-ilidēna un karbazolīda liganda ciklu plaknes ir praktiski koplanāras pamatstāvoklī S_0 un T_1 ierosinātajā stāvoklī. Savukārt S_1 ierosinātajā stāvoklī šīm plaknēm ir tendence ieņemt perpendikulāru novietojumu (3.8. att., b), savienojuma **34a** gadījumā ieņemot pagriešanās leņķi ∢β = 77°. Tikmēr 1,8-dimetilgrupu un *Dipp* grupu stēriskās mijiedarbības dēļ karbazolīda liganda pagriešanās savienojumā **34b** ir traucēta, tādēļ pagriešanās leņķis ir mazāks (∢β = 55°). Šī iemesla dēļ pārejas $S_1 \rightarrow S_0$ aprēķinātais oscilatora spēks savienojumam **34b** ir divas reizes lielāks nekā **34a**, kas noved arī pie divreiz ātrākas aizkavētās fluorescences. Tādējādi stēriski apjomīgo grupu mijiedarbība palielina radiatīvo procesu ātruma konstanti 1,3-tiazol-2-ilidēna *CMA* atvasinājumu sērijā.
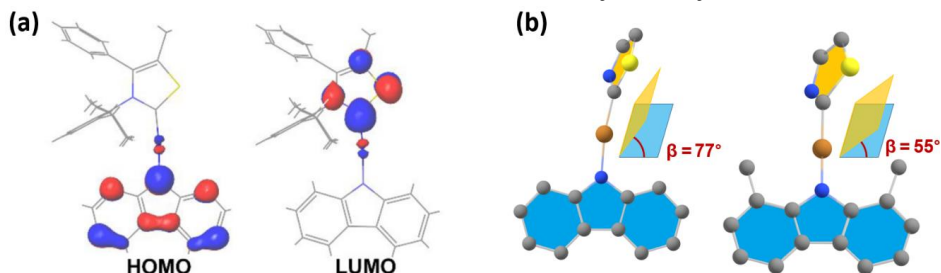
3.8. att. (a) *HOMO* un *LUMO*, savienojums **34a**, S_0 ģeometrija; (b) divplakņu kakta leņķi starp 1,3-tiazol-2-ilidēna un karbazolīda liganda ciklu plaknēm savienojumos **34a** un **34b**, S_1 ģeometrija.

Savienojums **34d** cietajā fāzē uzrāda gan visaugstāko Φ_{PL}, gan lielāko k_r, tāpēc tas kopā ar struktūras analogu **34c** tika izvēlēts *OLED* izveidei (*Dr. C. H. Chang*). No četriem izstarojošā slāņa matricas materiāliem (*CBP*, *mCBP*, *mCP* un *DPEPO*) kā visefektīvākais tika izvēlēts *mCBP*. *OLED* izveidei izmantota šāda struktūra – *ITO/TAPC* (35 nm)/*TCTA* (5 nm)/izstarojošais slānis (25 nm)/*TmPyPB* (50 nm)/LiF (1,5 nm)/Al (150 nm) ar izstarotāja masas koncentrāciju izstarojošā slāni 1 %, 5 %, 10 % un 20 %. Izstarojošais slānis tika pagatavots ar vakuuma uzklāšanas metodi. Visaugstākos veiktspējas parametrus uzrādīja ierīce, kurā kā izstarotājs izmantots savienojums **34c** 10 % masas koncentrācijā, sasniedzot 16,5 % ārējo kvantu efektivitāti un 44215 cd·m^{-2} maksimālo spožumu (3.3. tab.).
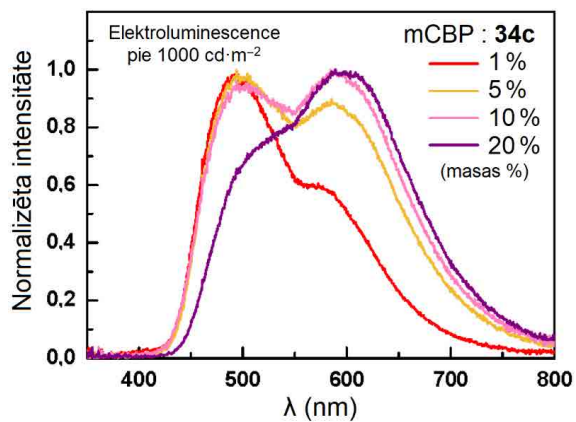
Savienojumam **34c** elektroluminiscences spektrā novērojamas divas izteiktas izstarošanas joslas ar maksimumiem pie 495 nm un 600 nm (3.9. att.). Turklāt, palielinoties izstarotāja koncentrācijai, izstarošanas joslas pie 600 nm relatīvā intensitāte pret izstarošanas joslu pie 495 nm pieaug. Elektroluminiscence pie 495 nm tiek skaidrota ar **34c** *TADF* izstarošanu, savukārt elektroluminiscence pie 600 nm varētu būt saistīta ar savienojuma **34c** dimēru izstarošanu, citiem vārdiem, eksimēru elektroluminiscenci. Rezultātā iegūts ļoti plats elektroluminiscences spektrālais profils, kas ir pielietojams baltās gaismas *OLED* izveidei. Savienojumam **34d** eksimēru elektroluminiscence ir novērojama daudz mazākā mērā nekā **34c**. Šajā gadījumā 1,8-dimetilgrupu ierosinātie stēriskie efekti samazina savienojuma **34d** iespējas izstarojošajā slānī veidot dimērus.

3.3. tabula

Savienojumu **34c** un **34d** *OLED* raksturlielumi

Izstarojošais slānis	$V_{on}{}^a$, V	L_{max}, cd·m^{-2}	$\eta_{ext}{}^b$, %	$\eta_c{}^c$, cd·A^{-1}	$\eta_p{}^d$, lm·W^{-1}
34c:*mCBP*					
1 %	3,8	13542	10,3/7,0^e	22,7/15,4^e	19,8/9,3^e
5 %	3,6	17839	13,7/9,8	25,9/18,6	22,3/11,6
10 %	3,5	44215	16,5/16,1	34,1/33,1	27,1/23,6
20 %	3,7	41695	15,7/14,6	26,0/25,5	20,2/17,0
34d:*mCBP*					
1 %	3,7	35947	12,9/10,6	31,5/25,8	25,4/17,0
5 %	3,6	42773	12,2/11,6	31,9/30,4	26,0/20,4
10 %	3,8	36478	9,2/9,1	21,7/21,6	15,5/13,2
20 %	3,8	37183	5,9/5,8	14,8/13,4	9,4/8,6

[a] Spriegums, pie kura iekārtas spilgtums ir 1 cd·m^{-2}. [b] *OLED* ārējā kvantu efektivitāte. [c] Strāvas efektivitāte. [d] Jaudas efektivitāte. [e] Maksimālās sasniegtās vērtības un vērtības noteiktas pie 100 cd·m^{-2}.

3.9. att. Savienojuma **34c** elektroluminiscences spektri pie 1000 cd·m^{-2} spožuma dažādām izstarotāja koncentrācijām.

Oriģinālpublikācijas par šajā nodaļā aprakstītajiem pētījumiem – promocijas darba 3.–6. pielikumā.

SECINĀJUMI

1. Organisko izstarotāju funkcionalizēšana ar tritilgrupām ir izmantojama, lai iegūtu luminiscentus materiālus, kas no viegli gaistošiem šķīdinātājiem veido morfoloģiski stabilas amorfās plānās kārtiņas. Tas ļauj iegūtos savienojumus lietot *OLED* iekārtu izgatavošanai ar rotācijas pārklāšanas metodi.

2. Tritilgrupas traucē lādiņnesēju pārnesi uz izstarotāja molekulām, tādējādi samazinot elektroluminiscences efektivitāti.

3. Demonstrētajiem ar fenilsulfonilgrupām funkcionalizētajiem un 1,3-tiazol-2-ilidēna karbēna fragmentu saturošajiem *CMA* tipa Cu(I) kompleksiem cietajā fāzē novērojama efektīva fotoluminiscence ar augstu Φ_{PL} un dažu mikrosekunžu dzīves laiku.

4. Ar fenilsulfonilgrupām funkcionalizēto *CMA* atvasinājumu sērijā *TADF* tiek īstenota ar caurtelpas (*through-space*) lādiņa pārneses mehānismu. Zemas ΔE_{ST} vērtības kombinācijā ar metāla atoma nodrošināto spina-orbītas sadarbību veicina efektīvu un ātru *TADF* tipa izstarošanu.

5. Stēriskie efekti ietekmē pētīto *CMA* atvasinājumu fotofizikālās īpašības. Ar fenilsulfonilgrupām funkcionalizēto *CMA* savienojumu sērijā karbazolīda liganda 1,8-dimetilgrupu stēriskie efekti noved pie labvēlīgāka D un A fragmentu savstarpējā novietojuma, tādējādi palielinot radiatīvo procesu konstanti. Savukārt 1,3-tiazol-2-ilidēna *CMA* atvasinājumu sērijā radiatīvos procesus veicina stēriski apjomīgu grupu mijiedarbība, kas samazina karbazolīda liganda pagriešanos ierosinātajā S_1 stāvoklī.

6. 1,3-Tiazol-2-ilidēna *CMA* atvasinājumu sērijā novērojama efektīva eksimēru elektroluminiscence, kas var tikt izmantota baltu gaismu izstarojošu *OLED* izveidē.

LITERATŪRAS SARAKSTS

[1]   B. Geffroy, P. le Roy, C. Prat, *Polym. Int.* **2006**, *55*, 572–582.

[2]   F. So, J. Kido, P. Burrows, *MRS Bull.* **2008**, *33*, 663–669.

[3]   S. Wang, H. Zhang, B. Zhang, Z. Xie, W.-Y. Wong, *Mater. Sci. Eng. R Reports* **2020**, *140*, 100547.

[4]   R. Karlicek, C. C. Sun, G. Zissis, R. Ma, *Handbook of Advanced Lighting Technology*, Springer International Publishing, Cham, **2017**.

[5]   L. Duan, L. Hou, T.-W. Lee, J. Qiao, D. Zhang, G. Dong, L. Wang, Y. Qiu, *J. Mater. Chem.* **2010**, *20*, 6392–6407.

[6]   Y. Zou, S. Gong, G. Xie, C. Yang, *Adv. Opt. Mater.* **2018**, *6*, 1800568.

[7]   L. Xiao, Z. Chen, B. Qu, J. Luo, S. Kong, Q. Gong, J. Kido, *Adv. Mater.* **2011**, *23*, 926–952.

[8]   Y. Im, M. Kim, Y. J. Cho, J. A. Seo, K. S. Yook, J. Y. Lee, *Chem. Mater.* **2017**, *29*, 1946–1963.

[9]   C. W. Tang, S. A. VanSlyke, *Appl. Phys. Lett.* **1987**, *51*, 913–915.

[10]   J. Bauri, R. B. Choudhary, G. Mandal, *J. Mater. Sci.* **2021**, *56*, 18837–18866.

[11]   C. Zhong, C. Duan, F. Huang, H. Wu, Y. Cao, *Chem. Mater.* **2011**, *23*, 326–340.

[12]   J.-H. Jou, S. Kumar, A. Agrawal, T.-H. Li, S. Sahoo, *J. Mater. Chem. C* **2015**, *3*, 2974–3002.

[13]   T. Chatterjee, K.-T. Wong, *Adv. Opt. Mater.* **2019**, *7*, 1800565.

[14]   H. Yersin, A. F. Rausch, R. Czerwieniec, T. Hofbeck, T. Fischer, *Coord. Chem. Rev.* **2011**, *255*, 2622–2652.

[15]   K.-L. Wong, J.-C. G. Bünzli, P. A. Tanner, *J. Lumin.* **2020**, *224*, 117256.

[16]   S. Ghosh, S. Mandal, C. Banerjee, V. G. Rao, N. Sarkar, *J. Phys. Chem. B* **2012**, *116*, 9482–9491.

[17]   G. Hong, X. Gan, C. Leonhardt, Z. Zhang, J. Seibert, J. M. Busch, S. Bräse, *Adv. Mater.* **2021**, *33*, 2005630.

[18]   K. Mori, T. P. M. Goumans, E. van Lenthe, F. Wang, *Phys. Chem. Chem. Phys.* **2014**, *16*, 14523–14530.

[19]   M. Y. Wong, E. Zysman-Colman, *Adv. Mater.* **2017**, *29*, 1605444.

[20]   T. Huang, W. Jiang, L. Duan, *J. Mater. Chem. C* **2018**, *6*, 5577–5596.

[21]   K. Traskovskis, I. Mihailovs, A. Tokmakovs, A. Jurgis, V. Kokars, M. Rutkis, *J. Mater. Chem.* **2012**, *22*, 11268–11276.

[22]   K. Traskovskis, K. Lazdovica, A. Tokmakovs, V. Kokars, M. Rutkis, *Dye. Pigment.* **2013**, *99*, 1044–1050.

[23]   E. Zarins, K. Balodis, A. Ruduss, V. Kokars, A. Ozols, P. Augustovs, D. Saharovs, *Opt. Mater.* **2018**, *79*, 45–52.

[24]   I. R. Laskar, T.-M. Chen, *Chem. Mater.* **2004**, *16*, 111–117.

[25]   T. Giridhar, W. Cho, Y.-H. Kim, T.-H. Han, T.-W. Lee, S.-H. Jin, *J. Mater. Chem. C* **2014**, *2*, 9398–9405.

[26]   J.-H. Jang, M. J. Kim, H. U. Kim, S. B. Lee, J. Lee, D.-H. Hwang, *J. Nanosci.*

Nanotechnol. **2016**, *16*, 8580–8584.

[27]   X. Jiang, J. Peng, J. Wang, X. Guo, D. Zhao, Y. Ma, *ACS Appl. Mater. Interfaces* **2016**, *8*, 3591–3600.

[28]   S. E. Zieger, A. Steinegger, I. Klimant, S. M. Borisov, *ACS Sensors* **2020**, *5*, 1020–1027.

[29]   T. Giridhar, W. Cho, J. Park, J.-S. Park, Y.-S. Gal, S. Kang, J. Y. Lee, S.-H. Jin, *J. Mater. Chem. C* **2013**, *1*, 2368–2378.

[30]   J. Li, R. Wang, R. Yang, W. Zhou, X. Wang, *J. Mater. Chem. C* **2013**, *1*, 4171–4179.

[31]   R. Wang, D. Liu, H. Ren, T. Zhang, X. Wang, J. Li, *J. Mater. Chem.* **2011**, *21*, 15494–15500.

[32]   C. Fan, L. Zhu, B. Jiang, Y. Li, F. Zhao, D. Ma, J. Qin, C. Yang, *J. Phys. Chem. C* **2013**, *117*, 19134–19141.

[33]   J.-H. Choi, C.-H. Jung, J. Y. Kwon, H.-J. Cho, J. Lee, J.-I. Lee, H.-Y. Chu, D.-H. Hwang, *Synth. Met.* **2009**, *159*, 1517–1521.

[34]   M. A. Baldo, S. Lamansky, P. E. Burrows, M. E. Thompson, S. R. Forrest, *Appl. Phys. Lett.* **1999**, *75*, 4–6.

[35]   M. G. Colombo, T. C. Brunold, T. Riedener, H. U. Guedel, M. Fortsch, H.-B. Buergi, *Inorg. Chem.* **1994**, *33*, 545–550.

[36]   Q. Zhang, B. Li, S. Huang, H. Nomura, H. Tanaka, C. Adachi, *Nat. Photonics* **2014**, *8*, 326–332.

[37]   M. Cai, M. Auffray, D. Zhang, Y. Zhang, R. Nagata, Z. Lin, X. Tang, C.-Y. Chan, Y.-T. Lee, T. Huang, X. Song, Y. Tsuchiya, C. Adachi, L. Duan, *Chem. Eng. J.* **2021**, *420*, 127591.

[38]   D. Di, A. S. Romanov, L. Yang, J. M. Richter, J. P. H. Rivett, S. Jones, T. H. Thomas, M. Abdi Jalebi, R. H. Friend, M. Linnolahti, M. Bochmann, D. Credgington, *Science* **2017**, *356*, 159–163.

[39]   R. Hamze, S. Shi, S. C. Kapper, D. S. Muthiah Ravinson, L. Estergreen, M.-C. Jung, A. C. Tadle, R. Haiges, P. I. Djurovich, J. L. Peltier, R. Jazzar, G. Bertrand, S. E. Bradforth, M. E. Thompson, *J. Am. Chem. Soc.* **2019**, *141*, 8616–8626.

[40]   R. Hamze, J. L. Peltier, D. Sylvinson, M. Jung, J. Cardenas, R. Haiges, M. Soleilhavoup, R. Jazzar, P. I. Djurovich, G. Bertrand, M. E. Thompson, *Science* **2019**, *363*, 601–606.

[41]   S. Shi, M. C. Jung, C. Coburn, A. Tadle, D. Sylvinson M. R., P. I. Djurovich, S. R. Forrest, M. E. Thompson, *J. Am. Chem. Soc.* **2019**, *141*, 3576–3588.

[42]   S. Leuthäußer, D. Schwarz, H. Plenio, *Chem. - A Eur. J.* **2007**, *13*, 7195–7203.

[43]   O. Santoro, A. Collado, A. M. Z. Slawin, S. P. Nolan, C. S. J. Cazin, *Chem. Commun.* **2013**, *49*, 10483–10485.

[44]   R. Hamze, M. Idris, D. S. Muthiah Ravinson, M. C. Jung, R. Haiges, P. I. Djurovich, M. E. Thompson, *Front. Chem.* **2020**, *8*.

[45]   T. Li, D. S. Muthiah Ravinson, R. Haiges, P. I. Djurovich, M. E. Thompson, *J. Am. Chem. Soc.* **2020**, *142*, 6158–6172.

[46]   A. S. Romanov, M. Linnolahti, M. Bochmann, *Dalt. Trans.* **2021**, *50*, 17156–17164.

[47]   M. Gernert, L. Balles-Wolf, F. Kerner, U. Müller, A. Schmiedel, M. Holzapfel, C. M. Marian, J. Pflaum, C. Lambert, A. Steffen, *J. Am. Chem. Soc.* **2020**, *142*, 8897–8909.

[48]   P. K. Samanta, D. Kim, V. Coropceanu, J.-L. Brédas, *J. Am. Chem. Soc.* **2017**, *139*, 4042–4051.

[49]   A. J. Lees, *Comments Inorg. Chem.* **1995**, *17*, 319–346.

[50]   J. Hossain, R. Akhtar, S. Khan, *Polyhedron* **2021**, *201*, 115151.

[51]   I. Piel, M. D. Pawelczyk, K. Hirano, R. Fröhlich, F. Glorius, *European J. Org. Chem.* **2011**, *2011*, 5475–5484.

[52]   R. Czerwieniec, J. Yu, H. Yersin, *Inorg. Chem.* **2011**, *50*, 8293–8301.

PATEICĪBAS

Liels paldies kolēģiem par ieguldījumu promocijas darba tapšanā!

- *Dr. chem.* Kasparam Traskovskim un *Dr. chem.* Valdim Kokaram par promocijas darba vadīšanu;
- Lietišķās ķīmijas institūta kolektīvam par atbalstu darba sagatavošanā;
- *Dr. chem.* Baibai Turovskai un *Dr. phys.* Sergejam Beļakovam par savienojumu cikliskās voltametrijas analīzi un rentgenstruktūranalīzi;
- Latvijas Universitātes Cietvielu fizikas institūta Organisko materiālu laboratorijas kolektīvam *Dr. phys.* Aivara Vembra vadībā par ieguldījumu *OLED* sagatavošanā un dažādu mērījumu veikšanā;
- starptautiskajiem sadarbības partneriem par ieguldījumu *OLED* sagatavošanā un *DFT* aprēķiniem;
- Laurai Drunkai par manuskripta labošanu.

Armands Rudušs

DOCTORAL THESIS PROPOSED TO RIGA TECHNICAL UNIVERSITY FOR THE PROMOTION TO THE SCIENTIFIC DEGREE OF DOCTOR OF SCIENCE

To be granted the scientific degree of Doctor of Science (Ph. D.), the present Doctoral Thesis has been submitted for the defence at the open meeting of RTU Promotion Council on December 15, 2022 at 14.00 at the Faculty of Materials Science and Applied Chemistry of Riga Technical University, 3 Paula Valdena Street, Room 272.

OFFICIAL REVIEWERS

Senior Researcher Dr. chem. Pāvels Arsenjans
Latvian Institute of Organic Synthesis, Latvia

Senior Researcher Dr. phys. Mārtiņš Rutkis
Institute of Solid State Physics, University of Latvia, Latvia

Professor Dr. habil. Juozas Vidas Gražulevičius,
Kaunas University of Technology, Lithuania

DECLARATION OF ACADEMIC INTEGRITY

I hereby declare that the Doctoral Thesis submitted for the review to Riga Technical University for the promotion to the scientific degree of Doctor of Science (Ph. D.) is my own. I confirm that this Doctoral Thesis had not been submitted to any other university for the promotion to a scientific degree.

Armands Rudušs   ………………………….
                         (*signature*)

Date: ....…......………………...…

The Doctoral Thesis has been prepared as a collection of thematically related scientific publications complemented by summaries in both Latvian and English. The Doctoral Thesis includes four scientific publications and two publications in conference proceedings. The publications have been written in English, with the total volume of 215 pages, including supplementary data.

CONTENTS

ABBREVIATIONS

A	acceptor
BPhen	4,7-diphenyl-1,10-phenanthroline
CBP	4,4′-bis(9*H*-carbazol-9-yl)-1,1′-biphenyl
Cbz	carbazole
CMA	carbene-metal-amide
CT	charge transfer
CzSi	9-(4-*tert*-butylphenyl)-3,6-bis(triphenylsilyl)-9*H*-carbazole
D	donor
DCC	dicyclohexylcarbodiimide
DCM	dichloromethane
DFT	density functional theory
Dipp	2,6-diisopropylphenyl group
DMAP	4-dimethylaminopyridine
DMF	dimethylformamide
DMSO	dimethyl sulfoxide
DPEPO	bis[2-(diphenylphosphino)phenyl]ether oxide
DSC	differential scanning calorimetry
HOMO	highest occupied molecular orbital
ISC	intersystem crossing
ITO	indium tin oxide
LCD	liquid crystal display
LE	local excitation
LLCT	ligand-to-ligand charge transfer
LUMO	lowest unoccupied molecular orbital
mCBP	3,3′-di(9*H*-carbazol-9-yl)-1,1′-biphenyl
mCP	1,3-di(9*H*-carbazol-9-yl)benzene
Me	methyl group
MLCT	metal-to-ligand charge transfer
NHC	*N*-heterocyclic carbenes
OLED	organic light-emitting diode
OXD-7	1,3-bis[2-(4-*tert*-butylphenyl)-1,3,4-oxadiazo-5-yl]benzene
PEDOT:PSS	poly(3,4-ethylenedioxythiophene) polystyrene sulfonate
Ph	phenyl group
PL	photoluminescence
PolyTPD	poly(4-butylphenyldiphenylamine)
PMMA	poly(methyl methacrylate)
ppy	2-phenylpyridine
PVK	polyvinylcarbazole
RISC	reverse intersystem crossing
RT	room temperature

S	singlet state
SOC	spin-orbital coupling
T	triplet state
TADF	thermally activated delayed fluorescence
TAPC	1,1-bis[(di-4-tolylamino)phenyl]cyclohexane
TCTA	tris(4-carbazoyl-9-ylphenyl)amine
TD-DFT	time-dependent density functional theory
THF	tetrahydrofuran
TmPyPB	1,3,5-tris(3-pyridyl-3-phenyl)benzene
TPBi	1,3,5-tris(1-phenyl-1*H*-benzimidazol-2-yl)benzene
UV	ultraviolet light
Vis	visible light

GENERAL OVERVIEW OF THE THESIS

Introduction

Organic light emitting diode (OLED) is a device that can be used for display and lighting applications. OLED technology provides an opportunity to develop displays that surpass the widely used liquid crystal display (LCD) technology both in performance and aesthetic aspects.[1] The ability to produce thin, flexible, large-area OLED panels opens up a new perspective for the design of decorative lighting elements.[2] Although OLED displays are widely applied in smartphones, such devices as larger area TVs, computer screens and lighting appliances are not available to a wider consumer range due to the high production cost. Potential directions for cost reduction mentioned in literature include an optimization of the OLED manufacturing process and the usage of low-cost materials.[3]

The deposition of the thin device structure-forming layers is the most important process in OLED manufacturing. Currently, the most widely used approach to the production of thin films is vacuum deposition technology. By this method the applicable material passes from solid state to gas phase under the influence of a vacuum and a heat source. Molecules in the gas phase move to the substrate and slowly condense to form a thin film.[4] The requirement for high vacuum, high evaporation temperature of some materials, the loss of material in the vacuum chamber and the technical difficulties associated with the production of large surface area thin layers together increase the cost of the vacuum deposition process.[5] Therefore, more cost efficient methods are required. One of the alternative approaches is the preparation of thin films from solutions, using methods such as spin coating and printing. However, most of the organic emitters used for vacuum deposition are not suitable for solution processing. The main reasons for that are the insufficient solubility of numerous materials as well as the ability of materials to form a homogeneous amorphous phase with high morphological and thermal stability.[6]

The opportunities for modification of the widely used phosphorescent iridium(III) complex OLED emitters in order to obtain solution-processable materials were explored in the first part of the Doctoral Thesis. Iridium(III) complexes were functionalized with trityl (-CPh$_3$) groups, which leads to an increase of the solubility of the compounds in organic solvents and to improvement of the optical quality and morphological stability of thin amorphous films produced by solution methods. The characterization of photophysical properties of the obtained complexes and assessment of their performance parameters in solution-processed OLEDs were carried in this part of the Thesis.

The costs of OLEDs are increased not only by the complicated manufacturing process. The cost of the used materials (the emitters in particular) should also be considered. Currently, the most important class of emitters with practical application in commercialized OLEDs are phosphorescent iridium(III) complexes.[7] The high cost of rare transition metals and the potential environmental risks encourage replacement of phosphorescent materials with alternatives such as thermally activated delayed fluorescence (TADF) emitters.[8]

In the second part of the Thesis, carbene-metal-amide (CMA) type TADF emitters were synthesized with copper as the complex-forming element. The characterization of the structure

and photophysical properties of the obtained compounds was carried out and the luminescence mechanism was investigated. The practical application of 1,3-thiazol-2-ylidene carbene fragment-based CMA derivatives in efficient white light emitting OLEDs has been demonstrated.

Aims and Objectives

The aim of the Doctoral Thesis is the synthesis of low-molecular weight organic emitters that would lead to reduced production costs of OLED devices. The following objectives are defined for the implementation of the aim of the Doctoral Thesis:

1. Synthesis of phosphorescent iridium(III) organometallic complexes functionalized with trityl groups. Characterization of the photophysical and morphological properties of the obtained compounds in thin amorphous films.
2. Evaluation of the trityl-functionalized iridium(III) complexes for the preparation of high-efficiency OLEDs.
3. Synthesis of luminescent carbene-metal-amide (CMA) type copper(I) organometallic complexes. Structural characterization of the obtained compounds and study of emitter TADF properties.
4. Evaluation of the newly obtained CMA derivatives for the preparation of high-efficiency OLEDs.

Scientific Novelty and Main Results

In the first part of the Doctoral Thesis, two series of trityl-functionalized heteroleptic 2-arylbenzo[d]thiazole ligand-containing and homoleptic 2-phenylpyridine ligand-containing phosphorescent iridium(III) complexes were synthesized. The photophysical and morphological properties of the obtained compounds in thin amorphous films enable the use of the trityl-functionalized iridium complexes for the preparation of solution-processed OLEDs. However, a systematic study of the effect of trityl groups on OLED performance shows that trityl groups negatively affect the charge carrier transport within the emitting layer, which reduces the emission efficiency of OLEDs. Although the obtained data show the limited application of trityl groups as efficient OLED emitters, the results give an insight into the prerequisites that should be taken into account regarding the molecular design of solution-processable iridium(III) complexes.

Two series of novel CMA type TADF emitters were synthesized within the second part of the Doctoral Thesis. In the first series of CMA emitters, imidazole type NHC derivatives with phenylsulfonyl acceptor groups added to the peripheral steric groups are used as carbene fragments. In the second series, 1,3-thiazol-2-ylidene type NHC derivatives serve as the carbene fragment. A novel TADF mechanism of CMA type emitters was observed for phenylsulfonyl-functionalized complexes. The influence of steric effects on the luminescence properties of the compounds was investigated for 1,3-thiazol-2-ylidene derivatives. The potential application of

1,3-thiazol-2-ylidene CMA derivatives in the development of high-efficiency OLED devices was demonstrated.

Structure and Volume of the Thesis

The Doctoral Thesis has been prepared as a collection of thematically related scientific publications dedicated to the synthesis of luminescent trityl-functionalized Ir(III) and CMA type Cu(I) metalorganic complexes, characterization of the photophysical properties and the assessment of the obtained emitters for the development of low-cost OLEDs.

Publications and Approbation of the Thesis

Results of the Thesis have been reported in four scientific publications and two publications in conference proceedings. The results have been presented in seven reports at five conferences.

Scientific publications:

1. **Ruduss, A.**; Turovska, B.; Belyakov, S.; Stucere, K. A.; Vembris, A.; Baryshnikov, G.; Ågren, H.; Lu, J.; Lin, W.; Chang, C.; Traskovskis, K. Thiazoline Carbene–Cu(I)–Amide Complexes: Efficient White Electroluminescence from Combined Monomer and Excimer Emission. *ACS Appl. Mater. Interfaces.* **2022**, *14* (13), 15478–15493. doi: 10.1021/acsami.2c00847. Impact factor of the journal (2021): 10.383.
2. **Ruduss, A.**; Turovska, B.; Belyakov, S.; Stucere, K. A.; Vembris, A.; Traskovskis, K. Carbene–Metal Complexes as Molecular Scaffolds for Construction of Through-Space Thermally Activated Delayed Fluorescence Emitters. *Inorg. Chem.* **2022**, *61* (4), 2174–2185. doi: 10.1021/acs.inorgchem.1c03371. Impact factor of the journal (2021): 5.436.
3. **Ruduss, A.**; Kokars, V.; Tetervenoka, N.; Vembris, A.; Traskovskis, K. Effects of Steric Encumbrance of Iridium(iii) Complex Core on Performance of Solution-Processed Organic Light Emitting Diodes. *RSC Adv.* **2020**, *10* (46), 27552–27559. doi: 10.1039/D0RA04652C. Impact factor of the journal (2021): 4.036.
4. Traskovskis, K.; **Ruduss, A.**; Kokars, V.; Mihailovs, I.; Lesina, N.; Vembris, A. Thiphenylmethane Based Structural Fragments as Building Blocks Towards Solution-Processable Heteroleptic Iridium(iii) Complexes for OLED Use. *New J. Chem.* **2019**, *43* (1), 37–47. doi: 10.1039/C8NJ04484H. Impact factor of the journal (2021): 3.925.

Publications in conference proceedings:

1. Jece, A.; **Ruduss, A.**; Štucere, K. A.; Vembris, A.; Traskovskis, K. TADF Active Carbene-Metal-Amide Complexes Exhibiting Through-Space Charge Transfer: An Impact of Metal Atom. *Organic Electronics and Photonics: Fundamentals and Devices III.* **2022**, 1214909. doi: 10.1117/12.2621156
2. **Ruduss, A.**; Sisojevs, Ž.; Vembris, A.; Štucere, K. A.; Traskovskis, K. Symmetrical versus Asymmetrical Molecular Configuration in Metal-Assisted-Through-Space Charge Transfer TADF Emitters. *Organic Electronics and Photonics: Fundamentals and Devices III*. **2022**, 1214908. doi: 10.1117/12.2620983

Results of the Thesis have been presented at the following conferences:

1. **Ruduss, A.;** Sisojevs, Z.; Vembris, A.; Stucere, K.; Traskovskis, K. Symmetrical Versus Asymmetrical Molecular Configuration in Metal Assisted-Through-Space Charge Transfer TADF Emitters. *SPIE Photonics Europe, Conference 12149, Organic Electronics and Photonics: Fundamentals and Devices III*, Strasbourg, France, April 4–6, **2022**.

2. Jece, A.; **Ruduss, A.;** Vembris, A.; Stucere, K.; Traskovskis, K. TADF active carbene-metal-amide complexes exhibiting through-space charge transfer: an impact of metal atom. *SPIE Photonics Europe, Conference 12149, Organic Electronics and Photonics: Fundamentals and Devices III*, Strasbourg, France, April 4–6, **2022**.

3. **Ruduss, A.;** Sisojevs, Z.; Jece, A. Thiazoline Carbene-Cu(I)-Carbazolide Complexes as Luminescent TADF Materials. *80th International Scientific Conference of the University of Latvia 2022. Chemistry Section*, Riga, Latvia, February 11, **2022**.

4. **Ruduss, A.;** Jece, A.; Balodis, K.; Traskovskis, K. The Use of Thiazoline-Based Carbenes for a Development of Metalorganic Thermally Activated Delayed Fluorescence Emitters. *Riga Technical University 62nd International Scientific Conference "Materials Science and Applied Chemistry"*, Riga, Latvia, October 22, **2021**.

5. Sisojevs, Z.; **Ruduss, A.;** Balodis, K.; Traskovskis, K. Synthesis and photophysical properties of metal-amide complexes of *N*-heterocyclic carbenes containing peripheral acceptor groups. *Riga Technical University 62nd International Scientific Conference "Materials Science and Applied Chemistry"*, Riga, Latvia, October 22, **2021**.

6. **Ruduss, A.;** Traskovskis, K.; Kokars, V. Photophysical Properties of 9,9'-Bis-Methoxypenyl Substituted 3,3'-Bicarbazoles. *13th International Conference on Optical Probes of Organic and Hybrid Optoelectronic Materials and Applications 2019*, Vilnius, Lithuania, July 7–13, **2019**.

7. **Ruduss, A.;** Traskovskis, K.; Otikova, E.; Vembris, A.; Grzibovskis, R.; Kokars, V. 3,3'-Bicarbazole Structural Derivatives as Charge Transporting Materials for Use in OLED Devices. *SPIE Photonics Europe, Conference 10687, Organic Electronics and Photonics: Fundamentals and Devices III*, Strasbourg, France, April 24–26, **2018**.

MAIN RESULTS OF THE THESIS

1. OLED Structure and Basic Principles of Operation

In organic light-emitting diode (OLED) light emission is realized from organic electroluminescent material in the presence of electric current.[9] A simplified model of OLED structure is given in Fig. 1.1.[10] A typical OLED device consists of several thin layers, which are stacked upon one another using glass or other transparent material as a substrate. The thin layers can be deposited using vacuum or solution methods. The utilized materials have to be compatible with the technique used in the deposition of thin layers. Materials must exhibit chemical, photochemical and morphological stability to prevent degradation during the operation of the device.[11]

An external source of electrical current is required for the operation of the device. By applying an electrical voltage, holes (positive charge carriers) and electrons (negative charge carriers) move from the anode and cathode to the emitting layer, respectively. Charge carrier injection layers (not depicted in Fig. 1.1), charge carrier transport layers, and charge carrier blocking layers could be inserted between electrodes and emitting layer to ensure low injection barrier and to provide balanced and effective charge carrier transport.[12] When holes and electrons recombine within an organic molecule in the emissive layer, it is excited. The return of the excited molecules to the ground state with the emission of light is called electroluminescence. The emitter is doped in a special charge carrying host matrix in low concentration. The blend of this type is called guest-host system. The emitter molecules are spatially separated from each other by mixing into the host matrix, therefore reducing intermolecular interactions and quenching of excited states.[13]
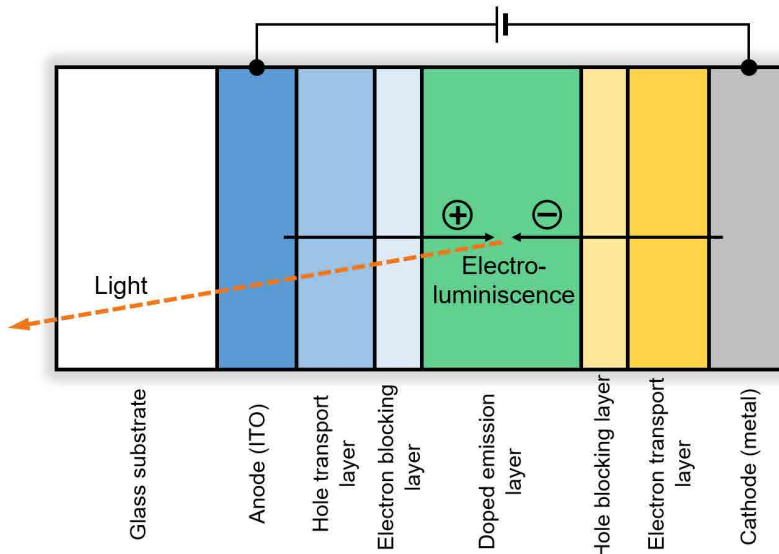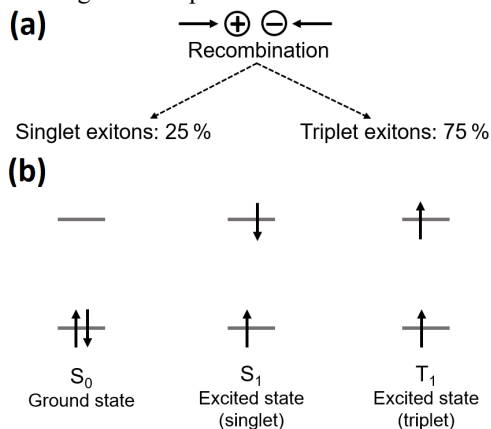

Fig. 1.1. Principal structure of OLED.

Closely bound electron and hole pairs called excitons are formed as a result of the charge carrier recombination. Further exciton relaxation from excited state to ground state can lead to the emission of photon. Therefore, efficient exciton energy transfer to the emitter molecules is essential for ensuring electroluminescence. Two types of excitons (singlet (S) and triplet (T)) are formed during the charge carrier recombination process (Fig. 1.2). Spin statistics determine that the ratio of the produced singlet and triplet excitons is 1:3.[14]

(a)

Recombination

Singlet exitons: 25 %   Triplet exitons: 75 %

(b)

S_0
Ground state

S_1
Excited state
(singlet)

T_1
Excited state
(triplet)

Fig. 1.2. (a) Singlet and triplet exciton formation ratio. (b) Electron spin configuration in ground state S_0 and S_1, T_1 excited states.

A quantitative measure – the luminescence quantum yield (Φ) – is used for the characterization of the emission efficiency of luminescent materials.[15] The quantum yield is defined as the proportion of excited states that emit a photon as a result of radiative relaxation:

$$\Phi = \frac{k_\mathrm{r}}{k_\mathrm{r} + k_\mathrm{nr}}, \qquad (1.1)$$

where: Φ – quantum yield;
k_r – radiative rate constant;
k_nr – non-radiative rate constant.

In practical measurements photoluminescence quantum yield (Φ_PL) of materials is determined relatively easily.[15] Photoluminescence quantum yield is measured as the ratio of the photons emitted by the material and the photons absorbed by the material:

$$\Phi_\mathrm{PL} = \frac{N_\mathrm{em}}{N_\mathrm{abs}}, \qquad (1.2)$$

where: Φ_PL – photoluminescence quantum yield;
N_em – the number of photons emitted;
N_abs – the number of photons absorbed.

It is necessary to determine photoluminescence quantum yield and photoluminescence lifetime for the calculation of the radiative rate constant[16]:

$$k_\mathrm{r} = \frac{\Phi_\mathrm{PL}}{\tau_\mathrm{PL}}, \qquad (1.3)$$

where τ_PL is photoluminescence lifetime.

In the case of fluorescent emitters, only singlet excitons (S_1) are able to relax to the ground state through a photon emission (Fig. 1.3 (a)). The relaxation of the triplet excited state (T_1) to the ground state (S_0) is a spin-forbidden transition and therefore this process (phosphorescence) is characterized with a very long lifetime. Consequently, the emission from the T_1 state is almost completely suppressed by various non-radiative relaxation processes. For this reason, fluorescent OLEDs have a maximum theoretical internal quantum efficiency of 25 %.[17]

The replacement of fluorescent emitters with phosphorescent analogues is considered as one of the methods for increasing the internal quantum efficiency from 25 % to 100 % (Fig. 1.3 (b)). Phosphorescent materials are usually organometallic complexes of heavy transition metals (Ir, Pt, Os, Ru, etc.). In this case heavy metal atoms provide an efficient spin-orbit coupling (SOC). SOC is a process that promotes spin inversion, thereby facilitating intersystem crossing (ISC) as well as phosphorescent relaxation of the T_1 state.[18]

Emitters with thermally activated delayed fluorescence (TADF) properties could be used as an alternative to the phosphorescent materials containing heavy transition metals (Fig. 1.3 (c)). In TADF materials the energy difference between the S_1 and T_1 (ΔE_{ST}) states is lower than 0.1 eV. In this way, reverse intersystem crossing (RISC) is promoted. Thus, the non-radiative triplet states are upconverted into radiative singlets, from which the so-called delayed fluorescence is possible. Both the phosphorescence and TADF mechanisms fully utilize the singlet and triplet excitons in radiative processes, thus achieving the maximum theoretically possible internal quantum efficiency (100 %).[19]
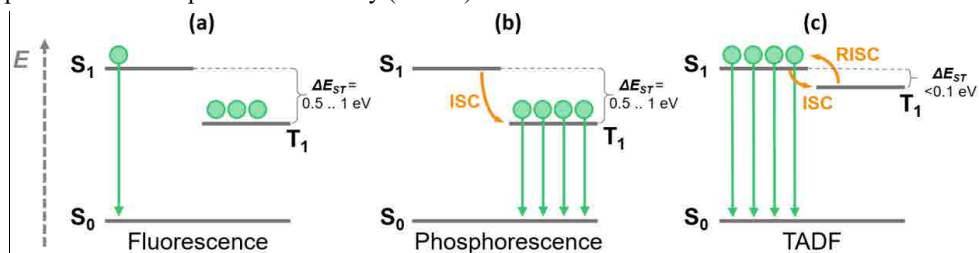
Fig. 1.3. Schematic representation of fluorescence, phosphorescence and TADF mechanisms.

2. Synthesis and Phosphorescence of the Trityl-Functionalized Ir(III) Complexes

The energy-intensive vacuum deposition of the active layer is considered as one of the main problems that leads to significant increases in the OLED manufacturing cost. The vacuum deposition of the OLED emitting layer is especially complicated due to the need to deposit the matrix material together with the emitter (guest-host system). Spin coating from concentrated solutions is as an alternative approach to the deposition of thin films.[20] In order for the material to be suitable for spin coating, not only it must be soluble in volatile organic solvents but also form a stable amorphous phase with a high glass transition temperature and good optical quality. In our previous studies we discovered that the functionalization of various low molecular weight compounds with trityl (-CPh$_3$) groups promotes the ability of these materials to form a stable amorphous phase.[21–23]

Phosphorescent 2-arylbenzo[d]thiazole ligand containing iridium(III) complexes described in literature[24–26] were used as the core structures in order to obtain effective solution-processable amorphous phase forming OLED emitters. Trityl-functionalized 2-arylbenzo[d]thiazole ligands **2**, **5** and **8** were first obtained as the complexing compounds (Scheme 2.1). The ligands were used in further synthesis by first preparing di-µ-chloro iridium(III) complex dimers and then adding picolinic acid (complexes **3a**, **6a** and **9a**) or acetylacetone (complexes **3b**, **6b** and **9b**) ancillary ligands, respectively.

The obtained compounds exhibit high solubility in various volatile organic solvents such as DCM, chloroform and THF. Amorphous thin films could be prepared easily from the corresponding solutions using the spin coating method. The glass transition temperatures of the synthesized compounds determined by the differential scanning calorimetry (DSC) method vary in the range from 124 °C to 188 °C. No signs of crystallization of the materials were observed during several heating-cooling cycles.
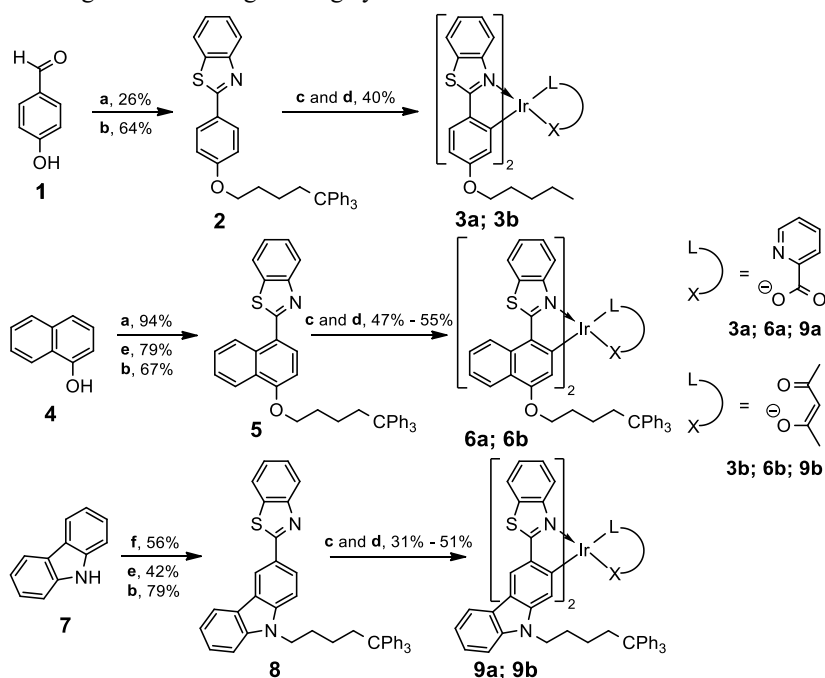
Scheme 2.1. Synthesis of the 2-arylbenzo[d]thiazole ligand containing iridium(III) complexes. (**a**) 1,1,1-Triphenyl-5-iodopentane, K_2CO_3, DMSO; (**b**) 2-aminothiophenol, DMSO; (**c**) $IrCl_3 \cdot 3H_2O$, 2-ethoxyethanol/H_2O; (**d**) acetylacetone or 2-picolinic acid, 2-ethoxyethanol, K_2CO_3; (**e**) $POCl_3$, DMF; (**f**) 1,1,1-triphenyl-5-iodopentane, NaH, THF.

The UV-Vis absorption patterns of the trityl-functionalized iridium(III) complexes are similar to the non-functionalized structural analogues described in the literature.[24–26] The highest energy UV-Vis absorption bands are attributed to metal-ligand charge transfer (MLCT) (Table 2.1). The largest bathochromic shift of absorption bands within the series is observed for complexes **6a** and **6b** containing 2-(naphthalen-1-yl)benzo[d]thiazole ligands. All

compounds exhibit intense phosphorescence with pronounced vibrational substructure, indicating that the emission is strongly associated with ligand-centred $^3\pi\rightarrow\pi^*$ transitions. Similarly to the UV-Vis absorption, complexes **6a** and **6b** have the largest bathochromic shift of the emission with orange-red phosphorescence, while complexes **3a**, **3b**, **9a**, and **9b** exhibit phosphorescence in the yellow part of the spectrum.

Measurements of the Φ_{PL} for both phosphorescent and TADF materials must be performed under degassed, oxygen-free conditions, as oxygen quenches the excited triplet states, thereby lowering the determined Φ_{PL} value.[27, 28] The compounds exhibit high Φ_{PL} in dilute solutions (0.64 to 0.90 in THF solution). In contrast, Φ_{PL} for amorphous thin films of pure emitters (without host matrix) drops to range 0.02–0.10. In this case, if the inert non-emissive 5,5,5-triphenylpentyl groups are not taken into account, the mass concentration of the active emitter in the thin amorphous films is approximately 50 wt %, which leads to a significant aggregation-induced quenching of the emission. During the preparation of the OLED active layer, the emitter is practically always mixed in a host matrix with emitter mass concentration lower than 10 wt %. Therefore, it was decided to determine the Φ_{PL} for thin amorphous films of guest-host systems with CBP and PVK. The inert 5,5,5-triphenylpentyl groups make up about half of the molecular weight of the compounds. For this reason, the complexes were mixed into the matrices at 20 wt % concentration, ensuring approximately 10 wt % concentration of the active emitter. In the CBP matrix, Φ_{PL} values reach 0.50. On the other hand, in the PVK matrix the values of Φ_{PL} are low and do not significantly differ from the Φ_{PL} of neat amorphous samples, what could be related to the increased aggregation of the emitter in the polymer type PVK matrix. In addition, a tendency of complexes containing picolinic acid ancillary ligands to exhibit a higher Φ_{PL} than the complexes containing acetylacetone ancillary ligands was observed.

Table 2.1

Photophysical Properties of Iridium(III) Complexes Containing 2-arylbenzo[d]thiazole Ligands

Comp.	$\lambda_{\mathrm{max\ abs}}{}^{a}$, nm (lg ε)	$\lambda_{\mathrm{max\ em}}{}^{b}$, nm	$\Phi_{PL}{}^{c}$	τ^{d}, µs	$k_{r}{}^{d}$, $\times 10^5$ s^{-1}	$k_{nr}{}^{d}$, $\times 10^5$ s^{-1}
3a	433 (3.7)	537, 576 (544, 576)	0.87/0.10/0.06/0.39	4.48	1.78	1.44
3b	464 (3.8)	552, 588 (553, 591)	0.78/0.02/0.15/0.31	3.32	1.56	0.45
6a	485 (4.3)	591, 641 (598, 644)	0.64/0.04/0.08/0.50	5.63	1.10	0.68
6b	496 (4.1)	595, 648 (604, 651)	0.64/0.03/0.06/0.27	3.75	1.15	2.49
9a	456 (4.0)	549, 588 (556, 587)	0.90/0.05/0.02/0.50	3.65	2.05	0.67
9b	464 (3.9)	568, 603 (568, 603)	0.69/0.02/0.02/0.12	2.61	1.34	1.52

^{a} Maxima of the lowest energy absorption band, THF solution. ^{b} Phosphorescence, THF solution (CBP film, 20 wt % concentration). ^{c} THF solution/pure amorphous film/PVK film (20 wt % concentration)/CBP film (20 wt % concentration). ^{d} PMMA film (1 wt % concentration).

Complexes **9a** and **9b** containing the carbazole fragment were used in the fabrication of OLEDs (Dr. phys. A. Vembris). OLEDs were prepared using the following structure: ITO/PEDOT:PSS (40 nm)/emitting layer (60 nm)/BPhen or TPBi (20 nm)/LiF (1 nm)/Al. The

hole-transporting PEDOT:PSS and the emitting layers were fabricated using the spin coating method, while the electron-transporting BPhen/TPBi, the electron-injection LiF layers and the aluminium electrode were fabricated by the vacuum deposition. The maximal performance parameters were achieved for the **9a**/CBP based device, with 7.9 % external quantum efficiency, 12.4 cd·A^{-1} current efficiency and 7.8 lm·W^{-1} power efficiency at 6000 cd·m^{-2} luminance, with a maximum luminance of 17451 cd·m^{-2} (Table 2.2). Like in the case of Φ_{PL} measurements, lower performance parameters are observed for devices using PVK matrix and complex **9b** containing acetylacetone ancillary ligand.

Table 2.2

Electroluminescence Characteristics of **9a-b** Based OLEDs

Emitting Layer [a]	V_{on} [b], V	L_{max}, cd·m^{-2}	η_{ext} [c], %	η_c [d], cd·A^{-1}	η_p [e], lm·W^{-1}	λ_{max}, nm
9a:PVK	6.5	3229	4.8/4.8 [f]	7.2/7.2 [f]	4.5/4.5 [f]	553
9a:CBP	5.5	17451	7.9/5.1	12.4/8.0	7.8/5.6	554
9b:PVK	7.0	1708	2.1/1.7	3.1/2.4	1.9/1.3	561
9b:CBP	6.5	7295	5.2/5.1	7.3/7.1	4.9/4.7	563

[a] The mass concentration of iridium(III) complexes in the emitting layer is 20 wt %. [b] Voltage at which the luminance of the device is 1 cd·m^{-2}. [c] OLED external quantum efficiency. [d] Current efficiency. [e] Power efficiency. [f] Maximum achieved values and values determined at 1000 cd·m^{-2}.

The OLED performance parameters of the trityl-functionalized iridium(III) complexes are higher if compared to other structurally similar yellow emitters described in the literature, where the emitting layer is deposited by the spin coating method.[29, 30] However, the obtained results and literature analysis show that in terms of performance OLEDs produced by solution methods fall behind those produced by vacuum methods.[31, 32] Furthermore, the introduction of inert insulating groups such as long alkyl chains, which should reduce aggregation-induced quenching of the excited states, not necessarily leads to improved OLED performance.[33] These results prompted us to conduct a systematic study for the determination of the effect of trityl groups on the OLED performance.

In order to achieve this goal, compounds **15a**, **15b**, and **15c** based on the widely used OLED emitter **Ir(ppy)₃**[34] were synthesized with one, two, and three attached trityl groups, respectively (Scheme 2.2). For this purpose, di-μ-chloro dimers **13a** and **13b** were complexed with a third cyclometalating ligand using method developed by Colombo et al.[35] This method gives octahedral iridium(III) complexes in *fac* configuration. The target compounds were obtained through the reduction with NaBH₄ of one, two, and three aldehyde groups-containing complexes **14a**, **14b**, and **14c** and subsequent esterification of the obtained alcohols with 3,3,3-triphenylpropanoic acid.

The obtained trityl-functionalized compounds are soluble in volatile organic solvents, and spin coating method can be used for the preparation of high-quality thin amorphous films. The glass transition temperatures of compounds **15a**, **15b**, and **15c** are 158 °C, 142 °C, and 131 °C,

respectively. The decrease in the glass transition temperature in the series could be related to the increase in conformational freedom with the increase in the number of the trityl groups.
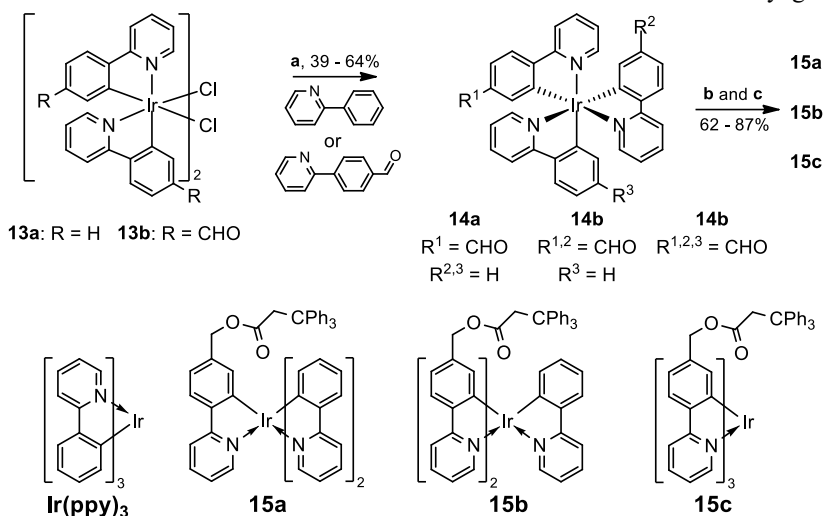
Scheme 2.2. Synthesis of trityl-functionalized Ir(ppy)$_3$ derivatives: (a) AgOTf, diglyme; (b) NaBH$_4$, CH$_2$Cl$_2$/MeOH; (c) CPh$_3$CH$_2$COOH, DCC, DMAP, CH$_2$Cl$_2$.

No significant influence of the trityl groups on absorption and emission properties of compounds in solution was observed within the series (Table 2.3). Φ_{PL} in THF solutions is high, reaching values between 0.90 and 0.94. Φ_{PL} for amorphous thin films of pure emitters drops to 0.01–0.08, indicating an intensive aggregation of compounds in the solid state. Although compound **15c** has three attached trityl groups, due to the *fac* configuration the ligands align the trityl groups spatially in the same direction, covering only one side of the molecule. This allows us to hypothesize that weakly emitting dimers of complex molecules are formed as a result of aggregation.

Table 2.3

Photophysical Properties of Trityl-functionalized Ir(ppy)$_3$ Derivatives

Comp.	$\lambda_{\text{max abs}}$[a], nm	$\lambda_{\text{max em}}$[b], nm	Φ_{PL}[c]	τ[d], µs	k_r[d], $\times 10^5$ s^{-1}	k_{nr}[d], $\times 10^5$ s^{-1}
Ir(ppy)$_3$	379	522	0.94/-	1.7	5.5	0.35
15a	380	525	0.91/0.01	1.8	5.1	0.50
15b	379	525	0.90/0.03	1.7	5.3	0.58
15c	379	525	0.93/0.08	1.8	5.2	0.38

[a] Absorption, THF solution. [b] Phosphorescence, THF solution. [c] THF solution/pure amorphous film. [d] THF solution.

The electroluminescence properties of the obtained complexes were studied (Dr. phys. A. Vembris) using the following OLED structure: ITO/PEDOT:PSS (40 nm)/emitting layer (50 nm)/TPBi (20 nm)/LiF (1 nm)/ Al. Three types of host matrices were used for the

fabrication of the emitting layer – first, a pure hole-transporting PVK matrix, second, a mixture of PVK and electron-transporting OXD-7 in a 7:3 mass ratio, and third, a mixture of PVK and OXD-7 in a 3:7 mass ratio. Iridium(III) complexes were mixed into the matrix at a constant concentration of 7 wt %, attributing the mass of the inert trityl groups to the mass of the matrix. The emissive layer was prepared by the spin coating method. The obtained results (Table 2.4) show that unmodified **Ir(ppy)₃** outperforms trityl-functionalized compounds in terms of OLED performance parameters. Moreover, as the number of trityl groups in the molecule increases, the performance parameters of the OLEDs have tendency to decrease. It was hypothesized that the inert trityl groups interfere with the charge carrier transfer to the emitter molecules, thereby reducing the effectiveness of electroluminescence. For this reason, the compound **Ir(ppy)₃** with the least sterical hindrance by the bulky inert groups for the interaction with the charge carrier matrix exhibits the most efficient electroluminescence. Based on these results, it can be concluded that passive insulating groups should not be used for the purpose of aggregation limitation in solution-processable OLED. Peripheral groups with good charge transport properties, and appropriate energy level tuning could be proposed as a better alternative.

Table 2.4

Electroluminescence Characteristics of Trityl-functionalized Ir(ppy)₃ Derivatives

Emitting Layer [a]	V_{on} [b], V	L_{max}, cd·m^{-2}	η_c [c], cd·A^{-1}	η_p [d], lm·W^{-1}	Roll-Off [e], %
PVK					
Ir(ppy)₃	4.5	2446	6.8	3.9	44
15a	4.5	844	4.8	2.4	71
15b	6	127	1.6	0.6	-
15c	7	136	1.0	0.3	-
PVK:OXD-7 (7:3)					
Ir(ppy)₃	3.5	2983	7.8	4.4	6
15a	4	3308	6.9	3.7	10
15b	4	2692	7.3	3.9	27
15c	3.5	1794	6.6	3.8	10
PVK:OXD-7 (3:7)					
Ir(ppy)₃	3.5	1048	2.2	1.1	27
15a	3.5	638	2.0	1.0	23
15b	3.5	680	2.4	1.3	28
15c	4	560	2.2	1.3	25

[a] The mass concentration of iridium(III) complexes in the emitting layer is 7 % (mass of the inert trityl groups is attributed to the mass of the matrix). [b] Voltage at which the luminance of the device is 1 cd·m^{-2}. [c] Current efficiency. [d] Power efficiency. [e] Decrease in current efficiency from peak current efficiency to peak luminance.

The publications that cover the studies described in this chapter are given in Appendices 1 and 2.

3. Synthesis and TADF Properties of Carbene–metal–amide Complexes

Due to the high cost of rare transition metals (Ir, Pt, etc.) and environmental concerns, a possible replacement of phosphorescent emitters with TADF materials have been proposed in the recent years. In order to achieve lower ΔE_{ST} and promote rapid RISC, the most commonly applied TADF molecular design strategy involves the spatial separation of the donor (D) and acceptor (A) fragments, minimizing HOMO and LUMO overlap.[36] However, weak spin-orbit coupling leads to a slow RISC and low radiative rates.[37] Carbene-metal-amide (CMA) complexes are considered as a new class of TADF materials. In CMAs the d^{10} metal (Cu, Ag or Au) atom forms a linear complex with an electron-accepting N-heterocyclic carbene (NHC) ligand and an electron-donating amide ligand. This ligand configuration provides effective spatial separation of the frontal molecular orbitals, reducing ΔE_{ST}. The metal atom facilitates the spin-orbit coupling necessary for fast RISC. Therefore it is possible to realize TADF with high Φ_{PL} and photoluminescence lifetime below 1 µs. As a result, CMA emitters in OLED devices show performance parameters comparable to phosphorescent emitters.[38–41]
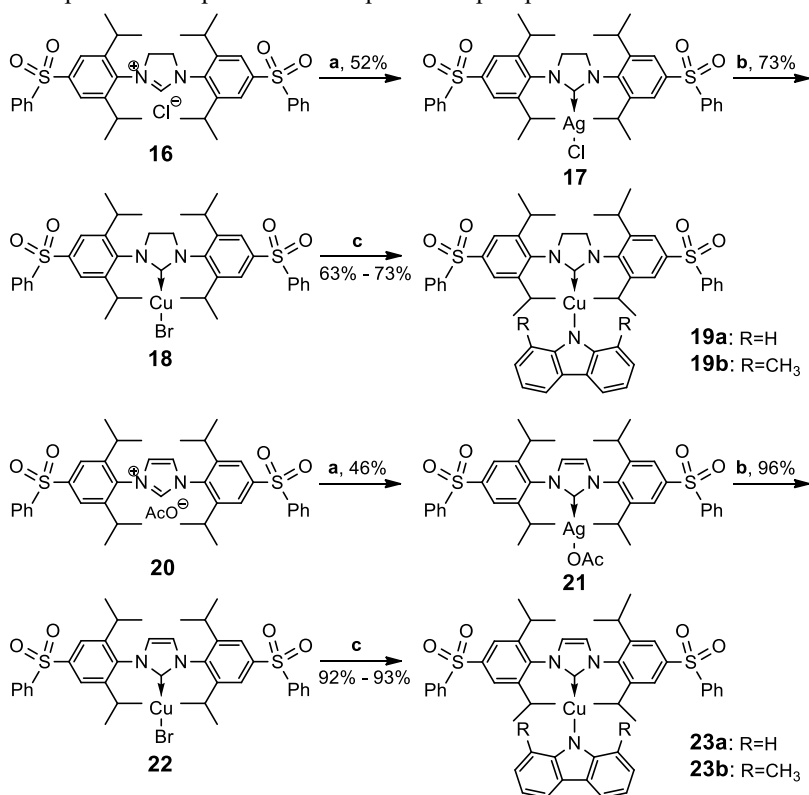
Scheme 3.1. Synthesis of Cu(I) CMA derivatives functionalized with phenylsulfonyl groups: (**a**) Ag$_2$O, MeCN; (**b**) CuBr, CH$_2$Cl$_2$; (**c**) derivative of carbazole, KOtBu, THF.

A series of CMA type complexes was synthesized within the scope of this Doctoral Thesis with phenylsulfonyl acceptor groups added to the 4- position of 2,6-diisopropylphenyl (Dipp)

groups of the imidazole type NHC derivatives. The 4,5-dihydro-1*H*-imidazolium and 1*H*-imidazolium salts **16** and **20** required for the synthesis of NHC derivatives were obtained using a modified method described in the literature.[42] Silver(I) complexes **17** and **21** were obtained in the reaction of compounds **16** and **20** with Ag$_2$O. The silver atom was replaced by copper in a transmetalation reaction with CuBr, yielding copper(I) complexes **18** and **22**. CMA complexes **19a**, **19b**, **23a**, and **23b** were afforded in the reaction of Cu(I) complexes and deprotonated carbazole (Cbz) or 1,8-dimethylcarbazole (MeCbz).

In order to determine the effect of the metal atom on the luminescence properties of the phenylsulfonyl-functionalized CMA emitters, the analogue of complex **19a**, complex **25** was obtained with copper atom replaced by a gold atom (Scheme 3.2). The precursor **24** required for the synthesis of complex **25** was synthesized by transmetalation of silver(I) complex **17** with AuCl·Me$_2$S.
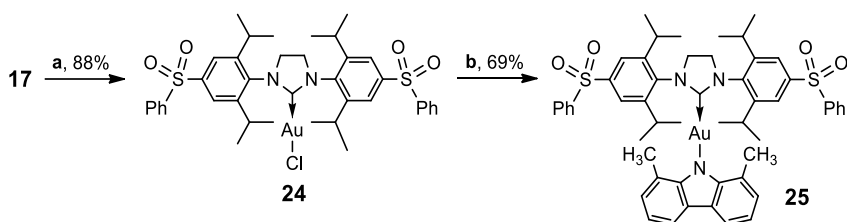
Scheme 3.2. Synthesis of phenylsulfonyl-functionalized Au(I) CMA derivative **25**:
(**a**) AuCl·Me$_2$S, DCM; (**b**) derivative of carbazole, KO*t*Bu, THF.

The series was further extended by the synthesis of unsymmetrical complexes **28a** and **28b**. In these compounds only one of the Dipp groups has the phenylsulfonyl substitution (Scheme 3.3). Copper(I) complex **27** was obtained from 4,5-dihydro-1*H*-imidazolium chloride **26** in one step using the procedure developed by Santoro et al.[43] This method eliminates the requirement to obtain the silver(I) complex first and then use it in the following transmetalation reaction.
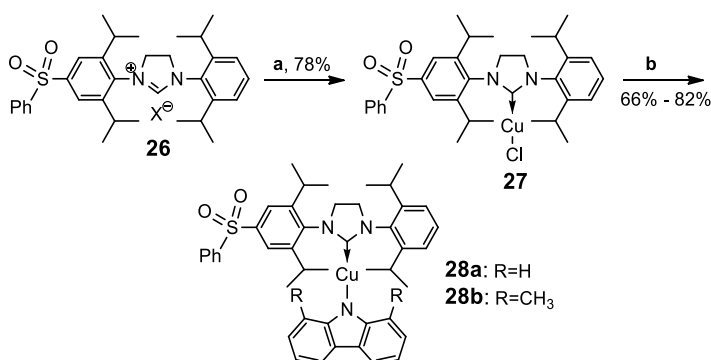
Scheme 3.3. Synthesis of unsymmetrical Cu(I) CMA derivatives functionalized with phenylsulfonyl group:
(**a**) CuCl, K$_2$CO$_3$, acetone; (**b**) derivative of carbazole, KO*t*Bu, THF.

The final complexes were afforded as white or slightly yellowish crystalline powders. In the solid state the compounds are stable in air and show no signs of decomposition after several months of storage. Complexes tend to decompose in solvents in the presence of proton donors (e.g., H_2O, HCl, etc.). The unsymmetrical complexes **28a** and **28b** containing one phenylsulfonyl group exhibit better solubility in non-polar solvents than the symmetric ones. The structures of compounds **19a**, **23b**, and **28a** in the crystalline state were characterized by X-ray crystallography (Fig. 3.1). The most significant structural variations were induced by different amide ligands. For compounds **19a** and **28a** (with a Cbz ligand), the Cu(I) metal coordination has a linear geometry with a slight bend at the metal centre (∡α) and a slight shift from the planar sp^2 geometry (∡β) at the carbazolide N atom. In these compounds the planes of Cbz and imidazolidine fragments are practically coplanar. Due to the steric effect of the methyl groups of MeCbz ligand, a significant shift from the linear geometry can be observed in compound **23b**, which is manifested as a pyramidalization of the carbazolide N atom (∡β = 147.3°). As a result, the alignment of the MeCbz ligand and Dipp cycle planes approaches coplanar (∡γ = 43.4°).
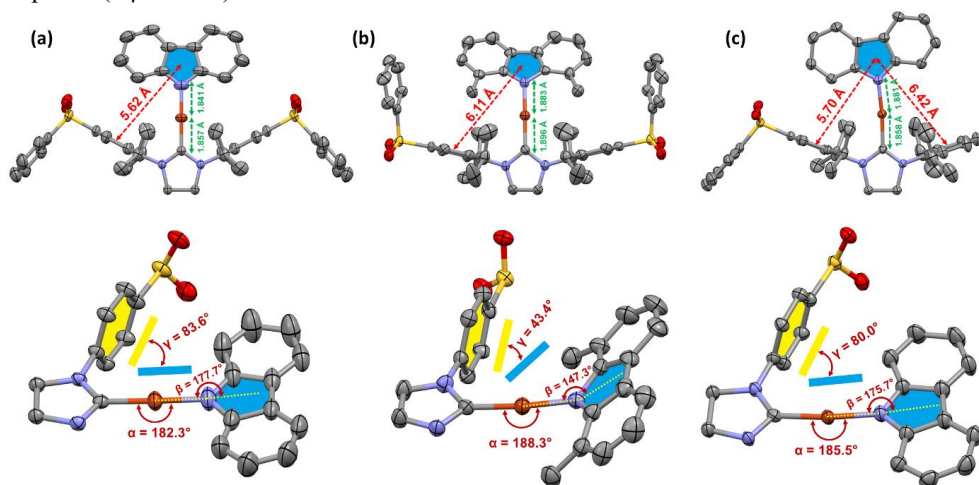

Fig. 3.1. X-ray structures of compounds **19a** (a), **23b** (b), **28a** (c) and the main structural parameters.

Time-dependent DFT (TD-DFT) calculations show that for all compounds in the series, the HOMO is located on the carbazolide ligand and has a small contribution from the metal atom (Fig. 3.2 (a)). The LUMO is located on the diphenylsulfone group. No contribution from either the central carbene ring or the metal atom to the LUMO was observed, marking a significant difference from the CMA emitters reported in the literature.[44–46] The orthogonal arrangement of the frontier molecular orbitals leads to a negligible overlap between the HOMO and LUMO.

The lowest energy singlet transition (S$_0$→S$_1$) takes place via through-space ligand-ligand charge transfer (LLCT) mechanism (Fig. 3.2 (c)). The calculated oscillator strength of the S$_0$→S$_1$ transition is low (in the range of 0.0021–0.0069). For the complexes with the MeCbz ligand, the S$_0$→S$_1$ transition is expected to have a higher oscillator strength than for the

complexes with the Cbz ligand, attributed to the decrease of angle γ between the donor carbazole and the acceptor Dipp planes (Fig. 3.1). Since the frontal molecular orbitals are spatially separated, the expected energy difference between the S_1 and T_1 states is low ($\Delta E_{ST} = 0.007$–0.021 eV). The SOC between the S_1 and T_1 states is lower than that of other CMA complexes due to the negligible contribution of the metal atom to the LUMO orbital (Fig. 3.2 (b)).[47] However, even a small SOC can provide fast RISC considering the low ΔE_{ST} values.[48]
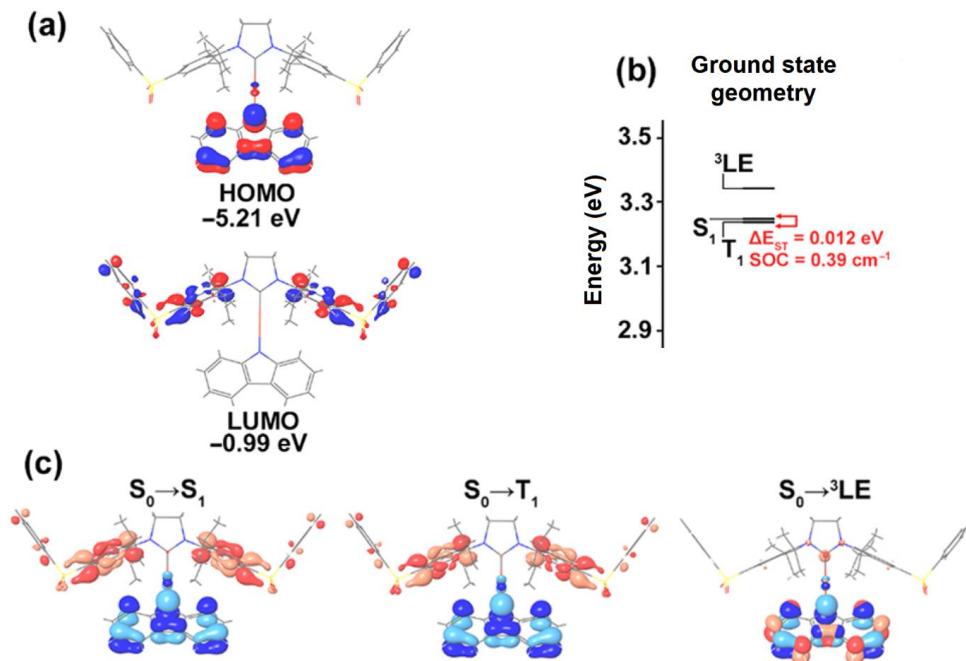

Fig. 3.2. (a) HOMO and LUMO orbitals for compound **19a**. (b) Energy diagram of the lowest energy excited states. (c) Natural transition orbitals.

A similar UV-Vis absorption pattern is observable for all compounds in the series. Several structured absorption bands can be observed in the 300–380 nm region. The position and shape of the structured absorption bands are not affected by changes of solvent polarity (Fig. 3.3 (a)). These absorption bands are attributed to local π–π* transitions of the carbazolide ligand. The CT transition in these compounds is shown as a broad absorption band of weak intensity, which extends up to 450 nm in less polar solvents. The LLCT nature of this absorption band is confirmed by the hypsochromic shift observed with increasing solvent polarity.[40] Accurate determination of the intensity of the CT band is difficult due to the overlap with the π–π* absorption bands of the carbazolide ligand. The extinction coefficient of the CT absorption band can be roughly estimated in the range of 1000 $M^{-1}cm^{-1}$ to 3000 $M^{-1}cm^{-1}$ in toluene solutions. Within the series the compounds with MeCbz ligand exhibit more intensive CT absorption than the compounds with Cbz ligand, confirming the predictions of TD-DFT calculations.
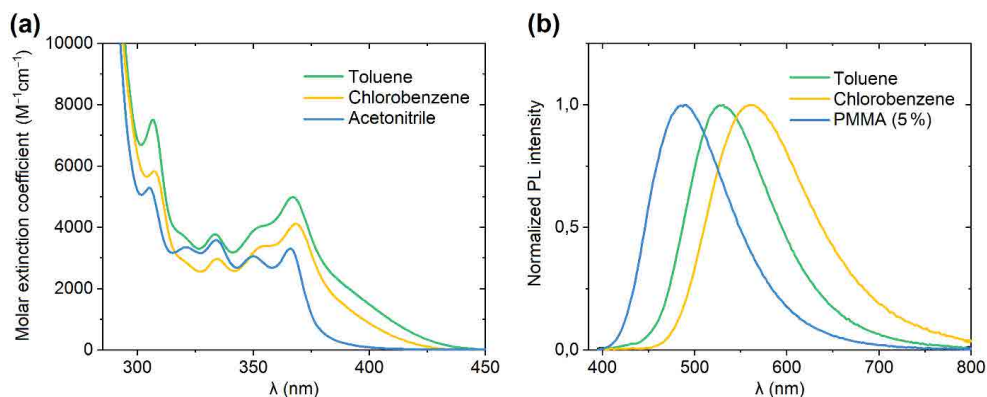
Fig. 3.3. (a) UV-Vis absorption of compound **19b** in different solvents (10^{-5} M).
(b) Photoluminescence of compound **19b** in toluene, chlorobenzene (10^{-5} M) and PMMA
(5 wt %).

The compounds have similar emissive properties in toluene solutions (Table 3.1). The complexes in toluene exhibit emission from the CT excited state with a maxima at 519–547 nm. A bathochromic shift is observed for the CT emission band as the polarity of the solvent increases (Fig. 3.3 (b)). The Φ_{PL} of the complexes in toluene solution does not exceed 0.39 due to the various possible vibrational relaxation processes. Similar to the phosphorescent iridium complexes, the Φ_{PL} of CMA complexes decreases in the presence of oxygen, indicating the involvement of triplet excited states in the emission mechanism.

Table 3.1

Emissive Properties of CMA Derivatives Functionalized with Phenylsulfonyl Groups

Comp.	$\lambda_{\text{max em}}$ [a], nm	Φ_{PL} [a]	$\lambda_{\text{max em}}$ [b], nm	Φ_{PL} [b]	τ_{prompt} [b], ns	τ_1 [b], μs	τ_2 [b], μs	k_r [b], $\times 10^5$ s^{-1}	k_{nr} [b], $\times 10^5$ s^{-1}
19a	523	0.31	472	0.86	6 (0.2 %)	2.5 (45.4 %)	10.6 (54.4 %)	1.25	0.20
19b	521	0.25	482	0.84	12 (0.4 %)	1.5 (61.6 %)	5.2 (38.0 %)	2.89	0.55
23a	547	0.21	488	0.90	10 (0.4 %)	2.0 (46.6 %)	8.3 (53.0 %)	1.68	0.19
23b	541	0.28	492	0.84	19 (0.8 %)	1.4 (59.8 %)	4.3 (39.4 %)	3.32	0.63
25	521	0.27	502	0.69	1 (0.2 %)	1.4 (31.8 %)	4.7 (68.0 %)	1.89	0.85
28a	519	0.38	464	0.80	19.4	2.3	9.9	-	-
28b	521	0.39	476	0.79	37.2 (0.7 %)	1.4 (44.3 %)	5.4 (55.0 %)	2.21	0.59

[a] Luminescence, toluene solution. [b] Luminescence, PMMA film (5 wt %).

In the solid state the molecular motion subsides and the Φ_{PL} of the complexes in thin amorphous films (PMMA, 5 % emitter mass concentration) increases significantly, reaching a maximum value of 0.90 for compound **23a**. In comparison to solutions, PMMA films show a hypsochromic shift of emission (rigidochromism[49]). The emission of compounds in PMMA films is characterized with a complex TADF mechanism with numerous variations within the series. All of the compounds exhibit three-exponential photoluminescence decay kinetics (Fig. 3.4 (a)). Prompt fluorescence ($\tau_{prompt} = 6 - 37$ ns) is observed for the compounds due to the low rates of ISC. The contribution of the prompt fluorescence to the total photoluminescence intensity does not exceed 1 %. The intersystem crossing rate is reduced by the low SOC between the S_1 and T_1 states. Two delayed fluorescence components are observed for the compounds: the first with a lifetime (τ_1) in the range of 1.36 μs to 2.50 μs and the second with a lifetime (τ_2) in the range of 4.25 μs to 10.59 μs. The contribution of the two delayed fluorescence components to the total photoluminescence intensity is similar. The TADF nature of the delayed fluorescence was demonstrated by cooling the samples and observing a gradual decrease of the radiative rate (k_r). The experimentally determined TADF activation energy (ΔE_{ST}) of the compounds varies from 0.0068 eV to 0.0110 eV, which is in agreement with the values predicted by TD-DFT calculations. The dual nature of the TADF can be explained by emission from two different conformations of the molecule. Au(I) complex **25** should be mentioned as an exception. In the case of this compound the fastest component (τ_1) is TADF emission, while the slowest component (τ_2) is related to phosphorescence from the T_2 state, which is energetically close to the S_1 state. The combined radiative rate in the series varies from $1.25 \cdot 10^5$ s^{-1} to $3.32 \cdot 10^5$ s^{-1}. Due to the higher oscillator strength for the lowest energy CT transition, the complexes with the MeCbz ligand have larger k_r values than those with the Cbz ligand.
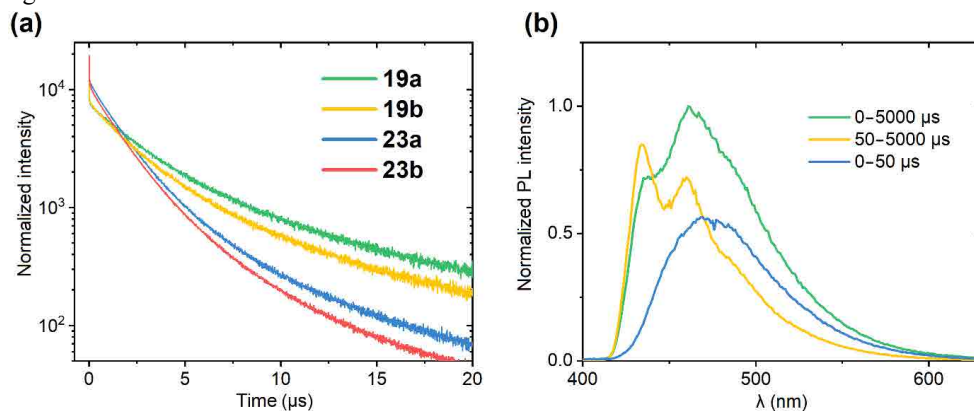
Fig. 3.4. (a) Photoluminescence kinetics of compounds **19a–b** and **23a–b** in PMMA.
(b) Time-dependent photoluminescence of compound **19b**, PMMA film (5 wt %.) at 77 K.

In addition to TADF and possible phosphorescence from the T_2 state (compound **25**), the emission from the carbazolide local triplet excited state (^{3}LE) should be considered as well. Compared to TADF, this emission has a very long lifetime (from several hundreds to a few

thousand microseconds), and time-resolved emission spectroscopy can be used to resolve this luminescence component (Fig. 3.4 (b)). The emission from ^{3}LE state exhibits a fine structure characteristic to the phosphorescence of carbazole derivatives.[41] In the case of compound **23a** (PMMA film), ^{3}LE phosphorescence of carbazolide ligand is observable at room temperature, while for the other compounds in the series it only appears when the samples are cooled. According to TD-DFT calculations, the ^{3}LE state is relatively close in energy to the S_1 state. Upon cooling the samples, the rigidification of PMMA matrix takes place, which destabilizes the S_1 state associated with the LLCT process. As a result, the energy of S_1 state can approach or even exceed the ^{3}LE state, making phosphorescence from the ^{3}LE excited state possible.

Although the new compounds belong to the class of CMA emitters structurally, the luminescence mechanisms differ significantly. In this case, TADF proceeds via through-space CT mechanism. Emitters therefore have very low ΔE_{ST} values, and a small SOC provided by the metal atom promotes RISC. As a result, the achieved Φ_{PL} and radiative rates are comparable to the currently best emitters of the CMA class.[50] From the point of photophysical functionality, the carbene cycle in the new compounds is an inert linking fragment between the donor and acceptor fragments.

In order to evaluate the electroluminescence properties of the compounds, complex **23b** was used to prepare an OLED (Dr. phys. A. Vembris) with the following structure: ITO/PEDOT:PSS (40 nm)/PolyTPD (30 nm)/**23b** (20 wt %): CzSi (40 nm)/TPBi (40 nm)/LiF (1 nm)/Al (100 nm). The emissive layer was prepared from compounds in a solution using the spin coating method. The device showed 6 V turn-on voltage, 1.7 cd/A current efficiency, 0.6 lm/W power efficiency, and 0.8 % external quantum efficiency. The electroluminescence spectrum of the device indicates emission from the CT state of the complex. The obtained results demonstrate the suitability of the compounds for the preparation of electroluminescent devices; however, further optimization is required to improve the performance of the devices.

In the last section of the Doctoral Thesis, the photophysical and electroluminescence properties of CMA derivatives based on 1,3-thiazol-2-ylidene carbene fragment were studied. The 1,3-thiazolium perchlorate salts **29**–**31** known in literature[51] were used as starting materials for the synthesis of the target compounds (Scheme 3.4). Carbene-Cu-Cl complexes were synthesized by *in situ* generation of free carbenes from perchlorate salts in the presence of CuCl. The carbene-Cu-Cl complexes were further used in the synthesis of CMA derivatives. A series of eight compounds were obtained by utilizing different carbazole derivatives as ligands: **32a**, **33a**, and **34a** with carbazole (Cbz) ligand, **32b**, **33b**, and **34b** with 1,8-dimethylcarbazole (MeCbz) ligand, **34c** with 3,6-di-*tert*-butylcarbazole (*t*BuCbz), and **34d** with a 3,6-di-*tert*-butyl-1,8-dimethylcarbazole (Me*t*BuCbz) ligand. The compounds are stable in the solid state and can be stored in air. Complexes exhibit moderate solubility in organic solvents such as toluene, chlorobenzene, dichloromethane and THF. The solubility of compounds is significantly improved by *tert*-butyl groups. An interesting exception is compound **34b**, which has very low solubility in organic solvents at room temperature.
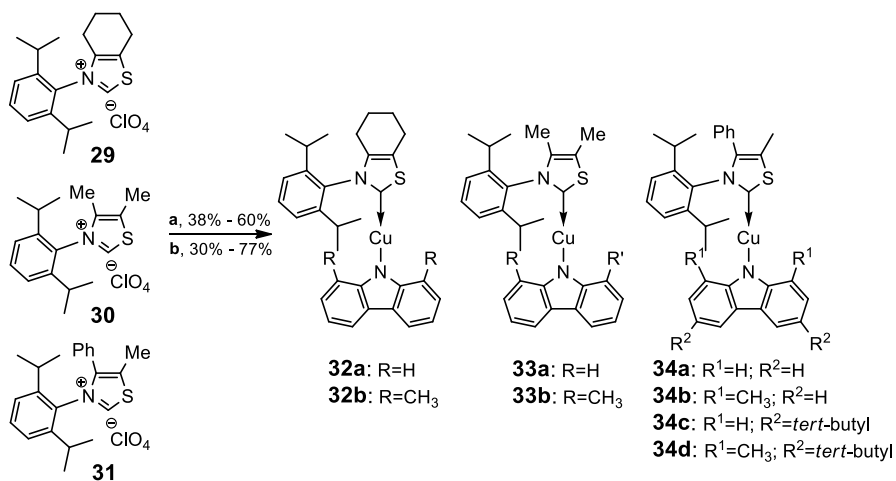
Scheme 3.4. Synthesis of Cu(I) CMA derivatives based on 1,3-thiazol-2-ylidene carbene fragment.
(**a**) CuCl, NaO*t*Bu, THF; (**b**) derivative of carbazole, KO*t*Bu, THF.

The compounds exhibit a practically linear geometry at the complex-forming metal atom and a coplanar arrangement of the carbazolide and carbene rings (Fig. 3.5). Various structural deformations are introduced by the substitution at the carbazolide ligand (1,8-dimethyl groups) and the 1,3-thiazol-2-ylidene ring (4-phenyl group). The steric effects of the 1,8-dimethyl groups of the carbazolide ligand cause repulsion from the Dipp group, turning ∡α towards the unhindered sulphur atom. The Cu-N and Cu-C$_{carbene}$ bonds are lengthened as well. The 4-phenyl group at the carbene ring causes the twist of the Dipp (∡γ) and carbazolide (∡β) planes relative to the plane of the carbene ring. The respective sterical groups introduce not only structural deformations, but also reduce the conformational freedom of the molecule by limiting the rotational freedom of Dipp group, 4-phenyl group and the carbazolide ligand. The low solubility of compound **34b** could be directly related to the rigid molecular structure, which increases the tendency of the molecule to form poorly soluble crystals.
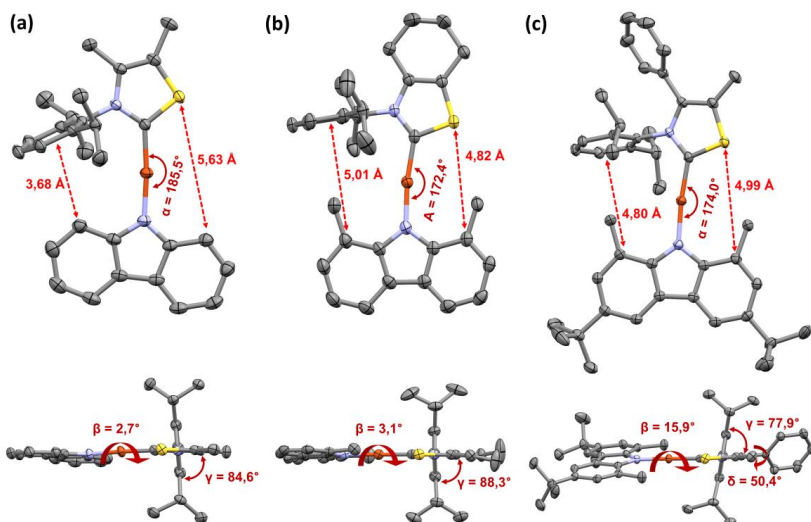
Fig. 3.5. X-ray structures of compounds **33a** (a), **32b** (b), and **34d** (c) and the main structural parameters.

Similarly to the phenylsulfonyl-functionalized CMAs, UV-Vis absorption bands attributed to the local π–π* transitions of the carbazolide ligand can be observed from 300 nm to 380 nm for 1,3-thiazol-2-ylidene derivatives in toluene solution (Fig. 3.6 (a)). The lowest energy absorption bands of the complexes correspond to the CT transition. The intensity of CT transition is significantly higher than that of the phenylsulfonyl-functionalized CMA derivatives, reaching a molar extinction coefficient of $8.0 \cdot 10^3$ $M^{-1} \cdot cm^{-1}$ in the case of compound **34c**. The position of the CT absorption maxima depends on the substituents of the carbazolide ligand. A slight bathochromic shift of the absorption peak is observed when weakly electron-donating methyl or *tert*-butyl groups are added to the carbazolide ligand. As in the case of other CMA type compounds, the CT absorption bands of the complexes shift hypsochromically with increasing solvent polarity.[40]
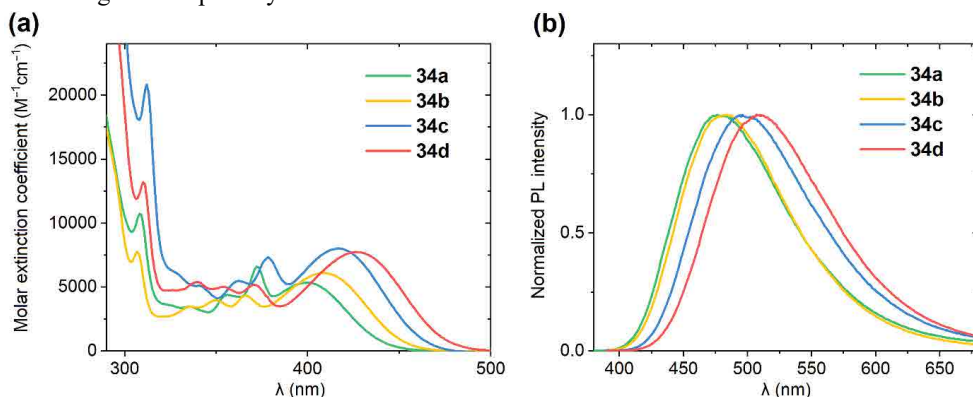

Fig. 3.6. (a) UV-Vis absorption of compounds **34a–d** in toluene (10^{-5} M).
(b) Photoluminescence of compounds **34a–d** in PMMA film (5 wt % concentration).

The luminescence properties of compounds in toluene solutions and thin amorphous films (PMMA, 5 % emitter mass concentration) are given in Table 3.2. The emission proceeds from the CT excited state. Just as the UV-Vis absorption, the position of the luminescence maxima depends on the substituents on the carbazolide ligand (Fig. 3.6 (b)). An increase of Φ_{PL} and a hypsochromic shift of the luminescence maxima can be observed in the solid state in comparison to the solutions. A correlation between the complex structure and k_r for thin amorphous film samples can be observed. Complexes with 1,8-dimethyl substituted carbazolide ligand exhibit k_r 1.1–1.6 times higher than structural analogues with 1,8-unsubstituted carbazolide. The highest k_r values were observed for complexes **34b** and **34d** with a 4-phenyl-substituted 1,3-thiazol-2-ylidene cycle in addition to the 1,8-dimethyl substituted carbazolide. Therefore, it can be concluded that limitations in the rotational freedom of the carbazolide ligand increase the k_r values.

Table 3.2

Emissive Properties of 1,3-thiazol-2-ylidene Carbene Cu(I) CMA Derivatives

Comp.	$\lambda_{\text{max em}}$[a], nm	Φ_{PL}[a]	$\lambda_{\text{max em}}$[b], nm	Φ_{PL}[b]	T[b], μs	k_r[b], ×10^5 s^-1	k_{nr}[b], ×10^5 s^-1
32a	511	0.37	471	0.74	2.6	2.8	1.0
32b	517	0.42	478	0.82	1.9	4.3	0.9
33a	507	0.41	467	0.68	1.9	3.6	1.6
33b	513	0.79	474	0.84	2.1	4.0	0.8
34a	521	0.39	479	0.71	2.1	3.4	1.4
34b	527	0.23	484	0.78	1.6	4.9	1.4
34c	549	0.73	499	0.73	1.6	4.6	1.7
34d	554	0.76	509	0.86	1.2	7.2	1.2

[a] Luminescence, toluene solution. [b] Luminescence, PMMA film (5 wt % concentration).

Compounds in PMMA films exhibit monoexponential photoluminescence decay kinetics with τ_{PL} ranging from 1.2 μs to 2.6 μs (Fig. 3.7 (a)). Upon cooling, all compounds in the series except for **34d** exhibit an emission from the local triplet excited state (^{3}LE) of the carbazolide ligand. Similarly to the phenylsulfonyl-functionalized CMAs, the luminescence from ^{3}LE state can be explained by the rigidification of the PMMA matrix and the resulting destabilization of the CT state. Compound **34d** is an exception because the energy level of the CT state is shifted too far from the energy level of the ^{3}LE state. Therefore, for compound **34d** only CT excited state emission is observable in the entire temperature range from RT to 10 K, with a hypsochromic shift with gradual cooling. An increase in τ_{PL} up to 140 μs at 10 K is also observed upon cooling (Fig. 3.7 (b)), which indicates the TADF nature of the CT emission. At room temperature TADF from the S_1 state is observed. The phosphorescence intensity from the T_1 state increases upon gradual cooling of the sample, until at 50 K the emission occurs only from the T_1 state. By fitting the temperature dependence of τ_{PL} to a modified Boltzmann equation[52] (Fig. 3.7 (b)), ΔE_{ST} was estimated at 0.044 eV for compound **34d**.
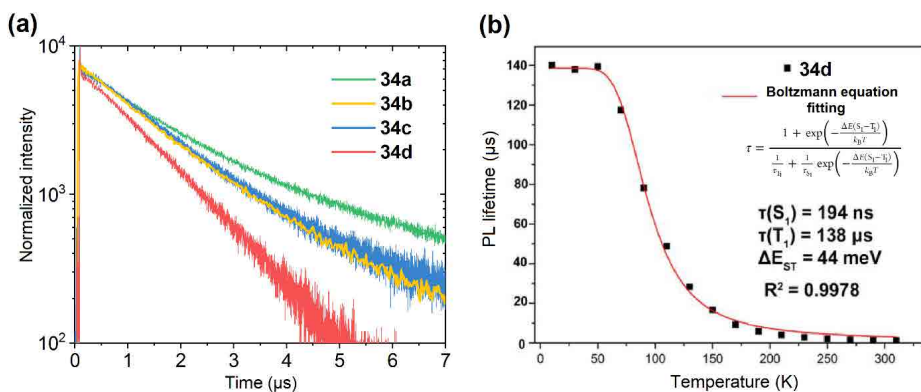
Fig. 3.7. (a) Photoluminescence decay kinetics of compounds **34a–d**, PMMA films (5 wt % concentration). (b) The temperature dependence of the photoluminescence lifetime of compound **34d** and fit against a modified Boltzmann equation, PMMA film (5 wt % concentration).

To investigate the luminescence mechanism and to characterize the influence of steric effects on the luminescence properties, TD-DFT calculations were performed for complexes **34a** and **34b** (Dr. chem. G. Baryshnikov). It was found that the HOMO is localized on the carbazolide ligand, while the LUMO is on the 1,3-thiazol-2-ylidene fragment (Fig. 3.8 (a)). Therefore, the transition to the S_1 excited state exhibit LLCT properties. Both the HOMO and LUMO have a small metal atom contribution, leading to an increase of the $S_0 \rightarrow S_1$ transition oscillator strength and increase of ΔE_{ST}.

According to TD-DFT calculations, the planes of the 1,3-thiazol-2-ylidene and carbazolide ligands are practically coplanar in the ground state S_0 and in the T_1 excited state. On the other hand, at the S_1 excited state these planes tend to rotate to an orthogonal position (Fig. 3.8 (b)), for **34a** assuming dihedral angle ∡β = 77°. Meanwhile, the rotation of the carbazolide ligand in compound **34b** is hindered due to the steric interaction of 1,8-dimethyl and Dipp groups, so the dihedral angle is smaller (∡β = 55°). For this reason, the calculated oscillator strength of the $S_1 \rightarrow S_0$ transition for compound **34b** is two times larger that of **34a**, leading to an equal increase in the predicted delayed fluorescence rate. Thus, the interaction of sterically bulky groups increases the radiative rate in the series of 1,3-thiazol-2-ylidene CMA derivatives.
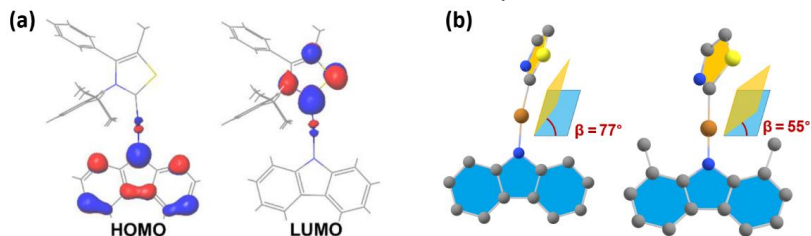

Fig. 3.8. (a) Geometry of HOMO and LUMO for compound **34a**, S_0 geometry. (b) Dihedral angles between the planes of the 1,3-thiazol-2-ylidene and carbazolide in compounds **34a** and **34b**, S_1 geometry.

Compound **34d** shows both the highest Φ_{PL} and the largest k_r in the solid state, therefore it was chosen together with the structural analogue **34c** for OLED preparation (Dr. C.H. Chang). mCBP was selected as the most effective emissive layer host matrix among the four tested materials (CBP, mCBP, mCP, and DPEPO). The following structure was used for the OLED preparation: ITO/TAPC (35 nm)/TCTA (5 nm)/emitting layer (25 nm)/TmPyPB (50 nm)/LiF (1.5 nm)/Al (150 nm) with 1 %, 5 %, 10 %, and 20 % emitter mass concentration in emitting layer. The emissive layer was prepared by the vacuum deposition method. The highest performance parameters were achieved for the device using compound **34c** as emitter, reaching 16.5 % external quantum efficiency and 44215 cd·m^{-2} luminance at 10 wt % emitter doping concentration (Table 3.3). Two distinct emission bands with maxima at 495 nm and 600 nm can be observed in the electroluminescence spectrum of compound **34c** (Fig. 3.9). As the emitter doping concentration increases, the relative intensity ratio between the emission bands at 495 nm and 600 nm increases in favour of the latter. The electroluminescence at 495 nm is recognized as the TADF emission of **34c**, while the electroluminescence at 600 nm could be related to the emission of dimers of compound **34c**, in other words, excimer electroluminescence. As a result, a very broad electroluminescence spectral profile is obtained, which is applicable for the production of white light OLEDs. For compound **34d**, excimer electroluminescence is observed to a much lesser extent than for **34c**. The steric effects induced by 1,8-dimethyl groups reduce the possibilities of compound **34d** to form dimers in the emitting layer.

Table 3.3

OLED Performance Parameters for Compounds **34c–d**

Emitting Layer	V_{on} [a], V	L_{max}, cd·m^{-2}	η_{ext} [b], %	η_c [c], cd·A^{-1}	η_p [d], lm·W^{-1}
34c:mCBP					
1 %	3.8	13542	10.3/7.0 [e]	22.7/15.4 [e]	19.8/9.3 [e]
5 %	3.6	17839	13.7/9.8	25.9/18.6	22.3/11.6
10 %	3.5	44215	16.5/16.1	34.1/33.1	27.1/23.6
20 %	3.7	41695	15.7/14.6	26.0/25.5	20.2/17.0
34d:mCBP					
1 %	3.7	35947	12.9/10.6	31.5/25.8	25.4/17.0
5 %	3.6	42773	12.2/11.6	31.9/30.4	26.0/20.4
10 %	3.8	36478	9.2/9.1	21.7/21.6	15.5/13.2
20 %	3.8	37183	5.9/5.8	14.8/13.4	9.4/8.6

[a] Voltage at which the luminance of the device is 1 cd·m^{-2}. [b] OLED external quantum efficiency. [c] Current efficiency. [d] Power efficiency. [e] Maximum achieved values and values determined at 100 cd·m^{-2}.
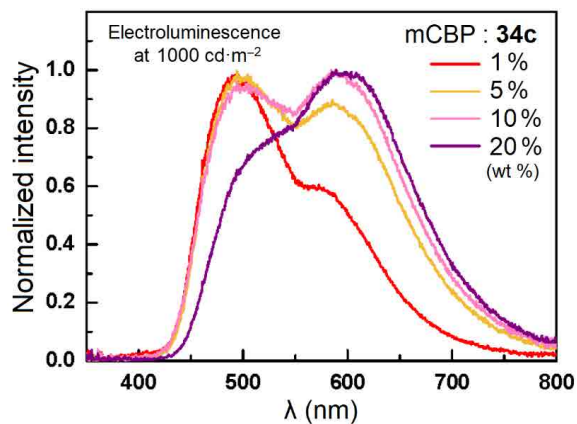
Fig. 3.9. Electroluminescence spectra of compound **34c** at 1000 cd·m^{-2} brightness.

The publications that cover the studies described in this chapter are given in Appendices 3–6.

CONCLUSIONS

1. The functionalization of organic emitters with trityl groups can be employed to obtain luminescent materials that form morphologically stable amorphous thin films from volatile organic solvents. Obtained compounds can be used for the production of OLED devices via the spin coating method.

2. Trityl groups obstruct the charge transfer to the emitter molecules, thus reducing the efficiency of electroluminescence.

3. The obtained phenylsulfonyl-functionalized and 1,3-thiazol-2-ylidene carbene based CMA type Cu(I) complexes exhibit solid state photoluminescence with high Φ_{PL} and a few microsecond lifetime.

4. For the phenylsulfonyl-functionalized CMA derivatives, TADF emission is related to a through-space charge transfer mechanism. Low ΔE_{ST} values in combination with the spin-orbit coupling provided by the metal atom contribute to efficient and fast emissive process.

5. Steric effects influence the photophysical properties of the studied CMA derivatives. In the series of phenylsulfonyl-functionalized CMA compounds, the steric effects of the 1,8-dimethyl groups of the carbazolide ligand lead to a more favourable spatial arrangement of the D and A fragments, thereby increasing the radiative rates. In the series of 1,3-thiazol-2-ylidene carbene based CMA derivatives, the radiative processes are promoted by the interaction of the sterically bulky groups that reduce the rotation of the carbazolide ligand in the S_1 excited state.

6. For the series of 1,3-thiazol-2-ylidene CMA derivatives, efficient excimer electroluminescence can be observed, which could be utilized for the preparation of white light OLEDs.

REFERENCES

[1]   B. Geffroy, P. le Roy, C. Prat, *Polym. Int.* **2006**, *55*, 572–582.

[2]   F. So, J. Kido, P. Burrows, *MRS Bull.* **2008**, *33*, 663–669.

[3]   S. Wang, H. Zhang, B. Zhang, Z. Xie, W.-Y. Wong, *Mater. Sci. Eng. R Reports* **2020**, *140*, 100547.

[4]   R. Karlicek, C. C. Sun, G. Zissis, R. Ma, *Handbook of Advanced Lighting Technology*, Springer International Publishing, Cham, **2017**.

[5]   L. Duan, L. Hou, T.-W. Lee, J. Qiao, D. Zhang, G. Dong, L. Wang, Y. Qiu, *J. Mater. Chem.* **2010**, *20*, 6392–6407.

[6]   Y. Zou, S. Gong, G. Xie, C. Yang, *Adv. Opt. Mater.* **2018**, *6*, 1800568.

[7]   L. Xiao, Z. Chen, B. Qu, J. Luo, S. Kong, Q. Gong, J. Kido, *Adv. Mater.* **2011**, *23*, 926–952.

[8]   Y. Im, M. Kim, Y. J. Cho, J. A. Seo, K. S. Yook, J. Y. Lee, *Chem. Mater.* **2017**, *29*, 1946–1963.

[9]   C. W. Tang, S. A. VanSlyke, *Appl. Phys. Lett.* **1987**, *51*, 913–915.

[10]   J. Bauri, R. B. Choudhary, G. Mandal, *J. Mater. Sci.* **2021**, *56*, 18837–18866.

[11]   C. Zhong, C. Duan, F. Huang, H. Wu, Y. Cao, *Chem. Mater.* **2011**, *23*, 326–340.

[12]   J.-H. Jou, S. Kumar, A. Agrawal, T.-H. Li, S. Sahoo, *J. Mater. Chem. C* **2015**, *3*, 2974–3002.

[13]   T. Chatterjee, K.-T. Wong, *Adv. Opt. Mater.* **2019**, *7*, 1800565.

[14]   H. Yersin, A. F. Rausch, R. Czerwieniec, T. Hofbeck, T. Fischer, *Coord. Chem. Rev.* **2011**, *255*, 2622–2652.

[15]   K.-L. Wong, J.-C. G. Bünzli, P. A. Tanner, *J. Lumin.* **2020**, *224*, 117256.

[16]   S. Ghosh, S. Mandal, C. Banerjee, V. G. Rao, N. Sarkar, *J. Phys. Chem. B* **2012**, *116*, 9482–9491.

[17]   G. Hong, X. Gan, C. Leonhardt, Z. Zhang, J. Seibert, J. M. Busch, S. Bräse, *Adv. Mater.* **2021**, *33*, 2005630.

[18]   K. Mori, T. P. M. Goumans, E. van Lenthe, F. Wang, *Phys. Chem. Chem. Phys.* **2014**, *16*, 14523–14530.

[19]   M. Y. Wong, E. Zysman-Colman, *Adv. Mater.* **2017**, *29*, 1605444.

[20]   T. Huang, W. Jiang, L. Duan, *J. Mater. Chem. C* **2018**, *6*, 5577–5596.

[21]   K. Traskovskis, I. Mihailovs, A. Tokmakovs, A. Jurgis, V. Kokars, M. Rutkis, *J. Mater. Chem.* **2012**, *22*, 11268-11276.

[22]   K. Traskovskis, K. Lazdovica, A. Tokmakovs, V. Kokars, M. Rutkis, *Dye. Pigment.* **2013**, *99*, 1044–1050.

[23]   E. Zarins, K. Balodis, A. Ruduss, V. Kokars, A. Ozols, P. Augustovs, D. Saharovs, *Opt. Mater.* **2018**, *79*, 45–52.

[24]   I. R. Laskar, T.-M. Chen, *Chem. Mater.* **2004**, *16*, 111–117.

[25]   T. Giridhar, W. Cho, Y.-H. Kim, T.-H. Han, T.-W. Lee, S.-H. Jin, *J. Mater. Chem. C* **2014**, *2*, 9398–9405.

[26]   J.-H. Jang, M. J. Kim, H. U. Kim, S. B. Lee, J. Lee, D.-H. Hwang, *J. Nanosci.*

Nanotechnol. **2016**, *16*, 8580–8584.

[27] X. Jiang, J. Peng, J. Wang, X. Guo, D. Zhao, Y. Ma, *ACS Appl. Mater. Interfaces* **2016**, *8*, 3591–3600.

[28] S. E. Zieger, A. Steinegger, I. Klimant, S. M. Borisov, *ACS Sensors* **2020**, *5*, 1020–1027.

[29] T. Giridhar, W. Cho, J. Park, J.-S. Park, Y.-S. Gal, S. Kang, J. Y. Lee, S.-H. Jin, *J. Mater. Chem. C* **2013**, *1*, 2368-2378.

[30] J. Li, R. Wang, R. Yang, W. Zhou, X. Wang, *J. Mater. Chem. C* **2013**, *1*, 4171-4179.

[31] R. Wang, D. Liu, H. Ren, T. Zhang, X. Wang, J. Li, *J. Mater. Chem.* **2011**, *21*, 15494-15500.

[32] C. Fan, L. Zhu, B. Jiang, Y. Li, F. Zhao, D. Ma, J. Qin, C. Yang, *J. Phys. Chem. C* **2013**, *117*, 19134–19141.

[33] J.-H. Choi, C.-H. Jung, J. Y. Kwon, H.-J. Cho, J. Lee, J.-I. Lee, H.-Y. Chu, D.-H. Hwang, *Synth. Met.* **2009**, *159*, 1517–1521.

[34] M. A. Baldo, S. Lamansky, P. E. Burrows, M. E. Thompson, S. R. Forrest, *Appl. Phys. Lett.* **1999**, *75*, 4–6.

[35] M. G. Colombo, T. C. Brunold, T. Riedener, H. U. Guedel, M. Fortsch, H.-B. Buergi, *Inorg. Chem.* **1994**, *33*, 545–550.

[36] Q. Zhang, B. Li, S. Huang, H. Nomura, H. Tanaka, C. Adachi, *Nat. Photonics* **2014**, *8*, 326–332.

[37] M. Cai, M. Auffray, D. Zhang, Y. Zhang, R. Nagata, Z. Lin, X. Tang, C.-Y. Chan, Y.-T. Lee, T. Huang, X. Song, Y. Tsuchiya, C. Adachi, L. Duan, *Chem. Eng. J.* **2021**, *420*, 127591.

[38] D. Di, A. S. Romanov, L. Yang, J. M. Richter, J. P. H. Rivett, S. Jones, T. H. Thomas, M. Abdi Jalebi, R. H. Friend, M. Linnolahti, M. Bochmann, D. Credgington, *Science* **2017**, *356*, 159–163.

[39] R. Hamze, S. Shi, S. C. Kapper, D. S. Muthiah Ravinson, L. Estergreen, M.-C. Jung, A. C. Tadle, R. Haiges, P. I. Djurovich, J. L. Peltier, R. Jazzar, G. Bertrand, S. E. Bradforth, M. E. Thompson, *J. Am. Chem. Soc.* **2019**, *141*, 8616–8626.

[40] R. Hamze, J. L. Peltier, D. Sylvinson, M. Jung, J. Cardenas, R. Haiges, M. Soleilhavoup, R. Jazzar, P. I. Djurovich, G. Bertrand, M. E. Thompson, *Science* **2019**, *363*, 601–606.

[41] S. Shi, M. C. Jung, C. Coburn, A. Tadle, D. Sylvinson M. R., P. I. Djurovich, S. R. Forrest, M. E. Thompson, *J. Am. Chem. Soc.* **2019**, *141*, 3576–3588.

[42] S. Leuthäußer, D. Schwarz, H. Plenio, *Chem. - A Eur. J.* **2007**, *13*, 7195–7203.

[43] O. Santoro, A. Collado, A. M. Z. Slawin, S. P. Nolan, C. S. J. Cazin, *Chem. Commun.* **2013**, *49*, 10483–10485.

[44] R. Hamze, M. Idris, D. S. Muthiah Ravinson, M. C. Jung, R. Haiges, P. I. Djurovich, M. E. Thompson, *Front. Chem.* **2020**, *8*.

[45] T. Li, D. S. Muthiah Ravinson, R. Haiges, P. I. Djurovich, M. E. Thompson, *J. Am. Chem. Soc.* **2020**, *142*, 6158–6172.

[46] A. S. Romanov, M. Linnolahti, M. Bochmann, *Dalt. Trans.* **2021**, *50*, 17156–17164.

[47] M. Gernert, L. Balles-Wolf, F. Kerner, U. Müller, A. Schmiedel, M. Holzapfel, C. M. Marian, J. Pflaum, C. Lambert, A. Steffen, *J. Am. Chem. Soc.* **2020**, *142*, 8897–8909.

[48] P. K. Samanta, D. Kim, V. Coropceanu, J.-L. Brédas, *J. Am. Chem. Soc.* **2017**, *139*, 4042–4051.

[49] A. J. Lees, *Comments Inorg. Chem.* **1995**, *17*, 319–346.

[50] J. Hossain, R. Akhtar, S. Khan, *Polyhedron* **2021**, *201*, 115151.

[51] I. Piel, M. D. Pawelczyk, K. Hirano, R. Fröhlich, F. Glorius, *European J. Org. Chem.* **2011**, *2011*, 5475–5484.

[52] R. Czerwieniec, J. Yu, H. Yersin, *Inorg. Chem.* **2011**, *50*, 8293–8301.

ACKNOWLEDGEMENTS

The author would like to express his gratitude to the following colleagues for their contribution to the Doctoral Thesis:

- Dr. chem. Kaspars Traskovskis and Dr. chem. Valdis Kokars for supervising the Doctoral Thesis;
- colleagues of the Institute of Applied Chemistry for providing support to the research of the Thesis;
- Dr. chem. Baiba Turovska and Dr. phys. Sergey Belyakov for cyclic voltammetry analysis and X-ray diffraction analyses;
- The team of the Laboratory of Organic Materials of Institute of Solid State Physics of University of Latvia under the leadership of Dr. phys. Aivars Vembris for contribution to various measurements and OLED preparation;
- international partners for their contribution to OLED preparation and DFT calculations;
- Laura Drunka for correcting the manuscript.

Armands Rudušs

PIELIKUMI / PUBLICATIONS

Traskovskis, K.; **Ruduss, A.**; Kokars, V.; Mihailovs, I.; Lesina, N.; Vembris, A.
Thiphenylmethane Based Structural Fragments as Building Blocks Towards
Solution-Processable Heteroleptic Iridium(iii) Complexes for OLED Use.
New J. Chem. **2019**, *43* (1), 37–47.

Check for updates

Thiphenylmethane based structural fragments as building blocks towards solution-processable heteroleptic iridium(III) complexes for OLED use†

Kaspars Traskovskis, *[a] Armands Ruduss,[a] Valdis Kokars,[a] Igors Mihailovs,[ab] Natalija Lesina[b] and Aivars Vembris[b]

A novel structural approach to solution-processable heteroleptic iridium(III) complexes is presented. On the basis of 2-arylbenzo[*d*]thiazole cyclometalating main ligands and picolinic acid (pic) and acetylacetone (acac) ancillary ligands six new yellow or orange emitting materials were obtained using attached 1,1,1-triphenylmethylpentane substituents as aggregation preventing and solubility enhancing functional fragments. The obtained compounds show high photoluminescence quantum yield values in the range of 0.64 to 0.90. OLEDs with a spin-coated emissive layer were successfully prepared, with the highest achieved external quantum efficiency of 7.9%, current efficiency of 12.4 cd A^{-1} and power efficiency of 7.8 lm W^{-1}, measured at luminance 6000 cd m^{-2}. Maximal device brightness of 17 451 cd m^{-2} was attained.

Introduction

During the last few decades the practical use of organic light emitting diodes (OLEDs) has increased significantly in such areas as flat panel displays and lighting devices.[1–3] Amongst the compounds used as light emitters, special interest can be attributed to phosphorescent transition metal complexes.[4] The inherent ability of these materials to harvest triplet excited states allows electroluminescent devices with 100% internal quantum efficiency to be obtained, in contrast to their fluorescent counterparts that are capped at 25%.[5] Amid a wide selection of the studied compounds, cyclometalated iridium(III) complexes can be named as the most extensively researched material class because of their chemical stability, large phosphorescence quantum yields, relatively short phosphorescence lifetimes and wide possibilities of color-tuning through modification of the chemical structure of the attached ligands.[6,7]

Yellow/orange-phosphorescent compounds can be outlined as a distinctive subset of light emitting materials.[8] By falling outside of the spectrum of primary colors (red, green and blue), the main proposed application direction of these emitters involves their incorporation in solid state lighting sources. Particularly, two-component white OLEDs, consisting of blue fluorescent and

yellow/orange phosphorescent emitters, are considered as a promising light-source device architecture due to a simple design and high efficiency parameters.[9–11] Iridium(III) complexes, based on a 2-phenylbenzo[*d*]thiazole (bt) cyclometalating ligand framework, are the most extensively researched and applied class of yellow phosphorescent materials, with the attained OLED external quantum efficiencies well over the 20% mark for vacuum-deposited devices.[12–16]

The high production cost of OLEDs is currently limiting a more widespread use of this technology. This is largely attributed to the complicated and energy-demanding vacuum deposition technique that is used to acquire the active layers of the devices. In order to avoid luminescence-quenching that takes place due to the intermolecular interactions, iridium(III) complexes are often mixed in host molecules, with typical concentrations up to 10 weight percent (wt%). As a consequence, this brings additional difficulties during the vacuum-deposition process. It is shown that the material distribution in the acquired films is not homogenous and guest molecules form aggregate networks at concentrations as low as 5 wt%, contributing to a fall in efficiency of OLEDs through the triplet–triplet annihilation process.[17] Additionally, a high thermal stability is a requirement for the emitters because chemical transformations can take place during the harsh conditions of thermal evaporation.[18] This greatly reduces the number of potentially useful compounds. Solution-processable iridium(III) complexes are being extensively developed in order to overcome these disadvantages, with the dendritic molecular design being the most widespread research direction.[19] The iridium(III) complex core is encapsulated by site-isolating and solubility enhancing groups in these compounds, allowing them to be

[a] *Riga Technical University, Faculty of Materials Science and Applied Chemistry, 3/7 Paula Valdena Street, Riga LV-1048, Latvia.*
E-mail: kaspars.traskovskis@rtu.lv; Tel: +371 29148070
[b] *Institute of Solid State Physics, University of Latvia, 8 Kengaraga Street, Riga LV-1063, Latvia*
† Electronic supplementary information (ESI) available. See DOI: 10.1039/c8nj04484h

processed with cost-effective solution based methods like spin-coating and ink-jet printing. The research in this direction continues, in order to achieve a right balance between solubility, stability of the solid state morphology, thermal rigidity and charge carrier mobility of materials. This is needed, as the attachment of additional functional fragments to the emitters compromises the efficiency of the devices.[20]

In this study we explore a novel structural design of solution-processable iridium(III) complexes. On the basis of three different 2-arylbenzo[d]thiazole main ligands, bearing 4-hydroxyphenyl, 4-hydroxynapthyl or carbazole aromatic fragments, and acetyl-acetone (acac) and 2-picolinic acid (pic) ancillary ligands, we acquired six new solution-processable and glass-forming materials. The phase-behavior of the low-solubility cyclometalated bt based compounds is modified by the introduction of a 1,1,1-triphenyl-methylpentane group. Triphenylmethyl-based substituents are known to enhance photo-physical performance characteristics of different organic dye systems by providing an efficient site-isolation and subsequent limitation of intermolecular interactions.[21,22] Here we explore the viability of this molecular design towards the acquisition of phosphorescent materials for use in OLEDs by measuring photo-physical, thermoplastic and electrolumi-nescence properties of the acquired compounds.

Results and discussion

Design and synthesis

Introduction of electron donating atoms (O, N) at the 4-position of the benzyl ring of the bt ligand has been shown to be beneficial to the light emission efficiency of the corresponding Ir(III) complexes.[23] On the other hand, the polar substituents are known to enhance molecular aggregation processes through electrostatic interactions or by hydrogen bonding, resulting in materials with reduced solubility and increased crystallinity. To overcome this, modified bt-derived ligands containing phenol (Phbt), naphthol (Nphbt) or carbazole (Cbzbt) fragments were acquired, where a phase-behavior-modifying 1,1,1-triphenylpentyl group was attached to the electronegative atoms (Scheme 1). The corresponding cyclometalated heteroleptic iridium(III) complexes were synthesized with satisfactory yields in two steps. First, Nonoyama's procedure[24] was applied to obtain μ-chloro-bridged dimers. Then ancillary ligands, acetylacetone (acac) or 2-picolinic acid (pic), were introduced by using 2-ethoxyethanol as the solvent and potassium carbonate as the base. The ^{1}H NMR spectra and the results of elemental analysis are consistent with the proposed structures. The acquired compounds show excellent solubility in volatile, low- to medium-polarity solvents like DCM and chloroform, forming glassy, amorphous mass under minimal solvent exposure. At the same time the compounds do not dissolve in alcohols, showing potential suitability for a sequential solvent-based layer-on-layer deposition during the device fabrication process.

Thermal properties and phase behavior

Thermal properties of the materials were examined employing differential scanning calorimetric (DSC) and thermogravimetric (TG) techniques. According to the acquired DSC thermograms (Fig. 1), all the compounds show closely similar phase behavior characteristics. Only one signal, corresponding to a glass transition
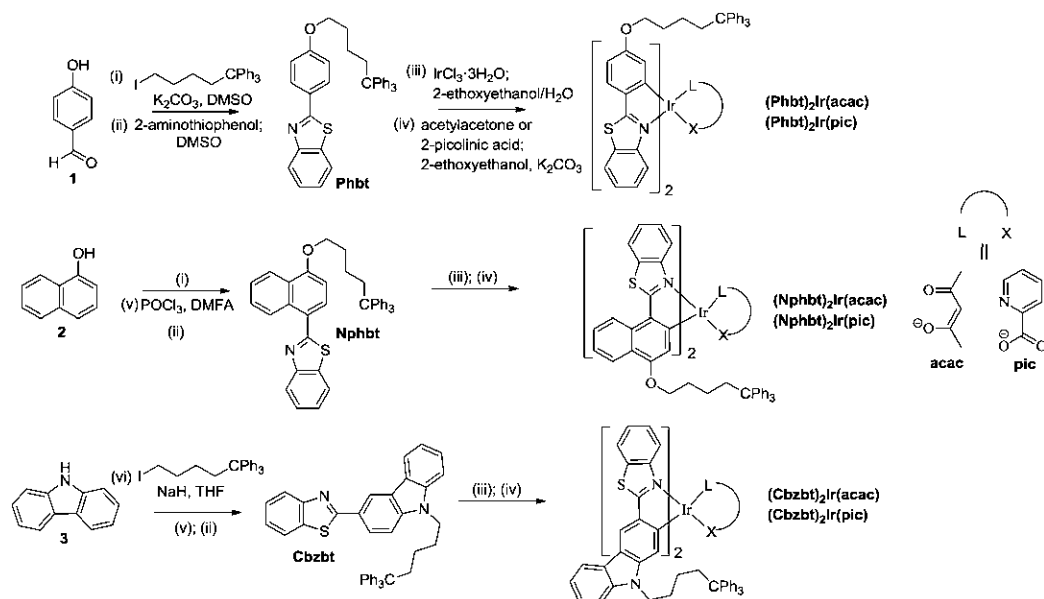
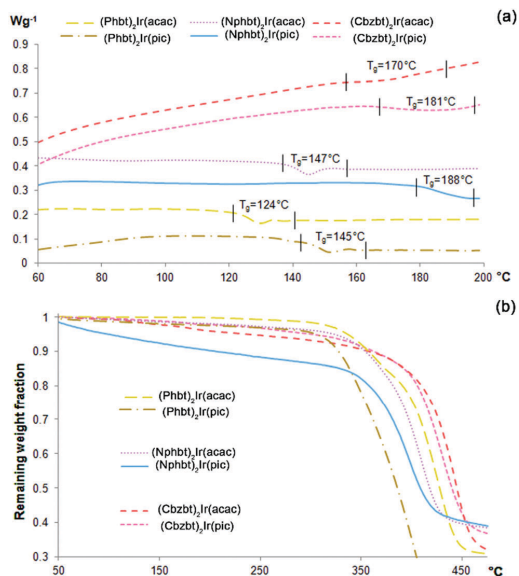Scheme 1 Synthesis of heteroleptic Ir(III) complexes.

Fig. 1 (a) DSC scans of the materials with outlined T_g values. (b) TG thermograms.

Regarding the thermal stability of the compounds, the results of the performed thermogravimetric analysis (TG) (Fig. 1b) reveal that compounds exhibit decomposition onset in the range 320–350 °C. A steady mass loss of several percent is observed for materials during the heating process that can be attributed to a gradual loss of residual solvent inclusions in the amorphous material bulk. It is worth noting that compounds containing pic ancillary ligands show a tendency of having slightly lower thermal stability in comparison to acac analogues.

Photophysical properties

UV-Vis absorption spectra of the synthesized compounds (Fig. 2 and Table 1) feature a broad absorption region in the 300–500 nm range that is similar to that of bt based close structural analogues.[15,23] The most intensive absorption bands, in the 300–350 nm region, can be attributed to the $^1\pi$–$\pi^\star$ transitions of cyclometalating ligands. Medium strength absorption in the 380–480 nm range marks spin allowed metal-to-ligand charge transitions (^{1}MLCT), while shoulders with a weak intensity stretching to lower-energy wavelengths can be attributed to a spin-forbidden ^{3}MLCT excitation. A bathochromic shift of the lowest energy absorption bands can be observed in the series of Phbt, Cbzt and Nphbt ligand based complexes. This shift can be associated with an extension of the delocalized π-electron

temperature (T_g), can be detected during the heating process, indicating that the synthesized materials form a highly stable amorphous phase. No signs of inherent crystallinity were detected either in DSC scans of the pristine samples, or during multiple heating–cooling scan cycles. Glassy, transparent films of the materials with high optical quality can be obtained *via* a spin-coating technique using volatile solvents (chloroform, DCM) with no observable phase changes after months of storage. Regarding the measured T_g values, a notable dispersion of this parameter is evident amongst the studied series, ranging from 124 to 188 °C. T_g increase in the class of low-molecular-weight glass-forming compounds (molecular glasses) can be correlated to larger molecular weight and reduced conformational freedom of molecules.[25] A combination of these parameters can partly explain the observed T_g variations, as the compounds based on heavier Nphbt and Cbzt ligands show higher glass transition temperatures, in contrast to their structural counterparts containing the smaller Phbt ligand. Besides the influence of the main ligand, T_g values of the materials strongly correlate with the structure of the applied ancillary ligand, as the compounds containing a pic moiety show higher glass transition values than those containing an acac group, ranging from 11 °C increase in the case of Cbzbt to 41 °C for Nphbt based complexes. It is known that iridium(III) complexes that contain a pic structural fragment tend to participate in C–H···O type hydrogen bonding processes due to the presence of sterically unshielded oxygen atoms of the unbound carboxyl group.[26] Thus the existence of solid-phase intermolecular hydrogen bonding is the most likely cause for the observed T_g increase.
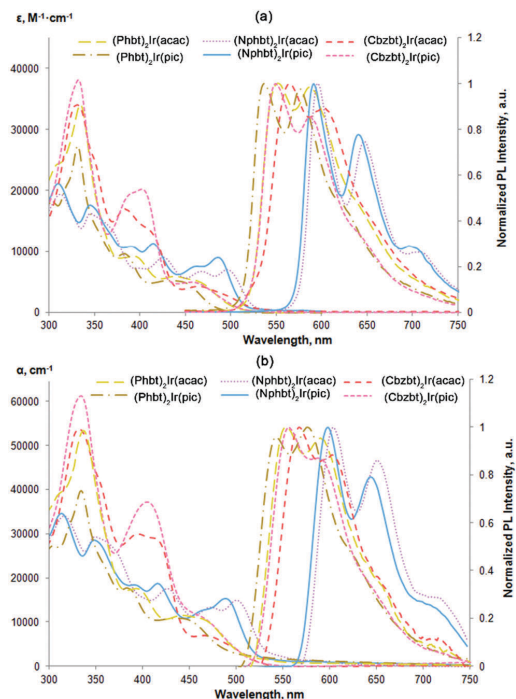

Fig. 2 (a) UV-Vis absorption and PL spectra in THF solution, (b) UV-Vis absorption of complexes in amorphous host-free films and PL spectra in the CBP host at 20 wt% emitter concentration.

Table 1 Photophysical properties of the synthesized compounds

Compound	Absorbance[a], λ_{max}, nm (lg ε)	Emission[b], λ_{max}, nm	Φ_{PL}[c] (THF)	τ[d], μs	k_r[e], $\times$ 10^5 s^{-1}	k_{nr}[f], $\times$ 10^5 s^{-1}	$\Delta E_{S0\rightarrow S1}$[g], eV	$\Delta E_{S0\rightarrow T1}$[g], eV
(Phbt)₂Ir(acac)	464(3.7), 437(3.8), 391(4.0), 334(4.5)	552, 588 (553, 591)	0.78/0.02/0.15/0.31	3.32	1.56	1.44	3.38	2.54
(Phbt)₂Ir(pic)	433(3.7), 382(4.0), 331(4.4)	537, 576 (544, 576)	0.87/0.10/0.06/0.39	4.48	1.78	0.45	3.41	2.56
(Nphbt)₂Ir(acac)	496(4.1), 467(4.1), 425(4.3), 398(4.2), 345(4.5)	595, 648 (604, 651)	0.64/0.03/0.06/0.27	3.75	1.15	2.49	3.19	2.21
(Nphbt)₂Ir(pic)	485(4.3), 462(4.2), 414(4.4), 389(4.3), 344(4.5)	591, 641 (598, 644)	0.64/0.04/0.08/0.50	5.63	1.10	0.68	3.21	2.22
(Cbzbt)₂Ir(acac)	464(3.9), 410(4.4), 383(4.5), 330(4.8)	568, 603 (568, 603)	0.69/0.02/0.02/0.12	2.61	1.34	1.52	3.26	2.52
(Cbzbt)₂Ir(pic)	456(4.0), 402(4.6), 387(4.6), 332(4.9)	549, 588 (556, 587)	0.90/0.05/0.02/0.50	3.65	2.05	0.67	3.34	2.53

[a] Measured in THF solution. [b] Values in THF solution (and CBP film at 20 wt% concentration). [c] Values in deoxygenated THF solution/host-free films/20 wt% PVK film/20 wt% CBP film. [d] Measured in PMMA film at 1% emitter concentration. [e] Radiative decay rate $k_r = \Phi_{PL}/\tau$. [f] Non-radiative decay rate $k_{nr} = (1 - \Phi_{PL})/\tau$. [g] Calculated excitation energy values of the lowest energy $S_0 \rightarrow S_1$ and $S_0 \rightarrow T_1$ transitions.

system in the corresponding 2-arylbenzo[d]thiazoles that leads to a lowering of local singlet and triplet bandgap values.[27]

Upon a photoexcitation at 450 nm all the compounds show strong phosphorescence (Fig. 2 and Table 1). Emission bands of the compounds feature a vibrionic fine structure, indicating that the emission is strongly associated with ligand centered $^3\pi-\pi^*$ transitions.[13] The observed gap of separation of these vibrational features is in the range of 1020–1370 cm^{-1} and can be associated with the stretching of aromatic double bonds in the cyclometalated ligands.[28] Just like in the case of absorption spectra, the photoluminescence (PL) bands red-shift depending on the present ligand, following the sequence: Phbt, Cbzbt and Nphbt. Compounds based on Phbt and Cbzbt emit yellow light, while in the case of Nphbt derivatives the emission is orange-red. A strong influence on PL characteristics can also be observed in relation to the present ancillary ligand. In the case of acac functionalized compounds a substantial red-shift of PL wavelength is observed in comparison to their pic counterparts. This effect can be explained by a stronger chemical bonding between pic and the iridium atom, resulting in a shorter ligand–metal distance and stronger ligand-induced stabilization of the occupied iridium d-orbitals.[29] As a result, bandgap values of d–π*transitions are expected to be larger in pic functionalized compounds.

The synthesized compounds possess relatively large PL quantum yields (Φ_{PL}), with the measured values in dilute degassed THF solutions ranging from 0.64 to 0.90 (Table 1). For reference, the reported PL quantum yield of the unmodified base compound **(bt)₂Ir(acac)** is 0.65.[14] As it is expected, larger Φ_{PL} is measured for the yellow Phbt and Cbzbt based emitters in comparison to orange-red Nphbt. The lower lying triplet energy levels for Nphbt increase the probability of nonradiative decay pathways of the excited state.

In the case of Phbt and Cbzbt based complexes the presence of the pic ancillary ligand leads to notably larger Φ_{PL} values. This observation can be explained by the fact that the non-symmetrical pic ligand changes the electron density of the molecule in such a way that the excited S_1 and T_1 states in the resulting heteroleptic complex are confined on one single cyclometalating C^N type ligand.[30] In the case where symmetrical acac is present, S_1 is delocalized on both the primary ligands, while in the emissive T_1 state only on one ligand.[30]

The more pronounced spatial distribution of the excited state orbitals in the case of acac derivatives and, consequently, increases the number of the available vibrational states and, consequently, the probability of the nonradiative decay. Additionally, in order to emit from the T_1 state, acac functionalized complexes must undergo an interligand charge transfer that potentially lowers the attainable Φ_{PL} value even more.

In order to validate the previous assumptions a series of density functional theory (DFT) calculations were performed. The optimized geometries and the corresponding highest occupied and lowest unoccupied molecular orbitals (HOMO and LUMO) for all synthesized complexes are given in Fig. 3. In all cases a distinctive difference in molecular orbital configuration between compounds bearing acac and pic ancillary ligands can be observed. While HOMO placement is fairly similar for all compounds, centered mainly on the electron rich aryl fragments of 2-arylbenzo[d]thiazole ligands, notable deviations can be seen in LUMO distribution. For acac containing compounds, the LUMO is symmetrically distributed over both the main ligands, particularly on the electron deficient benzothiazole ring. For pic, however, the asymmetry is induced by this ancillary group that shifts the LUMO to a single benzothiazole ring. **(Cbzbt)₂Ir(pic)** can be named as an outlier from this trend, as the asymmetry is present not only for the LUMO, but also for the HOMO level. As previously discussed, the more pronounced orbital containment would result in increased Φ_{PL}. This is the case, as the experimental observations follow computational predictions that the presence of the pic ligand leads to increased Φ_{PL} values of the compounds, with **(Cbzbt)₂Ir(pic)** being the most efficient, as its molecular orbitals have the least spatial spread. Additionally, excitation energies for the lowest singlet and triplet excitations were calculated (Table 1). The obtained values correlate well with the experimental absorption wavelengths, as larger calculated bandgaps correspond to lower measured absorption wavelengths.

In all cases the measured phosphorescence kinetics of the compounds can be expressed as a single exponential, with the lifetimes in the range 2.61–5.63 μs, which is typical for iridium(III) complexes. Radiative decay rates (k_r) are notably lower for orange emitting Nphbt derivatives indicating a poorer iridium metal mediated intersystem crossing. For Phbt and Cbzbt based complexes a slight increase in k_r is observed if a pic ancillary ligand is present.
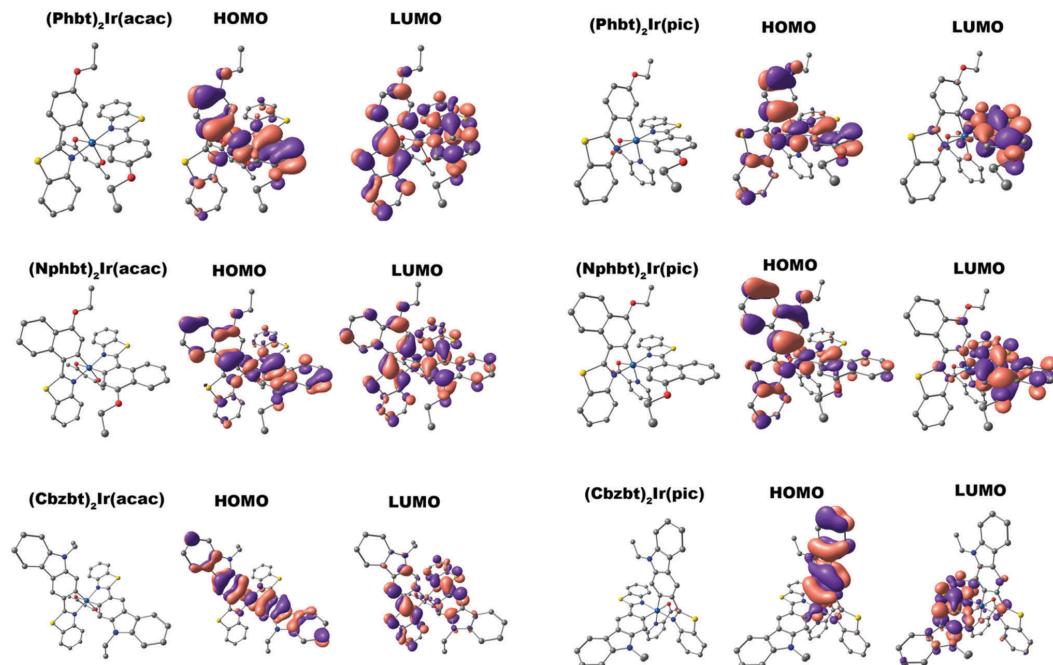
Fig. 3 DFT optimized structures of the complexes and corresponding HOMO and LUMO visualizations. Hydrogens are omitted for clarity.

The main purpose of the presented molecular design was to acquire materials that are suitable for applications in solution-processable OLED devices. The PL measurements of pure spin-coated films revealed that a strong PL quenching takes place due to the emitter aggregation and the Φ_{PL} values do not exceed 0.10 (Table 1). In some cases almost complete quenching of the emission was observed. This is expected, as the mass concentration (wt%) of the active emitting complex in the compounds, excluding the mass of non-emissive 5,5,5-triphenylpentyl groups, is approximately 50%. The optimal mass concentration of the emitters in the emissive layers of manufactured OLED devices is 8–10%, in order to provide a large enough spatial separation level of individual molecules and limit the negative effects of aggregation-induced emission quenching.[31] Two conventional hole transporting materials, polymeric PVK and molecular CBP, were used to prepare guest–host systems with an approximate emitter concentration of 10 wt% (corresponding to 20 wt% of the synthesized compounds). Under these conditions a sufficient level of emitter spatial isolation was achieved, and in CBP Φ_{PL} values of up to 0.50 were measured (Fig. 2 and Table 1). Interestingly, the synthesized materials showed a strong preference for the CBP host in comparison to PVK, as in PVK no notable improvement in solid state Φ_{PL} values was observed in comparison to host-free films. We attribute this behavior to the structure of PVK that features the presence of non-polar aliphatic polymer chains. When exposed to the polar emitter molecules, these lipophilic fragments induce phase separation,

creating non-emissive domains of iridium complex aggregates. Nevertheless, this is a convenient property of the compounds, because the use of the molecular host materials results in more efficient OLEDs due to enhanced charge carrier mobilities.[32]

Atomic force microscopy (AFM) was employed in order to closely evaluate the film forming properties of the synthesized compounds. Two spin-coated (from THF solution) samples were examined, where **(Cbzbt)$_2$Ir(pic)** (20 wt%) was dispersed in PVK and CBP hosts (Fig. 4). The root-mean-square (RMS) roughness values of these films were 2.1 and 1.5 nm. It should be noted that these values are measured by taking into account all surface areas, including the obvious defective sites. By measuring only the flat areas, values of 0.7 and 0.4 nm were acquired, indicating a highly homogenous structure for both samples. Still, a slightly higher overall clustering is detected for the polymeric PVK host. This is in accordance with the measured Φ_{PL} values that indicate much more pronounced emitter–emitter interaction if this host material is used.

Another noteworthy observation regarding the solid phase emissive properties of the compounds is a distinctive improvement in measured Φ_{PL} for pic functionalized compounds in comparison to their acac structural analogues, especially in the case of the CBP host. This difference cannot be simply attributed to the intrinsically higher PL efficiency of pic derivatives and indicates alternative solid state packing patterns between the two subtypes of the materials. Taking into consideration the practically identical emission spectra of the compounds in
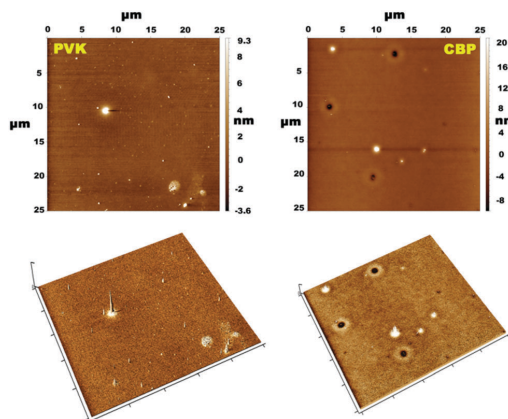
Fig. 4 AFM images of spin-coated films, composed of **(Cbzbt)₂Ir(pic)** (20 wt%) and PVK or CBP host.

THF and CBP (Fig. 2), but at the same time the notably reduced Φ_{PL} values, the logical explanation for such observation is that in CBP there are two populations of the complex molecules: highly isolated and aggregated. The isolated population behaves as in THF, giving a similar PL band. The aggregated molecules, on the other hand, are weakly emissive, as indicated by the small Φ_{PL} values in the host-free films. The notable difference between Φ_{PL} values of acac and pic derivatives in CBP indicates that the presence of acac induces a more pronounced emitter–emitter aggregation. The following explanation for this can be given. While the molecular surface of the complex core in pic containing compounds is fully aromatic, the presence of an acac ancillary ligand creates a local aliphatic region. The incompatibility between aromatic and aliphatic domains is known to influence solid state packing patterns of iridium complexes. The repulsion between the acac-functionalized face of the complex and the fully aromatic CBP host layer is considered as the origin for a non-isotropic spatial orientation of emitting molecules in vacuum-deposited OLEDs.[33] In our case this interaction between aromatic and aliphatic surfaces promotes the aggregation for acac containing compounds, as the complex molecules tend more to interact with each other.

Electroluminescence properties

In order to evaluate the suitability of the synthesized materials as the active electroluminescent components, OLEDs bearing compounds **(Cbzbt)₂Ir(acac)** and **(Cbzbt)₂Ir(pic)** were prepared. **(Cbzbt)₂Ir(pic)** was chosen, as it shows the highest Φ_{PL} value and the fastest radiative decay rate k_r amongst the studied series of the compounds. Its structural analogue **(Cbzbt)₂Ir(acac)** was picked to evaluate the difference between acac and pic ancillary ligands. Two series of devices were prepared, where solution-processed emissive layers contain either a polymeric PVK or molecular CBP host: (device-I) ITO/PEDOT:PSS (40 nm)/emitting layer (60 nm, PVK:emitter 20 wt%)/BPhen (20nm)/LiF (1 nm)/Al (100 nm) and (device-II) ITO/PEDOT:PSS (40 nm)/emitting layer

(60 nm, CBP:emitter 20 wt%)/TPBi (20 nm)/LiF (1 nm)/Al (100 nm). The obtained results (Fig. 5 and Table 2) are in good agreement with the previously discussed PL measurements that showed a strong Φ_{PL} increase in the cases where the CBP host material was used. The switch from PVK to CBP boosts the OLED's external quantum efficiency (η_{ext}) 2.5 times in the case of **(Cbzbt)₂Ir(acac)** and 1.6 times in the case of **(Cbzbt)₂Ir(pic)** with the corresponding increase in the maximal achievable luminance of 4.3 and 4.7 times, respectively. As expected, the use of a pic functionalized emitter increases the η_{ext} value 1.5 times and the maximal luminance by approximately 2 times in comparison to acac based devices.

No notable transformations were detected in the emission spectra of the OLEDs with the variation of either the applied voltage (Fig. S2, ESI†) or the type of host material (Fig. 5d). The emission is closely similar to that seen in the PL spectra of thin films, indicating that the origin of the emitted light is the phosphorescence of iridium(III) complexes. No detectable drop in OLED luminance was detected for the **(Cbzbt)₂Ir(pic)**:CBP device after 4 hours of continuous operation at 100 cd m^{-2}, indicating a sufficient stability of the emitting molecule. For all the devices a small diminishment of the current in the range of 6–8 V can be observed in the volt-ampere characteristics (Fig. 5a). The first recombination of the opposite charges in OLEDs can only take place with the reaching of the turn-on voltage; thereby the observed drop of the current is attributed to a small imbalance in the system's charge carrier concentration. This means that the energy level alignment of the layers can be improved to further increase the device efficiency. Systems with CBP as the host material exhibit a higher current density in the voltage region over 8 V, which together with the higher observed brightness points to a better electronic injection in the system compared to PVK based OLEDs.

All the examined devices start to show efficiency roll-off behavior at current densities in the 50–100 mA cm^{-2} range. While this may be attributed to many factors, like residual solvent inclusions, the efficiency roll-off in OLEDs is mainly ascribed to the aggregation of the emitters. In vacuum-deposited devices the spatial distribution of the complex molecules is more or less determined by the random molecular motion, while in solution there is a higher tendency for them to form aggregates. This process is especially likely to take place during the processing stage that often involves a steep concentration increase on a relatively long time-scale, determined by the slow solvent evaporation speed. Triplet–triplet annihilation is considered as the main mechanism for efficiency roll-off for aggregated molecules. This process takes place if the distance between iridium complex based emitters is less than 2 nm[31,34] and governs efficiency roll-off, as the density of triplet excited states in the bulk of the emissive layer increases with the growing current density. Additionally, not only do solution-processed emitter molecules tend to form unwanted aggregates, but this process also proceeds in the case of host materials (CBP).[35] As a result this causes a higher charge carrier trapping in the system. Thereby exciton quenching by polarons has high influence on the performance of the device. At higher current density it can dramatically reduce the efficiency of the OLEDs.
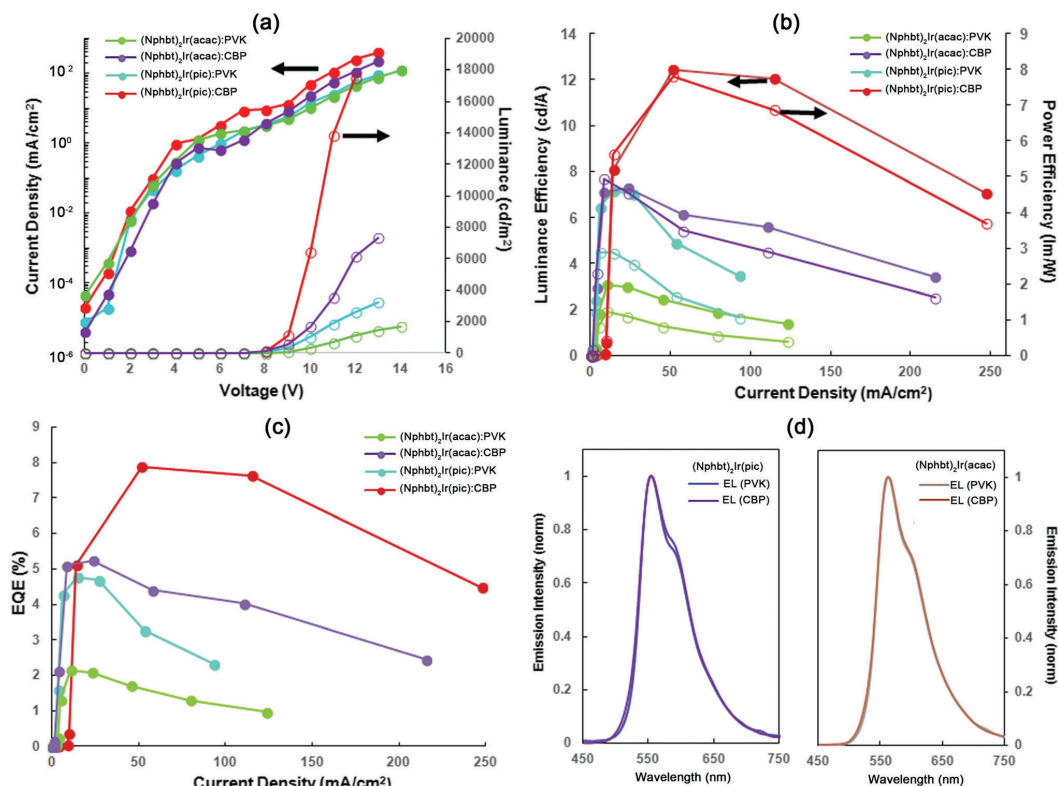
Fig. 5 Characteristics of **(Cbzbt)₂Ir(acac)** and **(Cbzbt)₂Ir(pic)** based OLEDs: (a) voltage–current density (filled circle)–luminance (empty circle) plots, (b) luminance (filled circle) and power efficiency (empty circle) *versus* current density, (c) external quantum efficiency *versus* current density and (d) EL spectra of OLEDs.

Table 2 Electroluminescence characteristics of **(Cbzbt)₂Ir(acac)** and **(Cbzbt)₂Ir(pic)** based OLEDs

Emissive layer[a]	V_{on}[b], V	L_{max}, cd m⁻²	η_{ext}[c], %	η_c[d], cd A⁻¹	η_p[e], lm W⁻¹	λ_{max}, nm	CIE (x, y)
(Cbzbt)₂Ir(acac):PVK	7.0	1708	2.1/1.7[f]	3.1/2.4[f]	1.9/1.3[f]	561	0.43, 0.46
(Cbzbt)₂Ir(acac):CBP	6.5	7295	5.2/5.1	7.3/7.1	4.9/4.7	563	0.43, 0.46
(Cbzbt)₂Ir(pic):PVK	6.5	3229	4.8/4.8	7.2/7.2	4.5/4.5	553	0.44, 0.53
(Cbzbt)₂Ir(pic):CBP	5.5	17 451	7.9/5.1	12.4/8.0	7.8/5.6	554	0.44, 0.53

[a] The concentration of the iridium(III) complex in the devices is 20 wt%. [b] Voltage at which luminance of 1 cd m⁻² is measured. [c] OLED's external quantum efficiency. [d] Current efficiency. [e] Power efficiency. [f] Maximal achieved values and values measured at 1000 cd m⁻².

The maximal achieved performance parameters of the **(Cbzbt)₂Ir(pic)**/CBP based OLED are the following: η_{ext} of 7.9%, current efficiency of 12.4 cd A⁻¹ and power efficiency of 7.8 lm W⁻¹ at luminance 6000 cd m⁻², with the highest measured luminance of 17 451 cd m⁻². These values exceed the characteristics of the other reported yellow emitting solution-processed devices that contain structurally similar thiazole based iridium(III) complexes, in terms of both the efficiency parameters and brightness.[13,36,37] This underlines the viability of the presented molecular design towards the development of large area OLEDs with a lowered production cost.

Conclusions

A novel structural approach to the synthesis of solution-processable yellow and orange light emitting heteroleptic iridium(III) complexes is presented. The materials can be acquired based on O and N functionalized 2-arylbenzo[d]thiazole cyclometalating ligands by an introduction of phase-behavior-modifying 1,1,1-triphenylpentyl substituents in a simple 4 to 5 step-reaction sequence. According to the results of DSC analysis the acquired compounds do not possess inherent crystallinity and form a stable amorphous phase, at the same time showing an

excellent solubility in a wide range of organic solvents. The presence of the modifying groups does not affect the emission efficiency, as large Φ_{PL} values in the range of 0.64 to 0.90 were measured for the synthesized complexes. Amongst the investigated compounds a clear improvement in solid-state emissive properties is observed if picolinic acid ancillary ligand is used instead of acetylacetone. Additionally, the presented materials show a distinctive preference for molecular charge transporting host materials in comparison to the polymeric alternatives. The compounds can be successfully used to produce solution-processed OLEDs and the best obtained device showed an external quantum efficiency of 7.9%, current efficiency of 12.4 cd A^{-1} and power efficiency of 7.8 lm W^{-1} at luminance 6000 cd m^{-2}, with the highest measured luminance of 17 451 cd m^{-2}. According to the observed volt-ampere characteristics, a further device optimization is possible, with the use of more appropriate electron or hole transport layers, in order to improve the charge balance. Despite this, the achieved performance parameters of the solution-processed OLEDs already exceed those reported for their close structural analogues, highlighting the viability of the presented material design.

Experimental

Materials and instruments

Starting materials and solvents were purchased from Alfa Aesar. 5,5,5-Triphenylpentan-1-iodide was prepared according to a known procedure.[22] NMR spectra were obtained using a Bruker Avance 300 MHz spectrometer using solvent residue as an internal reference. Mass spectra were acquired using a Waters EMD 1000 MS detector (ESI + mode, cone voltage 30 V). The elemental analysis was carried out using a Costech Instruments ECS 4010 CHNS-O Elemental Combustion System. Differential scanning calorimetry (DSC) thermograms were acquired using a Mettler Toledo DSC-1/200 W apparatus at a scanning rate of 10 °C min^{-1} while keeping the samples under N$_2$ atmosphere. Decomposition temperatures were obtained using a Perkin Elmer STA 6000 thermal analyzer. Optical measurements in solution were carried out using solutions of typical concentrations 1–4 × 10^{-5} mol L^{-1}. Solutions for Φ_{PL} measurements were prepared in a glovebox under Ar atmosphere using previously degassed solvents and filled in sealable cuvettes. The UV-Vis spectra were recorded using a Perkin Elmer Lambda 35 spectrometer. Emission spectra, absolute photoluminescence quantum yields (PLQY) and emission lifetimes were determined using a QuantaMaster 40 steady state spectrofluorometer (Photon Technology International, Inc.) equipped with a 6 inch integrating sphere (LabSphere). A Veeco AFM CP-II atomic force microscope was used in tapping mode.

Synthesis of Ir(III) complexes

Synthesis of 2-(4-((5,5,5-triphenylpentyl)oxy)phenyl)benzo-[*d*]thiazole (Phbt ligand). A mixture of 4-hydroxybenzaldehyde (0.72 g, 5.9 mmol), K$_2$CO$_3$ (0.32 g, 23.0 mmol) and DMSO (5 mL) was stirred at room temperature for 30 min. A solution of

1,1,1-triphenylpentan-5-iodide (2.30 g, 5.5 mmol) in DMSO (10 mL) was then added and the mixture was stirred for an additional 3 h. The contents of the reaction vessel were poured into water (75 mL) and extracted with CH$_2$Cl$_2$ (3 × 20 mL). After the evaporation of the solvent the crude product was purified by column chromatography over silica gel using gradient elution (toluene, then CH$_2$Cl$_2$) to yield the alkylation product as a white solid (0.61 g, 26%). ^{1}H NMR (300 MHz, CDCl$_3$) δ (ppm): 9.90 (s, 1H), 7.84 (d, J = 8.8 Hz, 2H), 7.39–7.09 (m, 15H), 6.96 (d, J = 8.8 Hz, 2H), 4.00 (t, J = 6.5 Hz, 2H), 2.68 (m, 2H), 1.87 (quint, J = 6.5 Hz, 2H), 1.32 (m, 2H). Alkylated hydroxybenzaldehyde (0.54 g, 1.3 mmol) and 2-aminothiophenol (0.31 g, 2.6 mmol) were stirred in DMSO (5 mL) under argon atmosphere at 130 °C for 3 h. The mixture was poured into water and the precipitate was collected by filtration and washed with ethanol. The crude product was purified by column chromatography over silica gel using toluene as an eluent to yield Phbt as a white glass (0.43 g, 64%). ^{1}H NMR (300 MHz, CDCl$_3$) δ (ppm): 8.05 (dd, J = 7.9 Hz, J = 1.1 Hz, 1H), 7.93 (d, J = 8.9 Hz, 2H), 7.56 (td, J = 7.9 Hz, J = 1.1 Hz, 1H), 7.42 (td, J = 7.9 Hz, J = 1.1 Hz, 1H), 7.32–7.10 (m, 15H), 6.96 (d, J = 8.9 Hz, 2H), 3.99 (t, J = 6.5 Hz, 2H), 2.68 (m, 2H), 1.85 (quint, 2H), 1.29 (m, 2H). MS ESI$^+$, m/z calcd: 526.7 [M + H]$^+$, found: 526.5 [M + H]$^+$.

Synthesis of 2-(4-((5,5,5-triphenylpentyl)oxy)naphthalen-1-yl)benzo[*d*]thiazole (Nphbt ligand). A mixture of 1-naphthol (0.71 g, 4.9 mmol), K$_2$CO$_3$ (0.28 g, 20.0 mmol) and DMSO (5 mL) was stirred at room temperature for 30 min. A solution of 1,1,1-triphenylpentan-5-iodide (2.10 g, 4.9 mmol) in DMSO (10 mL) was then added and the mixture was stirred for an additional 3 h. The contents of the reaction vessel were poured into water (75 mL), and the precipitate was collected by filtration and washed with ethanol and dried to afford 2.05 g of a practically pure alkylation product as a white solid. Then, under argon atmosphere, POCl$_3$ (0.84 mL, 9.0 mmol) was slowly added to DMF (0.80 mL, 10.3 mmol) while the reaction mixture was cooled in an ice bath. The solution of alkylated naphthol (2.0 g, 4.5 mmol) in DMF (2 mL) was then added to the reaction vessel. The temperature was raised to 100 °C and the mixture was stirred for 3 h. The contents of the reaction vessel were poured into water and the precipitate was collected by filtration and washed with ethanol. The crude product was purified by column chromatography over silica gel using toluene as an eluent to yield the resulting naphthaldehyde as a white solid (1.70 g, 79%). ^{1}H NMR (300 MHz, CDCl$_3$) δ (ppm): 10.14 (s, 1H), 9.25 (d, J = 8.6 Hz, 1H), 8.15 (d, J = 8.6 Hz, 1H), 7.84 (d, J = 8.1 Hz, 1H), 7.65 (m, 1H), 7.48 (m, 1H), 7.29–7.02 (m, 15H), 6.80 (d, J = 8.1 Hz, 1H), 4.13 (t, J = 6.2 Hz, 2H), 2.67 (m, 2H), 1.93 (quint, J = 6.2 Hz, 2H), 1.37 (m, 2H). The final product, benzothiazole Nphbt, was acquired following the same procedure as for Phbt. Yield: 67%. ^{1}H NMR (300 MHz, CDCl$_3$) δ (ppm): 9.06 (d, J = 8.5 Hz, 1H), 8.26 (d, J = 8.2 Hz, 1H), 8.18 (d, J = 8.5 Hz, 1H), 7.96 (d, J = 8.2 Hz, 1H), 7.89 (d, J = 8.5 Hz, 1H), 7.67 (m, 1H), 7.55 (m, 2H), 7.44 (m, 1H), 7.35–7.12 (m, 15H), 6.84 (d, J = 8.5 Hz, 1H), 4.18 (t, J = 6.1 Hz, 2H), 2.75 (m, 2H), 2.01 (quint, J = 6.1 Hz, 2H), 1.48 (m, 2H). MS ESI$^+$, m/z calcd: 576.8 [M + H]$^+$, found: 576.5 [M + H]$^+$.

Synthesis of 2-(9-(5,5,5-triphenylpentyl)-9H-carbazol-3-yl)benzo-[d]thiazole (Cbzbt ligand). Sodium hydride (1.0 g, 25 mmol, 60% dispersion in oil) was added to a mixture of 1,1,1-triphenylpentan-5-iodide (10.0 g, 23 mmol) and carbazole (3.0 g; 18 mmol) in THF (50 mL). The suspension was stirred for 3 h after which water (80 mL) was added and THF was removed under reduced pressure. The organic material was extracted with CH_2Cl_2 (3 × 40 mL) and the extract was dried over anhydrous Na_2SO_4. After the removal of the solvent the crude product was purified by column chromatography over silica gel using CH_2Cl_2 as an eluent to yield the alkylated carbazole as a white solid (4.69 g, 56%). ^{1}H NMR (300 MHz, CDCl_3) δ (ppm): 8.14 (d, J = 7.6 Hz, 2H), 7.54–7.44 (m, 2H), 7.39–7.33 (m, 2H), 7.32–7.18 (m, 15H), 4.22 (t, J = 6.1 Hz, 2H), 2.62 (m, 2H), 1.91 (quint, J = 6.1 Hz, 2H), 1.29 (m, 2H). 9-(5,5,5-Triphenylpentyl)-9H-carbazole (4.0 g, 9.9 mmol) was suspended in DMF (10 mL). $POCl_3$ (1.0 mL, 10.4 mmol) was slowly added while the mixture was cooled using an ice bath. The temperature was raised to 60 °C and the solution was stirred for 8 h. The contents of the reaction vessel were poured into a mixture of ice (100 g) and CH_2Cl_2 (20 mL) after which a solution of NaOH (2.5 g, 62 mmol) in water (20 mL) was added. The organic material was extracted with CH_2Cl_2 (3 × 40 mL) and the extract was dried over anhydrous Na_2SO_4. After the removal of the solvent the crude product was purified by column chromatography over silica gel using CH_2Cl_2 as an eluent to yield the resulting aldehyde as a white solid (1.44 g, 42%). ^{1}H NMR (300 MHz, CDCl_3) δ (ppm): 10.12 (1H, s), 8.61 (d, J = 1.2 Hz, 1H), 8.16 (d, J = 7.6 Hz, 1H), 7.99 (dd, J = 8.5 Hz, J = 1.2 Hz, 1H), 7.52 (t, J = 7.6 Hz, 1H), 7.41–7.32 (m, 3H), 7.31–7.11 (m, 15H), 4.24 (t, J = 6.5 Hz, 2H), 2.59 (m, 2H), 1.90 (quint, J = 6.5 Hz, 2H), 1.24 (m, 2H). The final product, benzothiazole Cbzbt, was acquired following the same procedure as for Phbt. Yield: 79%. ^{1}H NMR (300 MHz, CDCl_3) δ (ppm): 8.86 (s, 1H), 8.24–8.15 (m, 2H), 8.12 (d, J = 8.2 Hz, 1H), 7.94 (d, J = 7.8 Hz, 1H), 7.57–7.46 (m, 2H), 7.41 (d, J = 7.8 Hz, 1H), 7.39–7.32 (m, 3H), 7.32–7.12 (m, 15H), 4.24 (t, J = 6.8 Hz, 2H), 2.60 (m, 2H), 1.91 (quint, J = 6.8 Hz, 1H), 1.26 (m, 2H). MS ESI+, m/z calcd: 599.2 [M + H]+, found: 599.6 [M + H]+.

General method of the synthesis of heteroleptic iridium complexes. $IrCl_3 \cdot H_2O$ (1 mmol) and the corresponding benzothiazole ligand (2.3 mmol) were stirred under argon atmosphere in a mixture of 2-ethoxyethanol and water (4:1) at 130 °C for 24 h. The contents of the reaction vessel were poured into water; the precipitate was collected by filtration and washed with ethanol. Without further purification the acquired dichloro-bridged complex was dissolved in 2-ethoxyethanol and an excessive amount of auxiliary ligand (acetylacetone or 2-picolinic acid) and K_2CO_3 (in 1:3 molar ratio) was added under argon atmosphere. The reaction mixture was stirred at 100 °C for 2 h and then poured into water. The precipitate was collected by filtration, washed with ethanol and then purified by column chromatography over silica gel using toluene (or CH_2Cl_2/ethyl acetate 50:1 for compounds containing *pic* auxiliary ligand) as eluent to yield the desired heteroleptic iridium(III) complex.

(Phbt)₂Ir(acac). Yield: 40%. ^{1}H NMR (300 MHz, CDCl_3) δ (ppm): 7.93 (d, J = 7.3 Hz, 2H), 7.65 (d, J = 7.4 Hz, 2H), 7.46 (d, J = 8.4 Hz, 2H), 7.33 (2H, J = 7.3 Hz, 2H), 7.29–7.03 (m, 32H), 6.28 (dd, J = 8.4 Hz, J = 2.1 Hz, 2H), 5.75 (d, J = 2.1 Hz, 2H), 5.05 (s, 1H), 3.35 (m, 4H), 2.33 (m, 4H), 1.68 (s, 6H), 1.38 (m, 4H), 0.93 (m, 4H). Anal. calcd for $C_{77}H_{67}IrN_2O_4S_2$: C, 68.98; H, 5.04; N, 2.09. Found: C, 68.96; H, 5.11; N, 2.43.

(Phbt)₂Ir(pic). Yield: 40%. ^{1}H NMR (300 MHz, CDCl_3) δ (ppm): 8.35 (d, J = 8.2 Hz, 1H), 8.11 (d, J = 8.2 Hz, 1H), 7.86 (d, J = 7.7 Hz, 1H), 7.78 (t, J = 7.6 Hz, 1H), 7.65–7.47 (m, 4H), 7.34–7.25 (m, 2H), 7.21–7.06 (m, 32H), 6.80 (t, J = 7.5 Hz, 1H), 6.42 (dd, J = 8.6 Hz, J = 2.2 Hz, 1H), 6.33 (dd, J = 8.6 Hz, J = 2.2 Hz, 1H), 5.99–5.88 (m, 2H), 5.62 (d, J = 2.2 Hz, 1H), 3.51–3.20 (m, 4H), 2.40–2.29 (m, 4H), 1.42–1.29 (m, 4H), 1.05–0.81 (m, 4H). Anal. calcd for $C_{78}H_{64}IrN_3O_4S_2$: C, 68.70; H, 4.73; N, 3.08. Found: C, 68.41; H, 4.75; N, 3.18.

(Nphbt)₂Ir(acac). Yield: 47%. ^{1}H NMR (300 MHz, CDCl_3) δ (ppm): 8.45 (d, J = 8.4 Hz, 2H), 8.08 (d, J = 7.8 Hz, 2H), 7.98 (d, J = 8.1 Hz, 2H), 7.76 (d, J = 7.1 Hz, 2H), 7.58 (t, J = 7.1 Hz, 2H), 7.40–7.02 (m, 36H), 5.84 (s, 2H), 5.15 (s, 1H), 3.43–3.00 (m, 4H), 2.44 (m, 4H), 1.78 (s, 6H), 1.46 (m, 4H), 1.04 (m, 4H). Anal. calcd for $C_{85}H_{71}IrN_2O_4S_2$: C, 70.86; H, 4.97; N, 1.94. Found: C, 71.14; H, 5.05; N, 2.25.

(Nphbt)₂Ir(pic). Yield: 55%. ^{1}H NMR (300 MHz, CDCl_3) δ (ppm): 8.48 (m, 3H), 8.20 (d, J = 7.6 Hz, 1H), 8.08 (d, J = 8.2 Hz, 1H), 7.99 (d, J = 8.1 Hz, 1H), 7.92–7.82 (m, 2H), 7.75–7.55 (m, 4H), 7.45–7.35 (m, 2H), 7.35–7.05 (m, 34H), 6.90 (t, J = 8.1 Hz, 1H), 6.18 (d, J = 8.2 Hz, 1H), 6.08 (s, 1H), 5.67 (s, 1H), 3.51–3.01 (m, 4H), 2.43 (m, 4H), 1.56–1.35 (m, 4H), 1.06 (m, 4H). Anal. calcd for $C_{86}H_{68}IrN_3O_4S_2$: C, 70.56; H, 4.68; N, 2.87. Found: C, 70.54; H, 4.81; N, 3.05.

(Cbzbt)₂Ir(acac). Yield: 31%. ^{1}H NMR (300 MHz, CDCl_3) δ (ppm): 8.38 (s, 2H), 8.16 (d, J = 8.2 Hz, 2H), 7.97 (d, J = 7.7 Hz, 2H), 7.62 (d, J = 7.8 Hz, 2H), 7.37–7.15 (m, 42H), 7.10 (t, J = 7.5 Hz, 2H), 7.02 (d, J = 8.1 Hz, 2H), 6.27 (s, 2H), 5.19 (s, 1H), 3.59 (t, J = 7.4 Hz, 4H), 2.48–2.10 (m, 4H), 1.79 (s, 6H), 1.40–1.20 (m, 4H), 0.90 (m, 4H). Anal. calcd for $C_{89}H_{73}IrN_4O_2S_2$: C, 71.89; H, 4.95; N, 3.77. Found: C, 71.69; H, 5.17; N, 4.04.

(Cbzbt)₂Ir(pic). Yield: 51%. ^{1}H NMR (300 MHz, CDCl_3) δ (ppm): 8.55 (d, J = 8.3 Hz, 1H), 8.47 (s, 1H), 8.41 (s, 1H), 8.23 (d, J = 7.6 Hz, 1H), 8.04 (d, J = 7.6 Hz, 1H), 7.99 (d, J = 7.6 Hz, 1H), 7.89–7.80 (m, 2H), 7.55 (d, J = 7.9 Hz, 1H), 7.49 (d, J = 8.0 Hz, 1H), 7.44–7.34 (m, 2H), 7.34–7.10 (m, 35H), 7.10–7.01 (m, 3H), 6.90 (t, J = 7.8 Hz, 1H), 6.44 (s, 1H), 6.19–6.12 (m, 2H), 3.69–3.51 (m, 4H), 2.42–2.17 (m, 4H), 1.41–1.19 (m, 4H), 0.98–0.83 (m, 4H). Anal. calcd for $C_{90}H_{70}IrN_5O_2S_2$: C, 71.59; H, 4.67; N, 4.64. Found: C, 71.46; H, 4.90; N, 4.74.

DFT calculations

DFT calculations were performed using the Gaussian 09, rev. D.01 software package.[38] The *trans* disposition of C^N ligands was assigned for compounds due to the inherent reactivity pattern of iridium cyclometalating reactions.[7] The structures of the complexes were simplified by substituting the 1,1,1-triphenyl-methylpentane fragment with an ethyl group in order to reduce

the computational cost. Frontier molecular orbital levels were calculated under vacuum using the CAM-B3LYP[39] density functional, after optimizing the geometry. The basis set both for optimization and for energy calculations was chosen to be D95V(d,p) on C, N, O, and H and D95(2df) on S, with the LANL2DZ basis set and effective core potential being chosen for Ir atoms. Each geometry was at the end optimized with method-wise correct force constants and vibrational frequencies were checked to assure that the obtained structure truly corresponds to the energy minimum. SCF and geometry convergence were left at default values for Gaussian 09 (SCF: 10^{-8} for the commutator of the Fockian and density matrixes, and four different values for maximum and RMS force and coordinate change). The integration grid was also at the default "fine" level, which is a pruned (75 302) grid. Singlet–singlet and singlet–triplet excitations were modeled by LR-TD-DFT with the same method and basis set. The triplet excited state geometry was optimized by conventional SCF methods, specifying the spin multiplicity of 3 beforehand.

OLED preparation and characterization

Sandwich type samples with the pixel size of 16 mm^2 were prepared with the following structure: ITO/PEDOT:PSS(40 nm)/emitting layer (60 nm)/BPhen or TPBi (20nm)/LiF(1 nm)/Al(100 nm), where poly(3,4-ethylenedioxythiophene)–poly(styrenesulfonate)-(PEDOT:PSS), 2,2′,2″-(1,3,5-benzinetriyl)-tris(1-phenyl-1*H*-benzimidazole) (TPBi) (or 4,7-diphenyl-1,10-phenanthroline (BPhen)) and LiF were used as hole-injection, electron transport and electron-injection layers, respectively. BPhen was used for the PVK matrix and TPBi for the CBP matrix. This choice was made to get the best possible energy level alignment between the host and the electron transport layer. Indium tin oxide (ITO) glass (Präzisions Glas & Optik GmbH) with a sheet resistivity of 15 Ω per square was used as a substrate. A 12 mm wide ITO strip line was made by wet etching at the middle of the substrate. Afterwards, ITO substrates were cleaned by the following method: sonicated in CHCl$_3$; sonicated in acetone; 2× rinsed with distilled (DI) water; sonicated in water with 3 vol% of Hellmanex II detergent; rinsed with DI water; sonicated in DI water and isopropyl alcohol. Each sonication lasted for 15 min. Before deposition of PEDOT:PSS the ITO glass was blown dry with nitrogen and treated with UV-ozone for 20 min. The ITO layer was covered with PEDOT:PSS (from H.C. Starck, Al4083) using a Laurell WS650 spin coater. Rotation lasted for 1 minute with speed 2000 rpm. The sample was moved into a glovebox and heated at 200 °C for 10 minutes. The emitting layer consisted of the corresponding synthesized iridium(III) complex in poly(9-vinylcarbazole) (PVK, Sigma Aldrich 368350) or 4,4′-bis(*N*-carbazolyl)-1,1′-biphenyl (CBP) host. In all cases 20 wt% host:guest systems in tetrahydrofuran were prepared. A solution with a concentration of 5 mg ml^{-1} was spin-coated on the PEDOT:PSS layer with 2000 rpm for 40 sec and heated at 120 °C for 15 minutes afterwards. Furthermore, the samples were moved from the glovebox to a vacuum chamber, without exposure to air, for thermal evaporation of electron transport TPBi (Sigma Aldrich 806781) or BPhen (Sigma Aldrich 133159), and electron-injection of the LiF (Sigma Aldrich 449903) and electrodes at the pressure

6×10^{-6} Torr. The deposition speed was 1 Å s^{-1}, 0.1 Å s^{-1} and 5 Å s^{-1} for TPBi and BPhen, LiF and Al, respectively. In the end the samples were encapsulated using a two-component epoxide.

The current–voltage characteristics of the OLEDs were measured by a Keithley 2700 multimeter and the voltage source was a Keithley 230 unit. The electroluminescence brightness and CIE 1931 coordinates were measured using a Konica Minolta Luminance and Color Meter CS-150. The electroluminescence spectrum was recorded using a calibrated Ocean Optics HR4000 spectrometer. CIE 1931 coordinates and spectra presented in this work were obtained at the maximum brightness.

Conflicts of interest

There are no conflicts to declare.

Acknowledgements

References

1 B. W. D'Andrade and S. R. Forrest, *Adv. Mater.*, 2004, **16**, 1585–1595.

2 K. Walzer, B. Maennig, M. Pfeiffer and K. Leo, *Chem. Rev.*, 2007, **107**, 1233–1271.

3 L. Xiao, Z. Chen, B. Qu, J. Luo, S. Kong, Q. Gong and J. Kido, *Adv. Mater.*, 2011, **23**, 926–952.

4 X. Yang, G. Zhou and W. Y. Wong, *Chem. Soc. Rev.*, 2015, **44**, 8484–8575.

5 H. Yersin, A. F. Rausch, R. Czerwieniec, T. Hofbeck and T. Fischer, *Coord. Chem. Rev.*, 2011, **255**, 2622–2652.

6 Y. You and S. Y. Park, *Dalton Trans.*, 2009, 1267–1282.

7 S. Lamansky, P. Djurovich, D. Murphy, F. Abdel-Razzaq, H. E. Lee, C. Adachi, P. E. Burrows, S. R. Forrest and M. E. Thompson, *J. Am. Chem. Soc.*, 2001, **123**, 4304–4312.

8 C. Fan and C. Yang, *Chem. Soc. Rev.*, 2014, **43**, 6439–6469.

9 P. Chen, W. Xie, J. Li, T. Guan, Y. Duan, Y. Zhao, S. Liu, C. Ma, L. Zhang and B. Li, *Appl. Phys. Lett.*, 2007, **91**, 023505.

10 B. Zhao, Z. Su, W. Li, B. Chu, F. Jin, X. Yan, F. Zhang, D. Fan, T. Zhang, Y. Gao and J. Wang, *Appl. Phys. Lett.*, 2012, **101**, 053310.

11 X. Yang, X. Zhao, X. Zhang, R. Li, J. Dang, Y. Li, G. Zhou, Z. Wu, D. Ma, W. Y. Wong and X. Zhao, *J. Mater. Chem.*, 2012, **22**, 7136–7148.

12 M. Li, H. Zeng, Y. Meng, H. Sun, S. Liu, Z. Lu, Y. Huang and X. Pu, *Dalton Trans.*, 2011, **40**, 7153–7164.

13 J. Li, R. Wang, R. Yang, W. Zhou and X. Wang, *J. Mater. Chem. C*, 2013, **1**, 4171–4179.

14 C. Fan, L. Zhu, B. Jiang, Y. Li, F. Zhao, D. Ma, J. Qin and C. Yang, *J. Phys. Chem. C*, 2013, **117**, 19134–19141.

15 T. Giridhar, W. Cho, Y. H. Kim, T. H. Han, T. W. Lee and S. H. Jin, *J. Mater. Chem. C*, 2014, **2**, 9398–9405.

16 D. Liu, R. Yao, M. Fu, D. Li and S. Zhang, *RSC Adv.*, 2016, **6**, 34198–34203.

17 C. Tonnelé, M. Stroet, B. Caron, A. J. Clulow, R. C. Nagiri, A. K. Malde, P. L. Burn, I. R. Gentle, A. E. Mark and B. J. Powell, *Angew. Chem.*, 2017, **56**, 8402–8406.

18 E. Baranoff, S. Suarez, P. Bugnon, C. Barolo, R. Buscaino, R. Scopelliti, L. Zuppiroli, M. Graetzel and M. K. Nazeeruddin, *Inorg. Chem.*, 2008, **47**, 6575–6577.

19 X. Xu, X. Yang, J. Zhao, G. Zhou and W. Y. Wong, *Asian J. Org. Chem.*, 2015, **4**, 394–429.

20 Y. Wang, S. Wang, N. Zhao, B. Gao, S. Shao, J. Ding, L. Wang, X. Jing and F. Wang, *Polym. Chem.*, 2015, **6**, 1180–1191.

21 K. Traskovskis, I. Mihailovs, A. Tokmakovs, A. Jurgis, V. Kokars and M. Rutkis, *J. Mater. Chem.*, 2012, **22**, 11268–11276.

22 K. Traskovskis, K. Lazdovica, A. Tokmakovs, V. Kokars and M. Rutkis, *Dyes Pigm.*, 2013, **99**, 1044–1050.

23 I. R. Laskar and T. M. Chen, *Chem. Mater.*, 2004, **16**, 111–117.

24 M. Nonoyama, *J. Organomet. Chem.*, 1975, **86**, 263–267.

25 K. Naito and A. Miura, *J. Phys. Chem.*, 1993, **97**, 6240–6248.

26 I. R. Laskar, S. F. Hsu and T. M. Chen, *Polyhedron*, 2006, **25**, 1167–1176.

27 D. Kim, *J. Phys. Chem. C*, 2015, **119**, 12690–12697.

28 E. Baranoff, S. Fantacci, F. De Angelis, X. Zhang, R. Scopelliti, M. Grätzel and M. K. Nazeeruddin, *Inorg. Chem.*, 2010, **50**, 451–462.

29 A. F. Rausch, M. E. Thompson and H. Yersin, *J. Phys. Chem. A*, 2009, **113**, 5927–5932.

30 X. Gu, T. Fei, H. Zhang, H. Xu, B. Yang, Y. Ma and X. Liu, *J. Phys. Chem. A*, 2008, **112**, 8387–8393.

31 Y. Kawamura, K. Goushi, J. Brooks, J. J. Brown, H. Sasabe and C. Adachi, *Appl. Phys. Lett.*, 2005, **86**, 071104.

32 K. S. Yook and J. Y. Lee, *Adv. Mater.*, 2014, **26**, 4218–4233.

33 M. J. Jurow, C. Mayr, T. D. Schmidt, T. Lampe, P. I. Djurovich, W. Brütting and M. E. Thompson, *Nat. Mater.*, 2016, **15**, 85–91.

34 W. Staroske, M. Pfeiffer, K. Leo and M. Hoffmann, *Phys. Rev. Lett.*, 2007, **98**, 197402.

35 Y. J. Cho, S. Taylor and H. Aziz, *ACS Appl. Mater. Interfaces*, 2017, **9**, 40564–40572.

36 T. Giridhar, W. Cho, J. Park, J. S. Park, Y. S. Gal, S. Kang, J. Y. Lee and S. H. Jin, *J. Mater. Chem. C*, 2013, **1**, 2368–2378.

37 Y. Wu, H. Xu, J. Yang, J. Li, W. Liang, J. Sun, H. Wang and B. Xu, *New J. Chem.*, 2015, **39**, 8908–8914.

38 M. J. Frisch, G. W. Trucks, H. B. Schlegel, G. E. Scuseria, M. A. Robb, J. R. Cheeseman, G. Scalmani, V. Barone, G. A. Petersson, H. Nakatsuji, X. Li, M. Caricato, A. Marenich, J. Bloino, B. G. Janesko, R. Gomperts, B. Mennucci, H. P. Hratchian, J. V. Ortiz, A. F. Izmaylov, J. L. Sonnenberg, D. Williams-Young, F. Ding, F. Lipparini, F. Egidi, J. Goings, B. Peng, A. Petrone, T. Henderson, D. Ranasinghe, V. G. Zakrzewski, J. Gao, N. Rega, G. Zheng, W. Liang, M. Hada, M. Ehara, K. Toyota, R. Fukuda, J. Hasegawa, M. Ishida, T. Nakajima, Y. Honda, O. Kitao, H. Nakai, T. Vreven, K. Throssell, J. A. Montgomery, Jr., J. E. Peralta, F. Ogliaro, M. Bearpark, J. J. Heyd, E. Brothers, K. N. Kudin, V. N. Staroverov, T. Keith, R. Kobayashi, J. Normand, K. Raghavachari, A. Rendell, J. C. Burant, S. S. Iyengar, J. Tomasi, M. Cossi, J. M. Millam, M. Klene, C. Adamo, R. Cammi, J. W. Ochterski, R. L. Martin, K. Morokuma, O. Farkas, J. B. Foresman and D. J. Fox, *Gaussian 09, Revision D.01*, Gaussian, Inc., Wallingford CT, 2016.

39 T. Yanai, D. P. Tew and N. C. Handy, *Chem. Phys. Lett.*, 2004, **393**, 51–57.

Ruduss, A.; Kokars, V.; Tetervenoka, N.; Vembris, A.; Traskovskis, K. Effects of Steric Encumbrance of Iridium(iii) Complex Core on Performance of Solution-Processed Organic Light Emitting Diodes. *RSC Adv.* **2020**, *10* (46), 27552–27559.

PAPER

Check for updates

Effects of steric encumbrance of iridium(III) complex core on performance of solution-processed organic light emitting diodes†

Armands Ruduss,[a] Valdis Kokars,[a] Natalija Tetervenoka,[b] Aivars Vembris[b] and Kaspars Traskovskis [ID] *[a]

Iridium(III) complexes are the most frequently applied commercialized green and red emitters for organic light emitting diode (OLED) displays. Throughout years a significant research effort has been devoted to modify these compounds, in order to make them suitable for cost-effective solution-processing techniques, such as inkjet printing. To achieve this, the inherent tendency of the complex molecules to form poorly emissive aggregates needs to be suppressed. In many cases this has been achieved by an encapsulation of the iridium(III) complex core with dendritic structures, composed of either passive or charge-transporting fragments. In order to validate this approach, we acquired three structural analogues of the conventional green emitter **Ir(ppy)₃**, which possess gradually increasing sterical encumberment at the complex surface. Corresponding OLEDs were examined, with three distinctively different active emissive layer compositions in terms of charge transportation characteristics. The results show that in the all scenarios the unmodified **Ir(ppy)₃** outperforms the compounds with attached bulky groups. The in-device performance of the emitter is directly related to its charge trapping ability, which is being compromised in the presence of dendritic auxiliary substituents.

Introduction

Organic light emitting diodes (OLED) are currently considered as the most suitable technological solution for efficient, thin, fast-refresh-rate and high image quality displays.[1] Due to the unique properties, this technology is used in a variety of emerging innovative products, such as transparent[2] and flexible screens.[3] Regardless of the recent success considering the practical implementation, a transfer from the currently adopted vacuum-deposition to the much less complex solution-based manufacturing process would greatly promote the usage extent and economic viability of OLEDs.[4,5]

The widespread adoption of the wet processing mainly relies on a development of suitable light emitting molecules. Phosphorescent cyclometalated iridium(III) complexes are the most studied and applied OLED emitters due to their efficient triplet harvesting ability, color tuning possibilities and chemical stability.[6] **Ir(ppy)₃** (tris(2-phenylpyridine)iridium)[7] is, perhaps,

the most scrutinized compound among this material class. This green emitter has been used as a model compound for numerous studies due to near to 100% photoluminescence quantum yield (Φ_{PL}) and excellent chemical and thermal stability. When being vacuum-deposited in solid films together with a charge transporting host materials, the sparsely dispersed **Ir(ppy)₃** molecules retain Φ_{PL} value near unity.[8] If the concentration of the complex is increased, the relatively large dipole moment of **Ir(ppy)₃** (ref. 9) is inducing a solid-state aggregation.[10,11] The subsequent formation of poorly emissive excimers together with increased probability of triplet–triplet annihilation (TTA) leads to a diminished OLED performance and considerable efficiency roll-off at large current densities.[10,12] In the solution-processed films the aggregation of **Ir(ppy)₃** is even more pronounced, causing large-scale phase separation between emitter and host materials.[13,14] Again, this is governed by the attracting force, as the aggregation process between individual **Ir(ppy)₃** molecules is proven to take place even in solutions.[15]

As a consequence, wet-processed OLEDs based on **Ir(ppy)₃** show notably reduced performance characteristics in comparison to vacuum deposited analogues. Considerable effort has been made to chemically modify this emitter in order to overcome its limitations. In most cases this has been attempted by following an obvious path, where bulky groups with purely isolating or charge transporting functionality are being introduced to **Ir(ppy)₃** core to provide a physical barrier that suppress

[a]Faculty of Materials Science and Applied Chemistry, Riga Technical University, P. Valdena Str. 3, LV-1048, Riga, Latvia. E-mail: kaspars.traskovskis@rtu.lv

[b]Institute of Solid State Physics, University of Latvia, Kengaraga Str. 8, LV-1063, Riga, Latvia

the aggregate formation and helps to sustain large distance between individual emitter molecules. Accordingly, **Ir(ppy)₃** has been attached to side chains of hole transporting polymers.[16,17] Because of a well-defined structure, easier purification and reproducible synthesis of the resulting materials, the encapsulation with dendronic structures is the most frequently investigated molecular design. Structures composed of passive groups such as polyphenylenes[18–20] and carboranes[21] or hole transporting polycarbazoles[22] have been extensively investigated. Despite a large number of the screened materials, none of the approaches has demonstrated clear benefits in terms of OLED performance, as it notably falls behind the vacuum-deposited or sometimes even solution-processed devices composed of unmodified **Ir(ppy)₃**.[23] No clear design rules have yet been established that could guide the development of a new-generation of efficient solution-processable OLED emitters. In particular, the set of requirements regarding the right balance of sterical encumberment and charge transportation characteristics of the materials needs to be established.

We investigate **Ir(ppy)₃** and its three structural analogues with a gradually increasing number of attached electronically passive groups. A device integration of the compounds was performed by exploring three different active emissive layer (EML) composition scenarios: with hole-transporting, balanced or predominantly electron-transporting characteristics. The results give a deeper insight about excitation mechanism in **Ir(ppy)₃** based OLEDs. Based on these results the preferable structural prerequisites can be proposed towards efficient solution-processable iridium(III) complexes.

Experimental section

General procedures

Starting materials and solvents were acquired from commercial suppliers and were used without additional purification. NMR spectra were obtained on a Bruker Avance 300 MHz or Bruker Avance Neo 500 MHz spectrometer using solvent residue as an internal reference. The elemental analysis was carried out using a Costech Instruments ECS 4010 CHNS–O Elemental Combustion System. Differential scanning calorimetry (DSC) thermograms were acquired using a Mettler Toledo DSC-1/200 W apparatus at a scanning rate of 10 °C min⁻¹ while keeping the samples under N₂ atmosphere. Optical measurements were carried in tetrahydrofuran (THF) solutions with typical material concentrations of 1–4 × 10⁻⁵ mol L⁻¹. Solutions for Φ_{PL} and emission decay measurements were prepared in glovebox under Ar atmosphere using previously degassed solvents. Films for optical measurements were prepared using spin-coating technique with a Laurell WS-400B-6NPP/LITE spin coater on quartz slides, using solutions with material concentration of 30 mg mL⁻¹. After the preparation all films were dried in an oven at 100 °C for 2 h. The UV-vis spectra were recorded with a Perkin-nElmer Lambda 35 spectrometer. Emission spectra, Φ_{PL} and emission lifetimes were determined using QuantaMaster 40 steady state spectrofluorometer (Photon Technology International, Inc.) equipped with 6 inch integrating sphere (Lab-Sphere). The excitation wavelength in the all cases was 410 nm.

The molecular ionization potential (IP) and photoconductivity measurements (E_{th}) were carried out on a self-made experimental system, using a procedure described in our previous work.[24] Density functional theory (DFT) calculations for geometry optimization and excited state energies were performed using ORCA[25] program package (build 4.0.1.2). For auxiliary tasks Avogadro program was used.[26] DFT and TDDFT calculations employed non-local functional B3LYP with def2-TZVP[27] basis set. [SD(60,MWB)][28] effective core potentials (ECP) were used for iridium atom. To reduce the computational time, the structures were simplified by substituting 3,3,3-triphenylmethyl propionic acid with acetic acid fragment.

Results and discussion

Synthesis

For the purpose of the study three novel structural analogues of **Ir(ppy)₃** were acquired according to Scheme 1. The compounds feature the emissive **Ir(ppy)₃** core and one (**1TPY**), two (**2TPY**) or three (**3TPY**) attached bulky triphenylmethane groups (TR). In order to minimize the impact of the substituents on the photophysical properties of the emitter, the linkage between TR and the complex core is realized through an aliphatic bridge. Such approach has been previously applied to acquire solution-processable emitters with a solely purpose to provide a sterical barrier between complex molecules.[29] The synthesis was performed using μ-chloro-bridged iridium(III) complex dimers **1a**[30] and **1b**[31] as the starting materials. The introduction of the third cyclometalating ligand was accomplished by utilizing the procedure by Colombo *et al.*,[32] which strictly yields tris-cyclometalated complexes with a *fac*-structural configuration. Among the performed synthetic series, the rate and the yield of the cyclometalation reaction increases with the number of electron accepting benzaldehyde fragments in the resulting complex. The target compounds were acquired after the reduction of the aldehyde groups and subsequent esterification of the resulting alcohols with 3,3,3-triphenylpropionic acid.

NMR spectra and the elemental composition of the synthesized materials are consistent with the proposed structures. ¹³C spectra of **3TPY** indicate a chemical equivalence of 2-phenyl-pyridine (ppy) ligands and ancillary groups, underlining C_3 symmetry of the complex core. The symmetry is being broken in the case of **1TPY** and **2TPY**, resulting in an observation of three chemically inequivalent sets of ppy signals.

Characterization of emitters

The UV-vis absorption and emission spectra of **Ir(ppy)₃** and its three modified analogues are given in Fig. 1. No major deviations can be observed between the compounds, suggesting that the attachment of TR groups has not significantly altered the electronic configuration of **Ir(ppy)₃** core. In the region below 300 nm UV-vis absorption bands show increased absorbance with the number of attached TR groups, indicating an overlap between π–π* transitions of ppy ligands and TR phenyl rings. In the region between 300–500 nm, which features spin allowed metal-to-ligand charge transfer (¹MLCT) and the corresponding
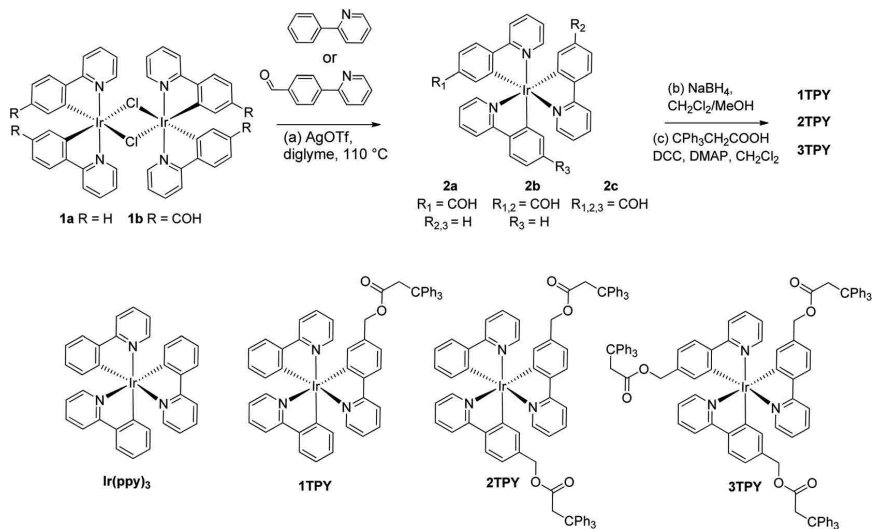
Scheme 1 Synthesis of the investigated structural analogues of **Ir(ppy)₃**.

triplet transitions (³MLCT),³³ the bands overlap with only minor deviations.

In deoxygenated THF solution the emission bands of the compounds assume an identical broad featureless shape. A bathochromic shift of the emission by 3 nm can be observed for TR-functionalized compounds in respect to the emission maximum of **Ir(ppy)₃** (at 522 nm). Φ_{PL} values of the compounds (Table 1) vary in the range of 0.94–0.90. A slight drop in the emission efficiency can be observed for TR-functionalized compounds, that can be associated with an increased molecular complexity that promotes the probability of non-radiative decay pathways. Emission decay times show very little

variation between the compounds and lay in the interval 1.7–1.8 µs. Radiative (k_r) and non-radiative (k_{nr}) decay rates are also close, although **Ir(ppy)₃** shows a slightly higher k_r and lower k_{nr} values.

The functionalization of **Ir(ppy)₃** with TR groups causes distinctive changes in a solid-state morphology of the corresponding compounds, as the unmodified complex is crystalline but its derivatives are amorphous. DSC analysis of the synthesized compounds reveal only one distinctive phase transition signal – glass transition temperature (T_g) (Fig. S1†). The measured T_g values of the compounds **1TPY**, **2TPY** and **3TPY** are, accordingly, 158, 142 and 131 °C, indicating that the
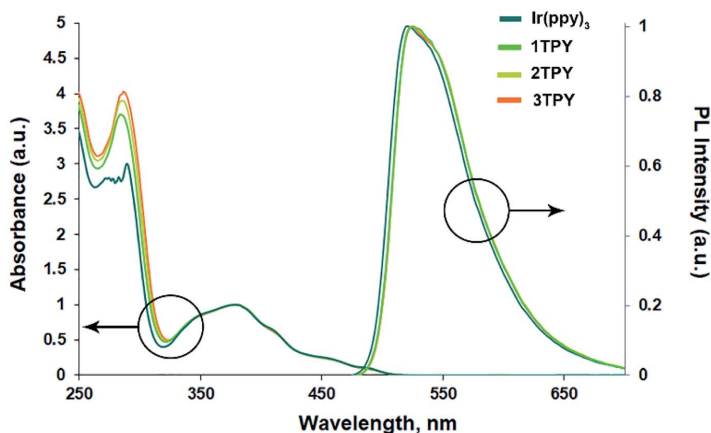

Fig. 1 UV-vis absorption and emission spectra of the compounds in THF.

Table 1 Photophysical properties of the investigated emitters

Compound	λ_{max} em., nm	$\Phi_{PL}{}^a$	τ, μs	$k_r{}^b$, ×10⁵ s⁻¹	$k_{nr}{}^c$, ×10⁵ s⁻¹	IP, eV	EA, eV	HOMO^d, eV	LUMO^d, eV	$\Delta E_{S0-S1}{}^d$, eV	$\Delta E_{S0-T1}{}^d$, eV
Ir(ppy)₃	522	0.94/—	1.7	5.5	0.35	5.15	2.85	−5.06	−1.47	2.85	2.66
1TPY	525	0.91/0.01	1.8	5.1	0.50	5.17	2.95	−5.15	−1.57	2.83	2.63
2TPY	525	0.90/0.03	1.7	5.3	0.58	5.21	2.95	−5.24	−1.66	2.84	2.64
3TPY	525	0.93/0.08	1.8	5.2	0.38	5.24	2.92	−5.32	−1.74	2.85	2.65

^{a} Measured in deoxygenated THF/amorphous films. ^{b} Radiative decay rate $k_r = \Phi_{PL}/\tau$. ^{c} Nonradiative decay rate $k_{nr} = (1 - \Phi_{PL})/\tau$. ^{d} Calculated values.

presence of additional TR groups causes a drop in softening temperature of the materials. This can be attributed to an increased overall conformational freedom of the molecular fragments,[34] as TR fragments are bound to the complex core through a flexible linker. Despite the lack of crystallinity, the amorphous spin-coated films of the corresponding compounds show poor Φ_{PL}, with the best value of 0.08 in the case of **3TPY**, indicating a strong emission quenching. While **3TPY** has a large number of attached TR groups that should partly prevent close contacts, the facial configuration of the complex core determines that only a half of its octahedral surface area is being sterically shielded. In order to deeper investigate the aggregation tendency between the compounds, emitter concentration impact on Φ_{PL} in guest–host systems with poly(9-vinylcarbazole) (PVK) was determined (Fig. 2). The results show that the presence of shielding groups has a minor impact on Φ_{PL} when the concentration of the emitters is below 10 wt%. Still, a little positive effect of the TR substituents can be seen in comparison to the unmodified complex. Above 10 wt% **Ir(ppy)₃** shows a steep drop in Φ_{PL} in comparison to the modified compounds. This can be associated with a large-scale phase separation and formation of poorly emissive crystalline inclusions. TR-functionalized compounds, on the other hand, show a gradual decrease in Φ_{PL} due to the lack of crystal formation ability. Still, the ongoing aggregation is apparent. Taking into consideration the partly-shielded structure of the complex molecules, the formation of predominantly dimeric aggregated

species is assumed instead of large-scale mass separation in the case of **Ir(ppy)₃**.

With an increasing mass concentration, the compounds generally show a broadening and redshift of the emission bands (Fig. S2, Table S1†). Notable transformations in the emission bands can be detected even at 5 wt% emitter content, indicating already ongoing aggregation. At 50 wt% emission in the all cases originate mainly from excimers, with the emission maxima located in the range of 544–551 nm.[12] At concentrations exceeding 20 wt% **3TPY** shows contrasting emission band transformations, with a less distinctive full width at half maximum (FWHM) increase. This can be attributed to the partly shielded molecular surface of the compound that limits the number of possible spatial arrangements of aggregated complex molecules. The structure of **3TPY** also determines that only pyridine ring of TR-ppy ligands can form direct close contacts, in such way reducing the extent of energy level shifts in the formed excimers.

In order to interpret the slight variations in photophysical properties between the compounds, density functional theory (DFT) calculations were performed. The distribution of the frontier molecular orbitals and their energies are outlined in Fig. 3a. The configuration of the highest occupied molecular orbital (HOMO) are similar in all the cases, with electron density being mainly localized on iridium d orbitals and the electron rich phenyl rings of the three ppy ligands. Regarding the lowest unoccupied molecular orbital (LUMO), it is evident that for TR-functionalized compounds LUMO resides on the TR-modified ppy ligand. As a result, LUMO in **1TPY** is localized on a single but in **2TPY** on two ligands, breaking the symmetry of the molecule. In **3TPY**, similarly to **Ir(ppy)₃**, LUMO is evenly distributed across all three ppy ligands. The localization of LUMO on the functionalized ppy ligands can be attributed to a weak negative inductive effect of the present benzyl ester substituent. Such substitution pattern is shown to stabilize LUMO level in ppy-type cyclometalating ligands.[35] TDDFT calculations were used to predict the lowest singlet (ΔE_{S0-S1}) and triplet (ΔE_{S0-T1}) transition energies (Table 1). In the all cases the obtained values show little variations, with the difference not exceeding 0.02 eV for singlets and 0.03 eV for triplets. A slight lowering in triplet level is predicted for all TR-functionalized compounds, this being consistent with the experimentally observed redshift of the corresponding phosphorescence bands. Electron density difference maps for the lowest singlet excitation predict that this process is mainly
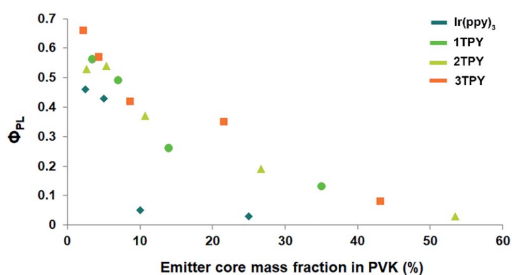

Fig. 2 Φ_{PL} values of spin-coated films composed of PVK host and Ir(ppy)₃-based emitters at different emitter mass fractions. For TR-functionalized compounds only the mass of the emitter core is counted towards the emitter mass content.
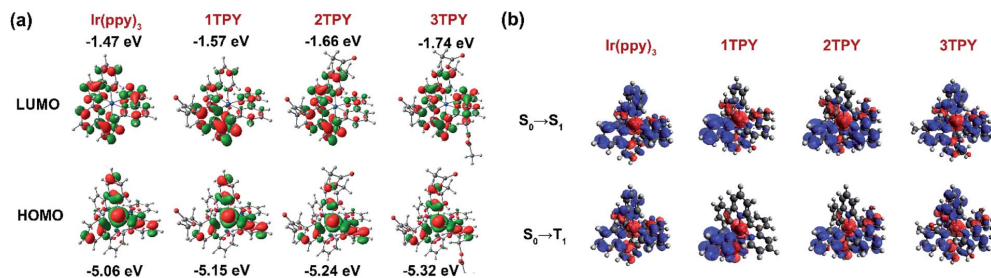
Fig. 3 (a) Calculated configuration and energies of HOMO and LUMO orbitals. (b) Calculated electron density difference maps for the lowest singlet and triplet excitations. Electron transfer proceeds from the red to blue regions.

associated with an electron density shift between HOMO and LUMO orbitals (Fig. 3b). As a result, the excitation is localized on two ligands for **2TPY** and one ligand for **1TPY**, in comparison to the involvement of all ligands in C_3-symmetric **Ir(ppy)$_3$** and **3TPY**. Among the TR-functionalized compounds a correlation between the number of TR-ppy ligands and $\Delta E_{S0–S1}$ and $\Delta E_{S0–T1}$ can be observed, where ΔE for the transitions gradually increases with the number of the modified ligands. This increase in transition energy can be attributed to the growing degeneracy of the excited states.[36]

Previous experimental and theoretical studies of the emissive properties of **Ir(ppy)$_3$** have shown that in experimental setting the C_3 symmetry of the complex is being reduced and the phosphorescence proceeds from C_1-symmetric excited triplet state, which is localized only on one of the cyclometalating ligands.[33,36–38] The main cause for this process is Jahn–Teller distortion, which lifts the energetically unfavorable degeneracy of the long-lived C_3-symmetric excited state through a transformation of the molecular geometry.[36–38] An interaction with surrounding solvent or host matrix molecules is also considered as a possible origin for the loss of the symmetry.[33] The aforementioned processes are also expected to take place in the case of the investigated derivatives of **Ir(ppy)$_3$**. The manifestation of this effect explains the closely similar emissive properties of **1TPY**, **2TPY** and **3TPY** despite the variations in their structural composition. The phosphorescence in all these compounds is expected to originate from an excited state that lies on a single TR-functionalized ppy ligand. This localization of the T_1 excitation is caused by the more stabilized LUMO level of TR-ppy (for **1TPY**) in a combination with a lift in the degeneracy of the T_1 state (for **2TPY** and **3TPY**).

The electronic levels in thin films of the investigated emitters were determined by photoemission yield spectroscopy, to find ionization potential (IP), and photoconductivity measurements, to determine photoconductivity threshold value (E_{th}). Electron affinity (EA) was then calculated as the difference between IP and E_{th} (Table 1). The determined IP and EA values correlate well with the calculated HOMO and LUMO energies, as IP and EA assume slightly deeper energies with an increased number of the attached TR groups.

All the previous measurements indicate that the studied compounds possess highly similar emissive properties both in solution and films and can be used as appropriate model compounds to investigate the influence of sterical encumberment on the OLED performance.

Electroluminescence properties

In order to evaluate the electroluminescence characteristics of the compounds, three-layer OLEDs composed of hole transporting PEDOT:PSS, emissive layer and electron transporting TPBi were examined. Spin-coated EMLs were composed of the **Ir(ppy)$_3$** or one of the three TR-functionalized emitters that were dispersed in a charge transporting host material. The **Ir(ppy)$_3$** complex core content in the all cases were set at 7 wt%, attributing the mass of TR groups to the host. Three configurations of EML were studied, in which the host material was predominantly hole-transporting PVK, a balanced mixture of PVK and electron-transporting OXD-7 (70 : 30 wt%) or a mostly electron-transporting blend of the same two materials (30 : 70 wt%). The device characteristics expressed in voltage–current density–luminance and luminance–current efficiency (η_c)–power efficiency (η_p) plots together with energy diagram are outlined in Fig. 4. Turn on voltage, maximal efficiency, luminance and roll-off parameters are given in Table 2.

For the devices with PVK host a clear correlation between the chemical composition of the emitter and performance can be observed, where an increasing sterical encumberment of the complex surface leads to a poorer electroluminescence. For **Ir(ppy)$_3$** the maximal brightness of the device reaches 2500 cd m^{-2}, while for **2TPY** and **3TPY** this parameter barely surpasses a 100 cd m^{-2} mark. The maximal attained efficiency (η_c and η_p) also decreases in accordance with the amount the attached TR groups. For a predominantly hole-transporting EML, such as PVK, it is expected that the emission originates in a close proximity to the interface of EML and electron transport layer, where holes can recombine with locally trapped electrons. In the particular case, the electrons are expected to reside mainly on the emitter molecules, due to a closer energetic level alignment with the electron transporting layer and about 0.4 eV deeper electron affinity level in respect to PVK. Further electron transfer between the closely packed complex molecules is not
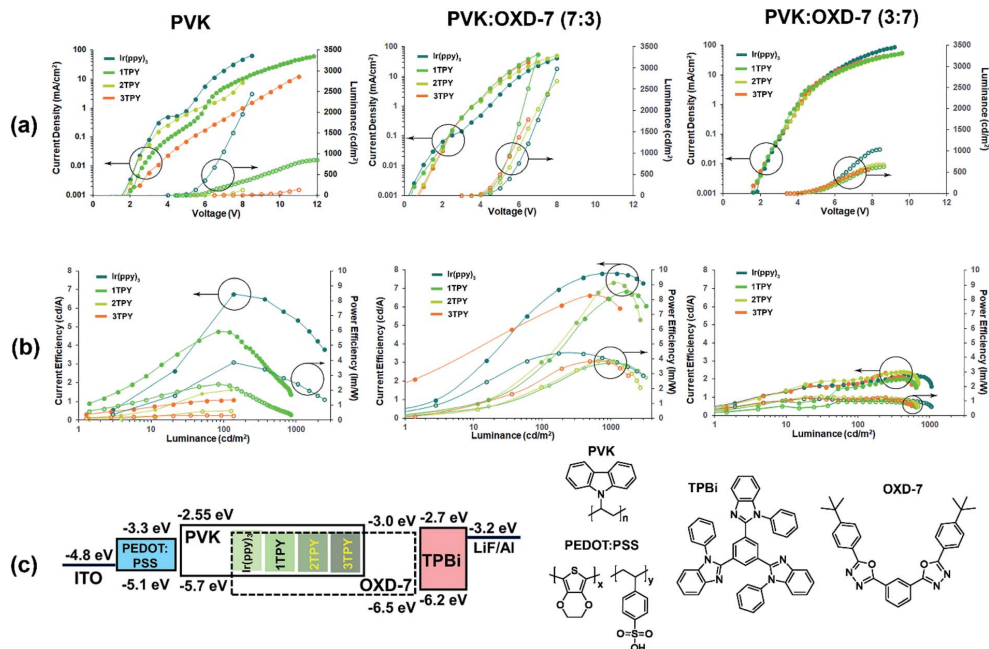
Fig. 4 OLED characteristics for devices with three different composition EMLs. (a) Voltage−current density (filled circle) and luminance (empty circle) plots. (b) Luminance−current efficiency (filled circle) and power efficiency plots. (c) Energy diagram and the used materials featuring experimentally obtained IP and EA values.

expected due to the poor charge mobilities of **Ir(ppy)₃** complex core.[39,40] A notably increased device charge density can be observed in the case of **Ir(ppy)₃**. This indicates that the complex molecule is directly aiding the electron transfer into EML. For TR-functionalized compounds such process is obstructed due to the present isolating groups, leading to lower current

densities and barely detectable electroluminescence, as the charge recombination zone is moved to the electron transport layer. The electroluminescence in devices bearing **Ir(ppy)₃** and **1TPY** emitters is accompanied with a steep and severe efficiency roll-off. This is another consequence of a narrow recombination zone. Due to the high localization of the emitting molecules the

Table 2   Characteristics of OLEDs with PVK, PVK : OXD-7 (70 : 30 wt%) or PVK : OXD-7 (30 : 70 wt%) EML host materials

Compound	V_{on}^{a}, V	η_c^{b}, cd A^{-1}	η_p^{c}, lm W^{-1}	L_{max}^{d}, cd m^{-2}	Roll-off^{e}, %	CIE^{f} (x, y)
PVK						
Ir(ppy)₃	4.5	6.8	3.9	2446	44	0.32, 0.62
1TPY	4.5	4.8	2.4	844	71	0.35, 0.58
2TPY	6	1.6	0.6	127	—	0.32, 0.62
3TPY	7	1.0	0.3	136	—	0.34, 0.59
PVK : OXD-7 (7 : 3)						
Ir(ppy)₃	3.5	7.8	4.4	2983	6	0.31, 0.63
1TPY	4	6.9	3.7	3308	10	0.31, 0.63
2TPY	4	7.3	3.9	2692	27	0.32, 0.62
3TPY	3.5	6.6	3.8	1794	10	0.31, 0.63
PVK : OXD-7 (3 : 7)						
Ir(ppy)₃	3.5	2.2	1.1	1048	27	0.30, 0.63
1TPY	3.5	2.0	1.0	638	23	0.31, 0.62
2TPY	3.5	2.4	1.3	680	28	0.32, 0.62
3TPY	4	2.3	1.3	560	25	0.32, 0.62

^{a} Turn-on voltage. ^{b} Current efficiency. ^{c} Power efficiency. ^{d} Maximal luminance. ^{e} Current efficiency drop between the maximal value and the value at the highest luminance. ^{f} Measured at maximal brightness.

electroluminescence is being quenched by TTA almost immediately after the emission onset.

OLEDs with EMLs composed of 70 : 30 wt% mixture of PVK and electron transporting material OXD-7 exhibit somewhat similar performance level across the all investigated emitters. At the same time a considerable efficiency improvement can be seen in a comparison with PVK-only devices. Due to a less restricted charge injection, the luminance onset values are significantly lowered, varying in the range of 3.5–4.5 V. Among the emitters, **Ir(ppy)₃** still performs the best in terms of η_c and η_p, with **3TPY** being the least efficient compound. This indicates that sterical shielding is obstructing electroluminescence process even in scenario, where molecules are surrounded by charge carriers of the both types. In a stark contrast to the devices with pure PVK host, the lowest current density is observed in the case of **Ir(ppy)₃** emitter. This can be attributed to a more pronounced charge trapping on **Ir(ppy)₃** molecules due to a direct exposure of the molecular surface to surrounding host molecules. Such process is aiding the radiative recombination and reduces leaked current, leading to increased current efficiency of the device. The much lower extent of efficiency roll-off, in a comparison to the previously characterized devices, indicates a much broader charge recombination zone.

Finally, OLEDs with a predominantly electron transporting mixture of host materials, PVK : OXD-7 (30 : 70 wt%), were examined. Among the investigated series, these devices exhibit the worst overall efficiency and luminance parameters. Regarding the emitter chemical composition, the least variations can be observed between the structures. The only notable difference is a slightly increased maximal attainable brightness in the case of **Ir(ppy)₃**. The analysis of the previously discussed OLEDs strongly suggests that charge trapping by emitter molecules is a crucial process towards attainment of efficient devices. This has been demonstrated previously for closely related iridium complexes, where the excitation of an emitter by charge trapping is clearly dominating over other possible excitation pathway – Förster energy transfer from excited host molecules.[41] Taking this into account, the lowered performance for the OXD-7 enriched OLEDs can be attributed to the excessive electron transport across EML. This results in a charge recombination zone being moved either at the interface with or inside hole injection layer. In an analogy with PVK-only devices, one would expect that the reduced hole transportation ability of OXD-7 saturated EML would promote a hole trapping process on the emitter molecules. Contrary, the minimal difference in the performance between the emitter structures suggest that an initial trapping of holes play a little role in the excitation process of the studied emitters, as such process would be clearly affected by sterical effects. This reduced tendency to host holes can be explained by about 0.5 eV deeper ionization potential of PVK in respect to the emitter molecules that effectively contains holes on the host material.

Conclusions

A series of three structural analogues of **Ir(ppy)₃** was acquired, where compounds possess a gradually increasing sterical

encumberment at the surface of the emitting complex core. The photophysical properties and solid-state behavior of the synthesized compounds are almost identical to those of the unmodified complex, providing an appropriate basis for OLED performance benchmarking. OLEDs with solution-processed EMLs, with three different configurations of charge transporting host materials, were investigated. The acquired results indicate that the electroluminescence process in the devices is mainly driven by an initial charge trapping on the emitter molecules. As a result, **Ir(ppy)₃** outperforms the emitters with attached bulky groups due to an unrestricted exposure of the complex surface to the neighboring charge transporting molecules.

The obtained results suggest that material design strategy towards efficient iridium(III) based solution-processable OLED emitters should avoid the use of passive isolating groups, as the resulting structures perform even worse than unmodified complex molecules. At the same time, it is clear that the strong tendency for aggregation within the compound class sets a requirement for a complete sterical encapsulation. The use of charge-transporting dendritic peripheral groups is an extensively investigated direction towards achieving this, but several shortcomings can be identified regarding this approach. First, the highly unordered structure of such dendritic fragments makes charge transportation within them unlikely, as close packing and regular crystal-like arrangement of the molecules is needed to realize an efficient charge transportation process.[42] As a result, in-device performance of such materials is not expected to be much different from the emitters with electronically passive peripheral groups. Second, such hypothetical charge transporting groups should provide pathways towards charge trapping on the emitter core by an appropriate energy level tuning. Unrestricted charge transport would result in a recombination zone shift towards charge transporting layers, similarly to the process observed in our examined OXD-7 saturated OLEDs.

Based on our findings, the use of isolating peripheral groups with a charge trapping functionality can be proposed as a promising design strategy. Such OLEDs should be composed of EMLs with carefully arranged electronical levels, where the sterical groups at the surface of the emitter would act as an intermediate charge trap, located energetically between the levels of the charge transporting host and the emissive core.

Conflicts of interest

There are no conflicts to declare.

Acknowledgements

References

1 H.-W. Chen, J.-H. Lee, B.-Y. Lin, S. Chen and S.-T. Wu, *Light: Sci. Appl.*, 2018, 7, 17168.

2   S. Park, J. T. Lim, W.-Y. Jin, H. Lee, B.-H. Kwon, N. S. Cho, J.-H. Han, J.-W. Kang, S. Yoo and J.-I. Lee, *ACS Photonics*, 2017, **4**, 1114–1122.

3   R.-P. Xu, Y.-Q. Li and J.-X. Tang, *J. Mater. Chem. C*, 2016, **4**, 9116–9142.

4   J.-H. Jou, S. Sahoo, D. K. Dubey, R. A. K. Yadav, S. S. Swayamprabha and S. D. Chavhan, *J. Mater. Chem. C*, 2018, **6**, 11492–11518.

5   X. Xu, X. Yang, J. Zhao, G. Zhou and W.-Y. Wong, *Asian J. Org. Chem.*, 2015, **4**, 394–429.

6   T.-Y. Li, J. Wu, Z.-G. Wu, Y.-X. Zheng, J.-L. Zuo and Y. Pan, *Coord. Chem. Rev.*, 2018, **374**, 55–92.

7   M. A. Baldo, S. Lamansky, P. E. Burrows, M. E. Thompson and S. R. Forrest, *Appl. Phys. Lett.*, 1999, **75**, 4–6.

8   Y. Kawamura, K. Goushi, J. Brooks, J. J. Brown, H. Sasabe and C. Adachi, *Appl. Phys. Lett.*, 2005, **86**, 071104.

9   S. Reineke, T. C. Rosenow, B. Lüssem and K. Leo, *Adv. Mater.*, 2010, **22**, 3189–3193.

10 S. Reineke, G. Schwartz, K. Walzer, M. Falke and K. Leo, *Appl. Phys. Lett.*, 2009, **94**, 163305.

11 A. R. G. Smith, J. L. Ruggles, H. Cavaye, P. E. Shaw, T. A. Darwish, M. James, I. R. Gentle and P. L. Burn, *Adv. Funct. Mater.*, 2011, **21**, 2225–2231.

12 Y. Q. Zhang, G. Y. Zhong and X. A. Cao, *J. Appl. Phys.*, 2010, **108**, 083107.

13 Y.-T. Kim, Y.-H. Kim, J.-B. Seol, T.-W. Lee and C.-G. Park, *Phys. Chem. Chem. Phys.*, 2015, **17**, 21555–21563.

14 Y.-T. Kim, J.-B. Seol, Y.-H. Kim, H.-J. Ahn and C.-G. Park, *Small*, 2017, **13**, 1602874.

15 S. Takayasu, T. Suzuki and K. Shinozaki, *J. Phys. Chem. B*, 2013, **117**, 9449–9456.

16 A. Kimyonok, B. Domercq, A. Haldi, J.-Y. Cho, J. R. Carlise, X.-Y. Wang, L. E. Hayden, S. C. Jones, S. Barlow, S. R. Marder, B. Kippelen and M. Weck, *Chem. Mater.*, 2007, **19**, 5602–5608.

17 C.-L. Lee, N.-G. Kang, Y.-S. Cho, J.-S. Lee and J.-J. Kim, *Opt. Mater.*, 2003, **21**, 119–123.

18 E. B. Namdas, A. Ruseckas, I. D. W. Samuel, S.-C. Lo and P. L. Burn, *J. Phys. Chem. B*, 2004, **108**, 1570–1577.

19 T. Qin, J. Ding, L. Wang, M. Baumgarten, G. Zhou and K. Müllen, *J. Am. Chem. Soc.*, 2009, **131**, 14329–14336.

20 J. C. Ribierre, A. Ruseckas, I. D. W. Samuel, S. V. Staton and P. L. Burn, *Phys. Rev. B: Condens. Matter Mater. Phys.*, 2008, **77**, 085211.

21 N. Van Nghia, S. Park, Y. An, J. Lee, J. Jung, S. Yoo and M. H. Lee, *J. Mater. Chem. C*, 2017, **5**, 3024–3034.

22 Y.-J. Pu, N. Iguchi, N. Aizawa, H. Sasabe, K. Nakayama and J. Kido, *Org. Electron.*, 2011, **12**, 2103–2110.

23 T. Earmme and S. A. Jenekhe, *J. Mater. Chem.*, 2012, **22**, 4660.

24 J. Latvels, R. Grzibovskis, K. Pudzs, A. Vembris and D. Blumberga, *Proc. SPIE*, 2014, 91371G.

25 F. Neese, *Wiley Interdiscip. Rev.: Comput. Mol. Sci.*, 2018, **8**, e1327.

26 M. D. Hanwell, D. E. Curtis, D. C. Lonie, T. Vandermeersch, E. Zurek and G. R. Hutchison, *J. Cheminf.*, 2012, **4**, 17.

27 F. Weigend and R. Ahlrichs, *Phys. Chem. Chem. Phys.*, 2005, **7**, 3297.

28 D. Andrae, U. Haeussermann, M. Dolg, H. Stoll and H. Preuss, *Theor. Chim. Acta*, 1990, **77**, 123–141.

29 K. Traskovskis, V. Kokars, S. Belyakov, N. Lesina, I. Mihailovs and A. Vembris, *Inorg. Chem.*, 2019, **58**, 4214–4222.

30 S. Lamansky, P. Djurovich, D. Murphy, F. Abdel-Razzaq, R. Kwong, I. Tsyba, M. Bortz, B. Mui, R. Bau and M. E. Thompson, *Inorg. Chem.*, 2001, **40**, 1704–1711.

31 S. Bettington, A. L. Thompson, A. Beeby and A. E. Goeta, *Acta Crystallogr., Sect. E: Struct. Rep. Online*, 2004, **60**, m827–m829.

32 M. G. Colombo, T. C. Brunold, T. Riedener, H. U. Guedel, M. Fortsch and H.-B. Buergi, *Inorg. Chem.*, 1994, **33**, 545–550.

33 T. Hofbeck and H. Yersin, *Inorg. Chem.*, 2010, **49**, 9290–9299.

34 K. Naito and A. Miura, *J. Phys. Chem.*, 1993, **97**, 6240–6248.

35 G. Zhou, C.-L. Ho, W.-Y. Wong, Q. Wang, D. Ma, L. Wang, Z. Lin, T. B. Marder and A. Beeby, *Adv. Funct. Mater.*, 2008, **18**, 499–511.

36 J. P. Gonzalez-Vazquez, P. L. Burn and B. J. Powell, *Inorg. Chem.*, 2015, **54**, 10457–10461.

37 K. Nozaki, *J. Chin. Chem. Soc.*, 2006, **53**, 101–112.

38 B. J. Powell, *Sci. Rep.*, 2015, **5**, 10815.

39 N. Matsusue, S. Ikame, Y. Suzuki and H. Naito, *Appl. Phys. Lett.*, 2004, **85**, 4046–4048.

40 N. Matsusue, Y. Suzuki and H. Naito, *Jpn. J. Appl. Phys.*, 2005, **44**, 3691–3694.

41 X. Gong, J. C. Ostrowski, D. Moses, G. C. Bazan and A. J. Heeger, *Adv. Funct. Mater.*, 2003, **13**, 439–444.

42 R. Noriega, J. Rivnay, K. Vandewal, F. P. V. Koch, N. Stingelin, P. Smith, M. F. Toney and A. Salleo, *Nat. Mater.*, 2013, **12**, 1038–1044.

Ruduss, A.; Turovska, B.; Belyakov, S.; Stucere, K. A.; Vembris, A.; Traskovskis, K. Carbene–Metal Complexes As Molecular Scaffolds for Construction of Through-Space Thermally Activated Delayed Fluorescence Emitters. *Inorg. Chem.* **2022**, *61* (4), 2174–2185.

Carbene−Metal Complexes As Molecular Scaffolds for Construction of through-Space Thermally Activated Delayed Fluorescence Emitters

Armands Ruduss, Baiba Turovska, Sergey Belyakov, Kitija A. Stucere, Aivars Vembris, and Kaspars Traskovskis*

ACCESS | 📊 Metrics & More | 📖 Article Recommendations | 🗐 Supporting Information

ABSTRACT: The through-space charge transfer (CT) process is observed in Cu(I) carbene−metal−amide complexes, where conventional imidazole or imidazoline N-heterocyclic (NHC) carbene fragments act as inert linkers and CT proceeds between a metal-bound carbazole donor and a distantly situated carbene-bound phenylsulfonyl acceptor. The resulting electron transfer gives a rise to efficient thermally activated delayed fluorescence (TADF), characterized with high photoluminescence quantum yields (Φ_{PL} up to 90%) and radiative rates (k_r) up to 3.32×10^5 s^{-1}. The TADF process is aided by fast reverse intersystem crossing (rISC) rates of up to 2.56×10^7 s^{-1}. Such emitters can be considered as hybrids of two existing TADF emitter design strategies, combining low singlet−triplet energy gaps (ΔE_{ST}) met in all-organic exciplex-like emitters (0.0062−0.0075 eV) and small, but non-negligible spin−orbital coupling (SOC) provided by a Cu atom, like in TADF-active organometallic complexes.
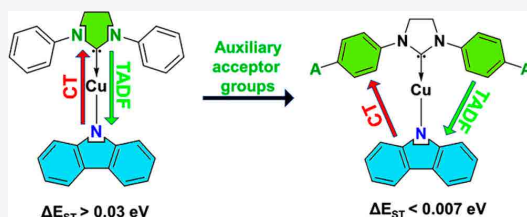
INTRODUCTION

The high cost and rarity of transition metals (Ir, Pt, Os and Re) commonly used for synthesis of triplet emitters have fueled large research interest in alternative structural approaches. Among those, metal-free organic compounds exhibiting thermally activated delayed fluorescence (TADF) have received the most attention.[1,2] Beside the main focus for applications in organic light emitting diodes (OLEDs), these compounds have found an extensive use in photocatalysis[3] and time-resolved imaging.[4] The emission from the singlet state in these materials is realized through a reverse intersystem crossing (rISC) process between T_1 and S_1 levels, provided that the singlet−triplet energy gap (ΔE_{ST}) is sufficiently small to be overcome at room temperature. The chemical composition of TADF emitters involves a presence of electron donating (D) and accepting (A) structural fragments, between which the emissive charge-transfer (CT) process takes place. Small ΔE_{ST} in these compounds is achieved by minimizing the overlap between HOMO and LUMO wave functions, usually confined on D and A moieties.[5] The majority of the studied structural examples feature D−A pairs that are coupled through π-conjugated bridging fragments, between which orbital overlap-reducing conformational twists are introduced. The necessity for covalent bonding can be abandoned, by applying physical mixtures of D and A components, which form TADF-active exciplexes with ultralow ΔE_{ST} values (<0.001 eV).[6−8] Such systems, however, often suffer from poor photoluminescence quantum yields (Φ_{PL}) and wide

emission bands due to highly randomized packing patterns of the constituting compounds. The next evolutionary step of TADF emitters introduced so-called intramolecular exciplexes, where through-space CT proceeds between covalently bound D and A fragments and through-bond electronic coupling is prevented by σ-bonding or multiple conformational twists.[9−11] While such conformationally rigid materials solve some of the previously mentioned issues, the SOC between ^{1}CT and ^{3}CT states is practically nonexistent due to almost identical orbital configurations, and the attainment of a rapid spin flip is often reliant on the aid of closely located local excited triplet states (^{3}LE).[12] Hence through-space TADF emitters often suffer from low radiative rates (k_r).[13]

Organometallic complexes bearing relatively abundant coinage metal atoms (Cu, Ag, Au) are a conceptually different class of low-cost TADF emitters.[14,15] While this element does not provide large enough SOC for fast room-temperature phosphorescence, the values are sufficient enough to promote a rapid TADF, despite the considerable ΔE_{ST} gaps met in such compounds (>0.05 eV). Recently, a new type of highly
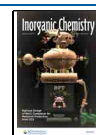
emissive materials has arisen among this compound class. Exhibiting strongly coupled CT transitions between metal-bound electrophilic carbene and electron-rich amide ligands, these compounds are often referred to as "carbene-metal-amides" (CMAs).[16−21] Due to a favorable electronic level configuration and metal involvement, TADF lifetimes below 1.0 μs can be achieved.[22,23]

Here, we present a novel approach toward TADF emitters that can be considered as a hybrid case between the previously discussed all-organic through-space and metal-assisted designs (Figure 1). Similarly to the existing CMA emitters, Cu
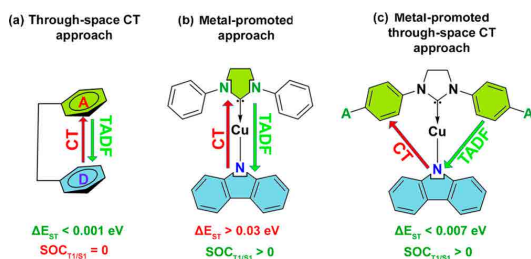

Figure 1. Schematic representation of TADF emitter architectures featuring all-organic through space CT (a), metal promoted (b), and our presented hybrid (c) approaches.

complexes bearing carbazolide and carbene ligands were synthesized. Imidazole-based N-heterocyclic carbenes (NHCs) were used, with electron-accepting sulfonyl groups introduced at the 4 position of the N-bound 2,6-diisopropyl-phenyl (Dipp) substituents (Scheme 1). The strong electron

Scheme 1. Chemical Structures of CMA Complexes 1−4
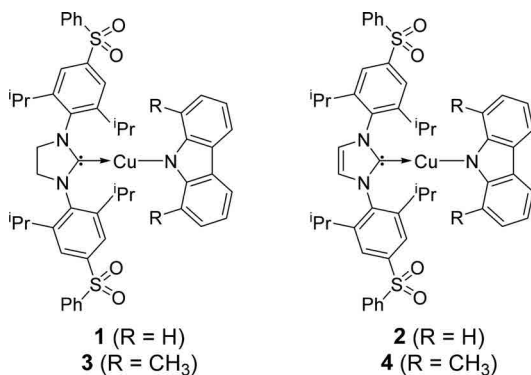
accepting nature of sulfonyls relocates LUMO from the carbene to the perpendicularly aligned Dipp rings, giving rise to a through-space CT process with the HOMO-hosting carbazolide fragment. The resulting compounds **1−4** exhibit unique photophysical behavior, combining low ΔE_{ST} (0.0062−0.0075 eV) with small, but non-negligible SOC due to the presence of Cu atoms. These structural examples demonstrate a new design strategy for the development of TADF emitters.

■ EXPERIMENTAL SECTION

Synthesis and Characterization. All procedures involving synthesis and purification of NHC derivatives were carried out

using Schlenk techniques. Solvents were dried using standard procedures. Unless specified further, the used materials and solvents were purchased from commercial suppliers. Starting compounds **5** and **9**[24] and 1,8-dimethylcarbazole[25] were prepared by following the procedures described in the literature. NMR spectra were obtained on a Bruker Avance 300 MHz spectrometer using DMSO-d_6 residual signals as an internal reference (^{1}H, δ 2.50; ^{13}C, δ 39.52). Elemental analysis was performed using a Costech Instruments ECS 4010 CHNS-O Elemental Combustion System. Differential scanning calorimetry (DSC) thermograms were acquired using a Mettler Toledo DSC-1/200 W apparatus at a scanning rate of 10 °C min^{-1}. Decomposition temperatures were obtained using a PerkinElmer STA 6000 thermal analyzer.

1,3-Bis(2,6-diisopropyl-4-(phenylsulfonyl)phenyl)-4,5-dihydro-1H-imidazol-3-ium Acetate (6). A solution of 1,3-bis(2,6-diisopropyl-4-(phenylthio)phenyl)-4,5-dihydro-1H-imidazol-3-ium chloride (**5**; 5.70 g, 8.86 mmol) and 30% H_2O_2 (14,0 mL) in acetic acid (120 mL) was stirred at 90 °C for 4 days. The mixture was cooled to room temperature, and volatiles were evaporated under reduced pressure. The obtained solid was dispersed in diethyl ether and collected by filtration to afford the product as a white solid. Yield: 5.92 g (91%). ^{1}H NMR δ_H (DMSO-d_6, 300 MHz): 9.60 (s, 1H, N=C**H**-N), 8.13 (d, *J* = 7.3 Hz, 4H, *o*-Ar**H** (Ph)), 7.95 (s, 4H, *m*-Ar**H** (dipp)), 7.77−7.61 (m, 6H, Ar**H** (Ph)), 4.56 (s, 4H, C**H**$_2$-C**H**$_2$), 3.12 (hept, *J* = 6.6 Hz, 4H, C**H** (CH$_3$)$_2$), 1.90 (s, 3H, C**H**$_3$COO), 1.35 (d, *J* = 6.4 Hz, 12H, CH(C**H**$_3$)$_2$), 1.28 (d, *J* = 6.6 Hz, 12H, CH(C**H**$_3$)$_2$). ^{13}C NMR δ_C (DMSO-d_6, 75.47 MHz): 172.01 (**C**H$_3$COO), 159.84 (N=**C**H−N), 148.74, 143.98, 140.42, 134.25, 134.04, 129.96, 127.83, 123.72, 53.86 (**C**H$_2$-**C**H$_2$), 28.60 (**C**H(CH$_3$)$_2$), 24.59 (CH(**C**H$_3$)$_2$), 22.96 (CH(**C**H$_3$)$_2$), 21.17 (**C**H$_3$COO).

1,3-Bis(2,6-diisopropyl-4-(phenylsulfonyl)phenyl)-1H-imidazol-3-ium Chloride (10). A solution of 1,3-bis(2,6-diisopropyl-4-(phenylthio)phenyl)-1H-imidazol-3-ium chloride (**9**; 4.01 g, 6.25 mmol) and potassium peroxymonosulfate (oxone) (18.00 g, 118.26 mmol) in a mixture of methanol (70 mL) and water (30 mL) was stirred at 60 °C for 16 h. Then, the mixture was cooled to room temperature and filtered. The inorganic solids were washed with an excess of acetone. Volatiles were evaporated from the filtrate under reduced pressure, and the resulting mixture was extracted with DCM (3 × 100 mL). The extract was dried over Na$_2$SO$_4$, filtered, and evaporated under reduced pressure. The obtained solid was dispersed in diethyl ether and collected by filtration to afford the product as a white solid. Yield: 3.81 g (86%). ^{1}H NMR δ_H (DMSO-d_6, 300 MHz): 10.12 (s, 1H, N=C**H**-N), 8.58 (s, 2H, CH=CH), 8.17 (d, *J* = 7.2 Hz, 4H, o-Ar**H**(Ph)), 8.05 (s, 4H m-Ar**H**(dipp)), 7.77−7.61 (m, 6H, Ar**H**(Ph)), 2.34 (hept, *J* = 6.2 Hz, 4H), 1.25 (d, *J* = 6.1 Hz, 12H, CH(C**H**$_3$)$_2$), 1.14 (d, *J* = 6.2 Hz, 12H, CH(C**H**$_3$)$_2$). ^{13}C NMR δ_C (DMSO-d_6, 75.47 MHz): 147.72, 144.89, 140.31, 138.93, 134.44, 133.93, 130.06, 127.98, 126.24, 123.56, 29.15 (**C**H(CH$_3$)$_2$), 23.72 (CH(**C**H$_3$)$_2$), 22.73 (CH(**C**H$_3$)$_2$).

Compound 7. A mixture of **6** (4.00 g, 5.47 mmol) and Ag$_2$O (1.33 g, 5.73 mmol) in acetonitrile (200 mL) was stirred for 1 h at room temperature. The mixture was filtered through a pad of Celite, and filtrate was evaporated under reduced pressure. The product was purified via column chromatography (silica gel, eluent: DCM to DCM/methanol, 100/5). Volatiles were evaporated under reduced pressure to afford the product as a white solid. An analytical sample was purified via crystallization from dioxane. Yield: 2.39 g (52%). ^{1}H NMR δ_H (DMSO-d_6, 300 MHz): 8.08 (d, *J* = 7.1 Hz, 4H, *o*-Ar**H** (Ph)), 7.86 (s, 4H, *m*-Ar**H** (dipp)), 7.75−7.59 (m, 6H, Ar**H** (Ph)), 4.12 (s, 4H, C**H**$_2$-C**H**$_2$), 3.10 (hept, *J* = 6.5 Hz, 4H, C**H** (CH$_3$)$_2$), 1.54 (s, 3H, C**H**$_3$COO), 1.34−1.20 (m, 24H, CH(C**H**$_3$)$_2$). ^{13}C NMR δ_C (DMSO-d_6, 75.47 MHz): 205.48 (dd, $J_{C-109Ag}$ = 266 Hz; $J_{C-107Ag}$ = 230 Hz, **C**-Ag), 175.31 (**C**H$_3$COO), 149.12, 142.33, 140.81, 139.29, 133.99, 129.88, 127.63, 123.51, 53.69 (d, J_{C-Ag} = 8.5 Hz, **C**H$_2$-**C**H$_2$), 28.49 (**C**H(CH$_3$)$_2$), 24.64 (CH(**C**H$_3$)$_2$), 23.27 (CH(**C**H$_3$)$_2$), 22.39 (**C**H$_3$COO).

Compound 11. A mixture of **10** (1.45 g, 2.06 mmol) and Ag$_2$O (1.43 g, 6.17 mmol) in acetonitrile (60 mL) was stirred for 1 h at room temperature. The mixture was filtered through a pad of Celite,

and filtrate was evaporated under reduced pressure. The product was purified via column chromatography (silica gel, eluent: DCM to DCM/methanol, 100/4). Volatiles were evaporated under reduced pressure to afford the product as a white solid. Yield: 0.77 g (46%). ^{1}H NMR δ_H (DMSO-d_6, 300 MHz): 8.15 (d, J = 7.0 Hz, 4H, o-ArH (Ph)), 8.10 (s, 2H, CH=CH), 7.95 (s, 4H, m-ArH (dipp)), 7.77–7.63 (m, 6H, ArH (Ph)), 2.52–2.41 (m, 4H, CH (CH$_3$)$_2$), 1.25–1.12 (m, 24H, CH(CH$_3$)$_2$). ^{13}C NMR δ_C (DMSO-d_6, 75.47 MHz): 181.86 (dd, $J_{C-109Ag}$ = 265 Hz; $J_{C-107Ag}$ = 230 Hz, **C**-Ag), 147.72, 143.37, 140.65, 138.53, 134.13, 129.92, 127.76, 124.96 (d, J_{C-Ag} = 6.5 Hz, **CH**=CH), 123.17, 28.70 (**CH**(CH$_3$)$_2$), 23.74 (CH(**CH$_3$**)$_2$), 23.04 (CH(**CH$_3$**)$_2$).

Compound 8. A mixture of **7** (1.50 g, 1.84 mmol) and CuBr (0.80 g, 5.58 mmol) in dry DCM (40 mL) was stirred for 16 h at room temperature. The mixture was filtered through a pad of Celite, and filtrate was evaporated under reduced pressure. The product was purified via column chromatography (silica gel, eluent: DCM/methanol, 100:1). Volatiles were evaporated under reduced pressure to afford a product as a white solid. Yield: 1.09 g (73%). ^{1}H NMR δ_H (DMSO-d_6, 300 MHz): 8.07 (d, J = 7.1 Hz, 4H, o-ArH (Ph)), 7.86 (s, 4H, m-ArH (dipp)), 7.75–7.59 (m, 6H, ArH (Ph)), 4.07 (s, 4H, CH$_2$-CH$_2$), 3.11 (hept, J = 6.7 Hz, 4H, CH (CH$_3$)$_2$), 1.32–1.22 (m, 24H, CH(CH$_3$)$_2$). ^{13}C NMR δ_C (DMSO-d_6, 75.47 MHz): 201.32 (**C**-Cu), 149.09, 142.28, 140.85, 138.96, 133.99, 129.89, 127.59, 123.41, 53.50 (**CH$_2$-CH$_2$**), 28.49 (**CH**(CH$_3$)$_2$), 24.75 (CH(CH$_3$)$_2$), 23.15 (CH(**CH$_3$**)$_2$).

Compound 12. A mixture of **11** (0.40 g, 0.49 mmol) and CuBr (0.14 g, 0.98 mmol) in dry DCM (20 mL) was stirred for 72 h. The mixture was filtered through a pad of Celite. The filtrate was collected, and DCM was evaporated under reduced pressure to afford product as white solid of sufficient purity for further reactions. Yield: 0.38 g (96%). ^{1}H NMR δ_H (DMSO-d_6, 300 MHz): 8.15 (d, J = 7.0 Hz, 4H, o-ArH (Ph)), 7.97 (s, 2H, CH=CH), 7.95 (s, 4H, m-ArH (dipp)), 7.77–7.62 (m, 6H, ArH (Ph)), 2.54–2.42 (m, 4H, CH (CH$_3$)$_2$), 1.23–1.15 (m, 24H, CH(CH$_3$)$_2$). ^{13}C NMR δ_C (DMSO-d_6, 75.47 MHz): 178.16 (**C**-Cu), 147.71, 143.25, 140.68, 138.38, 134.13, 129.93, 127.74, 124.45, 123.07, 28.73 (**CH**(CH$_3$)$_2$), 23.85 (CH(**CH$_3$**)$_2$), 22.92 (CH(**CH$_3$**)$_2$).

General Method for Synthesis of Complexes 1−4. All of the operations involving the synthesis and purification of NHC-Cu-Cbz complexes were carried out using dry, deoxygenated solvents (THF, hexane, and diethyl ether). Carbazole (or 1,8-dimethylcarbazole) and KOtBu or NaH was dissolved in THF and stirred for 30 min under an argon atmosphere. Then, a THF solution of NHC-CuBr was added dropwise via syringe to the solution of carbazole amide. The resulting mixture was stirred for 3 h under an argon atmosphere and then filtered through a pad of Celite into hexane (approximately 100 mL) to precipitate the product. The mixture was filtered, and the solid was washed with diethyl ether to afford product.

Complex 1. General procedure: A solution of carbazole (0.130 g, 0.78 mmol) and NaH (0.032 g, 0.80 mmol, 60% dispersion in mineral oil) in THF (5 mL) and a solution of **8** (0.30 g, 0.37 mmol) in THF (10 mL) were used. Yield: 0.22 g (63%), white solid. ^{1}H NMR δ_H (DMSO-d_6, 300 MHz): 8.20 (d, J = 7.4 Hz, 4H, o-ArH (Ph)), 8.04 (s, 4H, m-ArH (dipp)), 7.82–7.65 (m, 8H, ArH (Ph), CH^4(Cbz)), 6.66 (t, J = 7.3 Hz, 2H, CH^2(Cbz)), 6.44 (t, J = 7.6 Hz, 2H, CH^3(Cbz)), 5.65 (d, J = 8.1 Hz, 2H, CH^1(Cbz)), 4.26 (s, 4H, CH$_2$-CH$_2$), 3.32–3.20 (m, 4H, CH (CH$_3$)$_2$), 1.36 (d, J = 6.7 Hz, 12H, CH(CH$_3$)$_2$), 1.21 (d, J = 6.7 Hz, 12H, CH(CH$_3$)$_2$). ^{13}C NMR δ_C (DMSO-d_6, 75.47 MHz): 201.89 (NCN), 149.63, 148.84, 143.01, 141.00, 139.12, 134.06, 130.00, 127.80, 123.68, 123.27, 119.03, 115.18, 112.97, 53.65 (**CH$_2$-CH$_2$**), 28.67 (**CH**(CH$_3$)$_2$), 24.72 (CH(CH$_3$)$_2$), 23.17 (CH(**CH$_3$**)$_2$). Elemental analysis calculated for C$_{51}$H$_{54}$CuN$_3$O$_4$S$_2$: C, 68.01; H, 6.04; N, 4.67. Found: C, 68.06; H, 5.97; N, 4.60.

Complex 2. General procedure: A solution of carbazole (0.123 g, 0.74 mmol) and KOtBu (0.088 g, 0.78 mmol) in THF (5 mL) and a solution of **12** (0.30 g, 0.37 mmol) in THF (15 mL) were used. Yield: 0.31 g (93%), white solid. ^{1}H NMR δ_H (DMSO-d_6, 300 MHz): 8.27–8.18 (m, 6H, o-ArH (Ph), CH=CH), 8.12 (s, 4H, m-ArH (dipp)), 7.83–7.66 (m, 8H, ArH (Ph), CH^4(Cbz)), 6.72 (t, J = 7.3 Hz, 2H,

CH^2(Cbz)), 6.56 (t, J = 7.4 Hz, 2H, CH^3(Cbz)), 5.88 (d, J = 8.1 Hz, 2H, CH^1(Cbz)), 2.61 (hept, J = 6.5 Hz, 4H, CH (CH$_3$)$_2$), 1.26 (d, J = 6.7 Hz, 12H, CH(CH$_3$)$_2$), 1.19 (d, J = 6.7 Hz, 12H, CH(CH$_3$)$_2$). ^{13}C NMR δ_C (DMSO-d_6, 75.47 MHz): 178.87 (NCN), 148.93, 148.14, 143.82, 140.85, 138.54, 134.16, 130.01, 127.86, 124.61, 123.32, 119.13, 115.21, 113.00, 28.95 (**CH**(CH$_3$)$_2$), 23.90 (CH(CH$_3$)$_2$), 22.98 (CH(**CH$_3$**)$_2$). Elemental analysis calculated for C$_{51}$H$_{52}$CuN$_3$O$_4$S$_2$: C, 68.16; H, 5.83; N, 4.68. Found: C, 67.97; H, 6.11; N, 4.62.

Complex 3. General procedure: A solution of 1,8-dimethylcarbazole (0.082 g, 0.42 mmol) and KOtBu (0.048 g, 0.43 mmol) in THF (5 mL) and a solution of **8** (0.25 g, 0.31 mmol) in THF (10 mL) were used. The compound was recrystallized from chlorobenzene. Yield: 0.21 g (73%), white solid. ^{1}H NMR δ_H (DMSO-d_6, 300 MHz): 8.18 (d, J = 7.4 Hz, 4H, o-ArH (Ph)), 7.94 (s, 4H, m-ArH (dipp)), 7.85–7.67 (m, 6H, ArH (Ph)), 7.57 (d, J = 7.5 Hz, 2H, CH^2(Cbz)), 6.61 (t, J = 7.3 Hz, 2H, CH^3(Cbz)), 6.13 (d, J = 7.0 Hz, 2H, CH^1(Cbz)), 4.11 (s, 4H, CH$_2$-CH$_2$), 3.19 (hept, J = 6.6 Hz, 4H, CH (CH$_3$)$_2$), 1.32 (d, J = 6.7 Hz, 12H, CH(CH$_3$)$_2$), 1.16–1.07 (m, 18H, CH(CH$_3$)$_2$, **CH$_3$** (Cbz)). ^{13}C NMR δ_C (DMSO-d_6, 75.47 MHz): 201.36 (NCN), 148.75, 148.17, 142.71, 140.89, 139.73, 134.06, 129.96, 127.83, 124.17, 124.04, 123.68, 121.03, 116.50, 115.26, 54.03 (**CH$_2$-CH$_2$**), 28.59 (**CH**(CH$_3$)$_2$), 24.00 (CH(CH$_3$)$_2$), 23.78 (CH-(**CH$_3$**)$_2$), 18.10 (**CH$_3$**(Cbz)). Elemental analysis calculated for C$_{53}$H$_{58}$CuN$_3$O$_4$S$_2$: C, 68.54; H, 6.29; N, 4.52. Found: C, 68.50; H, 6.08; N, 3.96.

Complex 4. General procedure: A solution of 1,8-dimethylcarbazole (0.078 g, 0.40 mmol) and KOtBu (0.045 g, 0.40 mmol) in THF (5 mL) and a solution of **12** (0.25 g, 0.31 mmol) in THF (10 mL) were used. Yield: 0.26 g (91%), white solid. ^{1}H NMR δ_H (DMSO-d_6, 300 MHz): 8.24 (d, J = 7.4 Hz, 4H, o-ArH (Ph)), 8.12 (s, 2H, CH=CH), 8.04 (s, 4H, m-ArH (dipp)), 7.87–7.71 (m, 6H, ArH (Ph)), 7.61 (d, J = 7.5 Hz, 2H, CH^2(Cbz)), 6.65 (t, J = 7.3 Hz, 2H, CH^3(Cbz)), 6.20 (d, J = 6.9 Hz, 2H, CH^1(Cbz)), 2.64 (hept, J = 6.7 Hz, 4H, CH (CH$_3$)$_2$), 1.29–1.19 (m, 18H, CH(CH$_3$)$_2$, **CH$_3$** (Cbz)), 1.11 (d, J = 6.7 Hz, 12H, CH(CH$_3$)$_2$). ^{13}C NMR δ_C (DMSO-d_6, 75.47 MHz): 177.63 (NCN), 148.12, 147.56, 143.64, 140.75, 139.06, 134.23, 130.04, 127.95, 125.21, 123.99, 123.82, 120.83, 116.64, 115.26, 28.84 (**CH**(CH$_3$)$_2$), 23.36 (CH(CH$_3$)$_2$), 23.34 (CH(CH$_3$)$_2$), 18.34 (**CH$_3$**(Cbz)). Elemental analysis calculated for C$_{53}$H$_{56}$CuN$_3$O$_4$S$_2$: C, 68.69; H, 6.09; N, 4.53. Found: C, 68.42; H, 6.18; N, 4.60.

X-ray Crystallography. Suitable monocrystals of **1** were prepared by slow liquid−liquid diffusion between THF solution and diethyl ether. For **4**, a slow evaporation of chlorobenzene solution was employed. Crystallographic diffraction data for **1**, **4** (orthorhombic form), and **4** (monoclinic form) were collected with a Rigaku, XtaLAB Synergy, Dualflex, HyPix diffractometer (Cu Kα, λ = 1.54184 Å) equipped with a low temperature Oxford Cryosystems Cryostream Plus device. The crystal structures were solved by direct methods with the ShelXT[26] structure solution program using intrinsic phasing and refined with the SHELXL refinement package.[27] All calculations were performed with Olex2 software.[28] Temperature-induced polymorphism is observed for the studied monocrystal of **4**. At room temperature conditions, the crystal assumes a stable orthorhombic form, while cooling causes a phase transition to a monoclinic polymorph. The temperature dependence of crystal lattice parameters is outlined in Table S1, indicating that the phase transition proceeds at 219 K (Figure S1). This process is also evident by low-temperature differential scanning calorimetry (DSC) measurements (Figure S2). It should be noted that the change from the orthorhombic form to the monoclinic occurs without the destruction of the single crystals, and X-ray structures of both forms were obtained. Thus, a typical second-order phase transition is observed. Table S2 lists the main crystal data for these compounds. Crystallographic data for **1**, **4** (orthorhombic form), and **4** (monoclinic form) are deposited at the Cambridge Crystallographic Data Centre as supplementary publications CCDC 2047368, 2047337, and 2047338. Copies of the data can be obtained, free of charge, on application to CCDC, 12 Union Road, Cambridge CB2 1EZ, UK.

Scheme 2. Synthetic Route of CMA Complexes 1−4
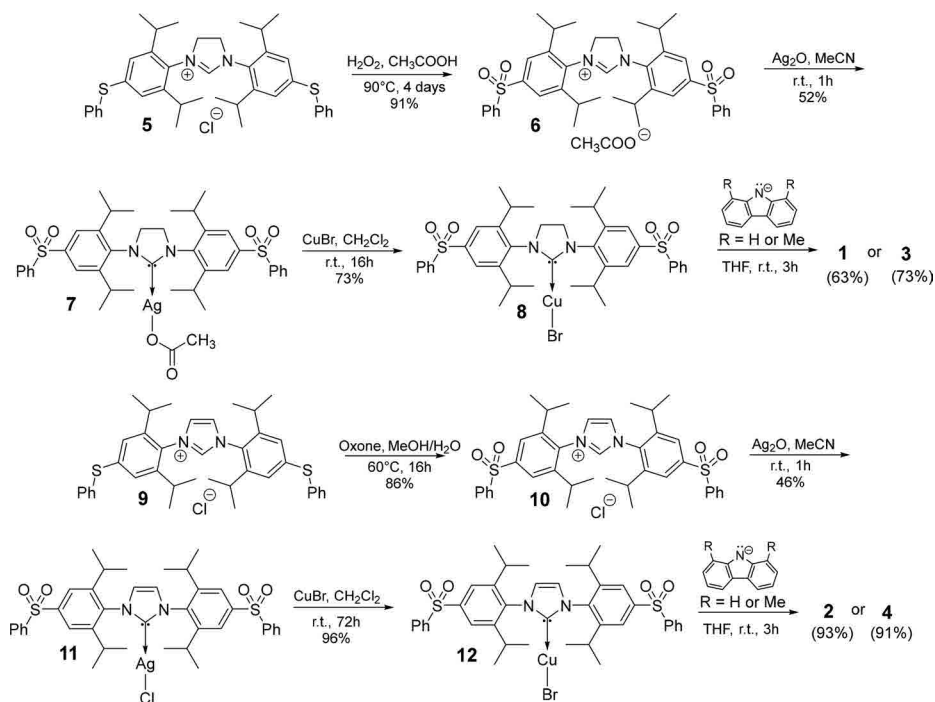
Cyclic Voltammetry Measurements. Cyclic voltammetry measurements were performed with a PARSTAT 2273 potentiostat. Electrochemical redox reactions were examined in 0.1 M *tetra*-butylammonium hexafluorophosphate (TBAPF$_6$) solutions in anhydrous acetonitrile under an Ar atmosphere. The measurements were carried out using a three-electrode cell configuration. A stationary glassy carbon disk (Ø 0.5 cm) was used as a working electrode and Pt wire as an auxiliary electrode. Potentials were measured vs a Ag wire electrode.

Photo Physical Measurements. UV−vis absorption measurements were carried out in solutions with a material concentration of 1 × 10^{-5} mol L^{-1}, while for photoluminescence measurements it was (1−2) × 10^{-4} mol L^{-1}. Solutions for Φ_{PL} and emission decay measurements were prepared in a glovebox under an Ar atmosphere using previously degassed solvents. PMMA films for optical measurements were prepared from chlorobenzene solutions (30 mg/mL material concentration) using a drop-casting method. After the deposition of the solution on glass slides, the samples were immediately placed in a preheated oven and dried for 2 h at 80 °C. The UV−vis spectra were recorded with a PerkinElmer Lambda 35 spectrometer. Depending on the nature of the experiment, photoluminescence properties were measured on two different spectroscopic systems. Emission spectra, Φ_{PL}, and PL lifetimes for solutions and thin films at room temperature, as well as PL spectra, time-resolved measurements, and PL lifetimes at 77 K (in liquid nitrogen filled quartz Dewar) were measured with QuantaMaster 40 spectrofluorometer (Photon Technology International, Inc.). The 375 nm laser with 60 ps pulse width and tunable repetition rate (between 1Mh and 50 kHz) was used for the fast (nanosecond to microsecond range) kinetics measurements. Steady state and pulsed (3 μs pulse width) xenon lamp was used for steady state and millisecond kinetics measurements. The excitation source for temperature-dependent (10−300 K) photoluminescence measurements in helium cryostat was a tunable Ekspla laser NT 342/3UV with the repetition rate 10 Hz and 5 ns pulse width. Photo-

luminescence spectra and PL decays were obtained with PMT attached to Andor monochromator.

Low temperature Φ_{PL} data were acquired by integrating the corresponding PL intensities and calibrating the values using Φ_{PL} data acquired at room temperature.[8] In order to correctly analyze CT emission and avoid the possible contribution of carbazolide ^{3}LE phosphorescence, only the CT emission was accounted for, when estimating low-temperature Φ_{PL} values. To do so, the PL intensities were collected in time-resolved mode, until the point where the collected CT emission intensity did not show any further increase, and no apparent contribution from ^{3}LE was detectable in the form of an overlapping structured emission band. The examples of such measurements conducted for **2** and **4** at a 60 K temperature are shown in Figure S3.

Quantum Chemical Calculations. Density functional theory (DFT) calculations for geometry optimization and time-dependent DFT (TD-DFT) calculations for excited state energies were performed using the Schrödinger Jaguar[29] software package (release 2020-2). Geometry optimization and TD-DFT calculations employed the MN15[30] functional and LACVP** basis. Tamm−Dancoff approximation (TDA) was used for TD-DFT. On the basis of symmetrical X-ray structures of **1** and **4**, C_S symmetry was set for the structures during the optimization. The conductor-like polarizable continuum model (CPCM) was used to account for solvation effects. Specifically, benzene ($\varepsilon = 2.27$) was chosen for TD-DFT calculations to closer simulate the media polarity in PMMA films ($\varepsilon = 3.9$).[31] Molecular orbital overlap integrals and the Cu atom contribution to orbitals (Becke method) were calculated with Multiwfn[32] program. T_1 geometries of **1** and **4** were obtained via spin-unrestricted SCF calculations. The attempts to obtain S_1 geometry were not successful, due to the tendency of the TD-DFT method to limit the distance between the through-space CT constituting the carbazolide and Dipp ring systems, resulting in the breakage of the complex structure. SOC values and phosphorescence rates for **1** were calculated with ADF

program.[33] The perturbative SOC (pSOC) TD-DFT method was used with TZP basis and MN15 functional.

OLED Preparation and Characterization. The necessary materials, poly(3,4-ethylenedioxythiophene) polystyrene sulfonate (PEDOT:PSS) as a hole injection material, poly(N,N′-bis-4-butylphenyl-N,N′-bisphenyl)benzidine (polyTPD) as a hole transport material, 9-(4-tert-butylphenyl)-3,6-bis(triphenylsilyl)-9H-carbazole (CzSi) as a host, and 2,2′,2″-(1,3,5-benzinetriyl)-tris(1-phenyl-1-H-benzimi-dazole) (TPBi) as an electron transport material were purchased from Ossila and used as received.

Electroluminescent devices with the structure ITO/PEDOT:PSS/PolyTPD/4:CzSi/TPBi/LiF/Al were fabricated in an inert atmosphere. ITO-coated glass with a sheet resistance of 15 Ω/sq was used. Hole injection, hole transport, and emitting layers were deposited by spin-coating on prepatterned ITO-coated glass substrates. For the emitting layer, chlorobenzene was used as the solvent. Electron transport, injection, and metal layers were subsequently deposited by thermal evaporation in a vacuum. Deposition was performed at a pressure lower than 2×10^{-6} mBar. Each sample contained six pixels with a size of 16 mm^2. The current−voltage characteristics of the OLEDs were measured with a Keithley 2450 SourceMeter. The electroluminescence brightness was measured with a Konica Minolta Luminance and Color Meter CS-150. Electroluminescence (EL) spectra were taken by the OceanOptics STS-VIS spectrometer.

■ RESULTS AND DISCUSSION

Synthesis and Structure. Sulfone-functionalized N,N′-bis(2,6-diisopropylphenyl)imidazol-2-ylidene and N,N′-bis-(2,6-diisopropylphenyl)-4,5-dihydroimidazol-2-ylidene carbene precursors **6** and **10** were acquired following a previously reported synthetic route for 2,6-dimethylphenyl-substituted structural analogues (Scheme 2).[24] NHC-Ag(I) complexes **7** and **11** were obtained by reaction between imidazolium or imidazolinium salts and Ag_2O. Transmetalation in the presence of CuBr and subsequent reaction with deprotonated carbazole (Cbz) or 1,8-dimethylcarbazole (MeCbz) afforded CMA complexes **1**−**4** as off-white crystalline solids. In the crystalline form, the compounds are stable and can be stored indefinitely under air exposure. The decomposition temperatures of the complexes vary in the range of 300−315 °C (Figure S4).

X-ray diffraction analysis was successfully performed for compounds **1** and **4** (Figure 2). As is evident from the acquired X-ray structures, the geometry of the complexes is largely affected by the structure of the attached carbazolide ligand. For

Figure 2. Top and side views of crystal X-ray structures for **1** (a) and monoclinic form of **4** (b). Thermal ellipsoids are drawn at the 50% probability level. Hydrogen atoms and solvent molecules are omitted for clarity. Only one of the two independent molecules in the unit cell are shown for **4**. Bond lengths are given in Å. Distance A is measured between centroids of the carbazolide five-membered ring and Dipp, while γ illustrates the dihedral angle between the planes of the corresponding rings.

complex **1**, the Cu(I) metal center's coordination sphere exhibits a nearly linear geometry with a slight bending at Cu (∠C1−Cu−N2 = 182.3°) and N2 (∠Cu−N2−"Cbz centroid" = 177.7°). The lengths of metal−ligand bonds, C1−Cu (1.857 Å) and Cu−N2 (1.841 Å), are slightly shorter than in the previously reported structural analogue IPr−Cu−Cz featuring unfunctionalized Dipp rings (1.874 and 1.877 Å),[34] thus indicating a slightly stronger bonding. The alignment between Cbz and imidazole planes is coplanar, in contrast to IPr−Cu−Cz, where these planes assume a perpendicular configuration. With the introduction of a bulkier MeCbz ligand in **4**, a steric repulsion between the Dipp ring and MeCbz methyls takes place, and the linearity of the axis C1−Cu−"Cbz centroid" cannot be retained. The structural strain in **4** is mainly relieved by the bending at MeCbz nitrogen (∠Cu−N2−"Cbz centroid" = 147.3°). This process can be related to a formal hybridization change of the carbazolide nitrogen from the typical sp^2- to the sp^3-like state, as indicated by the apparent structural pyramidalization at the N2 atom and by the carbazolide N2−C2 bond lengthening, from 1.374 to 1.406 Å. The release of the sterical strain by the 90° rotation of the carbazolide plane, like in several other reported CMAs,[17,34,35] in this case, is not possible due to the repulsion between the carbazolide methyls and the isopropyl groups of two Dipp fragments. In comparison to complex **1**, the interligand bridge in **4** (C1−Cu−N2) is slightly extended (by 0.081 Å).

Electrochemistry. The cyclic voltammetry measurements in acetonitrile solutions were conducted to examine electrochemical properties of the complexes (Figure S5, Table S3). All compounds show similar voltammetry traces. Oxidation potentials (E_{ox}) vary in a narrow range from −0.06 to −0.01 V and are assigned to an electron transfer at carbazolide ligands.[36] In contrast to Cbz-functionalized structural analogues, an identical anodic shift of about 0.04 V can be observed for MeCbz-bearing compounds **3** and **4**, thus indicating a similar electronic configuration that arises due to the sterical overcrowding-induced structural changes. A larger dispersity is observed among the reduction potentials (E_{red}). A cathodic shift of about 0.15 V is measured for compounds **1** and **2** in comparison to **3** and **4**. The fact that this E_{red} difference cannot be related to the structure of imidazoline or imidazole-based carbene fragments but, again, can be correlated to the attached carbazolide structures allows us to assume that the observed reduction process is related to electrochemical processes at the metal. This is also indicated by the low electrochemical bandgap. Such electrochemical behavior is common for Cu(I) complexes, for which voltammetry cannot be used to reliably determine LUMO energy levels.[37,38] Accordingly, a ferrocene/ferrocenium redox couple was used as the reference to convert E_{ox} into HOMO, while the LUMO value was subsequently estimated with the use of experimental optical bandgap values (Table S3).

Computational Analysis. An understanding about the molecular orbital configuration for **1**−**4** is provided by the Density Functional Theory (DFT) calculations. The theoretical investigations were performed at the MN15/LACVP** level.[30] In a similar fashion to the known CMAs, HOMO is predominantly situated on the carbazolide, with a small (5.8−6.1%) contribution of the metal atom (Figures 3a, S6; Table S4).[22,39,40] LUMO, on the other hand, shows contrasting behavior. This frontier orbital is relocated from the NHC ring to the electron deficient diphenylsulfone groups. Because of the orthogonal configuration, LUMO is completely separated
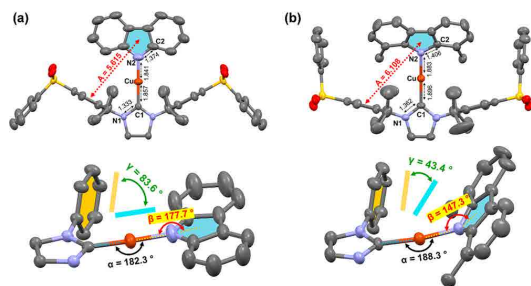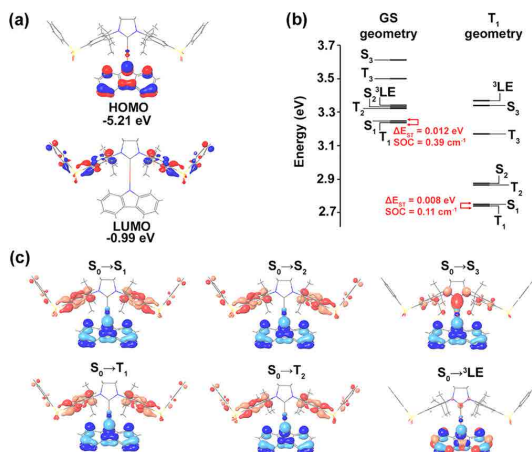
Figure 3. HOMO and LUMO orbitals (a), energy level diagram for the lowest energy excited states (b), and the corresponding natural transition orbitals (NTOs, c) for complex **1**. Blue NTOs correspond to a hole but red to a particle.

from the carbene-forming ring. This creates several distinctions from the previously reported CMAs. First, the calculated LUMOs have negligible metal contribution, in the range of 0.5−0.8%. For the compounds that host LUMO directly on the carbene moiety, these values usually reach a considerable level of 7−22%.[22,39−41] Second, relative to the HOMO-hosting carbazolide, LUMO has now been shifted to a more distant molecular region. Consequently, very small HOMO−LUMO overlap integrals of 0.05−0.08 are calculated for the synthesized structures (Table S3). For CMAs with LUMO-hosting carbene rings, this parameter usually exceeds 0.26, as

the frontier orbitals are placed closer and share a common metal atom.[39,40]

Time-dependent DFT (TD-DFT) calculations were performed to predict the nature and energy level configuration of the excited states of the complexes (Figure 3b; Table S5). At the ground state (GS) geometry, the lowest energy singlet transition (S$_0$ → S$_1$) in **1−4** has a through-space interligand CT character and proceeds with an electron transfer between the frontier orbital pair located on carbazolide and the Dipp rings (Figures 3c, S7). Through-bond electron transfer between the involved molecular fragments in this case is prevented by both the presence of the bridging metal atom and the orthogonal twist between NHC and diphenylsulfone planes. Consequently, the predicted S$_0$ → S$_1$ transitions show relatively small oscillator strength values in the range of 0.0027−0.0058. Among the investigated structures, the oscillator strength of the S$_0$ → S$_1$ transition is around 1.5−2 times higher for of MeCbz-containing compounds **3** and **4**. The extent of the electronic coupling in through-space charge transfer chromophores is affected by the spatial alignment of donor and acceptor aromatic ring systems, and face-to-face configuration leads to a much stronger coupling than edge-to-face arrangement.[42] As evident by the obtained X-ray (Figure 2) and DFT-optimized structures, the dihedral angle between Cbz and Dipp planes (γ) becomes substantially smaller, if the MeCbz ligand is present (in **3** and **4**) due to the sterical strain induced bending of the carbazolide plane.

Because of a complete spatial separation of the frontier molecular orbitals, the predicted energy gaps between S$_1$ and T$_1$ states are low (0.007−0.021 eV; Table S5). To evaluate the heavy metal effect on the potential enhancement of ISC and rISC rates, SOC values between S$_1$ and T$_1$ states were calculated for complex **1**. Despite the practically identical orbital configuration, a nonzero SOC value of 0.39 cm^{-1} is predicted at GS geometry. Because the Cu atom has practically
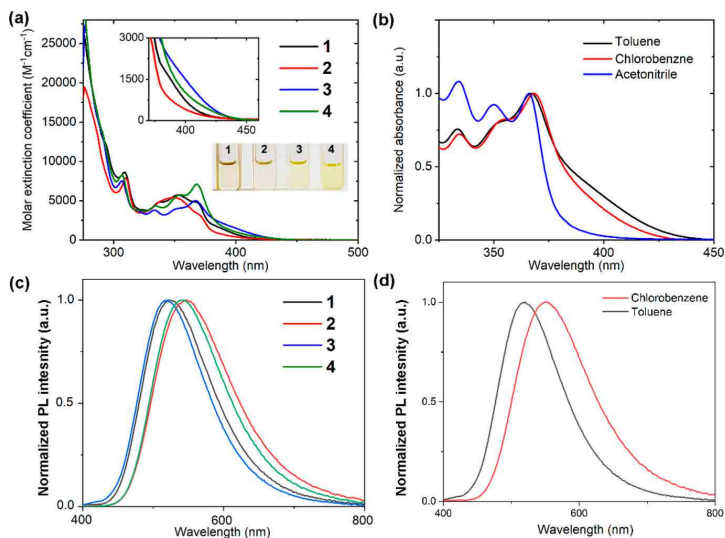
Figure 4. (a) UV−vis absorption spectra of complexes **1−4** in toluene solution. Inset shows magnified CT absorption bands, while the photograph shows the corresponding solutions. (b) Transformation of the CT band of **3** in solvents with varied polarity (ε_{tol} = 2.38; $\varepsilon_{chlorobenz.}$ = 5.62; ε_{ACN} = 37.5). (c) PL bands of **1−4** in toluene. (d) PL bands of complex **3** in various solvents.

no contribution to LUMO, the corresponding SOC is by approximately 2 orders of magnitude lower than the values typical for CMAs with carbazolide-to-NHC CT states.[43] Nevertheless, the calculated SOC value can be considered as sufficient to promote a rapid TADF, taking into account the low ΔE_{ST} values.[44] T_1 excited state geometries were obtained for **1** and **4**. No major structural changes are observed in comparison to GS, except for a slight planarization at the C1–Cu–N2 axis, indicating a decreased sterical strain. The excited state configuration at T_1 geometry is almost identical to that of GS, with lower excitations being carbazolide-to-Dipp CT states and with no major changes in ΔE_{ST} and SOC values.

Photophysical Properties. UV–vis absorption spectra of complexes **1**–**4** in toluene are shown in Figure 4a. In analogy to other CMAs, the structured bands at the 300–380 nm interval can be attributed to the $^1\pi\pi^*$ transitions of carbazolide ligands.[36] The lowest energy edge of the carbazolide absorption partly overlaps with weaker intensity bands that extend up to the 450 nm mark. These spectral features show extinction coefficients in the range of 1000–3000 M^{-1} cm^{-1} and exhibit a hypsochromic shift with increasing solvent polarity (Figure 4b). Negative solvatochromism designates the interligand CT nature of the corresponding transitions. Theoretical and experimental investigations of CMAs have related such CT-band properties to the inversion in molecular dipole direction upon photoexcitation.[17,18,45]

A correlation between the intensity of CT absorption bands and the structure of the complexed carbazolide can be made. For the MeCbz-containing complexes **3** and **4**, extinction coefficients are by a factor of 2 larger (Figure 4a, inset), giving the corresponding solutions a yellowish tint, whereas the solutions of Cbz-containing compounds **1** and **2** are practically colorless. This is in agreement with TD-DFT predictions, which designate larger oscillator strength values for **3** and **4** due to the increased coplanarity between the aromatic rings involved in the through-space CT process.

The results of photoluminescence (PL) measurements in toluene solutions are outlined in Table S6. All compounds show wide and featureless emission bands with maxima at 521–547 nm (Figure 4c), indicating the CT character of the emissive excited states. This is a contrasting behavior to tha of IPr–Cu–Cz and some other related structural analogues, which show structured emission bands due to the phosphorescence from ^{3}LE states.[34,35] In agreement with the theoretical predictions, which reveal more stabilized lowest energy CT states for imidazoline-based complexes **2** and **4**, these compounds show bathochromic PL shifts of 20–24 nm. The PL bands exhibit a characteristic positive solvatochromism, which arises due to the ^{1}CT state stabilization by the solvation shell, as evident by the emission spectra in toluene and chlorobenzene (Figures 4d, S8).[36] With a further solvent polarity increase (e.g., acetonitrile), the complexes become nonemissive. The emission efficiency of compounds in the dissolved state is relatively low. Among the screened solvents, the highest Φ_{PL} values are measured in toluene (0.21–0.31). As indicated by the rapid nonradiative decay rates (k_{nr}), the PL efficiency of **1**–**4** in fluid media is strongly affected by a vibrational relaxation. This can be related to the structural specifics of the complexes. Namely, two possible torsional motions can disrupt the emissive donor–acceptor system: the rotation around the carbazolide–metal (N_{Cbz}–Cu) and carbene–Dipp (N_{Carb}–C_{Dipp}) bonds.

Similarly to several other through-space CT emitters,[10,46] the PL efficiency of **1**–**4** substantially increases, when compounds are dispersed in a solid matrix, as the torsional degree of freedom in the molecules is reduced. In doped PMMA films (5 wt % emitter content), all compounds possess large Φ_{PL} values in the range of 0.84–0.90 (Table 1).

Table 1. Emissive Properties of Complexes 1–4^a

complex	λ_{max}, nm	Φ_{PL}	τ_{prompt}, ns	τ_{TADF}^1, μs	τ_{TADF}^2, μs	τ, μs (77 K)
1	472	0.86	6 (0.2%)	2.50 (45.4%)	10.59 (54.4%)	6.3 (CT);^{b} 3500 (^{3}LE)
2	488	0.90	10 (0.4%)	2.04 (46.6%)	8.30 (53.0%)	5.6 (CT);^{b} 3400 (^{3}LE)
3	482	0.84	12 (0.4%)	1.50 (61.6%)	5.20 (38.0%)	4.5 (CT);^{b} 3100 (^{3}LE)
4	492	0.84	19 (0.8%)	1.43 (59.8%)	4.25 (39.4%)	4.2 (CT);^{b} 2900 (^{3}LE)

^{a}Measurements taken in doped PMMA films with emitter concentration 5 wt %. ^{b}Weighted average of three PL decay components.

Complexes are susceptible to a strong concentration quenching, and in the neat films or crystalline form their Φ_{PL} drops to 0.03–0.08 (Figure S9). We note that this is a contrasting behavior to the previously reported CMAs possessing carbazolide-to-NHC CT states, which are able to retain relatively high quantum yields even in pure form.[36] This difference can be related to the fact that, for the CT states involving the NHC ring, the bulky side groups act as a buffer, preventing close contacts between the emissive regions of the molecule, whether **1**–**4** CT proceeds with the involvement of the peripheral fragments, allowing more pronounced emission quenching. The investigated samples experience a notable PL intensity drop, when exposed to oxygen, affirming that the mechanism of the emissive processes involves excited triplet states (Figure S10). Characteristically for through-space CT emitters, the measured PL bands are wide, with maxima in 472–492 nm interval (Figure 5a).

For all compounds, PL decays of PMMA film samples (Figure 5b) can be fitted with triexponential functions (Table 1). The fastest decay component in the 6–18 ns range is attributed to the prompt fluorescence. While the contribution of this low-lifetime emission toward the total PL intensity is quite small (0.2–0.8%), it still can be well resolved, in comparison to other emissive TADF-active Cu complexes, where the rapid ISC process leads to a complete excitation transfer to the triplet states.[22] For **1**–**4**, the ISC is limited by the small SOC between S_1 and T_1 levels. By applying conventional PL kinetics equations used for all-organic TADF emitters,[47] we estimate the ISC rate of the complexes (k_{ISC}) to vary in the range (5.22–16.66) × 10^7 s^{-1}, about 2 orders of magnitude higher than the radiative rate from the S_1 state (Table 2). It is worth noting that radiative rate of prompt fluorescence ($k_{r_{prompt}}$) lays in the interval (2.70–3.95) × 10^5 s^{-1}. Such a low radiative rate is characteristic for through-space CT emitters with weakly coupled donor–acceptor pairs.[48,49] Delayed emission decays over several microseconds and consists of two components with a comparable contribution to total PL intensity: one with a 1.43–2.50 μs and the other
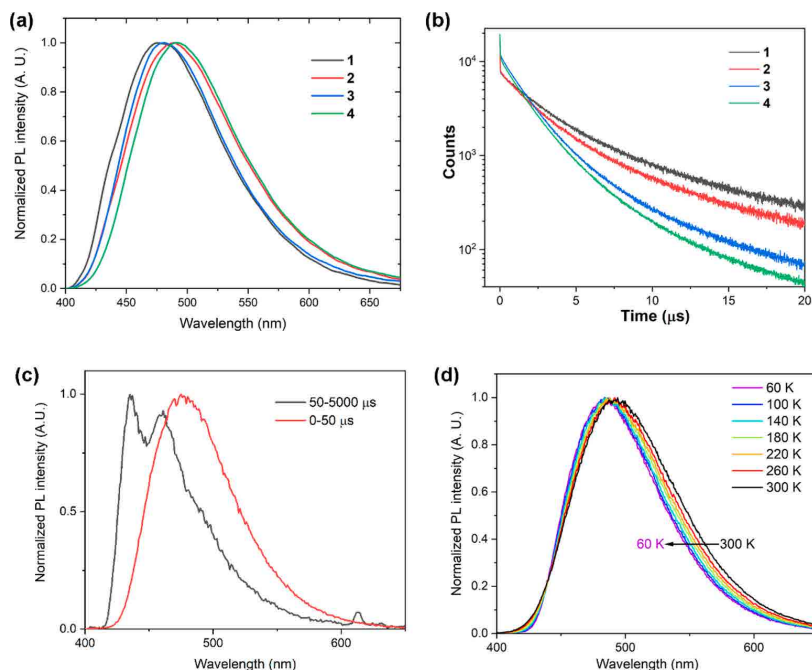
Figure 5. PL characteristics of PMMA-doped complexes **1**–**4** (5 wt % emitter content). (a) PL bands. (b) PL decays. (c) PL bands of **4** measured at a 77 K temperature. Time-resolved emission measurements show CT emission (red) and LE phosphorescence (black). (d) Temperature-induced CT emission band shifts for **4** obtained with time-resolved measurements in a 0−50 μs time window after the excitation.

Table 2. Rate Constants of Photophysical Processes for Complexes 1−4 in Doped PMMA Films with Emitter Concentration 5 wt %

complex	$k_{r_{prompt}}$, $\times 10^5$ s^{-1}	$k_{r_{TADF1}}$, $\times 10^5$ s^{-1}	$k_{r_{TADF2}}$, $\times 10^5$ s^{-1}	k_{ISC}, $\times 10^8$ s^{-1}	k_{rISC},[a] $\times 10^7$ s^{-1}	k_r,[b] $\times 10^5$ s^{-1}	k_{nr}, $\times 10^5$ s^{-1}
1	2.88	1.56	0.44	1.67	2.56	1.25	0.20
2	3.95	2.06	0.57	0.99	1.47	1.68	0.19
3	2.70	3.45	0.61	0.83	1.91	2.89	0.55
4	3.44	3.52	0.78	0.52	1.21	3.32	0.63

[a]Value calculated for the emissive process TADF₂. [b]Weighted average of three PL decay components.

with a 4.25−10.59 μs lifetime. The overall radiative rate of the complexes varies in the interval $k_r = (1.25-3.32) \times 10^5$ s^{-1}. An increase by a factor of 2 in k_r is evident for MeCbz-functionalized compounds **3** and **4**. As discussed previously, this observation can be related to the higher oscillator strength values for the lower energy CT states of these compounds.

Time resolved PL measurements at 77 K reveal that at low temperature conditions, CT emission is accompanied by long-lived ³LE phosphorescence of the carbazolide ligands (Figures 5c, S11). A similar effect has been observed for other CMAs and is related to the destabilizing effects of the solvation shell in the frozen host matrix, which raises ¹CT close to or above ³LE level.[17,40] In conformity with this assumption, the temperature scans show a gradual cooling-induced blueshift of the CT bands (Figure 5d). Interestingly, while Cbz and MeCbz donor fragments show identical phosphorescence spectra in the pure form, in the complexed state the shapes

and spectral placement of the ³LE phosphorescence bands exhibit pronounced differences (Figure S12). This disparity is attributed to the overcrowding-induced change in hybridization of the N atom in MeCbz ligand. In addition, the ³LE level in **3** and **4** is slightly destabilized and lies 0.04 eV higher, in theory providing a tool for energy level tuning.

To gain an understanding about the delayed emission mechanism of the complexes, PL kinetics were investigated in the 10−300 K temperature range (Table S7). Compounds **2** and **4** were characterized to assess the impact of carbazolide ligand structure. The intensity of CT emission gradually decreases with the cooling, revealing a behavior that is more in line with all-organic than heavy-metal-promoted TADF emitters. In the absence of strong SOC, the emission from ³CT states proceeds on a time scale that cannot compete with the nonradiative vibrational relaxation. This means that for such emitters PL intensity drops at low temperatures, as the lack of thermal activation traps the excitation in the dark triplet state.[1] For TADF-active Cu complexes the situation is different. The moderate SOC values promote efficient ³CT phosphorescence with typical lifetimes of a few hundred microseconds, and PL intensity remains practically constant, as with the temperature decrease the dominating emission mechanism gradually shifts from TADF to phosphorescence.[37] The behavior of **1**−**4** belongs to the former case. This assumption is additionally supported by TD-DFT calculations, which estimate phosphorescence lifetimes from the T_1 state of **1** to be 0.22 s, too long for this to be a viable emissive pathway. A slight deviation from the before-mentioned trend is observed for complex **4**, for which the maximal PL efficiency is measured at 220 K ($\Phi_{PL} = 0.93$). This is attributed to the cooling
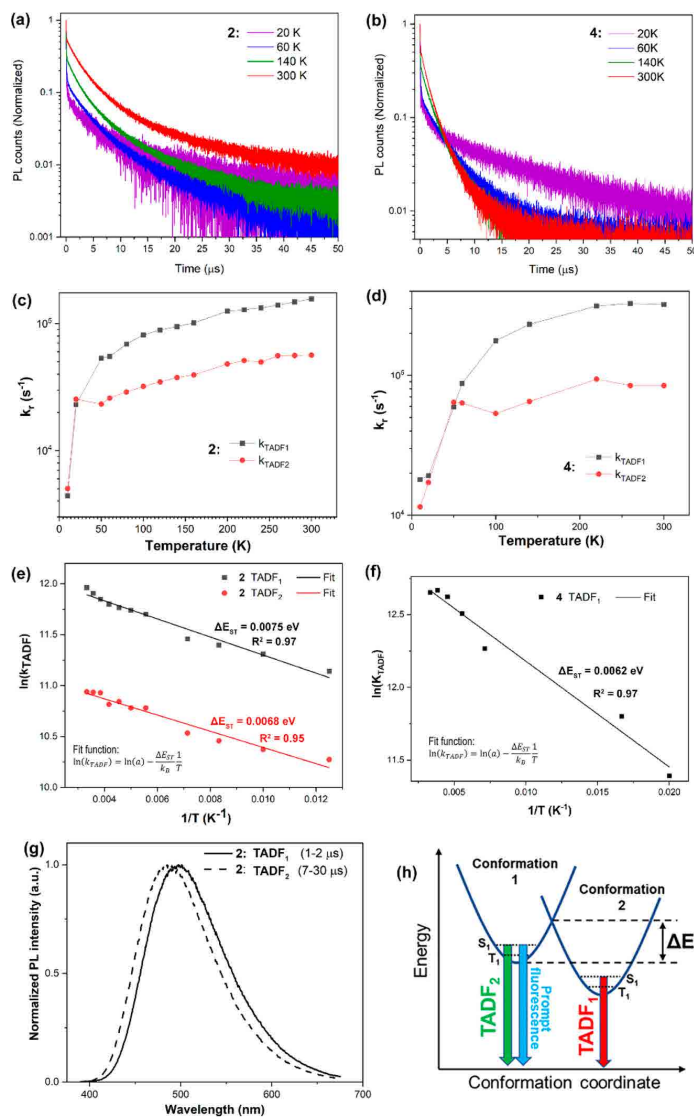
Figure 6. PL decay at selected temperatures for **2** (a) and **4** (b). Temperature dependence of delayed emission component rates for **2** (c) and **4** (d). Arrhenius plots (circles) showing the correlation between k_{TADF} and temperature for **2** (e) and **4** (f). Fit function formula, corresponding fits (lines), and obtained ΔE_{ST} values are shown. Time resolved PL spectra of **2** measured at room temperature (g). Emissions collected at $1-2$ μs intervals show predominantly TADF$_1$, while a $7-30$ μs interval is dominated by TADF$_2$. The proposed mechanism for dual delayed emission (h).

induced solidification of the host matrix and consequent suppression of emission-quenching torsional motions.

Throughout the explored temperature interval, the compounds retain triexponential decay curves, featuring a prompt and two delayed emission components (Figure 6a,b; S13; Table S7). The temperature-induced changes in emission rate constants for the two long-lived PL constituents provide more direct evidence for the TADF process (Figure 6c,d). For both the fastest (TADF$_1$) and slowest (TADF$_2$) delayed emission components, a gradual radiative emission rate ($k_{r_{TADF}}$) decrease is observed throughout the cooling range, designating a

thermally activated nature of the emissive process. In contrast, the prompt PL component does not exhibit a rate decrease. The corresponding ΔE_{ST} values were estimated from the fits of Arrhenius plots relating temperature and the experimental $k_{r_{TADF}}$ values (Figure 6e,f).[22] For all examined emissive processes, highly similar activation energies were obtained, in the range of $0.0062-0.0075$ eV. These values correspond well with the TD-DFT predictions for the energy gaps between T$_1$ and S$_1$ levels of the carbazolide-to-Dipp related CT states.

To explain the origin of two distinct TADF processes for **1**–**4**, time-resolved PL spectra were obtained by collecting PL

intensities in TADF$_1$ dominated (1–2 μs) and TADF$_2$ (7–30 μs) dominated time intervals (Figures 6g, S14). Except for complex **4**, where PL bands of TADF$_1$ and TADF$_2$ almost overlap, TADF$_2$ is blue-shifted in relation to TADF$_1$. This is the opposite behavior to that of many triplet emitters, where longer lived emissive states usually attain lower energies due to the progressive exciton migration to lower energy states.[50] Additionally, the ratio of the PL intensities between TADF$_1$ and TADF$_2$ is temperature dependent (Table S7), and below 50 K the overall CT emission becomes almost completely dominated by TADF$_2$. The before-mentioned observations let us propose a mechanism for the dual TADF (Figure 6h), attributing each emissive process to an individual structural conformation of the complex molecule. Initially, upon photoexcitation, conformation 1 is assumed, from which the TADF$_2$ emissive process occurs. In conformity with low-temperature measurements, a subsequent molecular geometry transformation to conformation 2 takes place, from which TADF$_1$ emission originates. Due to the observed heating induced PL intensity transfer from TADF$_2$ to TADF$_1$, this process is associated with an energetical barrier (ΔE), even though in the relaxed state conformation 2 provides the emitting state with the lowest energy.

In accordance with the proposed emissive mechanism, the prompt fluorescence should arise solely from conformation 1, as the Cu-induced rapid ISC to the triplet state is expected to outpace the molecular geometry transformation to conformation 2. This assumption is also supported by a radiative rate comparison, as for **3** and **4** $k_{r_{TADF1}}$ is larger than $k_{r_{prompt}}$, a situation that is not plausible for emissive processes that arise from a shared singlet state.[51] However, a reasonable radiative rate relation is observed between $k_{r_{TADF2}}$ and $k_{r_{prompt}}$. Accordingly, by relating prompt fluorescence to the TADF$_2$ process, the corresponding rISC rates for **1–4** are estimated at $(1.21–2.56) \times 10^7$ s^{-1} (Table 2). In conformity with the hybrid nature of the proposed TADF emitter architecture, these values fall in between the conventional metal-promoted designs ($k_{rISC} \sim 10^8$ s^{-1})[22] and state-of-the-art all-organic through-space emitters ($k_{rISC} \sim 10^6$ s^{-1}).[48,52]

The rate $k_{r_{TADF1}}$ is by a factor 2 larger than $k_{r_{TADF2}}$. As indicated by ΔE_{ST} values obtained for **2**, this cannot be explained by a lower activation energy for TADF$_1$, as, in fact, it is lower for TADF$_2$. Accordingly, the rate difference arises due to a substantial oscillator strength increase for ^{1}CT states associated with conformation 2. For the through-space CT process, this can be induced by arranging the D and A fragments closer to the face-to-face configuration. The consequence of such structural change is a characteristic PL redshift,[42,53] which, indeed, is observed in the case of TADF$_1$ emission. In terms of structures **1–4**, this dual emission is thought to be caused by energetic minima that arise due to possible Renner–Teller distortions, resulting in a decrease in the C1–Cu–N2 angle,[41,54] or by the pyramidization at the carbazolide N atom, like it is observed in the X-ray structure of complex **4**. Both of these structural changes would shift the plane of the carbazolide ligand in a more coplanar arrangement with Dipp fragments. To further elaborate on this, we have carried DFT modeling for complex **1** (Figure S15). Two conformations of the compound were analyzed. The first was based on X-ray structure and features a coplanar alignment of carbazolide and carbene planes (flattened conformation). The second conformation corresponds to the global energy minimum found

through DFT optimization and, similarly to the X-ray structure of **4**, exhibits a pyramidization at the carbazolide N atom (bent conformation). Because of the different alignment of the amide ligand, the dihedral angle between the Dipp and carbazole planes changes substantially between the two structures, from 86.2° to 54.1°. This structural transformation causes a large difference in the oscillator strength value for S$_0 \rightarrow$ S$_1$ transition, where about a 3-fold increase in f_{osc} is predicted for the bent conformation. Consequently, this complex geometry would possess a notably increased radiative rate from the lowest energy singlet excited state. The energy difference between the two conformations is only 0.82 kcal/mol, meaning that both conformations are easily accessible at room temperature conditions and can, in theory, contribute to the emissive process, resulting in the observed dual TADF process.

To assess the prospects of the compounds for electro-luminescence related applications, solution-processed test devices were prepared with the architecture ITO/PEDOT:PSS(40 nm)/PolyTPD(30 nm)/**4** (20 wt %):CzSi(40 nm)/TPBi(40 nm)/LiF (1 nm)/Al (100 nm). The non-optimized OLED was characterized with a turn-on voltage of 6 V, a current efficiency of 1.7 cd/A, a power efficiency of 0.6 lm/W, and an external quantum efficiency of 0.8%. Electro-luminescence spectra of the device indicate that emission originates from the CT state of the complex (Figure S16). At the same time, a substantial red shift in emission can be seen in comparison to the PMMA film with an identical complex concentration. Such an emission band shift can be related to a surrounding medium polarity increase, which is expected in the case of molecular charge transporting host CzSi. These results show that the presented molecular design is potentially suitable for OLED use, but further device optimization is needed to improve device efficiency parameters.

■ CONCLUSIONS

On the basis of structural examples **1–4**, we have demonstrated a novel concept to the development of efficient TADF emitters. By combining through-space CT architecture, giving compounds the characteristic low ΔE_{ST} values, with the presence of a heavy metal atom, which provides small, but still present SOC, rISC values exceeding 10^7 s^{-1} can be attained. While the examined compounds can still be classified as carbene–metal–amide complexes, from the point of photo-physical functionality, the carbene fragment acts as an inert linking fragment between a carbene-bound acceptor and a metal-bound donor. In such a way, conventional and easy to obtain imidazole-based carbenes can serve as building blocks toward such emitters, in contrast to carbene-to-carbazolide CT state emitters, where a careful tuning of carbene electronic levels is necessary.[18] Additionally, we demonstrate that a direct metal bonding to only one of the CT-constituting aromatic systems is sufficient to provide a rapid TADF process. Emissive rates in the presented emitters can be substantially increased by ensuring face-to-face alignment between D and A fragments, which can be achieved through a sterical over-crowding-induced twist of the carbazolide plane. The presented findings provide valuable guidelines toward further development of TADF-active molecules.

■ ASSOCIATED CONTENT

ⓈI Supporting Information

The Supporting Information is available free of charge at https://pubs.acs.org/doi/10.1021/acs.inorgchem.1c03371.

Additional figures and tables, formulas used for the calculation of emission kinetics parameters, NMR spectra, cyclic voltammetry curves, atomic coordinates of DFT optimized structures (PDF)

■ AUTHOR INFORMATION

Corresponding Author

    Kaspars Traskovskis − *Faculty of Materials Science and Applied Chemistry, Riga Technical University, LV-1048 Riga, Latvia;* ● orcid.org/0000-0003-1416-7533; Email: kaspars.traskovskis@rtu.lv

Authors

    Armands Ruduss − *Faculty of Materials Science and Applied Chemistry, Riga Technical University, LV-1048 Riga, Latvia*

    Baiba Turovska − *Latvian Institute of Organic Synthesis, Riga LV-1006, Latvia*

    Sergey Belyakov − *Latvian Institute of Organic Synthesis, Riga LV-1006, Latvia*

    Kitija A. Stucere − *Institute of Solid State Physics, University of Latvia, LV-1063 Riga, Latvia*

    Aivars Vembris − *Institute of Solid State Physics, University of Latvia, LV-1063 Riga, Latvia*

Complete contact information is available at:
https://pubs.acs.org/10.1021/acs.inorgchem.1c03371

Notes

The authors declare no competing financial interest.

■ REFERENCES

(1) Uoyama, H.; Goushi, K.; Shizu, K.; Nomura, H.; Adachi, C. Highly Efficient Organic Light-Emitting Diodes from Delayed Fluorescence. *Nature* **2012**, *492* (7428), 234−238.

(2) Yang, Z.; Mao, Z.; Xie, Z.; Zhang, Y.; Liu, S.; Zhao, J.; Xu, J.; Chi, Z.; Aldred, M. P. Recent Advances in Organic Thermally Activated Delayed Fluorescence Materials. *Chem. Soc. Rev.* **2017**, *46* (3), 915−1016.

(3) Bryden, M. A.; Zysman-Colman, E. Organic Thermally Activated Delayed Fluorescence (TADF) Compounds Used in Photocatalysis. *Chem. Soc. Rev.* **2021**, *50* (13), 7587−7680.

(4) Ni, F.; Li, N.; Zhan, L.; Yang, C. Organic Thermally Activated Delayed Fluorescence Materials for Time-Resolved Luminescence Imaging and Sensing. *Adv. Opt. Mater.* **2020**, *8* (14), 1902187.

(5) Köhler, A.; Beljonne, D. The Singlet-Triplet Exchange Energy in Conjugated Polymers. *Adv. Funct. Mater.* **2004**, *14* (1), 11−18.

(6) Goushi, K.; Adachi, C. Efficient Organic Light-Emitting Diodes through up-Conversion from Triplet to Singlet Excited States of Exciplexes. *Appl. Phys. Lett.* **2012**, *101* (2), 023306.

(7) Graves, D.; Jankus, V.; Dias, F. B.; Monkman, A. Photophysical Investigation of the Thermally Activated Delayed Emission from Films of M-MTDATA:PBD Exciplex. *Adv. Funct. Mater.* **2014**, *24* (16), 2343−2351.

(8) Kim, K.-H.; Yoo, S.-J.; Kim, J.-J. Boosting Triplet Harvest by Reducing Nonradiative Transition of Exciplex toward Fluorescent Organic Light-Emitting Diodes with 100% Internal Quantum Efficiency. *Chem. Mater.* **2016**, *28* (6), 1936−1941.

(9) Shao, S.; Hu, J.; Wang, X.; Wang, L.; Jing, X.; Wang, F. Blue Thermally Activated Delayed Fluorescence Polymers with Non-conjugated Backbone and Through-Space Charge Transfer Effect. *J. Am. Chem. Soc.* **2017**, *139* (49), 17739−17742.

(10) Tsujimoto, H.; Ha, D.-G.; Markopoulos, G.; Chae, H. S.; Baldo, M. A.; Swager, T. M. Thermally Activated Delayed Fluorescence and Aggregation Induced Emission with Through-Space Charge Transfer. *J. Am. Chem. Soc.* **2017**, *139* (13), 4894−4900.

(11) Li, J.; Shen, P.; Zhao, Z.; Tang, B. Z. Through-Space Conjugation: A Thriving Alternative for Optoelectronic Materials. *CCS Chem.* **2019**, *1* (2), 181−196.

(12) Etherington, M. K.; Gibson, J.; Higginbotham, H. F.; Penfold, T. J.; Monkman, A. P. Revealing the Spin-Vibronic Coupling Mechanism of Thermally Activated Delayed Fluorescence. *Nat. Commun.* **2016**, *7* (1), 13680.

(13) Wang, Y.; Huang, C.; Ye, H.; Zhong, C.; Khan, A.; Yang, S.; Fung, M.; Jiang, Z.; Adachi, C.; Liao, L. Through Space Charge Transfer for Efficient Sky-Blue Thermally Activated Delayed Fluorescence (TADF) Emitter with Unconjugated Connection. *Adv. Opt. Mater.* **2020**, *8* (2), 1901150.

(14) Ma, Y.; Che, C.-M.; Chao, H.-Y.; Zhou, X.; Chan, W.-H.; Shen, J. High Luminescence Gold(I) and Copper(I) Complexes with a Triplet Excited State for Use in Light-Emitting Diodes. *Adv. Mater.* **1999**, *11* (10), 852−857.

(15) Harkins, S. B.; Peters, J. C. A Highly Emissive Cu 2 N 2 Diamond Core Complex Supported by a [PNP] - Ligand. *J. Am. Chem. Soc.* **2005**, *127* (7), 2030−2031.

(16) Di, D.; Romanov, A. S.; Yang, L.; Richter, J. M.; Rivett, J. P. H.; Jones, S.; Thomas, T. H.; Abdi Jalebi, M.; Friend, R. H.; Linnolahti, M.; Bochmann, M.; Credgington, D. High-Performance Light-Emitting Diodes Based on Carbene-Metal-Amides. *Science (80-.).* **2017**, *356* (6334), 159−163.

(17) Hamze, R.; Peltier, J. L.; Sylvinson, D.; Jung, M.; Cardenas, J.; Haiges, R.; Soleilhavoup, M.; Jazzar, R.; Djurovich, P. I.; Bertrand, G.; Thompson, M. E. Eliminating Nonradiative Decay in Cu(I) Emitters: > 99% Quantum Efficiency and Microsecond Lifetime. *Science (80-.).* **2019**, *363* (6427), 601−606.

(18) Gernert, M.; Balles-Wolf, L.; Kerner, F.; Müller, U.; Schmiedel, A.; Holzapfel, M.; Marian, C. M.; Pflaum, J.; Lambert, C.; Steffen, A. Cyclic (Amino)(Aryl)Carbenes Enter the Field of Chromophore Ligands: Expanded π System Leads to Unusually Deep Red Emitting Cu I Compounds. *J. Am. Chem. Soc.* **2020**, *142* (19), 8897−8909.

(19) Hamze, R.; Idris, M.; Muthiah Ravinson, D. S.; Jung, M. C.; Haiges, R.; Djurovich, P. I.; Thompson, M. E. Highly Efficient Deep Blue Luminescence of 2-Coordinate Coinage Metal Complexes Bearing Bulky NHC Benzimidazolyl Carbene. *Front. Chem.* **2020**, *8*, 8.

(20) Cao, L.; Huang, S.; Liu, W.; Zhao, H.; Xiong, X.; Zhang, J.; Fu, L.; Yan, X. Thermally Activated Delayed Fluorescence from d 10 -Metal Carbene Complexes through Intermolecular Charge Transfer and Multicolor Emission with a Monomer-Dimer Equilibrium. *Chem. - A Eur. J.* **2020**, *26* (71), 17222−17229.

(21) Yang, J.-G.; Song, X.-F.; Wang, J.; Li, K.; Chang, X.; Tan, L.-Y.; Liu, C.-X.; Yu, F.-H.; Cui, G.; Cheng, G.; To, W.-P.; Yang, C.; Che, C.-M.; Chen, Y. Highly Efficient Thermally Activated Delayed Fluorescence from Pyrazine-Fused Carbene Au(I) Emitters. *Chem. - A Eur. J.* **2021**, *27*, 17834.

(22) Hamze, R.; Shi, S.; Kapper, S. C.; Muthiah Ravinson, D. S.; Estergreen, L.; Jung, M.-C.; Tadle, A. C.; Haiges, R.; Djurovich, P. I.; Peltier, J. L.; Jazzar, R.; Bertrand, G.; Bradforth, S. E.; Thompson, M. E. Quick-Silver" from a Systematic Study of Highly Luminescent, Two-Coordinate, d 10 Coinage Metal Complexes. *J. Am. Chem. Soc.* **2019**, *141* (21), 8616−8626.

(23) Thompson, M. E.; Li, T. Y.; Djurovich, P.; Shlian, D. A Luminescent Two-Coordinate Au(I) Bimetallic Complex with a Tandem-Carbene Structure: A Molecular Design for the Enhancement of TADF Radiative Decay Rate. *Chem. - A Eur. J.* **2021**, *27*, 6191.

(24) Leuthäußer, S.; Schwarz, D.; Plenio, H. Tuning the Electronic Properties of N-Heterocyclic Carbenes. *Chem. - A Eur. J.* **2007**, *13* (25), 7195−7203.

(25) Bedford, R. B.; Betham, M. N -H Carbazole Synthesis from 2-Chloroanilines via Consecutive Amination and C-H Activation. *J. Org. Chem.* **2006**, *71* (25), 9403−9410.

(26) Sheldrick, G. M. SHELXT - Integrated Space-Group and Crystal-Structure Determination. *Acta Crystallogr. Sect. A Found. Adv.* **2015**, *71* (1), 3−8.

(27) Sheldrick, G. M. A Short History of SHELX. *Acta Crystallogr. Sect. A Found. Crystallogr.* **2008**, *64* (1), 112−122.

(28) Dolomanov, O. V.; Bourhis, L. J.; Gildea, R. J.; Howard, J. A. K.; Puschmann, H. OLEX2: A Complete Structure Solution, Refinement and Analysis Program. *J. Appl. Crystallogr.* **2009**, *42* (2), 339−341.

(29) Bochevarov, A. D.; Harder, E.; Hughes, T. F.; Greenwood, J. R.; Braden, D. A.; Philipp, D. M.; Rinaldo, D.; Halls, M. D.; Zhang, J.; Friesner, R. A. Jaguar: A High-performance Quantum Chemistry Software Program with Strengths in Life and Materials Sciences. *Int. J. Quantum Chem.* **2013**, *113* (18), 2110−2142.

(30) Yu, H. S.; He, X.; Li, S. L.; Truhlar, D. G. MN15: A Kohn-Sham Global-Hybrid Exchange-Correlation Density Functional with Broad Accuracy for Multi-Reference and Single-Reference Systems and Noncovalent Interactions. *Chem. Sci.* **2016**, *7* (8), 5032−5051.

(31) Zhang, H. Q.; Jin, Y.; Qiu, Y. The Optical and Electrical Characteristics of PMMA Film Prepared by Spin Coating Method. *IOP Conf. Ser. Mater. Sci. Eng.* **2015**, *87*, 012032.

(32) Lu, T.; Chen, F. Multiwfn: A Multifunctional Wavefunction Analyzer. *J. Comput. Chem.* **2012**, *33* (5), 580−592.

(33) te Velde, G.; Bickelhaupt, F. M.; Baerends, E. J.; Fonseca Guerra, C.; van Gisbergen, S. J. A.; Snijders, J. G.; Ziegler, T. Chemistry with ADF. *J. Comput. Chem.* **2001**, *22* (9), 931−967.

(34) Li, J.; Wang, L.; Zhao, Z.; Li, X.; Yu, X.; Huo, P.; Jin, Q.; Liu, Z.; Bian, Z.; Huang, C. Two-Coordinate Copper(I)/NHC Complexes: Dual Emission Properties and Ultralong Room-Temperature Phosphorescence. *Angew. Chemie Int. Ed.* **2020**, *59* (21), 8210−8217.

(35) Tzouras, N. V.; Martynova, E. A.; Ma, X.; Scattolin, T.; Hupp, B.; Busen, H.; Saab, M.; Zhang, Z.; Falivene, L.; Pisanò, G.; Van Hecke, K.; Cavallo, L.; Cazin, C. S. J.; Steffen, A.; Nolan, S. P. Simple Synthetic Routes to Carbene-M-Amido (M = Cu, Ag, Au) Complexes for Luminescence and Photocatalysis Applications. *Chem. - A Eur. J.* **2021**, *27* (46), 11904−11911.

(36) Shi, S.; Jung, M. C.; Coburn, C.; Tadle, A.; Sylvinson, M. R. D.; Djurovich, P. I.; Forrest, S. R.; Thompson, M. E. Highly Efficient Photo- and Electroluminescence from Two-Coordinate Cu(I) Complexes Featuring Nonconventional N-Heterocyclic Carbenes. *J. Am. Chem. Soc.* **2019**, *141* (8), 3576−3588.

(37) Leitl, M. J.; Zink, D. M.; Schinabeck, A.; Baumann, T.; Volz, D.; Yersin, H. Copper(I) Complexes for Thermally Activated Delayed Fluorescence: From Photophysical to Device Properties. *Top. Curr. Chem.* **2016**, *374* (3), 25.

(38) Leiva, A. M.; Rivera, L.; Loeb, B. Analysis of Copper(I) Stability in the Cationic [Cu(CH3CN)4-n(Ph3P)n]+ Series of Complexes. *Polyhedron* **1991**, *10* (3), 347−350.

(39) Chotard, F.; Sivchik, V.; Linnolahti, M.; Bochmann, M.; Romanov, A. S. Mono- versus Bicyclic Carbene Metal Amide Photoemitters: Which Design Leads to the Best Performance? *Chem. Mater.* **2020**, *32* (14), 6114−6122.

(40) Romanov, A. S.; Jones, S. T. E.; Gu, Q.; Conaghan, P. J.; Drummond, B. H.; Feng, J.; Chotard, F.; Buizza, L.; Foley, M.; Linnolahti, M.; Credgington, D.; Bochmann, M. Carbene Metal Amide Photoemitters: Tailoring Conformationally Flexible Amides for Full Color Range Emissions Including White-Emitting OLED. *Chem. Sci.* **2020**, *11* (2), 435−446.

(41) Lin, S.; Ou, Q.; Wang, Y.; Peng, Q.; Shuai, Z. Aggregation-Enhanced Thermally Activated Delayed Fluorescence Efficiency for Two-Coordinate Carbene-Metal-Amide Complexes: A QM/MM Study. *J. Phys. Chem. Lett.* **2021**, *12* (11), 2944−2953.

(42) Li, Q.; Hu, J.; Lv, J.; Wang, X.; Shao, S.; Wang, L.; Jing, X.; Wang, F. Through-Space Charge-Transfer Polynorbornenes with Fixed and Controllable Spatial Alignment of Donor and Acceptor for High-Efficiency Blue Thermally Activated Delayed Fluorescence. *Angew. Chemie Int. Ed.* **2020**, *59* (45), 20174−20182.

(43) Eng, J.; Thompson, S.; Goodwin, H.; Credgington, D.; Penfold, T. J. Competition between the Heavy Atom Effect and Vibronic Coupling in Donor-Bridge-Acceptor Organometallics. *Phys. Chem. Chem. Phys.* **2020**, *22* (8), 4659−4667.

(44) Samanta, P. K.; Kim, D.; Coropceanu, V.; Brédas, J.-L. Up-Conversion Intersystem Crossing Rates in Organic Emitters for Thermally Activated Delayed Fluorescence: Impact of the Nature of Singlet vs Triplet Excited States. *J. Am. Chem. Soc.* **2017**, *139* (11), 4042−4051.

(45) Lüdtke, N.; Föller, J.; Marian, C. M. Understanding the Luminescence Properties of Cu (¹) Complexes: A Quantum Chemical Perusal. *Phys. Chem. Chem. Phys.* **2020**, *22* (41), 23530−23544.

(46) Wang, X.; Wang, S.; Lv, J.; Shao, S.; Wang, L.; Jing, X.; Wang, F. Through-Space Charge Transfer Hexaarylbenzene Dendrimers with Thermally Activated Delayed Fluorescence and Aggregation-Induced Emission for Efficient Solution-Processed OLEDs. *Chem. Sci.* **2019**, *10* (10), 2915−2923.

(47) Dias, F. B.; Penfold, T. J.; Monkman, A. P. Photophysics of Thermally Activated Delayed Fluorescence Molecules. *Methods Appl. Fluoresc.* **2017**, *5* (1), 012001.

(48) Wu, C.; Liu, W.; Li, K.; Cheng, G.; Xiong, J.; Teng, T.; Che, C.; Yang, C. Face-to-Face Orientation of Quasiplanar Donor and Acceptor Enables Highly Efficient Intramolecular Exciplex Fluorescence. *Angew. Chemie Int. Ed.* **2021**, *60* (8), 3994−3998.

(49) Mahmoudi, M.; Keruckas, J.; Leitonas, K.; Kutsiy, S.; Volyniuk, D.; Grazulevicius, J. V. Exciplex-Forming Systems with Extremely High RISC Rates Exceeding 107 S-1 for Oxygen Probing and White Hybrid OLEDs. *J. Mater. Res. Technol.* **2021**, *10*, 711−721.

(50) Mikhnenko, O. V.; Blom, P. W. M.; Nguyen, T.-Q. Exciton Diffusion in Organic Semiconductors. *Energy Environ. Sci.* **2015**, *8* (7), 1867−1888.

(51) Ravinson, D. S. M.; Thompson, M. E. Thermally Assisted Delayed Fluorescence (TADF): Fluorescence Delayed Is Fluorescence Denied. *Mater. Horizons* **2020**, *7* (5), 1210−1217.

(52) Huang, T.; Wang, Q.; Xiao, S.; Zhang, D.; Zhang, Y.; Yin, C.; Yang, D.; Ma, D.; Wang, Z.; Duan, L. Simultaneously Enhanced Reverse Intersystem Crossing and Radiative Decay in Thermally Activated Delayed Fluorophors with Multiple Through-space Charge Transfers. *Angew. Chem., Int. Ed.* **2021**, *60*, 23771.

(53) Moon, C.-K.; Huh, J.-S.; Kim, J.-M.; Kim, J.-J. Electronic Structure and Emission Process of Excited Charge Transfer States in Solids. *Chem. Mater.* **2018**, *30* (16), 5648−5654.

(54) Taffet, E. J.; Olivier, Y.; Lam, F.; Beljonne, D.; Scholes, G. D. Carbene-Metal-Amide Bond Deformation, Rather Than Ligand Rotation, Drives Delayed Fluorescence. *J. Phys. Chem. Lett.* **2018**, *9* (7), 1620−1626.

4.pielikums

Ruduss, A.; Turovska, B.; Belyakov, S.; Stucere, K. A.; Vembris, A.; Baryshnikov, G.; Ågren, H.; Lu, J.; Lin, W.; Chang, C.; Traskovskis, K. Thiazoline Carbene–Cu(I)–Amide Complexes: Efficient White Electroluminescence from Combined Monomer and Excimer Emission. *ACS Appl. Mater. Interfaces*. **2022**, *14* (13), 15478–15493.

doi: 10.1021/acsami.2c00847

Thiazoline Carbene−Cu(I)−Amide complexes: Efficient White Electroluminescence from Combined Monomer and Excimer Emission

Armands Ruduss, Baiba Turovska, Sergey Belyakov, Kitija A. Stucere, Aivars Vembris, Glib Baryshnikov, Hans Ågren, Jhao-Cheng Lu, Wei-Han Lin, Chih-Hao Chang,* and Kaspars Traskovskis*

Cite This: https://doi.org/10.1021/acsami.2c00847

Read Online

ACCESS | lıl Metrics & More | ▤ Article Recommendations | ⓢ Supporting Information

ABSTRACT: Luminescent carbene−metal−amide complexes bearing group 11 metals (Cu, Ag, Au) have recently attracted great attention due to their exceptional emission efficiency and high radiative decay rates (k_r). These materials provide a less costly alternative to organic light-emitting diode (OLED) emitters based on more scarce metals, such as Ir and Pt. Herein, a series of eight Cu(I) complexes bearing as yet unexplored 1,3-thiazoline carbenes have been investigated and analyzed with respect to their light emission properties and OLED application. For the first time among the class of copper-based organometallic compounds the formation of efficient electroluminescent excimers is demonstrated. The prevalence of electroluminescence (EL) from either the monomer (bluish green) or the excimer (orange-red) can be adjusted in vacuum-deposited emissive layers by altering the extent of steric encumbrance of the emitter or its concentration. Optimized conditions in terms of the emitter structure and mass fraction allowed a simultaneous EL from the monomer and excimer, which laid the basis for a preparation of a single-emitter white OLED (WOLED) with external quantum efficiency of 16.5% and a maximum luminance of over 40000 cd m^{-2}. Wide overlapping emission bands of the monomer and excimer ensure a device color rendering index (CRI) of above 80. In such a way the prospects of copper complexes as cost-effective materials for lighting devices are demonstrated, offering expense reduction through a cheaper emissive component and a simplified device architecture.
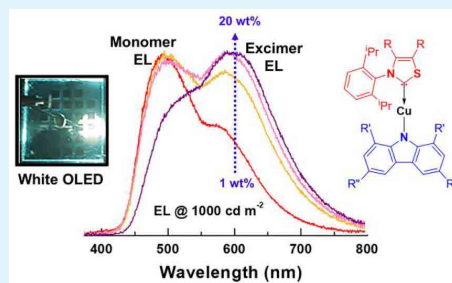
■ INTRODUCTION

Advancements in organic light-emitting diode (OLED) technology has aided the rise of innovative consumer-grade products, such as mobile devices and TV displays with unmatched power consumption characteristics, form factors, refresh rates and image quality.[1] In addition, great attention has recently been devoted to the development of white OLEDs (WOLEDs) for next-generation lighting devices.[2] Emitters with suitable photophysical properties play a crucial role in attaining the desired efficiency and longevity parameters of these devices. Due to the intrinsic nature of electronic excitations, which generate singlet (S) and triplet (T) excitons in a 25%:75% ratio, the ability to ensure emission by circumventing the forbidden nature of the $T_1 \rightarrow S_0$ transition is the main requirement for efficient emitters.[3] Organometallic transition-metal complexes bearing Ir, Pt, Os, and Re atoms possess strong spin−orbit coupling (SOC), allowing fast phosphorescence with radiative rates (k_r) in the range of 10^5−10^6 s^{-1}.[4−6] Although these materials have experienced the most widespread practical use,

the rarity and high cost of the mentioned elements have fueled research interest in compounds that feature more abundant metals.[7,8] Particularly, Cu complexes have attracted attention due to the absence of efficiency-reducing d → d* transitions in the d^{10}-configured outer electron shell.[9−13] While Cu does not promote a rapid emission directly from the T_1 state due to insufficient SOC strength, the presence of this heavy atom aids in efficient and fast triplet state harvesting through a thermally activated delayed fluorescence (TADF) mechanism.[14] The early structural examples of such compounds mostly possessed metal to ligand charge transfer (MLCT) states. Due to the formal oxidation of the metal center upon photoexcitation, the
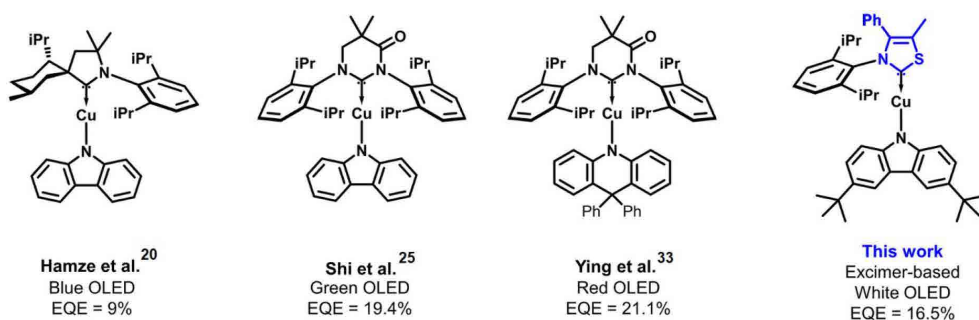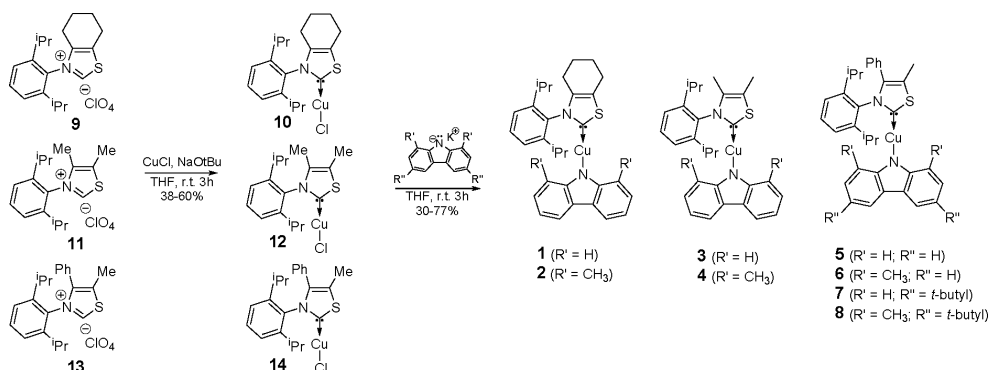
Figure 1. Known Cu(I)-based CMA emitters with a demonstrated OLED use.

Scheme 1. Synthesis of CMA Emitters 1−8

geometry of these complexes transforms, so reducing the attainable photoluminescence quantum yield (Φ_{PL}).[15,16]

Recently a new class of highly emissive d^{10}-element (Cu, Ag, Au)-based emitters have emerged in the form of two-coordinate linear geometry complexes. Composed of metal-bound electrophilic carbene and electron-rich amide ligands, these compounds are often referred to as "carbene−metal−amides" (CMAs).[17−20] The TADF emission in these complexes predominantly originates from ligand to ligand charge transfer (LLCT) states, and Φ_{PL} values of up to 1.0 can be attained due to the limited metal involvement. Spatial separation of the highest occupied and lowest unoccupied molecular orbitals (HOMO and LUMO) ensures that the energy gap between the lowest energy S and T states (ΔE_{ST}) is small, resulting in fast direct and reverse intersystem crossing rates (k_{ISC} and k_{RISC}) and allowing TADF lifetimes of below 1.0 μs.[21−24] In addition to systematically tunable emission color, covering the visible spectrum,[25−29] these compounds show characteristics and OLED performance that are comparable to those of state of the art Ir and Pt emitters.[19,25]

Structure−property relations for this compound class have been well established. Emission lifetimes (τ) become shorter in the sequence Cu, Au, and Ag, partially in relation to the ΔE_{ST} values of the corresponding complexes.[21] The structure of the ligands mainly influences the emission wavelength. The electron-donating amide determines the HOMO energy level of the emitter, which can be modified with an introduction of electron-accepting or -donating structural fragments.[25,30] All of the known strongly emissive CMAs feature carbenes with an electrophilic nature.[27,31] In particular, cyclic alkyl amino carbenes (CAAC),[19,32] monoamido and diamido carbenes (MAC, DAC),[25,33] and aryl-fused carbenes[27,34,35] have been successfully used to synthesize such emitters. Despite these examples the structural diversity of CMAs is still rather low due to the small number of accessible carbenes that can provide emitters with a combination of high emission efficiency and chemical stability. Particularly, this can be addressed to the emitters based on the more abundant Cu atom, for which only a small number of reports have demonstrated a practical OLED use (Figure 1).

Here we investigate the novel structures of highly luminescent CMAs, which contain an as yet unexplored 1,3-thiazoline carbene fragment. A series of complex molecules 1−8 was synthesized by altering the substituents at the 4- or 5-position of either the 1,3-thiazoline carbene or the carbazole amide (Scheme 1). In doped PMMA films the compounds possess high Φ_{PL} values (0.71−0.86) with radiative rates in the range $k_r = (2.8−7.2) \times 10^5$ s^{-1}. As we show, the emissive rates of the complexes can be substantially increased by the simultaneous introduction of sterically demanding groups at both the thiazoline carbene 4-position and the carbazolide 1,8-positions. The results of X-ray structural analyses and DFT calculations relate this effect to a conformational locking that limits the degree of torsional motion of the carbazolide ligand. On the basis of the investigated compounds, for the first time among the class of Cu(I) emitters we demonstrate the formation of efficient electroluminescent excimers. The formation of emissive dimers is related to the favorable molecular structure of 1,3-thiazoline-
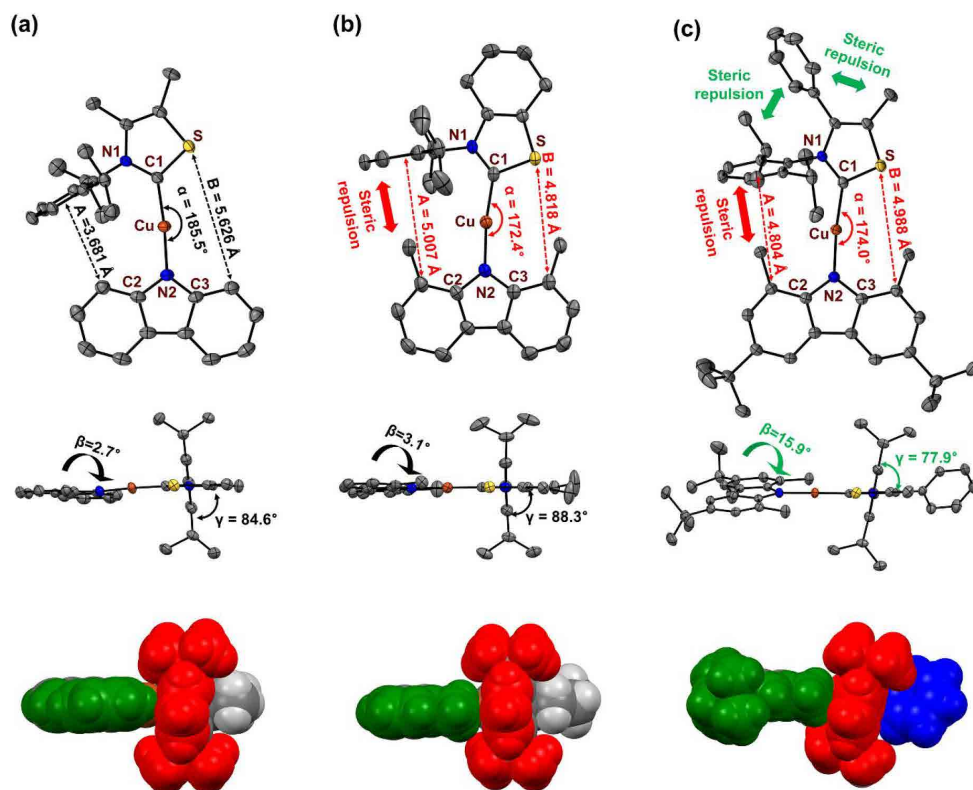
Figure 2. Top and side views of X-ray structures for **3** (a), **2** (b) and **8** (c). Ellipsoids are shown at 50% probability level. Hydrogen atoms are removed for clarity. Definitions: *A*, distance between the carbon at the carbazolide 1-position and the Dipp centroid; *B*, distance between the carbon at the carbazolide 8-position and carbene sulfur; α, N2−Cu−C1 angle; β, dihedral angle between carbazolide and carbene planes; γ, dihedral angle between Dipp and carbene planes. The bottom row shows space-filling representations of the molecules. Carbazolides are highlighted in green, Dipp rings are shown in red, and the phenyl ring at the 1,3-thiazol-2-ylidene is presented in blue.

based emitters, featuring a flat molecular geometry and reduced steric encumbrance of the carbene moiety. A simultaneous electroluminescence from the bluish green emitting monomer and orange-red emitting excimer allowed the preparation of efficient single-emitter WOLEDs, following the concept widely applied in the case of square-planar-coordinated Pt(II) complexes.[36,37] A vacuum-deposited WOLED featuring emitter **7** achieved an external quantum efficiency (EQE) of 16.5%, a maximum brightness exceeding 40000 cd/m^2, and a color rendering index (CRI) of over 80. The presented results not only expand the structural diversity of coinage-metal-based carbene−metal−amide emitters by introducing a novel carbene building block but also demonstrate a novel application direction for this emitter class. Namely, the compounds can be applied to develop highly cost effective WOLEDs for lighting applications, offering expense reduction through cheaper emitters and a simplified device architecture.

■ RESULTS AND DISCUSSION

Synthesis. *N*-2,6-Diisopropylphenyl (Dipp)-substituted 1,3-thiazol-3-ium perchlorate carbene precursors, modified with 4,5-dialkyl or 4-phenyl 5-methyl substituents (**9**, **11**, and **13**) were synthesized following literature procedures.[38] The preparation of two-coordinate carbene−Cu(I)−chloride complexes (**10**, **12**,

and **14**) was carried out by *in situ* generation of a free carbene in the presence of CuCl (Scheme 1). Amide ligands were introduced by reactions of the chloride complexes and various deprotonated carbazolides: carbazole (Cbz), 1,8-dimethylcarbazole (MeCbz), 3,6-di-*tert*-butylcarbazole (*t*BuCbz), and 3,6-di-*tert*-butyl-1,8-dimethylcarbazole (Me*t*BuCbz). The target complexes **1**−**6** were obtained as white crystalline powders, whereas **7** was a light green and **8** a yellow solid. The compounds, with the exception of **6**, show moderate to good solubility in various aprotic organic solvents such as toluene, chlorobenzene, dichloromethane, and THF. Complex **6** exhibits much lower solubility and is only sparingly soluble upon heating. In the crystalline form the compounds are stable and can be stored indefinitely in the air. The decomposition temperatures (thermogravimetric analysis, 5% weight loss) vary in the range of 275−300 °C (Figure S1). A slight increase in decomposition temperatures (by approximately 15 °C) was observed for 4-phenyl-substituted 1,3-thiazol-2-ylidene derivatives **5**−**8** in comparison to 4-alkyl-substituted compounds **1**−**4**. Due to their sufficient thermal stability the compounds can be processed with a vacuum deposition technique.

Compound Structures. Suitable single crystals for X-ray crystallographic analysis were successfully prepared for complexes **1**−**5** and **8** by layering solutions of THF with pentane.
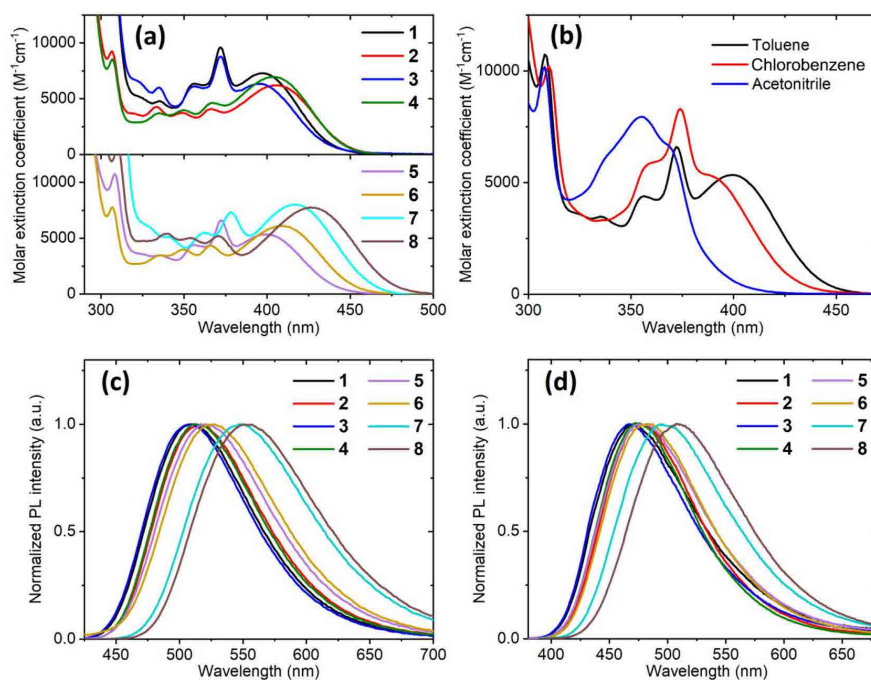
Figure 3. Photophysical properties of complexes **1−8**: (a) UV−vis absorption of complexes in toluene (10^{-5} M); (b) UV−vis absorption of **5** in toluene, chlorobenzene, and acetonitrile (10^{-5} M); (c) PL bands of complexes in deoxygenated toluene (10^{-5} M); (d) PL bands of complexes in doped PMMA films (5 wt %).

Crystal structures of the complexes and their key structural parameters are given in the Tables S1−S3 in the Supporting Information. While generally the complexes can be characterized with a near-linear geometry and an almost coplanar configuration between the carbazolide and carbene planes, the introduction of sterically demanding substituents at the 1,3-thiazol-2-ylidene (4-phenyl group) or at the carbazolide (1,8-dimethyl groups) causes various structural deformations (Figure 2). In the absence of steric strain the angle α ($\angle$N2−Cu−C1) is slightly bent ($\sim$5°) in the direction of the Dipp ring (Figure 2a). If methyl groups are introduced at the 1,8-positions of the carbazolide, a repulsion takes place between the carbazolide methyl and the Dipp ring, twisting α in the direction of the unhindered side of the carbene ligand (Figure 2b). This steric interaction also causes a slight elongation of the metal−ligand bonds. The distances N2−Cu and Cu−C1 vary in the ranges of 1.845−1.855 and 1.859−1.871 Å, respectively, when Cbz is present, while for the complexes hosting MeCbz or Met-BuCbz ligands these values reach 1.866−1.871 and 1.873−1.887 Å, respectively. When a phenyl group is attached at the 4-position of the thiazol-2-ylidene, an additional structural deformation is introduced (Figure 2c). Due to a steric overcrowding at the carbene, phenyl and Dipp rings form a fan-shaped geometrical motif. As a result the Dipp ring is pushed out of the perpendicular alignment with the 1,3-thiazol-2-ylidene plane. Since the ring plane of the attached carbazolide is conformationally constrained to reside between the two isopropyl groups of Dipp, the rotation of the former structural fragment additionally moves the carbazolide outside of the coplanar alignment with the carbene ligand. Consequently, for structures

5 and **8**, the dihedral angle between carbazolide and carbene planes (β) reaches a value of about 15°. On consideration of the previous points, the molecules in which both previously mentioned steric factors are present should possess a reduced conformational freedom in terms of the ability of the carbazolide, Dipp, and phenyl rings to rotate around the corresponding linking bonds. Due to steric pressure from both the carbene and carbazolide sides, the isopropyl groups of Dipp act as a conformational lock, as can be seen in the space-filling representation of molecule **8** (Figure 2c). We directly relate the low outlier solubility of complex **6** to the increased structural rigidity of the compound, as it enhances the compound's crystallization tendency. While a similar low solubility would be expected for **8**, it is presumably prevented by the *tert*-butyl groups at the carbazolide, which limit close contacts between the molecules upon solid-state packing. As will be discussed further, the introduction of the previously discussed steric factors have a direct influence on the photophysical properties of the compounds.

Electrochemistry. Cyclic voltammetry (CV) measurements for solutions in acetonitrile were carried out to gain insight into the electrochemical properties of the complexes (Figure S2 and Table S4). Redox potentials were calibrated against the potential of the Fc$^+$/Fc reference. The compounds exhibit similar electrochemical behavior with quasi-reversible oxidation and irreversible reduction waves. The measured reduction potentials (E_{red}) are almost identical (approximately −2.28 V) for the whole series and are assigned to the reduction of the thiazol-2-ylidene carbene ligand. The oxidation process, on the other hand, is related to the carbazolide fragment. A small cathodic

Table 1. Emissive Properties of Complexes 1−8 in Different Media

compound	λ_{max}, nm	Φ_{PL}	τ, μs	k_r,[a] 10^5 s^{-1}	k_{nr},[b] 10^5 s^{-1}	τ, μs (77 K)
			Toluene Solution			
1	511	0.37	0.58	6.4	10.9	
2	517	0.42	0.75	5.6	7.7	
3	507	0.41	0.36	11.4	16.4	
4	513	0.79	0.85	9.3	2.5	
5	521	0.39	0.46	8.5	13.3	
6	527	0.23	0.41	5.6	18.8	
7	549	0.73	0.72	10.1	3.6	
8	554	0.76	0.76	10.0	3.2	
			PMMA Films (5 wt %)			
1	471	0.74	2.6	2.8	1.0	187 (CT), 2536 (^{3}LE)
2	478	0.82	1.9	4.3	0.9	91 (CT), 2429 (^{3}LE)
3	467	0.68	1.9	3.6	1.6	199 (CT), 2919 (^{3}LE)
4	474	0.84	2.1	4.0	0.8	98 (CT), 2791 (^{3}LE)
5	479	0.71	2.1	3.4	1.4	167 (CT), 2367 (^{3}LE)
6	484	0.78	1.6	4.9	1.4	90(CT), 3046 (^{3}LE)
7	499	0.73	1.6	4.6	1.7	157 (CT), 2417 (^{3}LE)
8	509	0.86	1.2	7.2	1.2	117 (CT)

$^a k_r = \Phi_{PL}/\tau$. $^b k_{nr} = (1 - \Phi_{PL})/\tau$.

shift of the oxidation potential (E_{ox}) was observed with the introduction of electron-donating methyl and *tert*-butyl substituents. As a result, the E_{ox} value of the amide-centered process varies from 0.06 V for the Cbz-hosting complex **5** to −0.14 V for the Me*t*BuCbz-bearing complex **8**. In such a way the carbazolide ligand plays the main role in tuning the band gap (ΔE) values of the complexes. ΔE values vary in the range from 2.37 V for complex **3** to 2.13 V for complex **8**.

Photophysical Properties. UV−vis absorption spectra of the investigated compounds in toluene solutions are shown in Figure 3a. The structured absorption bands between 300 and 380 nm are assigned to local transitions of the carbazolide ligand.[25] The lowest-energy region features a single broad and structureless band, which undergoes a hypsochromic shift with increasing solvent polarity (Figure 3b). The solvatochromic response indicates a charge transfer (CT) nature of the transition. The negative solvatochromism of the CT bands is a distinctive characteristic of CMA complexes and is related to an inversion of the molecular dipole direction upon photo-excitation.[20,27,31] Similarly to other known CMAs, the CT transition is intense, with molar extinction coefficients ranging in the interval $(5.3-8.0) \times 10^3$ M^{-1} cm^{-1}. A direct correlation between CT absorption energies and electrochemically determined band gap values can be made (Figure S3). The absorption onset energy of **8** is red-shifted by 0.23 eV in comparison to **3**, which corresponds well with the decrease in the ΔE value (0.24 V). This provides further evidence for the proposed carbazolide−carbene interligand CT character of the lowest-energy absorption bands.

The results of photoluminescence (PL) measurements in toluene solutions and doped PMMA films (5 wt %) are shown in Table 1. In toluene the complexes exhibit bluish green to green emission (λ_{max} = 507−554 nm; Figure 3c). The broad and featureless profile of the PL bands indicates emission from CT excited states. The relative spectral placement of PL bands is consistent with the CV and UV−vis absorption measurements. A large variation in the measured Φ_{PL} values is evident, ranging from 0.23 to 0.76, and is related to substantial differences in the nonradiative decay rates (k_{nr}). A clear correlation with regard to the complex structure can be made, where the compounds

bearing 1,8-dimethyl carbazolide ligands (**2**, **4**, and **8**) show considerably lower k_{nr} values in comparison to the structural analogues with the Cbz fragment (**1**, **3**, and **5**). As recently demonstrated by Li et al.,[39] the rotation of the donor ligand in CMA complexes plays a significant role in the excited-state deactivation process and the limitation of this conformational motion can be applied to significantly increase the PL efficiency of the compounds. As was discussed previously, a steric interaction between Dipp and the methyl groups of carbazolide is evident in the obtained X-ray structures and a conformational constraint is expected to take place in the corresponding complex molecules, limiting the ability of the carbazolide plane to rotate around the Cu−N bond and thus substantially reducing k_{nr}. The only exception from the observed trend is compound **6**, which shows the highest k_{nr} value among the series, despite the presence of the MeCbz ligand. This is attributed to the poor solubility of the compound and the prevalence of an additional nonradiative relaxation pathway, related to an aggregate formation.

Upon doping in PMMA (5 wt % emitter concentration) the complexes experience a substantial PL efficiency increase (Φ_{PL} = 0.71−0.86). This can be related to a nonradiative decay rate decrease, which arises due to the suppression of conformational motions in the solid state. Additionally, PL bands exhibit a pronounced hypsochromic shift in comparison to solutions, an effect that can be attributed to a characteristic rigidochromism of the CMA complexes.[20] While a slight variation is observed between nonradiative rates, k_r values of the compounds differ substantially, in the range of $(2.8-7.2) \times 10^5$ s^{-1}. Again, a clear correlation with the complex structure can be made, where compounds with 1,8-dimethyl-substituted carbazolide ligands show a k_r increase by a factor of 1.1−1.6 in comparison to the structural analogues bearing a Cbz fragment. Notably, the highest radiative rates are observed for compounds **6** and **8**, which, in addition to s sterically demanding carbazole, feature a second steric factor—a phenyl substituent at the carbene ligand. These observations indicate that the limitation of the torsional motion of the carbazolide fragment has a positive effect on an enhancement in the k_r values.
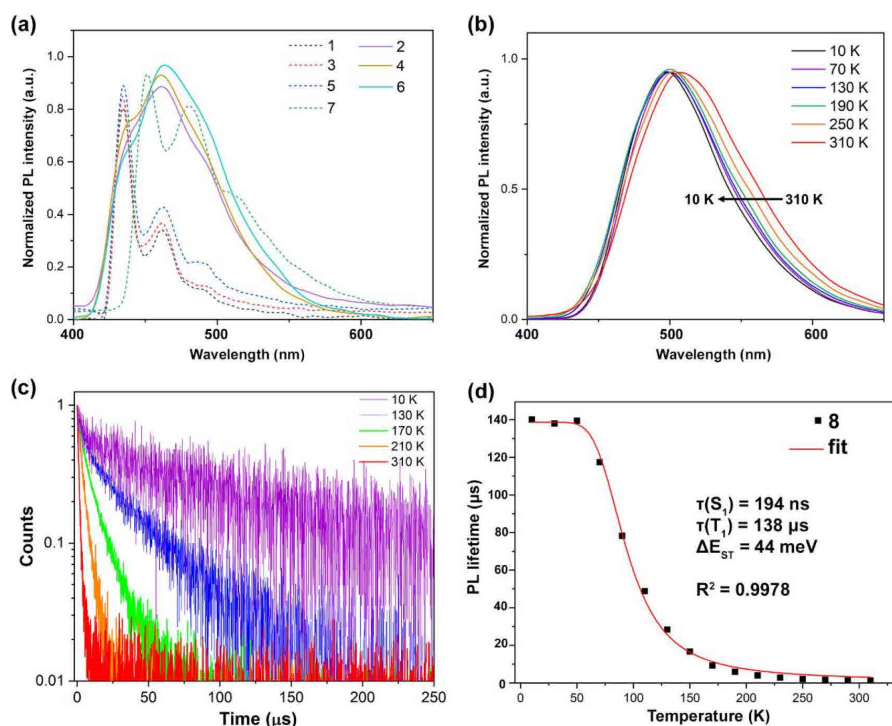
E

Figure 4. (a) PL bands of complexes **1−7** at 77 K in doped PMMA films (5 wt %). (b) PL bands of complex **8** at different temperatures. (c) PL decays of complex **8** at different temperatures. (d) PL lifetime and temperature correlation for complex **8** and fit against the Boltzmann relation. The parameters obtained from the fit, $\tau(S1)$, $\tau(T1)$, and ΔE_{ST} are provided.

In the examined PMMA films all of the compounds show monoexponential PL decay profiles (Figure S4). The lack of well-resolved prompt fluorescence and PL lifetimes in the range of a few microseconds indicates that the emission originates solely from the triplet states. This is a typical behavior for CMAs and is governed by large k_{ISC} values, which arise due to the significant SOC provided by the Cu atom.[21,40] Temperature-dependent measurements were performed for doped PMMA films to more deeply investigate the emissive mechanism of the compounds. PL spectra taken at 77 K (Figure 4a) indicate that for compounds **1−7** the emission bands transform, exhibiting a well-resolved vibrational substructure. The PL bands resemble the spectra of carbazole phosphorescence (Figure S5), demonstrating that the emission involves a relaxation from the local amide excited triplet (^3LE) states. The corresponding PL decays reveal a biexponential nature of the emission consisting of shorter ($\sim$90−200 μs)- and longer-lived ($\sim$2300−3000 μs) components (Figure S6). The CT and ^3LE nature of these two emissive processes is illustrated by time-resolved PL measurements (Figure S7). The prevalence of a ^3LE state emission under low-temperature conditions is characteristic among CMA emitters and is related to the destabilizing effect of the frozen host matrix, which shifts ^1CT and ^3CT levels above the ^3LE state, enabling the phosphorescence of the donor fragment.[20] A contrasting behavior is observed for compound **8**, which retains a structureless PL with CT character up to 10 K (Figure 3b). A blue shift of emission is evident, again illustrating the

destabilizing effect on the CT state in response to the gradually solidifying host.

The PL kinetics of complex **8** was examined in the temperature interval 310−10 K (Figure 4c,d). The emission decays retain a monoexponential nature throughout the examined temperature range. A significant increase in PL lifetime is observed upon cooling, from 1.2 μs at room temperature to 140 μs at 10 K, illustrating a thermal activation of the emissive process and providing evidence for the TADF mechanism. Similarly to other TADF-active copper complexes three distinct temperature regions can be resolved.[14,41] At room temperature the emission originates predominantly from the ^1CT state, enabled by the TADF process. Upon cooling the ^1CT emission is progressively accompanied by a phosphorescence from ^3CT. Finally, below 50 K the emission lifetime no longer shows a temperature dependence, thus indicatint the sole contribution of ^3CT phosphorescence. A fit against the modified Boltzmann equation[41] was performed to obtain the ΔE_{ST} energy gap of the complex, yielding a value of 44 meV, which is comparable to the values observed in other high-performance CMA emitters.[21,35]

Theoretical Calculations. In order to gain a deeper insight into the mechanism of the emissive processes and establish the impact of steric effects on the emissive properties, a DFT analysis was performed. Compounds **5** and **6** were chosen for the calculations to account for structures with Cbz and bulky MeCbz amide ligands. Despite some small differences in S_1 and T_1 excited state energies for the two studied systems, the orbital
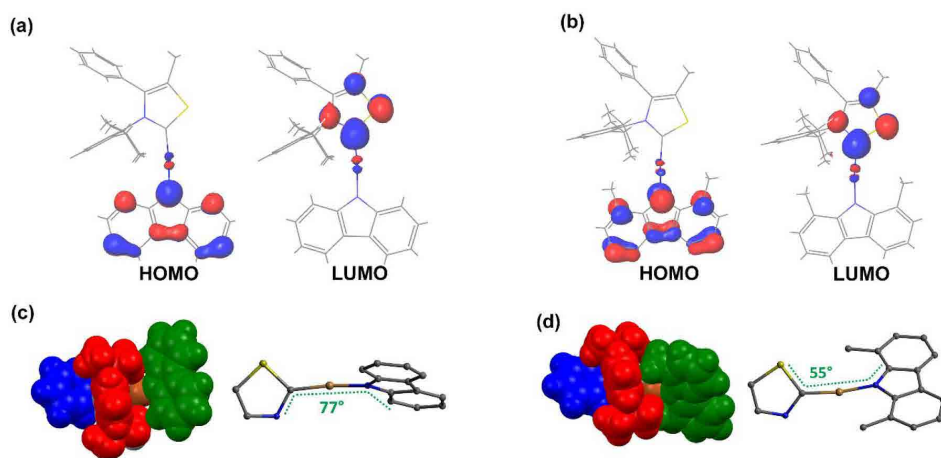
Figure 5. Frontier molecular orbitals of complexes **5** (a) and **6** (b) represented at the S_0 geometry of the compounds. Space-filling representations of the optimized S_1 state geometries and dihedral angles between the carbene and carbazolide planes for **5** (c) and **6** (d). Carbazolides are highlighted in green, Dipp rings are shown in red, and the phenyl ring at thiazol-2-ylidene is presented in blue.

Table 2. Selected Calculated Spectroscopic Parameters, Energetic Characteristics, and Rate Constants for Complexes 5 and 6

complex	ΔE_{ST}(ad), eV	λ_{abs}, nm ($f(S_0{\to}S_1)^a$)	λ_{fl}, nm ($f(S_0{\to}S_1)^a$)	λ_{phos}, nm ($f(S_0{\to}T_1)^a$)	$\langle S_1|\hat{H}_{so}|T_1\rangle$, cm^{-1}	$\lambda(S)$,^{b} eV	$\lambda(T)$,^{c} eV	k_p, s^{-1}	k_f, s^{-1}	k_{ISC}, s^{-1}	k_{RISC}, s^{-1}
5	0.25	409 (0.115)	512 (0.011)	551 (3×10^{-5})^a	42.5	0.07	0.19	2.2×10^3	2.7×10^6	8.9×10^{11}	1.2×10^6
6	0.23	418 (0.125)	538 (0.025)	568 (3×10^{-5})^a	44.0	0.08	0.15	2.4×10^3	5.8×10^6	8.5×10^{11}	1.5×10^7

^{a}The f value is given for the $S_0 \to T_1$ transition for the brightest triplet spin sublevel. ^{b}Reorganization energy associated with the RISC process. ^{c}Reorganization energy associated with the ISC process.

natures of these states are closely similar: the HOMO is localized on the carbazolide fragment, while the LUMO is situated on the carbene ring (Figure 5a,b). This allows us to assign the S_1 and T_1 states of complexes **5** and **6** to ligand to ligand charge-transfer (LLCT) excitations. The localization of HOMO and LUMO wave functions is found to be independent of the geometry (S_0, S_1, or T_1) at which they are computed. The HOMO and LUMO both contain some small contribution on the central Cu atom that affects the nonzero oscillator strength values for vertical $S_0 \to S_1$ absorption and $S_1 \to S_0$ emission, but that also leads to a considerably increased calculated adiabatic ΔE_{ST}(ad) gap (Table 2). In addition, our calculations reproduce well the small red shift in absorption and fluorescence maxima observed in experimental measurements of complex **6**.

In accordance with the X-ray structural data, the planes of the carbene and carbazolide ligand ring systems are practically coplanar at the optimized S_0 geometry. The same situation is observed for the T_1 state. However, at the S_1 geometry these planes tend to assume a perpendicular alignment (Figure 5c,d), as is commonly predicted among CMA emitters.[27,32,40] At the same time, the degrees of this structural transformation are not equal for the two complex molecules. While for compound **5** the dihedral angle between the carbene and carbazolide planes is 77°, in the case of **6** this value reaches only 55°. This can be directly attributed to the conformational locking effect, as during the rotation around the carbazolide−metal bond the methyls of the carbazolide in complex **6** cannot cross past the isopropyl groups of Dipp. Consequently, in the excited state the compound is bound to assume a semitwisted conformation.

This has a profound effect on the predicted photophysical properties of the compound. While at the S_0 geometry the oscillator strengths (f) of the $S_0 \to S_1$ transition are almost identical for the two complexes, at the optimized S_1 state a 2-fold increase in f is observed for **6**, resulting in an equal increase in the predicted fluorescence rate (k_f). In CMA emitters the extent of electronic coupling between the two fragments involved in the LLCT process is directly dependent on the dihedral angle between them, where f is maximum at the coplanar configuration but practically zero at the perpendicular alignment.[40,42]

Combining the calculated values of adiabatic singlet−triplet splittings, reorganization energy values, and computed SOC matrix elements (SOCMEs) within the semiclassical Marcus theory expression,[43] we have estimated the rates of ISC (k_{ISC}) to be at the levels of 8.9×10^{11} and 8.5×10^{11} s^{-1} for complexes **5** and **6**, respectively. Using the calculated ΔE_{ST}(ad) gap, we predict the corresponding k_{RISC} values to be equal to 1.2×10^6 and 1.5×10^7 s^{-1}, respectively. The photophysical pattern of the delayed fluorescence phenomenon in the complexes can be characterized accordingly: the rate of ISC is much faster than the rate of prompt fluorescence k_f, and thus prompt fluorescence is almost completely quenched by the ISC. Consequently, the rate-determining step of the emissive TADF relaxation pathway is the reverse intersystem crossing rate. When the experimental observations are taken into account, where the radiative rate of complex **6** is larger by a factor of 1.4 than for **5**, this difference can be attributed to a combination of increased oscillator strength and k_{RISC} parameters in the case of compound **6**. The phosphorescence of the studied complexes is predicted to be a
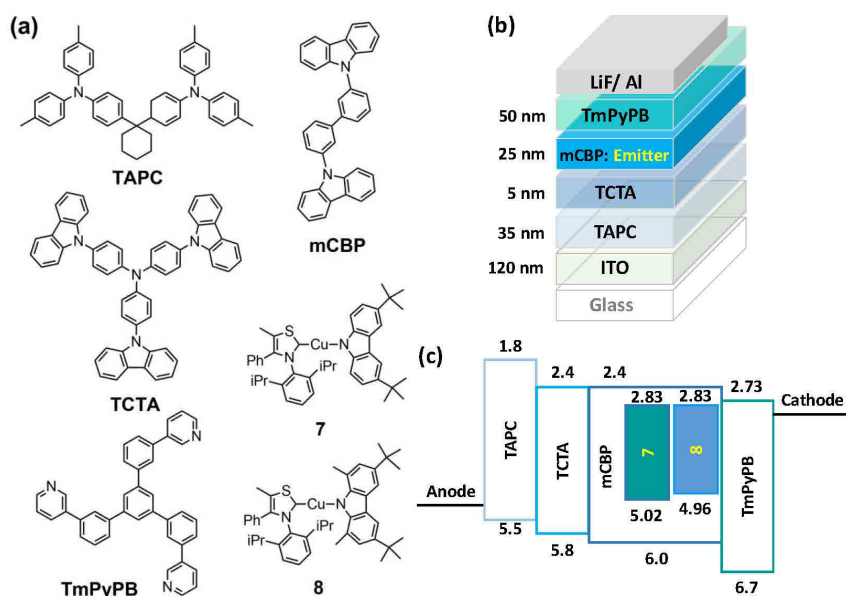
Figure 6. (a) Structural drawings of the materials used in the OLEDs. (b) Schematic structures of the fabricated OLEDs with different emitters. (c) Energy level diagram of the devices.

process that is too slow ($k_p \approx 2 \times 10^3$ s^{-1}) to compete with the fluorescence channel under room-temperature conditions. Only one individual sublevel of T$_1$ state demonstrates the ability to phosphorescence with a reasonable radiative lifetime (152 and 140 μs for **5** and **6**, respectively), while the two other spin sublevels are degenerate and demonstrate 2 orders of magnitude longer radiative lifetimes. The calculated values of ZFS between these dark spin sublevels and the upper bright spin substate are 2.9 and 5.7 cm^{-1} for **5** and **6**, respectively.

Electroluminescence Properties. To investigate the electroluminescent (EL) applications of thiazoline-based Cu(I) complexes **7** and **8**, we fabricated OLEDs to examine the carrier balance conditions using several potential hosts with adequate triplet energy gaps, including 4,4′-N,N′-dicarbazole-biphenyl (CBP),[44] 3,3′-bis(9H-carbazol-9-yl)-1,1′-biphenyl (mCBP),[45] 3-bis(9-carbazolyl)benzene (mCP),[46] and bis(2-(diphenylphosphino)phenyl)ether oxide (DPEPO).[47] Furthermore, the hole-transporting 1,1-bis[(di-4-tolylamino)phenyl]-cyclohexane (TAPC) and 4,4′,4″-tris(N-carbazolyl)-triphenylamine (TCTA) were combined to form a stepwise hole-transport layer (HTL), aiming to promote a smooth hole injection from the HTL into the emitting layer (EML).[48] On the other hand, 1,3,5-tris[(3-pyridyl)-phen-3-yl]benzene (TmPyPB) was used as the electron transport layer (ETL),[49] due to its excellent carrier transport capability of 1×10^{-3} cm^2/(V s) and a wide triplet energy gap (E_T) of 2.78 eV. The device with mCBP outperformed those with the other host materials. Furthermore, given the different inherent properties of the target compounds, we carefully regulated the thicknesses of each layer to optimize the EL efficiency. Consequently, two series of devices (i.e., compound **7** for device A and compound **8** for device B) were fabricated with the following generalized architecture: ITO/TAPC (35 nm)/TCTA (5 nm)/mCBP doped with a certain weight percent of compound **7** or **8** (25 nm)/TmPyPB (50 nm)/LiF (1.5 nm)/Al (150 nm), where the

ITO and aluminum were respectively used as the anode and cathode. The doping concentrations used were set to 1, 5, 10, and 20 wt % to examine the influence of the emitter spatial distance and device carrier balance. The materials used, schematic architectures, and energy level diagrams of the fabricated OLEDs are given in Figure 6.

Figure 7 shows the EL characteristics of the device series A, featuring different doping concentrations. The corresponding numerical data collected from the figures are summarized in Table 3. As shown in Figure 7a, all tested devices regardless of emitter concentration display two distinct emission bands in the EL spectra. It is notable that the tested devices presented a similar behavior, that is, two-peak spectral profiles, with all screened host materials. The EL spectra of the tested devices with different host−guest systems are shown in Figure S8. As indicated, the emission peak at around 600 nm was akin to those using mCBP as a host. Accordingly, we can rule out the host material being responsible for the origin of the peak at around 590−600 nm. In addition, the slight red shift in the emission peak at around 495 nm with higher doping concentrations is likely due to solvation effects. With an increase in the doping concentration the relative intensity ratio between the emission peaks around 495 and 590 nm increased in the favor of the latter. Consequently, as the doping concentration is increased, the EL color changes from bluish green to warm white. The peak at around 495 nm was recognized as compound **7**'s TADF emission, while the 590 nm peak was preliminarily speculated to be an excimer emission originating from compound **7**'s dimer.[50,51] The observed emission with a broad spectral profile benefits the design of high-quality WOLEDs with high color rendering indices (CRI). With the EL spectrum of device A3 measured at a luminance of 1000 cd/m^2 as an example, the CRI and correlated color temperature (CCT) were respectively estimated to be 83.2 and 4240 K, demonstrating compound **7**'s potential for the construction of a high-quality lighting source.[52]
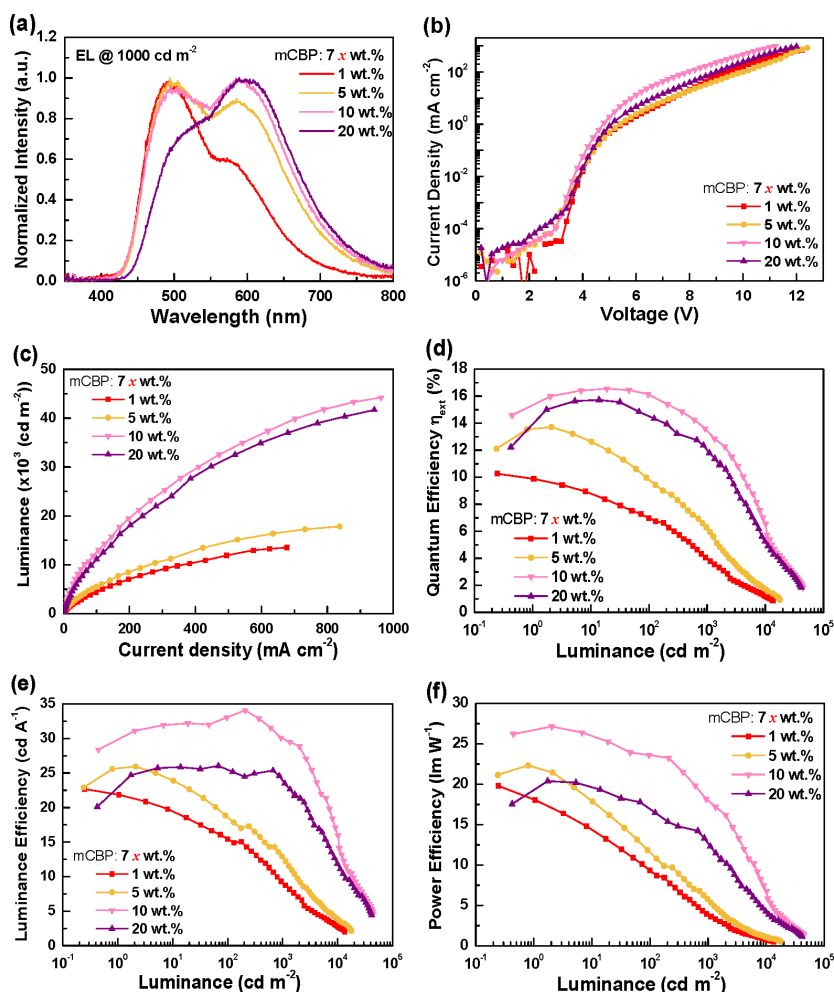
Figure 7. (a) Normalized EL spectra at a luminance of 10^3 cd m^{-2}, (b) current density−voltage (J−V) characteristics, (c) luminance−current density (L−J) characteristics, (d) external quantum efficiency vs luminance, (e) luminance efficiency vs luminance, and (f) power efficiency vs luminance for devices A1−A4.

The PL spectra of the doped films and the corresponding lifetime measurements were obtained and are discussed later, in order to clarify the origin of the emission.

Figure 7b,c respectively show the current density−voltage (J−V) curves and luminance−current density (L−J) curves. As indicated, device A3 (10 wt %) possesses the highest current density and luminance of all the devices. The higher current density suggests the adequate carrier transport capability of **7**. The device's turn-on voltage (defined at a luminance of 1 cd/m^2) was also slightly decreased from 3.8 to 3.5 V as the doping concentration increased from 1 to 10 wt %. However, excessive doping concentrations might negatively affect the carrier transport characteristics of the EML. The EL spectrum of device A3 presents a dual emission consisting of a relatively weaker **7** emission and a stronger excimer emission. Therefore, the higher turn-on voltage might also be the result of the slightly inferior excimer efficiency. On the other hand, the EL spectra of

all the devices presented emissions originating from compound **7**, indicating that in all cases excitons formed in the EML and energy were effectively transferred from the host to the emitter. Hence, in comparison to the luminance at the same current density, we speculate that the higher luminance observed in device A3 might result from the relatively better carrier balance and the higher current density. When the doping concentrations exceeded 10 wt %, the carrier balance was gradually destroyed, leading to a reduction in device luminance. The maximum luminance of device A3 measured at 11.2 V reached 44215 cd/m^2, while that of device A4 with a higher doping concentration of 20 wt % was lowered to 41695 cd/m^2.

Similarly, the efficiency curves shown in Figures 7d−f indicate that device A3 outperformed the devices using other doping concentrations. The maximum external quantum efficiency (EQE) of device A3 reached 16.5%. Clearly, the peak efficiency of the tested devices rose with doping concentrations of 1−10 wt

Table 3. EL Characteristics of Tested Devices with Different Emitters

	device							
	host/emitter							
	mCBP/**7**				mCBP/**8**			
	A1	A2	A3	A4	B1	B2	B3	B4
doping concentration (wt %)	1	5	10	20	1	5	10	20
external quantum efficiency (%)	10.3	13.7	16.5	15.7	12.9	12.2	9.2	5.9
a								
b	7.0	9.8	16.1	14.6	10.6	11.6	9.1	5.8
luminance efficiency (cd A^{-1})								
a	22.7	25.9	34.1	26.0	31.5	31.9	21.7	14.8
b	15.4	18.6	33.1	25.5	25.8	30.4	21.6	13.4
power efficiency (lm W^{-1})								
a	19.8	22.3	27.1	20.2	25.4	26.0	15.5	9.4
b	9.3	11.6	23.6	17.0	17.0	20.4	13.2	8.6
V_{on} (V)^c	3.8	3.6	3.5	3.7	3.7	3.6	3.8	3.8
max luminance (cd m^{-2}) [V]	13542 [12.2]	17839 [12.4]	44215 [11.2]	41695 [12.0]	35947 [11.2]	42773 [11.2]	36478 [11.6]	37183 [12.4]
CIE1931 coordinates^b	(0.30, 0.41)	(0.36, 0.42)	(0.38, 0.42)	(0.43,0.46)	(0.25,0.42)	(0.26,0.45)	(0.30, 0.45)	(0.36, 0.48)

^{a}Maximum efficiency; ^{b}Measured at 10^2 cd m^{-2}. ^{c}Turn-on voltage measured at 1 cd m^{-2}.
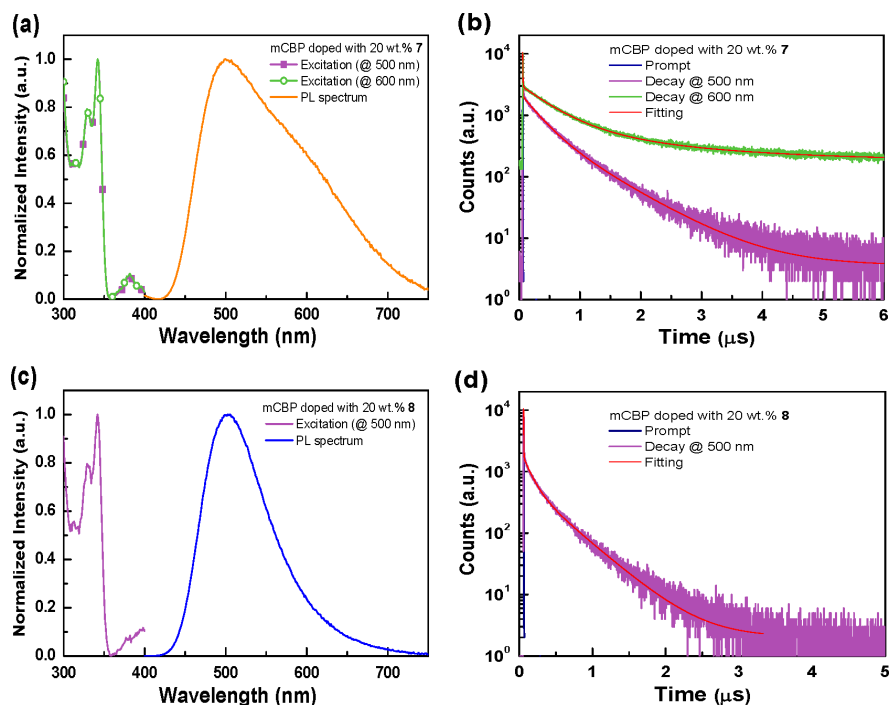

Figure 8. Photophysical properties of 20 wt % **7** doped in an mCBP host: (a) excitation and PL spectra; (b) the transient decay. Photophysical properties of 20 wt % **8** doped in an mCBP host: (c) excitation and PL spectra; (d) the transient decay.

% and then decreased when the doping was increased to 20 wt %, displaying an optimum range of the doping concentrations for compound **7**. At a higher practical luminance of 10^2 cd/m^2, the EQE values of devices A1–A4 presented efficiency drops of 30.8%, 28.5%, 2.4%, and 7.0% of their respective peak values in comparison to those recorded at 10^2 cd/m^2, respectively. The mitigated efficiency rolloff obtained in devices A3 and A4 might be attributed to the extended exciton formation zone with a stable carrier balance, thus mitigating triplet–triplet annihilation

(TTA).[53] On closer investigation of the EL spectra (see Figure S9 in the Supporting Information), all tested devices revealed TADF and excimer dual emissions at low operating voltages. The excimer emission peak gradually weakened as the voltage increased. Notably, the high efficiency of device A3 was due to both the TADF and excimer, illustrating the adequate efficiency of the excimer.

The device architecture of series B (compound **8**) was the same as that of series A except for the emitter, as shown in Figure

6. The EL characteristics and the corresponding numeric data of the series B devices are presented in Figure S10 and S11 and Table 3. Figure S10a shows the EL spectra of the devices with different doping concentrations of compound 8 recorded at 1000 cd/m^2. The lack of additional emission resulting from the host or carrier transport materials indicated an effective carrier recombination and excellent exciton confinement. A scenario similar to that for series A was observed for series B, where the excimer emission increased with the doping concentration. Nevertheless, the EL spectra revealed that the excimer emission was negligible when the doping concentrations were less than or equal to 5 wt %. In comparison to series A, the generalized excimer was considerably weaker in the series B devices, indicating that compound 8 with methyl groups at the 1,8-positions of carbazolide provides a steric repulsion to avoid molecular stacking.

Figure S10b shows the $J-V$ curves. As indicated, the tested devices exhibited similar current densities, indicating that the doping concentrations did not significantly affect the carrier transport. Nevertheless, the turn-on voltages of the series B devices gradually decreased to 3.6 V when the doping concentrations increased to 5 wt %. The turn-on voltages then increased to 3.8 V when doping concentrations exceeded 5 wt %, similar to the case for the series A devices. As shown in Figure S10c, devices B1, B3, and B4 possessed similar maximum luminances of around 36000–37000 cd/m^2 while a relatively higher value of 42773 cd/m^2 was obtained in device B2.

In contrast to the efficiency parameters observed in series A, the maximum efficiency was achieved in device B1 with the smallest doping amount of compound 8 (i.e., 1 wt %). With reference to Figures S10d−f, the optimized doping range of compound 8 is from 1 to 5 wt %. As indicated, the efficiencies of the series B devices were slightly inferior to those of series A. The respective peak efficiencies of devices B1−B4 reached 12.9%, 12.2%, 9.2%, and 5.9%. At a higher practical luminance of 10^2 cd/m^2, the devices B1−B4 represented efficiency drops of 17.8%, 4.9%, 1.1%, and 1.7% of their respective peak values in comparison to those recorded at 10^2 cd/m^2, respectively. In comparison to the series A devices, series B exhibited significantly mitigated efficiency rolloff, possibly due to the superior obstruction in space, inhibiting TTA. Overall, device doping concentrations with compounds 7 and 8 could be carefully adjusted to regulate the carrier balance and emission, tailoring the devices to meet specific application needs: single-color or white emission.

A comparison between the investigated CMA compounds and the previously reported top-performing structures in the terms of the device performance is outlined in Table S5.[19,20,23,25,26,28,33,54] While compound 7 does not show the highest EL efficiency, it is the only emitter that generates dual emission with tunable intensity via varying the doping concentration, realizing white-light emission with a single emitter. In addition, the maximum luminance of the white-emitting device with 7 can be as high as 44215 cd/m^2, indicating that the device has an excellent potential for lighting applications.

Excimer Characterization. To further corroborate the suspected excimer emission observed in the devices, two mCBP-hosted films with 20 wt % 7 or 8 content were fabricated by vacuum deposition to study the photodynamics in the solid state. Parts a and c of Figure 8 respectively show the excitation and photoluminescence (PL) spectra of films FA (compound 7) and FB (compound 8). The PL spectrum of film FA exhibits

dual-emission peaks at around 500 and 600 nm, akin to the EL spectrum of device A4. Thus, we separately monitored the excitation spectra at 500 and 600 nm, aiming to distinguish the origins of the two peaks. Nevertheless, both excitation spectra are nearly identical, indicating the same structural origin of the two emissive processes. In other words, the newly formed peak at 600 nm retains the excitation profile of compound 7 and thus can be reasonably recognized as the excimer emission.[55] Parts b and d of Figure 8 respectively show the time-resolved photoluminescence (TRPL) measurements of films FA and FB. The TRPL measurement of film FA was also monitored at 500 and 600 nm. Interestingly, in comparison to measurements in diluted PMMA films, where the decay was predominantly monoexponential, the curves present a three-component decay, including a nanosecond-scale prompt term and two micro-second-scale delayed components. The fitting results are collected in Table S6. The prompt component of the lifetime (t_p) monitored at 500 nm was 2.74 ns, while the two delayed terms (t_d) were evaluated as 0.282 and 0.754 μs. For the 600 nm case, the respective t_p and t_d values were estimated to be 3.85 ns, 0.497 μs, and 1.875 μs. Although the measurements at 500 and 600 nm cannot strictly distinguish between monomer and excimer emissions, the significant difference in PL lifetimes affirm that the emission at each respective wavelength originates from a separate excited entity.[55] In contrast, the PL spectrum of film FB presents only a single peak (cf. Figure 8c), indicating a weaker excimer formation by photopumping. The lifetimes t_p and t_d of film FB monitored at 500 nm were respectively estimated to be 2.28 ns, 0.111 μs, and 0.424 μs. Clearly, the delayed terms (t_d) of 8 were shorter than those of 7, which facilitates the fast relaxation of the excited state, thereby reducing the efficiency rolloff, as seen for the series B devices.

Only a few reports have attributed excimer formation to Cu(I)-based CMAs or closely related structures, where this phenomenon was observed in either doped films or solutions.[20,56] Practical EL from excimers, however, until now has not been reported among the class of Cu organometallic complexes. From a structural point of view, the more pronounced excimer formation tendency of thiazoline-based CMAs seems logical, as the lack of a bulky substituent at the sulfur atom differentiates this structure from its counterparts, which feature two isolating groups at each side of the carbene-forming carbon. In such way face to face close contacts are more likely to take place.

The relationship between the degree of steric encumbrance of the CMA emitter and its excimer formation tendency can be clearly seen among the investigated series of compounds. PL measurements of crystalline powders of complexes 1−4, 7, and 8 (samples 5 and 6 were not emissive) are given in Figure 9a. The PL band placement of the crystalline samples in almost all cases is close to that observed in solution or the diluted PMMA films (Figure 3c,d). The only exception is the benzene-grown crystal polymorph of complex 3, which shows a substantial emission band red shift with a maximum at 570 nm. Subsequent PL measurements in highly concentrated (50 wt %) PMMA films (Figure 9b) relate this red-shifted band to the excimer emission, as the sample containing complex 3 exhibits two PL bands, a weaker band at approximately 500 nm, attributed to monomer emission, and a stronger band at 560 nm, originating from an exciplex. As in the case of the previously examined mCBP-hosted samples, the PL lifetime of the red-shifted emission band (560 nm) is about 2-fold longer than that for the emission at 500 nm (Figure S12). In contrast, complex 4, which features a
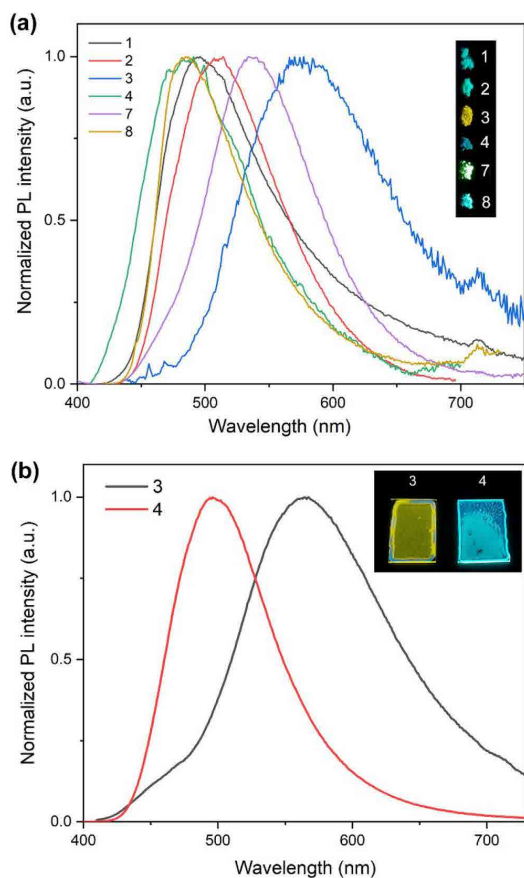
Figure 9. PL bands of crystalline powders of complexes **1**−**4**, **7**, and **8** (a). PL bands of PMMA doped (50 wt %) films containing emitters **3** and **4** (b). Insets show photographs of the corresponding UV (365 nm)-irradiated samples.

bulkier 1,8-dimethylcarbazole donor fragment, exhibits only monomer emission. Such a relation can be seen for the rest of the compound series (Figure S13), where the introduction of bulky substituents at the carbazolide leads to the disappearance of the excimer emission band (see PL bands **1** vs **2** and **5** vs **6**). This clearly illustrates that the steric shielding of the complex surface obstructs the formation of emissive dimers. In such a context it is not surprising that the most pronounced excimer formation is observed for complex **3**, which, in addition to the unsubstituted carbazole donor, is composed of a 1,3-thiazoline acceptor with the smallest methyl substituents.

Neither crystals nor concentrated PMMA films of compounds **7** and **8** show notable signs of excimer emission. This can be explained by the more pronounced steric shielding of the molecules, due to the presence of the massive *tert*-butyl groups at the carbazolide moiety. In contrast to the previously discussed vacuum-deposited samples, no excimer formation was evident in solution-processed mCBP films of **7** (20 wt %) (Figure S14). On this basis, we speculate that the excimer formation for **7** and **8** is aided by vacuum deposition, which may facilitate specific packing patterns and enable formation of emissive dimers

despite the presence of the bulkier substituents. The tendency of formation of alternatively emissive polymorphs among the investigated emitter class is demonstrated in the case of complex **3**, for which THF/pentane-grown crystals show a PL band with a maximum at 500 nm, characteristic of monomer emission (Figure S15), in contrast to the previously discussed excimer-forming polymorph obtained from benzene (Figure 9a).

The planar geometry and reduced steric encumbrance relate the structures of the studied thiazoline CMA emitters to square-planar-coordinated Pt(II) complexes, a compound class that is well-known for its excimer formation ability.[57] Such a property of Pt(II) emitters is frequently exploited to construct excimer-based single-emitter WOLEDs.[36,37,58−60] It is evident that the performance level of our presented device A3 is comparable to that of the aforementioned examples. In addition to the use of much cheaper Cu metal atoms, thiazaoline-based CMA emitters provide a potential benefit in the form of improved device CRI, as EL originates from wide overlapping emission bands of the monomer and excimer, whereas monomer emission in the case of Pt(II) complexes often has a narrower and structured emission band profile.

CONCLUSIONS

We have demonstrated that 1,3-thiazoline carbenes can be successfully used as building blocks for efficient CMAs, yielding emitters with Φ_{PL} values of up to 0.86. With the structural modification of the attached carbazolide the emission color of the compounds can be varied from bluish green to green. Similarly to other known CMA emitters the emissive mechanism is attributed to the TADF process. The radiative rates of the compounds are relatively high and vary in the range of $(2.8−7.2) \times 10^5$ s^{-1}. X-ray structural analysis and DFT modeling relate the k_r increase among the investigated structural derivatives to the conformational locking of the carbazolide, which increases the coplanarity between the constituting fragments involved in the charge transfer process. This effect can be induced by a simultaneous attachment of bulky substituents at the carbene and carbazolide ring systems. The compounds possess a sufficient chemical stability for vacuum deposition and subsequent OLED integration. Together with the known structures featuring CAAC or MAC carbenes, this makes 1,3-thiazoline-based emitters the third example of copper-containing CMAs with a demonstrated OLED use.

For the first time among the compound class of organo-metallic copper complexes we have observed an efficient excimer electroluminescence. From a structural point of view this can be attributed to the reduced steric encumbrance of the 1,3-thiazoline-based complex surface, which allows closer solid-state molecular packing in comparison to the previously investigated CMA designs. At an optimal emitter concentration the devices based on emitter **7** showed a dual emission from monomers and excimers, producing single-emitter white color emission, with an EQE value of up to 16.5%. With the attained performance level being comparable to that of Pt(II) complex-based single-emitter WOLEDs, these results illustrate the prospects of copper-based materials as highly cost effective emitters for lighting devices.

EXPERIMENTAL SECTION

Synthesis and Characterization. All procedures involving the synthesis and purification of N-heterocyclic carbenes (NHC) derivatives were carried out under an inert atmosphere using Schlenk techniques. Unless specified otherwise, the materials and solvents used were purchased from commercial suppliers. Solvents (hexane, pentane,

chlorobenzene, benzene, toluene, and acetonitrile) were distilled over CaH_2 and stored over molecular sieves (4 Å). Dry, air-free THF was distilled over K/benzophenone under N_2 prior to use. $CDCl_3$ was distilled over K_2CO_3 and stored over molecular sieves (4 Å). The starting compounds 9, 11, and 13[38] and 1,8-dimethylcarbazole[61] were prepared by following the procedures described in the literature. NMR spectra were obtained on a Bruker Avance 300 MHz spectrometer using solvent residual signals as an internal reference ($CDCl_3$, ^1H δ 7.26 and ^{13}C δ 77.16; C_6D_6, ^1H δ 7.16 and ^{13}C δ 128.06). Elemental analysis was performed using a Costech Instruments ECS 4010 CHNS-O Elemental Combustion System. Decomposition temperatures were obtained using a PerkinElmer STA 6000 thermal analyzer.

General Method for Synthesis of Complexes 1−8. The synthesis and purification of complexes **1−5**, **7**, and **8** was carried out using dry, deoxygenated solvents (THF, hexane, and benzene). The carbazole (1,8-dimethylcarbazole, 3,6-di-*tert*-butylcarbazole, or 3,6-di-*tert*-butyl-1,8-dimethylcarbazole) and KOtBu were dissolved in THF and stirred for 30 min under an argon atmosphere. Then a THF solution of NHC-Cu-Cl was added dropwise via a syringe to the solution of the carbazole amide. The resulting mixture was stirred for 3 h at room temperature under an argon atmosphere and then filtered through a pad of Celite into hexane (approximately 200 mL) to precipitate the product. The resulting mixture was filtered to afford the product as a solid. Complexes **1−5** were recrystallized from benzene.

Compound 1. A solution of carbazole (0.161 g, 0.96 mmol) and KOtBu (0.108 g, 0.96 mmol) in THF (5 mL) and a solution of **10** (0.350 g, 0.88 mmol) in THF (13 mL) were used. Yield: 0.25 g (54%), white solid (after recrystallization from benzene). Crystals suitable for X-ray diffraction analysis were obtained by layering a solution of THF with pentane. ^1H NMR δ(H) ($CDCl_3$, 300 MHz): 8.00 (d, J = 7.6 Hz, 2H), 7.66 (t, J = 7.8 Hz, 1H), 7.43 (d, J = 7.8 Hz, 2H), 7.14 (t, J = 7.5 Hz, 2H), 7.01−6.86 (m, 4H), 2.92−2.83 (m, 2H), 2.32−2.20 (m, 4H), 1.96−1.80 (m, 4H), 1.28−1.17 (m, 12H). ^{13}C NMR δ(C) ($CDCl_3$, 75.47 MHz): 202.74, 150.12, 145.24, 143.91, 136.95, 133.10, 130.93, 125.07, 124.36, 123.39, 119.56, 115.39, 114.57, 28.75, 25.37, 24.32, 23.87, 23.37, 22.23, 21.71. Anal. Calcd for $C_{31}H_{33}CuN_2S$: C, 70.36; H, 6.29; Cu, 12.01; N, 5.29; S, 6.06. Found: C, 70.49; H, 6.36; N, 5.36.

Compound 2. A solution of 1,8-dimethylcarbazole (0.120 g, 0.61 mmol) and KOtBu (0.069 g, 0.61 mmol) in THF (3 mL) and a solution of **10** (0.222 g, 0.56 mmol) in THF (8 mL) were used. Yield: 0.21 g (68%), white solid (after recrystallization from benzene). Crystals suitable for X-ray diffraction analysis were obtained by layering a solution of THF with pentane. ^1H NMR δ(H) ($CDCl_3$, 300 MHz): 7.95 (d, J = 7.5 Hz, 2H), 7.60 (t, J = 7.8 Hz, 1H), 7.38 (d, J = 7.8 Hz, 2H), 7.10−7.03 (m, 2H), 2.90−2.82 (m, 2H), 2.58 (s, 6H), 2.36−2.21 (m, 4H), 1.95−1.79 (m, 4H), 1.28−1.14 (m, 12H). ^{13}C NMR δ(C) ($CDCl_3$, 75.47 MHz): 148.92, 144.72, 144.25, 136.87, 133.05, 130.98, 125.17, 124.88, 124.48, 122.01, 117.55, 115.60, 28.69, 25.26, 24.60, 23.84, 23.58, 22.28, 21.76, 21.15. Anal. Calcd for $C_{33}H_{37}CuN_2S$: C, 71.12; H, 6.69; Cu, 11.40; N, 5.03; S, 5.75. Found: C, 71.19; H, 6.79; N, 5.07.

Compound 3. A solution of carbazole (0.172 g, 1.03 mmol) and KOtBu (0.116 g, 1.03 mmol) in THF (5 mL) and a solution of **12** (0.350 g, 0.94 mmol) in THF (20 mL) were used Yield: 0.14 g (30%), white solid (after recrystallization from benzene). Crystals suitable for X-ray diffraction analysis were obtained by layering a solution of THF with pentane. ^1H NMR δ(H) ($CDCl_3$, 300 MHz): 8.03 (d, J = 7.6 Hz, 2H), 7.69 (t, J = 7.7 Hz, 1H), 7.46 (d, J = 7.8 Hz, 2H), 7.17 (t, J = 7.5 Hz, 2H), 7.02−6.99 (m, 4H), 2.42 (s, 3H), 2.27 (hept, J = 6.8 Hz, 2H), 2.04 (s, 3H), 1.31−1.17 (m, 12H). ^{13}C NMR δ(C) ($CDCl_3$, 75.47 MHz): 202.58, 150.12, 145.18, 141.41, 138.06, 130.96, 130.67, 125.15, 124.35, 123.38, 119.55, 115.39, 114.58, 28.72, 25.35, 23.37, 12.62, 12.25. Anal. Calcd for $C_{29}H_{31}CuN_2S$: C, 69.22; H, 6.21; Cu, 12.63; N, 5.57; S, 6.37. Found: C, 69.47; H, 6.17; N, 5.74.

Compound 4. A solution of 1,8-dimethylcarbazole (0.202 g, 1.03 mmol) and KOtBu (0.116 g, 1.03 mmol) in THF (5 mL) and a solution of **12** (0.350 g, 0.94 mmol) in THF (20 mL) were used. Yield: 0.20 g (40%), white solid (after recrystallization from benzene). Crystals suitable for X-ray diffraction analysis were obtained by layering a solution of THF with pentane. ^1H NMR δ(H) ($CDCl_3$, 300 MHz):

7.96 (d, J = 7.6 Hz, 2H), 7.61 (t, J = 7.8 Hz, 1H), 7.39 (d, J = 7.8 Hz, 2H), 7.12−7.05 (m, 2H), 7.01−6.93 (m, 2H), 2.57 (s, 6H), 2.45 (s, 3H), 2.28 (hept, J = 6.5 Hz, 2H), 2.02 (s, 3H), 1.27−1.17 (m, 12H). ^{13}C NMR δ(C) ($CDCl_3$, 75.47 MHz): 148.91, 144.66, 141.72, 137.94, 131.01, 130.58, 125.23, 124.86, 124.48, 122.01, 117.54, 115.59, 28.66, 25.23, 23.55, 21.13, 12.61, 12.54. Anal. Calcd for $C_{31}H_{35}CuN_2S$: C, 70.09; H, 6.64; Cu, 11.96; N, 5.27; S, 6.04. Found: C, 70.16; H, 6.68; N, 5.31.

Compound 5. A solution of carbazole (0.148 g, 0.88 mmol) and KOtBu (0.099 g, 0.88 mmol) in THF (5 mL) and a solution of **14** (0.350 g, 0.81 mmol) in THF (15 mL) were used. Yield: 0.26 g (57%), white solid (after recrystallization from benzene). Crystals suitable for X-ray diffraction analysis were obtained by layering a solution of THF with pentane. ^1H NMR δ(H) ($CDCl_3$, 300 MHz): 8.02 (d, J = 7.6 Hz, 2H), 7.54 (t, J = 7.8 Hz, 1H), 7.41−7.23 (m, 5H), 7.21−7.05 (m, 4H), 7.03−6.89 (m, 4H), 2.50−2.36 (m, 5H), 1.33 (d, J = 6.7 Hz, 6H), 1.10 (d, J = 6.8 Hz, 6H). ^{13}C NMR δ(C) ($CDCl_3$, 75.47 MHz): 203.53, 150.09, 146.31, 145.25, 138.34, 133.26, 130.78, 130.29, 129.90, 128.66, 128.04, 124.69, 124.37, 123.39, 119.57, 115.40, 114.59, 28.98, 26.37, 22.63, 13.23. Anal. Calcd for $C_{34}H_{33}CuN_2S$: C, 72.24; H, 5.88; Cu, 11.24; N, 4.96; S, 5.67. Found: C, 72.24; H, 6.04; N, 5.04.

Compound 6. 1,8-Dimethylcarbazole (0.248 g, 1.27 mmol) and KOtBu (0.142 g, 1.27 mmol) were dissolved in a dry THF (15 mL) and stirred for 30 min under an argon atmosphere. Then a THF (40 mL) solution of **14** (0.50 g, 1.15 mmol) was added dropwise via syringe to a solution of carbazole amide. After approximately 5 min precipitation of the product was observed. The resulting mixture was stirred for 3 h at room temperature under an argon atmosphere and then filtered to offer the crude product as a solid. The crude product was purified by recrystallization from chlorobenzene and washed with dry THF. Yield: 0.35 g (51%), white solid. ^1H NMR δ(H) ($CDCl_3$, 300 MHz): 7.94 (d, J = 7.6 Hz, 2H), 7.47 (t, J = 8.0 Hz, 1H), 7.36−7.30 (m, 3H), 7.24−7.18 (m, 2H), 7.14−7.02 (m, 4H), 6.95 (t, J = 7.4 Hz, 2H), 2.65−2.53 (m, 6H), 2.50−2.37 (m, 5H), 1.29 (d, J = 6.7 Hz, 6H), 1.05 (d, J = 6.8 Hz, 6H). ^{13}C NMR data were not obtained due to the low solubility of the product in $CDCl_3$. Anal. Calcd for $C_{36}H_{37}CuN_2S$: C, 72.88; H, 6.29; Cu, 10.71; N, 4.72; S, 5.40. Found: C, 72.34; H, 6.47; N, 4.56.

Compound 7. A solution of 3,6-di-*tert*-butylcarbazole (0.281 g, 1.01 mmol) and KOtBu (0.113 g, 1.01 mmol) in THF (15 mL) and a solution of **14** (0.400 g, 0.92 mmol) in THF (20 mL) were used Yield: 0.30 g (48%), greenish yellow solid. ^1H NMR δ(H) (C_6D_6, 300 MHz): 8.47 (s, 2H), 7.59 (d, J = 8.0 Hz, 2H), 7.30−7.23 (m, 2H), 6.93 (d, J = 7.6 Hz, 2H), 6.86−6.67 (m, 6H), 2.34 (hept, J = 6.5 Hz, 2H), 1.57 (s, 18H), 1.42−1.32 (m, 9H), 0.86 (d, J = 6.3 Hz, 3H). ^{13}C NMR δ(C) (C_6D_6, 75.47 MHz): 203.70, 149.70, 145.81, 145.40, 138.08, 138.09, 133.60, 130.92, 130.31, 129.59, 125.55, 124.85, 121.61, 116.20, 114.55, 34.81, 32.73, 29.11, 26.32, 22.55, 12.04. Anal. Calcd for $C_{42}H_{49}CuN_2S$: C, 74.46; H, 7.29; Cu, 9.38; N, 4.14; S, 4.73. Found: C, 74.06; H, 7.22; N, 4.15.

Compound 8. A solution of 3,6-di-*tert*-butyl-1,8-dimethylcarbazole (0.309 g, 1.00 mmol) and KOtBu (0.113 g, 1.01 mmol) in THF (15 mL) and a solution of **14** (0.400 g, 0.92 mmol) in THF (20 mL) were used Yield: 0.50 g (77%), yellow solid. Crystals suitable for X-ray diffraction analysis were obtained by layering a solution of THF with pentane. ^1H NMR δ(H) (C_6D_6, 300 MHz): 8.44 (s, 2H), 7.54 (s, 2H), 7.06 (t, J = 7.8 Hz, 1H), 6.85−6.77 (m, 5H), 6.72−6.66 (m, 2H), 2.85 (s, 6H), 2.28 (hept, J = 6.8 Hz, 2H), 1.65−1.54 (m, 21H), 1.22 (d, J = 6.7 Hz, 6H), 0.78 (d, J = 6.8 Hz, 6H). ^{13}C NMR δ(C) (C_6D_6, 75.47 MHz): 205.50, 148.61, 146.20, 144.80, 138.47, 138.28, 133.18, 131.00, 130.31, 129.59, 126.11, 124.97, 123.16, 121.07, 114.29, 34.73, 32.75, 29.06, 26.20, 22.79, 22.08, 12.32. Anal. Calcd for $C_{44}H_{53}CuN_2S$: C, 74.91; H, 7.57; Cu, 9.01; N, 3.97; S, 4.54. Found: C, 74.87; H, 7.58; N, 4.14.

X-ray Crystallography. Single crystals of **1−5** and **8** ware obtained by layering the corresponding THF solutions with pentane. Crystallographic diffraction data were collected with a Rigaku XtaLAB Synergy, Dualflex, HyPix diffractometer (Cu $K\alpha$, λ = 1.54184 Å) equipped with a low-temperature Oxford Cryosystems Cryostream Plus device. The crystal structures were solved by direct methods with the ShelXT[62] structure solution program using an intrinsic phasing solution method. The crystal structures of **1** and **3** were refined with the SHELXL[63]

refinement package using least-squares minimization. All of the other crystal structures were refined with a version of the program olex2.refine[64] using Levenberg−Marquardt minimization (for the structure of **2** using Gauss−Newton minimization). All calculations were performed with Olex2 software.[65] Table S1 gives the main crystal data for these compounds. Crystallographic data for **1−5** and **8** are deposited at the Cambridge Crystallographic Data Centre as the corresponding supplementary publications CCDC 2114050, 2114049, 2114046, 2114047, 2114048, and 2114045. Copies of the data can be obtained, free of charge, on application to the CCDC, 12 Union Road, Cambridge CB2 1EZ, U.K.

Cyclic Voltammetry Measurements. Cyclic voltammetry measurements were performed with a PARSTAT 2273 potentiostat. Electrochemical redox reactions were performed in anhydrous acetonitrile solutions under an Ar atmosphere using 0.1 M tetrabutylammonium hexafluorophosphate (TBAPF$_6$) as the supporting electrolyte. The measurements were carried out using a three-electrode cell configuration. A stationary glassy-carbon disk (∅ 0.5 cm) was used as the working electrode, Pt wire as the auxiliary electrode, and silver wire as the pseudoreference electrode.

Photophysical Measurements. UV−vis absorption and PL measurements in solution were carried with a material concentration of 1×10^{-5} mol L^{-1}. Solutions for Φ_{PL} and emission decay measurements were prepared in a glovebox under an Ar atmosphere using moisture-free and previously degassed solvents. PMMA films for optical measurements were prepared from chlorobenzene solutions (30 mg/mL material concentration) using a drop-casting method. After the deposition of the solution on glass slides the samples were immediately placed in a preheated oven and dried for 2 h at 80 °C. The UV−vis spectra were recorded with a PerkinElmer Lambda 35 spectrometer. Depending on the nature of the experiment, photoluminescence properties were measured on two different spectroscopic systems. Emission spectra, Φ_{PL}, and PL lifetimes for solution and thin films at room temperature, as well as PL spectra, time-resolved measurements, and PL lifetimes at 77 K (in a liquid-nitrogen-filled quartz Dewar), were measured with a QuantaMaster 40 spectrofluorometer (Photon Technology International, Inc.). Room-temperature PL measurements for doped films were carried out under an N$_2$ atmosphere. A 375 nm laser with a 60 ps pulse width and tunable repetition rate (between 1 mHz and 50 kHz) was used for the fast (nanosecond−microsecond range) kinetics measurements. A steady-state and pulsed (3 μs pulse width) xenon lamp was used for steady-state and millisecond kinetics measurements. The excitation source for temperature-dependent (10− 300 K) photoluminescence measurements in a helium cryostat was a tunable Ekspla NT 342/3UV laser with a repetition rate of 10 Hz and 5 ns pulse width. Photoluminescence spectra and PL decays were obtained with a PMT apparatus attached to an Andor monochromator.

To acquire ΔE_{ST} values, PL lifetimes of compound **8**, measured in the temperature interval 310−10 K, were fitted against a modified Boltzmann equation[41]

$$\tau = \frac{1 + \exp\left(-\frac{\Delta E(S_1 - T_1)}{k_B T}\right)}{\frac{1}{\tau_{T_1}} + \frac{1}{\tau_{S_1}} \exp\left(-\frac{\Delta E(S_1 - T_1)}{k_B T}\right)} \tag{1}$$

where k_B is the Boltzmann constant, τ_{T_1} is the decay time of the emitting triplet state, τ_{S_1} is the decay time of the emitting singlet state, and $\Delta E(S_1 - T_1)$ is the energy gap between the S$_1$ and T$_1$ states.

OLED Preparation and Characterization. Organic materials purchased from Shine Materials Technology were subjected to temperature-gradient sublimation under high vacuum before use. After a routine cleaning procedure of ultrasonication of the ITO-coated glass in deionized water and organic solvents, the ITO substrate was pretreated with plasma for 5 min. The organic and metal layers were deposited by thermal evaporation in a vacuum chamber with a base pressure of <10^{-6} Torr. Device fabrication was completed in a single cycle without breaking the vacuum. The deposition rates of organic materials and aluminum were respectively kept at around 0.1 and 0.5 nm s^{-1}. The active area was defined by a shadow mask (2×2 mm^2).

Current density−voltage−luminance characterization was done using two Keysight B2901A current source-measure units equipped with a calibrated Si photodiode. The electroluminescent spectra of the devices were recorded using an Ocean Optics spectrometer (Ocean Optics 2000).

■ ASSOCIATED CONTENT

Ⓢ Supporting Information

The Supporting Information is available free of charge at https://pubs.acs.org/doi/10.1021/acsami.2c00847.

> Synthetic procedures for intermediate compounds **10**, **12**, **14**, and 3,6-di-*tert*-butyl-1,8-dimethylcarbazole, description of procedures for theoretical calculations, thermogravimetry and single-crystal X-ray diffraction data, results of electrochemical and photophysical measurements, OLED characterization, NMR spectra, and coordinates for DFT-optimized structures (PDF)
>
> Crystallographic information for complexes **1−5** and **8** (CIF)

■ AUTHOR INFORMATION

Corresponding Authors

Chih-Hao Chang − *Department of Electrical Engineering, Yuan Ze University, Chungli 32003, Taiwan;* ⓘ orcid.org/0000-0002-5586-9526; Email: chc@saturn.yzu.edu.tw

Kaspars Traskovskis − *Faculty of Materials Science and Applied Chemistry, Riga Technical University, LV-1048 Riga, Latvia;* ⓘ orcid.org/0000-0003-1416-7533; Email: kaspars.traskovskis@rtu.lv

Authors

Armands Ruduss − *Faculty of Materials Science and Applied Chemistry, Riga Technical University, LV-1048 Riga, Latvia*

Baiba Turovska − *Latvian Institute of Organic Synthesis, Riga LV-1006, Latvia*

Sergey Belyakov − *Latvian Institute of Organic Synthesis, Riga LV-1006, Latvia*

Kitija A. Stucere − *Institute of Solid State Physics, University of Latvia, LV-1063 Riga, Latvia*

Aivars Vembris − *Institute of Solid State Physics, University of Latvia, LV-1063 Riga, Latvia*

Glib Baryshnikov − *Laboratory of Organic Electronics, Department of Science and Technology, Linköping University, SE-60174 Norrköping, Sweden;* ⓘ orcid.org/0000-0002-0716-3385

Hans Ågren − *Department of Physics and Astronomy, Uppsala University, SE-751 20 Uppsala, Sweden;* ⓘ orcid.org/0000-0002-1763-9383

Jhao-Cheng Lu − *Department of Electrical Engineering, Yuan Ze University, Chungli 32003, Taiwan*

Wei-Han Lin − *Department of Electrical Engineering, Yuan Ze University, Chungli 32003, Taiwan*

Complete contact information is available at:
https://pubs.acs.org/10.1021/acsami.2c00847

Notes

The authors declare no competing financial interest.

■ ACKNOWLEDGMENTS

■ REFERENCES

(1) Chen, H.-W.; Lee, J.-H.; Lin, B.-Y.; Chen, S.; Wu, S.-T. Liquid Crystal Display and Organic Light-Emitting Diode Display: Present Status and Future Perspectives. *Light Sci. Appl.* **2018**, 7 (3), 17168–17168.

(2) Yin, Y.; Ali, M. U.; Xie, W.; Yang, H.; Meng, H. Evolution of White Organic Light-Emitting Devices: From Academic Research to Lighting and Display Applications. *Mater. Chem. Front.* **2019**, 3 (6), 970–1031.

(3) Yersin, H.; Rausch, A. F.; Czerwieniec, R.; Hofbeck, T.; Fischer, T. The Triplet State of Organo-Transition Metal Compounds. Triplet Harvesting and Singlet Harvesting for Efficient OLEDs. *Coord. Chem. Rev.* **2011**, 255 (21–22), 2622–2652.

(4) Lamansky, S.; Djurovich, P.; Murphy, D.; Abdel-Razzaq, F.; Lee, H.-E.; Adachi, C.; Burrows, P. E.; Forrest, S. R.; Thompson, M. E. Highly Phosphorescent Bis-Cyclometalated Iridium Complexes: Synthesis, Photophysical Characterization, and Use in Organic Light Emitting Diodes. *J. Am. Chem. Soc.* **2001**, 123 (18), 4304–4312.

(5) Sotoyama, W.; Satoh, T.; Sawatari, N.; Inoue, H. Efficient Organic Light-Emitting Diodes with Phosphorescent Platinum Complexes Containing N∧C∧N-Coordinating Tridentate Ligand. *Appl. Phys. Lett.* **2005**, 86 (15), 153505.

(6) Yang, X.; Zhou, G.; Wong, W.-Y. Functionalization of Phosphorescent Emitters and Their Host Materials by Main-Group Elements for Phosphorescent Organic Light-Emitting Devices. *Chem. Soc. Rev.* **2015**, 44 (23), 8484–8575.

(7) Bizzarri, C.; Spuling, E.; Knoll, D. M.; Volz, D.; Bräse, S. Sustainable Metal Complexes for Organic Light-Emitting Diodes (OLEDs). *Coord. Chem. Rev.* **2018**, 373, 49–82.

(8) Wenger, O. S. Photoactive Complexes with Earth-Abundant Metals. *J. Am. Chem. Soc.* **2018**, 140 (42), 13522–13533.

(9) Ma, Y.; Che, C.-M.; Chao, H.-Y.; Zhou, X.; Chan, W.-H.; Shen, J. High Luminescence Gold(I) and Copper(I) Complexes with a Triplet Excited State for Use in Light-Emitting Diodes. *Adv. Mater.* **1999**, 11 (10), 852–857.

(10) Harkins, S. B.; Peters, J. C. A Highly Emissive Cu 2 N 2 Diamond Core Complex Supported by a [PNP] - Ligand. *J. Am. Chem. Soc.* **2005**, 127 (7), 2030–2031.

(11) Chen, X.-L.; Yu, R.; Zhang, Q.-K.; Zhou, L.-J.; Wu, X.-Y.; Zhang, Q.; Lu, C.-Z. Rational Design of Strongly Blue-Emitting Cuprous Complexes with Thermally Activated Delayed Fluorescence and Application in Solution-Processed OLEDs. *Chem. Mater.* **2013**, 25 (19), 3910–3920.

(12) Hupp, B.; Schiller, C.; Lenczyk, C.; Stanoppi, M.; Edkins, K.; Lorbach, A.; Steffen, A. Synthesis, Structures, and Photophysical Properties of a Series of Rare Near-IR Emitting Copper(I) Complexes. *Inorg. Chem.* **2017**, 56 (15), 8996–9008.

(13) Hofbeck, T.; Monkowius, U.; Yersin, H. Highly Efficient Luminescence of Cu(I) Compounds: Thermally Activated Delayed Fluorescence Combined with Short-Lived Phosphorescence. *J. Am. Chem. Soc.* **2015**, 137 (1), 399–404.

(14) Leitl, M. J.; Zink, D. M.; Schinabeck, A.; Baumann, T.; Volz, D.; Yersin, H. Copper(I) Complexes for Thermally Activated Delayed Fluorescence: From Photophysical to Device Properties. *Top. Curr. Chem.* **2016**, 374 (3), 25.

(15) Linfoot, C. L.; Leitl, M. J.; Richardson, P.; Rausch, A. F.; Chepelin, O.; White, F. J.; Yersin, H.; Robertson, N. Thermally Activated Delayed Fluorescence (TADF) and Enhancing Photoluminescence Quantum Yields of [Cu I (Diimine)(Diphosphine)] +

(16) Czerwieniec, R.; Kowalski, K.; Yersin, H. Highly Efficient Thermally Activated Fluorescence of a New Rigid Cu(i) Complex [Cu(Dmp)(Phanephos)]+. *Dalt. Trans.* **2013**, 42 (27), 9826.

(17) Gómez-Suárez, A.; Nelson, D. J.; Thompson, D. G.; Cordes, D. B.; Graham, D.; Slawin, A. M. Z.; Nolan, S. P. Synthesis, Characterization and Luminescence Studies of Gold(I)–NHC Amide Complexes. *Beilstein J. Org. Chem.* **2013**, 9, 2216–2223.

(18) Romanov, A. S.; Becker, C. R.; James, C. E.; Di, D.; Credgington, D.; Linnolahti, M.; Bochmann, M. Copper and Gold Cyclic (Alkyl)(Amino)Carbene Complexes with Sub-Microsecond Photoemissions: Structure and Substituent Effects on Redox and Luminescent Properties. *Chem. - A Eur. J.* **2017**, 23 (19), 4625–4637.

(19) Di, D.; Romanov, A. S.; Yang, L.; Richter, J. M.; Rivett, J. P. H.; Jones, S.; Thomas, T. H.; Abdi Jalebi, M.; Friend, R. H.; Linnolahti, M.; Bochmann, M.; Credgington, D. High-Performance Light-Emitting Diodes Based on Carbene-Metal-Amides. *Science (80-.)* **2017**, 356 (6334), 159–163.

(20) Hamze, R.; Peltier, J. L.; Sylvinson, D.; Jung, M.; Cardenas, J.; Haiges, R.; Soleilhavoup, M.; Jazzar, R.; Djurovich, P. I.; Bertrand, G.; Thompson, M. E. Eliminating Nonradiative Decay in Cu(I) Emitters: 99% Quantum Efficiency and Microsecond Lifetime. *Science (80-.)* **2019**, 363 (6427), 601–606.

(21) Hamze, R.; Shi, S.; Kapper, S. C.; Muthiah Ravinson, D. S.; Estergreen, L.; Jung, M.-C.; Tadle, A. C.; Haiges, R.; Djurovich, P. I.; Peltier, J. L.; Jazzar, R.; Bertrand, G.; Bradforth, S. E.; Thompson, M. E. Quick-Silver" from a Systematic Study of Highly Luminescent, Two-Coordinate, d 10 Coinage Metal Complexes. *J. Am. Chem. Soc.* **2019**, 141 (21), 8616–8626.

(22) Thompson, M. E.; Li, T. Y.; Djurovich, P.; Shlian, D. A Luminescent Two-Coordinate Au(I) Bimetallic Complex with a Tandem-Carbene Structure: A Molecular Design for the Enhancement of TADF Radiative Decay Rate. *Chem. - Eur. J.* **2021**, 27, 6191.

(23) Romanov, A. S.; Jones, S. T. E.; Yang, L.; Conaghan, P. J.; Di, D.; Linnolahti, M.; Credgington, D.; Bochmann, M. Mononuclear Silver Complexes for Efficient Solution and Vacuum-Processed OLEDs. *Adv. Opt. Mater.* **2018**, 6 (24), 1801347.

(24) Romanov, A. S.; Yang, L.; Jones, S. T. E.; Di, D.; Morley, O. J.; Drummond, B. H.; Reponen, A. P. M.; Linnolahti, M.; Credgington, D.; Bochmann, M. Dendritic Carbene Metal Carbazole Complexes as Photoemitters for Fully Solution-Processed OLEDs. *Chem. Mater.* **2019**, 31 (10), 3613–3623.

(25) Shi, S.; Jung, M. C.; Coburn, C.; Tadle, A.; Sylvinson, M. R. D.; Djurovich, P. I.; Forrest, S. R.; Thompson, M. E. Highly Efficient Photo- and Electroluminescence from Two-Coordinate Cu(I) Complexes Featuring Nonconventional N-Heterocyclic Carbenes. *J. Am. Chem. Soc.* **2019**, 141 (8), 3576–3588.

(26) Conaghan, P. J.; Matthews, C. S. B.; Chotard, F.; Jones, S. T. E.; Greenham, N. C.; Bochmann, M.; Credgington, D.; Romanov, A. S. Highly Efficient Blue Organic Light-Emitting Diodes Based on Carbene-Metal-Amides. *Nat. Commun.* **2020**, 11 (1), 1758.

(27) Gernert, M.; Balles-Wolf, L.; Kerner, F.; Müller, U.; Schmiedel, A.; Holzapfel, M.; Marian, C. M.; Pflaum, J.; Lambert, C.; Steffen, A. Cyclic (Amino)(Aryl)Carbenes Enter the Field of Chromophore Ligands: Expanded π System Leads to Unusually Deep Red Emitting Cu I Compounds. *J. Am. Chem. Soc.* **2020**, 142 (19), 8897–8909.

(28) Conaghan, P. J.; Menke, S. M.; Romanov, A. S.; Jones, S. T. E.; Pearson, A. J.; Evans, E. W.; Bochmann, M.; Greenham, N. C.; Credgington, D. Efficient Vacuum-Processed Light-Emitting Diodes Based on Carbene–Metal–Amides. *Adv. Mater.* **2018**, 30 (35), 1802285.

(29) Feng, J.; Yang, L.; Romanov, A. S.; Ratanapreechachai, J.; Reponen, A. M.; Jones, S. T. E.; Linnolahti, M.; Hele, T. J. H.; Köhler, A.; Bässler, H.; Bochmann, M.; Credgington, D. Environmental Control of Triplet Emission in Donor–Bridge–Acceptor Organometallics. *Adv. Funct. Mater.* **2020**, 30 (9), 1908715.

(30) Romanov, A. S.; Jones, S. T. E.; Gu, Q.; Conaghan, P. J.; Drummond, B. H.; Feng, J.; Chotard, F.; Buizza, L.; Foley, M.;

Linnolahti, M.; Credgington, D.; Bochmann, M. Carbene Metal Amide Photoemitters: Tailoring Conformationally Flexible Amides for Full Color Range Emissions Including White-Emitting OLED. *Chem. Sci.* **2020**, *11* (2), 435−446.

(31) Lüdtke, N.; Föller, J.; Marian, C. M. Understanding the Luminescence Properties of Cu Complexes: A Quantum Chemical Perusal. *Phys. Chem. Chem. Phys.* **2020**, *22* (41), 23530−23544.

(32) Chotard, F.; Sivchik, V.; Linnolahti, M.; Bochmann, M.; Romanov, A. S. Mono- versus Bicyclic Carbene Metal Amide Photoemitters: Which Design Leads to the Best Performance? *Chem. Mater.* **2020**, *32* (14), 6114−6122.

(33) Ying, A.; Huang, Y.-H.; Lu, C.-H.; Chen, Z.; Lee, W.-K.; Zeng, X.; Chen, T.; Cao, X.; Wu, C.-C.; Gong, S.; Yang, C. High-Efficiency Red Electroluminescence Based on a Carbene−Cu(I)−Acridine Complex. *ACS Appl. Mater. Interfaces* **2021**, *13* (11), 13478−13486.

(34) Hamze, R.; Idris, M.; Muthiah Ravinson, D. S.; Jung, M. C.; Haiges, R.; Djurovich, P. I.; Thompson, M. E. Highly Efficient Deep Blue Luminescence of 2-Coordinate Coinage Metal Complexes Bearing Bulky NHC Benzimidazolyl Carbene. *Front. Chem.* **2020**, *8*, 1.

(35) Yang, J.-G.; Song, X.-F.; Wang, J.; Li, K.; Chang, X.; Tan, L.-Y.; Liu, C.-X.; Yu, F.-H.; Cui, G.; Cheng, G.; To, W.-P.; Yang, C.; Che, C.-M.; Chen, Y. Highly Efficient Thermally Activated Delayed Fluorescence from Pyrazine-Fused Carbene Au(I) Emitters. *Chem. - Eur. J.* **2021**, *27*, 17834.

(36) Fleetham, T.; Ecton, J.; Wang, Z.; Bakken, N.; Li, J. Single-Doped White Organic Light-Emitting Device with an External Quantum Efficiency Over 20%. *Adv. Mater.* **2013**, *25* (18), 2573−2576.

(37) Cocchi, M.; Kalinowski, J.; Virgili, D.; Fattori, V.; Develay, S.; Williams, J. A. G. Single-Dopant Organic White Electrophosphorescent Diodes with Very High Efficiency and Its Reduced Current Density Roll-Off. *Appl. Phys. Lett.* **2007**, *90* (16), 163508.

(38) Piel, I.; Pawelczyk, M. D.; Hirano, K.; Fröhlich, R.; Glorius, F. A Family of Thiazolium Salt Derived N-Heterocyclic Carbenes (NHCs) for Organocatalysis: Synthesis, Investigation and Application in Cross-Benzoin Condensation. *Eur. J. Org. Chem.* **2011**, *2011* (28), 5475−5484.

(39) Li, T.; Muthiah Ravinson, D. S.; Haiges, R.; Djurovich, P. I.; Thompson, M. E. Enhancement of the Luminescent Efficiency in Carbene-Au (I) -Aryl Complexes by the Restriction of Renner−Teller Distortion and Bond Rotation. *J. Am. Chem. Soc.* **2020**, *142* (13), 6158−6172.

(40) Eng, J.; Thompson, S.; Goodwin, H.; Credgington, D.; Penfold, T. J. Competition between the Heavy Atom Effect and Vibronic Coupling in Donor−Bridge−Acceptor Organometallics. *Phys. Chem. Chem. Phys.* **2020**, *22* (8), 4659−4667.

(41) Czerwieniec, R.; Yu, J.; Yersin, H. Blue-Light Emission of Cu(I) Complexes and Singlet Harvesting. *Inorg. Chem.* **2011**, *50* (17), 8293−8301.

(42) Föller, J.; Marian, C. M. Rotationally Assisted Spin-State Inversion in Carbene−Metal−Amides Is an Artifact. *J. Phys. Chem. Lett.* **2017**, *8* (22), 5643−5647.

(43) Marcus, R. A. Electron Transfer Reactions in Chemistry. Theory and Experiment. *Rev. Mod. Phys.* **1993**, *65* (3), 599−610.

(44) O'Brien, D. F.; Baldo, M. A.; Thompson, M. E.; Forrest, S. R. Improved Energy Transfer in Electrophosphorescent Devices. *Appl. Phys. Lett.* **1999**, *74* (3), 442−444.

(45) Gong, S.; He, X.; Chen, Y.; Jiang, Z.; Zhong, C.; Ma, D.; Qin, J.; Yang, C. Simple CBP Isomers with High Triplet Energies for Highly Efficient Blue Electrophosphorescence. *J. Mater. Chem.* **2012**, *22* (7), 2894−2899.

(46) Holmes, R. J.; Forrest, S. R.; Tung, Y.-J.; Kwong, R. C.; Brown, J. J.; Garon, S.; Thompson, M. E. Blue Organic Electrophosphorescence Using Exothermic Host−Guest Energy Transfer. *Appl. Phys. Lett.* **2003**, *82* (15), 2422−2424.

(47) Xu, H.; Wang, L.-H.; Zhu, X.-H.; Yin, K.; Zhong, G.-Y.; Hou, X.-Y.; Huang, W. Application of Chelate Phosphine Oxide Ligand in Eu III Complex with Mezzo Triplet Energy Level, Highly Efficient Photoluminescent, and Electroluminescent Performances. *J. Phys. Chem. B* **2006**, *110* (7), 3023−3029.

(48) Yi, R.; Liu, G.; Luo, Y.; Wang, W.; Tsai, H.; Lin, C.; Shen, H.; Chang, C.; Lu, C. Dicyano-Imidazole: A Facile Generation of Pure Blue TADF Materials for OLEDs. *Chem. - Eur. J.* **2021**, *27* (51), 12998−13008.

(49) Ye, H.; Chen, D.; Liu, M.; Su, S.-J.; Wang, Y.-F.; Lo, C.-C.; Lien, A.; Kido, J. Pyridine-Containing Electron-Transport Materials for Highly Efficient Blue Phosphorescent OLEDs with Ultralow Operating Voltage and Reduced Efficiency Roll-Off. *Adv. Funct. Mater.* **2014**, *24* (21), 3268−3275.

(50) Wu, J.; Ameri, L.; Cao, L.; Li, J. Efficient Excimer-Based White OLEDs with Reduced Efficiency Roll-Off. *Appl. Phys. Lett.* **2021**, *118* (7), 073301.

(51) Pander, P.; Zaytsev, A. V.; Sil, A.; Williams, J. A. G.; Lanoe, P.-H.; Kozhevnikov, V. N.; Dias, F. B. The Role of Dinuclearity in Promoting Thermally Activated Delayed Fluorescence (TADF) in Cyclometallated, N∧C∧N-Coordinated Platinum Complexes. *J. Mater. Chem. C* **2021**, *9* (32), 10276−10287.

(52) Liao, J.-L.; Chi, Y.; Su, Y.-D.; Huang, H.-X.; Chang, C.-H.; Liu, S.-H.; Lee, G.-H.; Chou, P.-T. Os Metal Phosphors Bearing Tridentate 2,6-Di(Pyrazol-3-Yl)Pyridine Chelate: Synthetic Design, Characterization and Application in OLED Fabrication. *J. Mater. Chem. C* **2014**, *2* (31), 6269.

(53) Baldo, M. A.; Adachi, C.; Forrest, S. R. Transient Analysis of Organic Electrophosphorescence. II. Transient Analysis of Triplet-Triplet Annihilation. *Phys. Rev. B* **2000**, *62* (16), 10967−10977.

(54) Cho, H.; Romanov, A. S.; Bochmann, M.; Greenham, N. C.; Credgington, D. Matrix-Free Hyperfluorescent Organic Light-Emitting Diodes Based on Carbene−Metal−Amides. *Adv. Opt. Mater.* **2021**, *9* (5), 2001965.

(55) Birks, J. B. Excimers. *Rep. Prog. Phys.* **1975**, *38* (8), 903−974.

(56) Hamze, R.; Jazzar, R.; Soleilhavoup, M.; Djurovich, P. I.; Bertrand, G.; Thompson, M. E. Phosphorescent 2-, 3- and 4-Coordinate Cyclic (Alkyl)(Amino)Carbene (CAAC) Cu Complexes. *Chem. Commun.* **2017**, *53* (64), 9008−9011.

(57) Li, K.; Ming Tong, G. S.; Wan, Q.; Cheng, G.; Tong, W.-Y.; Ang, W.-H.; Kwong, W.-L.; Che, C.-M. Highly Phosphorescent Platinum Emitters: Photophysics, Materials and Biological Applications. *Chem. Sci.* **2016**, *7* (3), 1653−1673.

(58) Williams, E. L.; Haavisto, K.; Li, J.; Jabbour, G. E. Excimer-Based White Phosphorescent Organic Light-Emitting Diodes with Nearly 100% Internal Quantum Efficiency. *Adv. Mater.* **2007**, *19* (2), 197−202.

(59) Kui, S. C. F.; Chow, P. K.; Tong, G. S. M.; Lai, S.-L.; Cheng, G.; Kwok, C.-C.; Low, K.-H.; Ko, M. Y.; Che, C.-M. Robust Phosphorescent Platinum(II) Complexes Containing Tetradentate O∧N∧C∧N Ligands: Excimeric Excited State and Application in Organic White-Light-Emitting Diodes. *Chem. - Eur. J.* **2013**, *19* (1), 69−73.

(60) Li, G.; Fleetham, T.; Li, J. Efficient and Stable White Organic Light-Emitting Diodes Employing a Single Emitter. *Adv. Mater.* **2014**, *26* (18), 2931−2936.

(61) Bedford, R. B.; Betham, M. N -H Carbazole Synthesis from 2-Chloroanilines via Consecutive Amination and C−H Activation. *J. Org. Chem.* **2006**, *71* (25), 9403−9410.

(62) Sheldrick, G. M. SHELXT − Integrated Space-Group and Crystal-Structure Determination. *Acta Crystallogr. Sect. A Found. Adv.* **2015**, *71* (1), 3−8.

(63) Sheldrick, G. M. A Short History of SHELX. *Acta Crystallogr. Sect. A Found. Crystallogr.* **2008**, *64* (1), 112−122.

(64) Bourhis, L. J.; Dolomanov, O. V.; Gildea, R. J.; Howard, J. A. K.; Puschmann, H. The Anatomy of a Comprehensive Constrained, Restrained Refinement Program for the Modern Computing Environment − Olex2 Dissected. *Acta Crystallogr. Sect. A Found. Adv.* **2015**, *71* (1), 59−75.

(65) Dolomanov, O. V.; Bourhis, L. J.; Gildea, R. J.; Howard, J. A. K.; Puschmann, H. OLEX2 : A Complete Structure Solution, Refinement and Analysis Program. *J. Appl. Crystallogr.* **2009**, *42* (2), 339−341.

Ruduss, A.; Sisojevs, Ž.; Vembris, A.; Štucere, K. A.; Traskovskis, K. Symmetrical versus Asymmetrical Molecular Configuration in Metal-Assisted-Through-Space Charge Transfer TADF Emitters. *Organic Electronics and Photonics: Fundamentals and Devices III*. **2022**, 1214908.

Symmetrical versus asymmetrical molecular configuration in metal-assisted-through-space charge transfer TADF

Armands Ruduss*[a], Zanis Sisojevs[a], Aivars Vembris[b], Kitija Stucere[b], Kaspars Traskovskis[a]

[a]Institute of Applied Chemistry, Riga Technical University, 3/7 Paula Valdena Str., Riga, LV-1048, Latvia; [b]Institute of Solid State Physics, University of Latvia, 8 Kengaraga Str., Riga, LV-1064, Latvia

ABSTRACT

The synthesis of a novel imidazolidine type *N*-heterocyclic carbene (NHC) Cu (I) complex with asymmetrically attached phenylsulfonyl- acceptor group is presented. The asymmetrical ligand was used for the preparation two Cu(I) carbene-metal-amide (CMA) complexes with carbazolide (complex **1**) or 1,8-dimethylcarbazolide (complex **2**) as the amide donors. Obtained complexes exhibit efficient thermally activated delayed fluorescence (TADF) with luminescence quantum yields (QY) reaching 0.80 in PMMA matrix. Metal promoted through-space charge transfer approach in the emitter design lowers the ΔE_{ST} gap and the small spin-orbit coupling (SOC) provided by metal atom enables high radiative rates ($k_r = 2.21 \times 10^5$ s^{-1} for complex **2**). The photophysical properties of the asymmetrical (**1-2**) and previously reported symmetrical (**3-6**) molecular designs are compared. Obtained results suggest a closely similar photophysical behavior for both the asymmetrical and symmetrical CMA complexes.

Keywords: Thermally activated delayed fluorescence, through-space charge transfer, carbene-metal-amides, *N*-heterocyclic carbenes

1. INTRODUCTION

Molecules exhibiting thermally activated delayed fluorescence (TADF) have generated a considerable interest from the research community due to application possibilities in organic light emitting diodes (OLEDs).[1] In TADF materials emission is realized by upconversion of non-emissive excited triplet state (T_1) to the emissive excited singlet state (S_1) via reverse intersystem crossing (rISC) process.[2] A key parameter to this process is the energy difference (ΔE_{ST}) between the T_1 and S_1 states. Minimization of the ΔE_{ST} by spatial separation of donor (D) and acceptor (A) molecular fragments is essential for enabling efficient rISC in TADF emitters.[3] However, relatively weak spin orbit coupling (SOC) of the T_1 and S_1 states compels to long delayed fluorescence lifetimes in purely organic TADF emitters.[4] Luminescent two-coordinate linear carbene-metal-amide (CMA, metal = Cu, Ag, Au) complexes with short radiative lifetimes have recently emerged as a highly promising direction towards TADF materials.[5–9] The spatial separation of the D and A fragments by a d^{10} coinage metal linkage provides small ΔE_{ST}, while highly efficient rISC and fast radiative rates in CMA's are enabled by SOC via the metal atom.[10]

Recently we have discovered a novel photophysical behavior in CMA-type compounds. By introducing electron withdrawing moieties at bulky peripheral groups of *N*-heterocyclic carbenes (NHCs), an emissive through-space charge transfer (CT) process can be induced (complexes **3-6**, Scheme 1).[11] Through-space CT significantly lowers singlet-triplet energy gap of CMAs. At the same time, small but still SOC is provided by the metal atom, resulting in high reverse intersystem crossing (rISC) rates. This leads to highly efficient TADF with PL quantum yield (Φ_{pl}) reaching 0.90 and radiative emission rates (k_r) up to 3.3×10^5 s^{-1}.

In this work we further expand the investigation of structurally similar CMA type Cu(I) complexes with through-space CT emission properties. A novel asymmetrical imidazolidine type NHC ligand bearing an attached electron-withdrawing phenylsulphonyl- substituent at the *para*- position of one of the N-bound bulky 2,6-diisopropylphenyl- groups was synthesized. The asymmetrical NHC ligand was used for the preparation of CMA complexes **1** and **2** (Scheme 1). In such manner through-space CT takes place with only one acceptor fragment instead of two. The asymmetrical complexes retain the unique photophysical properties displayed by the symmetrical complexes **3-6**. Furthermore, complexes **1** and **2** exhibit the increased solubility in organic solvents and reduced luminescence concentration quenching.

---

*armands.ruduss@rtu.lv
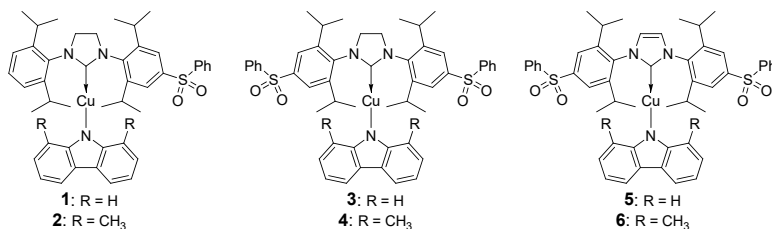
Scheme 1. Comparison of the chemical structures of asymmetrical (complexes **1** and **2**, this report) and symmetrical CMA complex design (complexes **3-6**, our previous report[11]).

2. EXPERIMENTAL SECTION

2.1 Synthesis characterization of the target compounds

The necessary solvents and reagents were purchased from commercial suppliers like *Sigma Aldrich*, *Alfa Aesar* and *Flourochem*. Solvents were dried using standard procedures. Procedures involving synthesis and purification of air/moisture sensitive NHC derivatives were carried out using Schlenk technique. Dry, air-free THF was distilled over K/benzophenone under N_2 prior to use. 4-Iodo-2,6-diisopropylaniline[12] and 1,8-dimethylcarbazole[13] were prepared according to procedures described in literature. NMR spectra were obtained on a Bruker Avance 300 MHz or a Bruker Avance 500 MHz spectrometer using CDCl₃ and DMSO-d6 residual signals as an internal reference. Crystallographic diffraction data for complex **1** were collected with Rigaku, XtaLAB Synergy, Dualflex, HyPix diffractometer (Cu-K$_\alpha$, λ = 1.54184 Å) equipped with a low temperature Oxford Cryosystems Cryostream Plus device. Detailed procedures regarding to the solving of the crystal structure are given in our previous report.[11]

2,6-Diisopropyl-4-(phenylthio)aniline (**8**): A mixture of 4-iodo-2,6-diisopropylaniline **7** (30.00 g, 98.95 mmol), thiophenol (21.83g, 198.11 mmol), CuI (3.80 g, 19.95 mmol), K₂CO₃, (27.38 g, 198.11 mmol), ethylene glycol (13 ml) and isopropyl alcohol (120 ml) was refluxed for 72 hours under Ar atmosphere. After cooling to room temperature, the mixture was filtered and water (400 ml) was added to the filtrate. The resulting mixture was extracted with EtOAc (3x300 ml) and the combined extracts were washed with brine and dried over Na₂SO₄. The volatiles were evaporated under reduced pressure and the product was purified via column chromatography (silica gel, toluene). The solvent was evaporated under reduced pressure to afford product as brown oil, yield: 26.09 g (92%). **¹H NMR** δH (CDCl₃, 300 MHz): 7.29-7.21 (m, 4H), 7.17-7.08 (m, 3H), 3.98 (br. s, 2H), 2.94 (hept, J = 6.7 Hz, 2H), 1.30 (d, J = 6.8 Hz, 12H). **¹³C NMR** δC (CDCl₃, 125.77 MHz): 141.21, 140.39, 133.62, 130.03, 128.86, 126.74, 124.99, 119.78, 28.16, 22.43.

Ethyl 2-((2,6-diisopropylphenyl)amino)-2-oxoacetate (**11**): To a solution of 2,6-diisopropylaniline **9** (17.73 g, 100.00 mmol) and triethylamine (15.8 ml, 113.31 mmol) in dry DCM (400 ml) ethyl 2-chloro-2-oxoacetate **10** (11.2 ml, 100.24 mmol) was added dropwise at 0 °C. The resulting mixture was stirred at 0 °C for 30 minutes. Then 1M HCl (200 ml) solution was added and the mixture was extracted. The extract was washed two additional times with 1M HCl solution, saturated NaHCO₃ solution, brine and dried over Na₂SO₄. The extract was evaporated under reduced pressure to afford product as white powder, yield: 26.92 g (97%). **¹H NMR** δH (CDCl₃, 300 MHz): 8.38 (s, 1H), 7.34 (t, J = 7.7 Hz, 1H), 7.20 (d, J = 7.7 Hz, 2H), 4.44 (q, J = 7.2 Hz, 2H), 3.01 (hept, J = 6.8 Hz, 2H), 1.46 (t, J = 7.2 Hz, 3H), 1.20 (d, J = 6.9 Hz, 12H). **¹³C NMR** δC (CDCl₃, 125.77 MHz): 161.20, 156.00, 145.96, 129.46, 129.11, 123.85, 63.80, 29.02, 23.76, 14.14.

2-((2,6-Diisopropylphenyl)amino)-2-oxoacetic acid (**12**): To a solution of **11** (10.00 g, 36.05 mmol) in THF (150 ml) a saturated solution of K₂CO₃ in H₂O (50 ml) was added and the resulting mixture was stirred at room temperature for 16 hours. Then pH was adjusted to pH=1 by slow addition of 12M HCl and THF was evaporated under reduced pressure, to precipitate the product. The mixture was filtered and washed with water to afford product as white solid, yield: 7.67 g (85%). **¹H NMR** δH (DMSO-d6, 500 MHz): 14.39-13.81 (br. s, 1H), 10.19 (s, 1H), 7.29 (t, J = 7.5 Hz, 1H), 7.17 (d, J = 7.6 Hz, 2H), 2.98 (hept, J = 6.6 Hz, 2H), 1.11 (d, J = 6.4 Hz, 12H). **¹³C NMR** δC (DMSO-d6, 125.77 MHz): 162.42, 158.94, 145.63, 131.35, 127.94, 123.03, 28.05, 23.40.

N¹-(2,6-Diisopropyl-4-(phenylthio)phenyl)-N²-(2,6-diisopropylphenyl)oxalamide (**13**): To a solution of **12** (7.00 g, 28.08 mmol), **8** (6.29 g, 22.04 mmol) and 4-dimethylaminopyridine (0.24 g, 1.96 mmol) in dry DCM (50 ml) dicyclohexylcarbodiimide (6.15 g, 29.81 mmol) was added. The reaction mixture was stirred at room temperature for 3 hours. Then reaction mixture was filtered, methanol (50 ml) was added to the filtrate and DCM was selectively evaporated to precipitate the product. The mixture was filtered and washed with cold methanol to afford product as white solid, yield: 7.32 g (64%). **¹H NMR** δH (CDCl₃, 300 MHz): 9.16-9.02 (m, 2H), 7.48-7.27 (m, 6H), 7.27-7.12 (m, 4H), 3.11-2.95 (m, 4H), 1.25-1.09 (m, 24H). **¹³C NMR** δC (CDCl₃, 75.47 MHz): 159.90, 159.68, 146.91, 145.81, 136.35, 135.44, 131.17, 129.85, 129.30, 128.99, 128.96, 127.28, 126.09, 123.75, 29.20, 29.11, 23.57, 23.39.

N¹-(2,6-Diisopropyl-4-(phenylthio)phenyl)-N²-(2,6-diisopropylphenyl)ethane-1,2-diaminium chloride (**14**): To a solution of **13** (9.26 g, 17.92 mmol) in dry THF (30 ml) BF₃·OEt₂ (4.42 ml, 35.81 mmol) and BH₃ (1M solution in THF, 71.6 ml, 71.6 mmol) was added and the resulting mixture was refluxed for 16 hours. Then mixture was cooled to room temperature, water was slowly added and pH was adjusted to pH=12 by addition of 6M NaOH. THF was evaporated and the mixture was extracted with DCM (3x150 ml). The combined extracts were washed with water, brine and dried over Na₂SO₄. DCM was evaporated, the residue was dissolved in THF (100 ml) and 12M HCl (15 ml) was added to precipitate product. The mixture was filtered and washed with cold THF to afford product as white solid, yield: 5.52 g (55%). **¹H NMR** δH (DMSO-d6, 300 MHz): 7.41-7.23 (m, 8H), 7.09 (s, 2H), 3.51-3.25 (m, 8H), 1.19 (d, J = 6.3 Hz, 12H), 1.09 (d, J = 6.4 Hz, 12H). **¹³C NMR** δC (DMSO-d6, 125.77 MHz): 144.10, 142.77, 135.45, 129.78, 129.46, 129.00, 128.23, 127.07, 125.45, 51.00, 47.57, 27.29, 27.25, 24.51, 24.15.

1-(2,6-Diisopropyl-4-(phenylthio)phenyl)-3-(2,6-diisopropylphenyl)-4,5-dihydro-1H-imidazol-3-ium chloride (**15**): To a mixture of **14** (5.42 g, 10.13 mmol) and triethyl orthoformate (9.00 ml) one drop of formic acid was added and the mixture was heated at 120 °C for 4 hours. After cooling the mixture to room temperature diethyl ether (100 ml) was added to precipitate the product. The mixture was filtered and washed with cold diethyl ether to afford product as white solid, yield: 3.84 g (71%). **¹H NMR** δH (DMSO-d6, 300 MHz): 9.50 (s, 1H), 7.59-7.38 (m, 8H), 7.15 (2H, s), 4.55-4.49 (m, 4H), 3.13-2.98 (m, 4H), 1.33 (d, J = 6.5 Hz, 6H), 1.27-1.07 (m, 18H). **¹³C NMR** δC (DMSO-d6, 75.47 MHz): 160.20, 147.26, 146.09, 140.15, 132.97, 132.06, 131.12, 129.96, 129.82, 128.89, 128.19, 124.86, 124.33, 53.75, 53.65, 28.28, 28.25, 25.01, 24.79, 23.31, 23.04.

1-(2,6-Diisopropyl-4-(phenylsulfonyl)phenyl)-3-(2,6-diisopropylphenyl)-4,5-dihydro-1H-imidazol-3-ium chloride (**16**): To a hot solution of **15** (3.74 g, 6.99 mmol) in methanol (55 ml) deionized water (20 ml) and oxone® (16.37 g, 107.56 mmol) was added. The mixture was refluxed for 72 hours. After cooling the mixture to room temperature methanol was selectively evaporated under reduced pressure to precipitate the product. The mixture was filtered and washed with water to afford product as white solid, yield: 3.68 g (94%). **¹H NMR** δH (DMSO-d6, 300 MHz): 9.43 (s, 1H), 8.14 (d, J = 8.3 Hz, 2H), 7.97 (s, 2H), 7.76-7.62 (m, 3H), 7.55 (t, J = 7.3 Hz, 1H), 7.42 (d, J = 7.8 Hz, 2H), 4.62-4.50 (m, 4H), 3.22-2.98 (m, 4H), 1.41-1.30 (m, 12H), 1.23-1.12 (m, 12H). **¹³C NMR** δC (DMSO-d6, 75.47 MHz): 159.87, 148.86, 146.03, 143.92, 143.92, 140.47, 134.27, 131.25, 129.97, 129.63, 127.84, 124.93, 123.71, 53.93, 53.62, 28.67, 28.22, 25.03, 24.58, 23.31, 22.97.

Compound (**17**): To a mixture of **16** (2.00 g, 3.53 mmol), CuCl (0.42 g, 4.24 mmol) and K₂CO₃ (2.52 g, 18.23 mmol) acetone (80 ml) was added and the resulting mixture was refluxed for 1 hour. Reaction mixture was cooled to room temperature and solvent was evaporated under reduced pressure. DCM (50 ml) was added and the resulting mixture was filtered through a short pad of silica gel. Hexane (300 ml) was added to the filtrate and the residual DCM was selectively evaporated under reduced pressure to precipitate the product. The mixture was filtered and washed with hexane to afford product as white solid, yield: 1.73 g (78%). **¹H NMR** δH (CDCl₃, 500 MHz): 7.98 (d, J = 7.5 Hz, 2H), 7.80 (s, 2H), 7.64-7.53 (m, 3H), 7.40 (t, J = 7.5 Hz, 1H), 7.25-7.21 (m, 2H), 4.08-3.92 (m, 4H), 3.09 (hept, J = 6.7 Hz, 2H), 2.99 (hept, J = 6.7 Hz, 2H), 1.39-1.30 (m, 24H). **¹³C NMR** δC (CDCl₃, 125.77 MHz): 202.91, 149.00, 146.49, 143.01, 141.04, 138.93, 134.02, 133.77, 130.29, 129.69, 127.93, 124.80, 124.26, 53.84, 53.71, 29.45, 29.10, 25.55, 25.33, 24.01, 23.78.

Compound (**1**): A mixture of carbazole (0.106 g, 0.63 mmol) and KOtBu (0.072 g, 0.64 mmol) was stirred in dry, deoxygenated THF (25 ml) for 30 minutes. Then compound **17** (0.200 g, 0.32 mmol) was added and the resulting mixture was stirred for 2h at room temperature. The mixture was filtered through a pad of Celite into dry, deoxygenated hexane (200 ml) to precipitate the product. The mixture was filtered and washed with hexane to afford product as off-white solid, yield: 0.20 g (82%). **¹H NMR** δH (CDCl₃, 300 MHz): 8.08 (d, J = 7.1 Hz, 2H), 7.97 (s, 1H), 7.85 (d, J = 7.5 Hz, 2H), 7.71-7.55 (m, 4H), 7.40 (d, J = 7.8 Hz, 2H), 6.79 (t, J = 7.0 Hz, 2H), 6.66 (t, J = 7.4 Hz, 2H), 5.94 (d, J = 8.1 Hz, 2H), 4.24-4.11 (m, 4H), 3.24 (hept, J = 6.8 Hz, 2H), 3.16 (hept, J = 6.8 Hz, 2H), 1.44-1.36 (m, 12H), 1.33-1.25 (m, 12H). **¹³C NMR** δC (CDCl₃, 75.47 MHz): 204.73, 149.73, 149.63, 147.22, 143.45, 141.32, 139.14, 134.34, 133.77,

130.28, 129.82, 127.89, 124.99, 124.25, 123.97, 123.32, 119.33, 115.17, 113.82, 53.84, 53.71, 29.64, 29.29, 25.46, 25.28, 24.09, 23.86.

Compound (**2**): A mixture of 1,8-dimethylcarbazole (0.167 g, 0.86 mmol) and KOtBu (0.096 g, 0.86 mmol) was stirred in dry, deoxygenated THF (50 ml) for 30 minutes. Then compound **17** (0.300 g, 0.48 mmol) was added and the resulting mixture was stirred for 2h at room temperature. The mixture was filtered through a pad of Celite into dry, deoxygenated hexane (300 ml) to precipitate the product. The mixture was filtered and washed with hexane to afford product as off-white solid, yield: 0.25 g (66%). **^{1}H NMR** δH (CDCl$_3$, 300 MHz): 8.03 (d, J = 7.4 Hz, 2H), 7.88 (s, 2H), 7.77 (d, J = 7.3 Hz, 2H), 7.68 (t, J = 7.2 Hz, 1H), 7.59 (t, J = 7.4 Hz, 2H), 7.48 (t, J = 7.7 Hz, 1H), 7.30-7.25 (m, 2H), 6.79 (t, J = 7.2 Hz, 2H), 6.55 (d, J = 6.7 Hz, 2H), 4.08-3.95 (m, 4H), 3.23 (hept, J = 6.6 Hz, 2H), 3.10 (hept, J = 6.7 Hz, 2H), 1.55 (s, 6H), 1.39-1.16 (m, 24H). **^{13}C NMR** δC (CDCl$_3$, 125.77 MHz): 204.78, 149.00, 146.39, 143.23, 141.20, 139.92, 135.08, 133.90, 130.35, 129.84, 127.84, 125.38, 124.89, 124.76, 123.94, 121.85, 117.00, 115.36, 54.43, 53.99, 29.49, 29.11, 25.05, 24.79, 24.57, 24.46, 19.54.
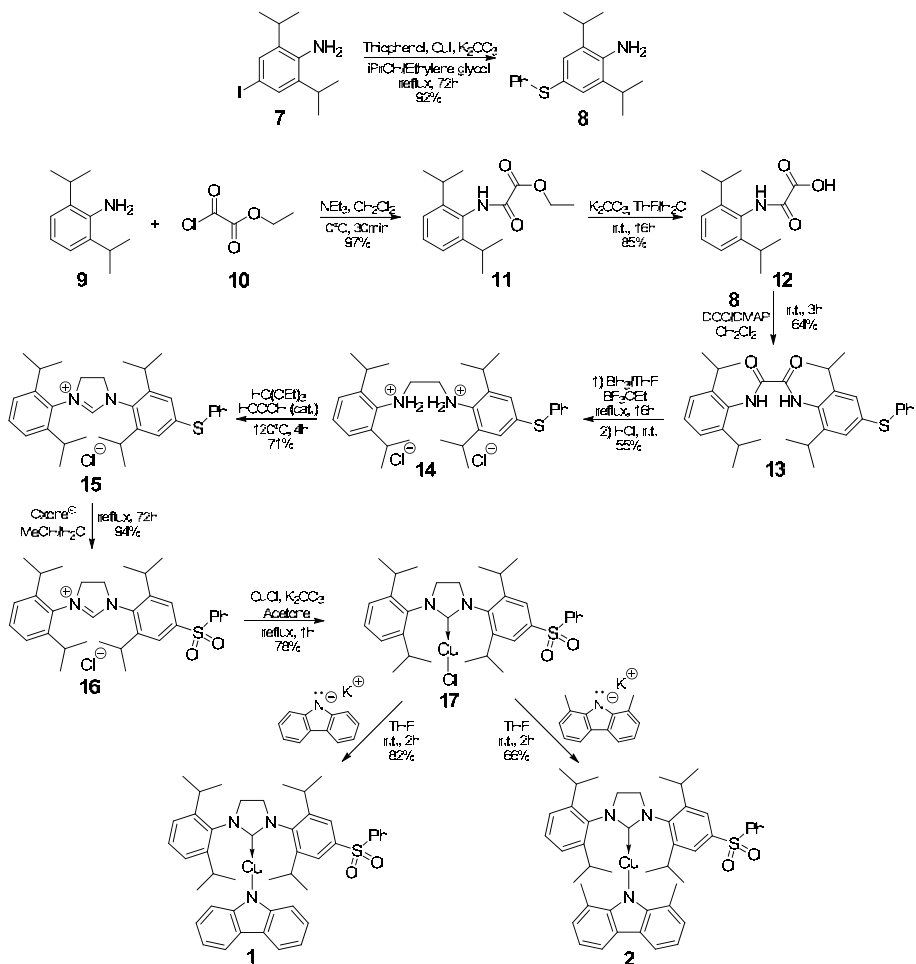
Scheme 2. Synthesis pathway for asymmetrical CMA complexes **1** and **2**.

2.2 Density Functional Theory (DFT) Calculations

Ground-state geometry optimization and time-dependent DFT (TD-DFT) calculations for complex **2** were performed at the MN15 functional and LACVP** level. These calculations were performed using Schrödinger Jaguar software package (release 2020-2).[14] Solvent effects (benzene, $\varepsilon = 2.27$) were taken into account using the conductor-like polarizable CPCM solvation model. SOC-TD-DFT calculations were performed at MN06/ ZORA-DEF2-TZVP level using Orca 5.0.1 software.

2.3 Photo physical measurements

Dry, degassed solvents were used to prepare solutions for the optical measurements. PMMA films for optical measurements were prepared using drop-casting method (chlorobenzene solution, 30 mg/ml material concentration). After the solution deposition on glass slides the samples were dried at 80 °C for 2 hours. UV-Vis spectra were obtained using a Perkin Elmer Lambda 650 spectrometer. Emission spectra, PL quantum yields (Φ_{pl}), PL lifetimes (τ_{PL}) and time-resolved emission spectra were recorded with a QuantaMaster 40 steady state spectrofluorometer (Photon Technology International, Inc), equipped with 6 inch integrating sphere (LabSphere). Unless stated otherwise, PL measurements at room temperature were performed under N_2 atmosphere for thin film samples. Time-resolved emission and long-time range (0-5000 µs) phosphorescence measurements were carried out using a pulsed xenon lamp (3 µs pulse width) as excitation source. Sample cooling (77 K) for the time-resolved emission measurements was carried out in a liquid nitrogen filled transparent quartz Dewar flask. The 375 nm laser with 60 ps pulse width and tunable repetition rate (between 1MHz and 50 kHz) was used for the fast (nanosecond to microsecond range) kinetics measurements. For the estimation of ΔE_{ST}, PL lifetimes (PMMA film of complex **2**) were measured in temperature interval 50–300 K. Helium cryostat was used for temperature-dependent PL measurements with a tunable Ekspla NT 342/3UV laser (10 Hz repetition rate, 5 ns pulse width) as the excitation source. Photoluminescence spectra and PL decays were obtained with PMT attached to Andor monochromator. To acquire ΔE_{ST} values, fits to the Arrhenius plots relating temperature and experimental k_{TADF} values were used.[7] Low temperature Φ_{pl} were estimated by calibrating the intensity of PL spectra against Φ_{pl} acquired at room temperature.[15] Contribution of the long-lived ^{3}LE carbazolide emission was effectively excluded from the overall Φ_{pl} by obtaining low temperature PL spectra in time-resolved mode (0-27 µs). Detailed methods for the calculation of photophysical parameters for individual emission components are given in our previous report.[11]

3. RESULTS AND DISCUSSION

3.1 Synthesis and structure of the asymmetrical CMA complexes

The synthesis of the asymmetrical CMA complexes **1** and **2** is outlined in Scheme 2. A convergent synthetic approach was utilized for the preparation of the asymmetrical mono-phenylthio substituted oxamide **13**. The reduction of oxamide **13** with borane in the presence of boron trifluoride yielded diaminium chloride **14** in moderate yield. Compound **14** was reacted with triethyl orthoformate to form the central imidazolium motif in **15** and phenylthio- group was consequently oxidized to phenylsulfonyl- group to yield compound **16**. NHC-Cu(I)-Cl complex **17** was conveniently synthesized in mild reaction conditions using a protocol developed by Santoro et al.[16] The reactions of **17** and deprotonated potassium salts of carbazol-9-ide and 1,8-dimethylcarbazol-9-ide yielded the target complexes **1** and **2** as off-white crystalline powders with green luminescence in solid state. Complexes **1** and **2** are stable in solid state and could be stored indefinitely under air exposure. The asymmetrical CMA complexes **1** and **2** show slightly better solubility in organic solvents like toluene, chlorobenzene or THF in comparison to the symmetrical complexes **3-6**. This could be related to the presence of only one polar phenylsulphonyl- group instead of two in complexes **1** and **2**. It must be noted that trace solvent impurities (like H_2O) lead to the degradation of complexes in solutions.

Monocrystals of complex **1** suitable for X-ray crystallographic analysis were prepared by slow liquid-liquid diffusion between THF and pentane (Figure 1). Due to the asymmetric structure molecules of **1** exhibit complex packing pattern in crystal structure. The obtained monocrystals are chiral with asymmetric cell containing four complex molecules and three disordered solvent (THF) molecules. The geometry of **1** closely resembles the previously reported X-ray structure of complex **3**. A slight bending towards the direction of the phenylsulfonyl- functionalized Dipp group was observed at the nearly linear metal center geometry ($\angle C_{NHC}$-Cu-$N_{Cbz} = 174.5°$) with bond lengths C_{NHC}-Cu = 1.881 Å and Cu-N_{Cbz} = 1.858 Å. The planes of the carbazolide ligand and central imidazolidine fragment are aligned coplanary with a small dihedral angle (8.7°). Contrary, due to the sterical factors carbazolide and phenylsulfonyl- functionalized Dipp planes exhibit orthogonal face-to-face alignment (dihedral angle β = 80°).
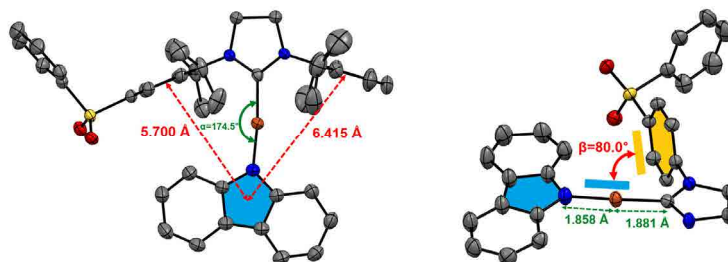
Figure 1. Top and side view of X-ray structures for complex **1**. Ellipsoids shown at 50% probability level. Hydrogen atoms are removed for clarity. Only one of the four independent molecules within the asymmetric cell is shown. β – Dihedral angle between the carbazolide and phenylsulfonyl- functionalized Dipp planes.

3.2 Quantum chemical calculations

To gain insight in the characteristics and energy level configuration of the excited states of the complexes TD-DFT calculations were performed for complex **2** at the MN15/LACVP** level (Figure 2). The nature of the excited state transitions for complex **2** is closely similar to the previously reported complexes **3-6**. The $S_0 \rightarrow S_1$ transition proceeds via spatially well-separated through-space interligand CT in the ground state geometry and involves electron transfer from carbazolide ligand to the phenylsulphonyl- acceptor group functionalized Dipp ring. The unfunctionalized Dipp ring has little to none contribution in this transition. The spatial separation of the frontier molecular orbitals causes a weak electronic coupling in through-space CT chromophores.[17] This leads to a low calculated oscillator strength (0.0069) for $S_0 \rightarrow S_1$ transition. At the same time, the well-separated molecular orbitals induce very low singlet-triplet energy gap ($\Delta E_{S1/T1}$ = 0.016 eV). Due to the low contribution of the metal atom to the frontier molecular orbitals SOC is low ($SOC_{S1/T1}$ = 0.19 cm^{-1}). However, it could be sufficient to promote rapid rISC given that singlet-triplet energy gap is low. It has been shown previously that low SOC value of 0.27 cm^{-1} promotes highly efficient TADF in high-performance green emitter 4CzIPN.[4] Although the role of the unfunctionalized Dipp ring in the lowest-energy electron transitions is negligible, the bulky Dipp group could act as an inert spacer decreasing intermolecular interactions and limiting PL quenching in high dopant concentrations.
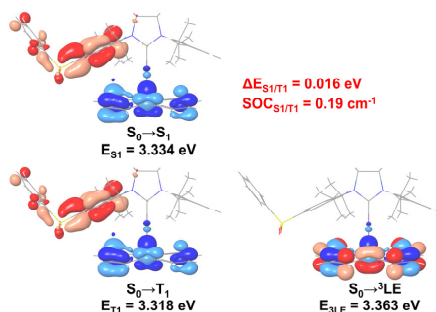

Figure 2. Natural transition orbitals (NTOs) for complex **2**, blue – hole; red – particle.

3.3 Photo physical properties

The UV-Vis absorption spectra of complexes **1** and **2** in toluene solution are shown in Figure 3a. Distinctive structured absorption bands at the 300-380 nm region are related to the transitions localized on carbazole ligands. Changes in the solvent polarity (Figure 3b) have little effect on the position of these bands.[8] A weak interligand CT band could be resolved at the lowest energy edge of the carbazolide absorption. This wide, featureless band exhibits negative solvatochromism with the decrease of solvent polarity. Negative solvatochromism for interligand CT absorption has been established as a distinctive feature of the CMA complexes.[18] The CT absorption extends up to 440 nm in toluene solutions, but the intensity and maximum of this band could not be estimated precisely due to the overlap of carbazolide

absorption. However, as in the case of the symmetrically phenylsulphonyl- substituted complexes **3-6**, relatively larger intensity of the CT absorption was observed for complex **2** containing 1,8-dimethylcarbazole ligand.
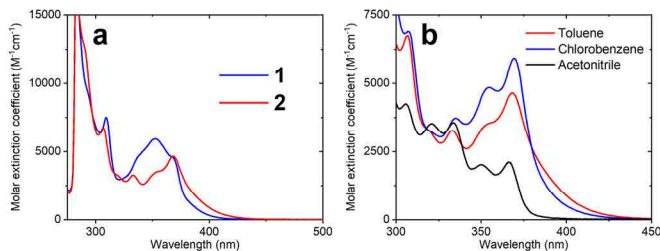

Figure 3. (a) UV-Vis absorption of complexes **1** and **2** in toluene solution (10^{-5} M). (b) UV-Vis absorption of complex **2** in toluene, chlorobenzene and acetonitrile solutions (10^{-5} M).

Emission spectra, PL efficiencies and kinetic parameters of complexes **1** and **2** in deoxygenated toluene solutions (5% emitter concentration) and PMMA films are given in Figure 4a, Figure 5a and Table 1. Both of the complexes exhibit similar PL properties in toluene solution with maxima at approximately 520 nm. The wide, featureless emission band is an indication for the CT nature of this transition. PL kinetics in toluene solutions show a predominantly monoexponential decay profile. A weak prompt fluorescence signal was observed for complex **1**. The luminescence efficiency for toluene solutions is similar for both complexes (Φ_{pl} = 0.38-0.39) with rapid nonradiative decay being the main excited state relaxation process. The rotation of amide ligands has been established as one of the nonradiative deactivation routes for CMA complexes in fluid solution.[19] However, a larger non-radiative decay rate is observed for complex **2** (k_{nr} = 7.01×10^5 s^{-1}) with sterically demanding 1,8-dimethylcarbazolide ligand compared to complex **1** (k_{nr} = 4.22×10^5 s^{-1}). The conformational strain induced by 1,8-dimethyl- groups could limit carbazolide plane rotation. This observation suggests that carbazolide ligand rotation is not dominant nonradiative deactivation process and other relaxation pathways may take place for complexes in toluene solution.
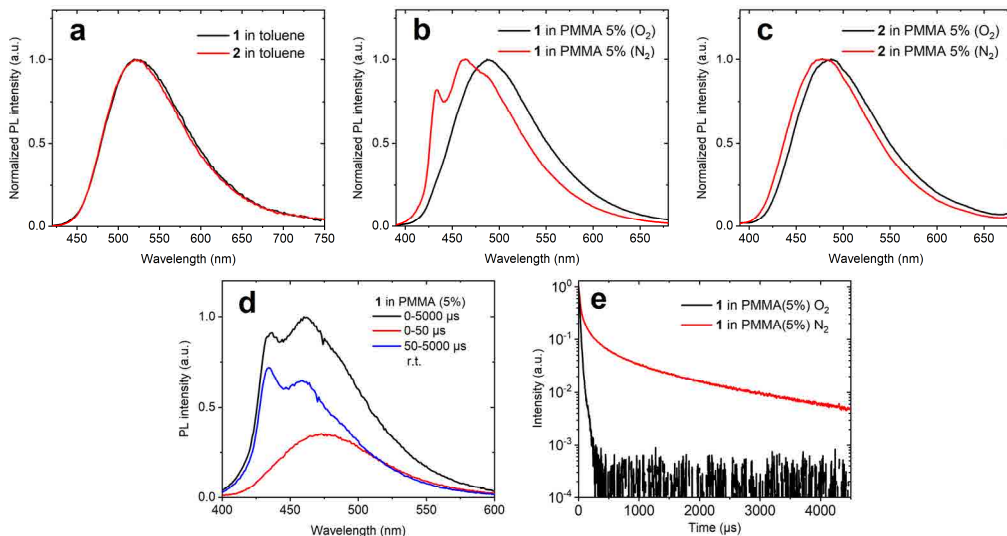

Figure 4. (a) Photoluminescence of complexes **1** and **2** in deoxygenated toluene solution (10^{-4} M). Photoluminescence of complexes **1** (b) and **2** (c) doped in PMMA (5% emitter concentration) in ambient conditions and inert nitrogen atmosphere. (d) Time-resolved emission of complex **1** in PMMA matrix (5% emitter concentration) at r.t. (e) Long-time range (0-5000 μs) phosphorescence decay measurements of complex **1** in PMMA matrix (5% emitter concentration) at r.t.

An increase of PL efficiency (Φ_{pl} = 0.79-0.80) and hypsochromic shift (rigidochromism) in comparison to the emission of toluene solutions was observed upon doping complexes in PMMA. The increase of the Φ_{pl} is attributed to the suppression of the emitter molecule torsional freedom in rigid matrix.[19] Same as the symmetrical complexes **3-6**, the unsymmetrical complexes **1** and **2** are susceptible to concentration quenching. The PL efficiency for **1** and **2** drops to 0.16 and 0.26 in neat films, accordingly. However, the concentration quenching for the unsymmetrical complexes is not as profound as for the symmetrical complexes, for which Φ_{pl} in the margins of 0.03 to 0.08 in neat films was observed. As stated before, it could be assumed that unfunctionalized Dipp group acts as inert buffer that prevents intermolecular interactions and nonradiative deactivation mechanisms.

Complexes dispersed in PMMA matrix exhibit unusual luminescence properties. By exposure of thin film samples to inert atmosphere (N_2) significant changes in PL spectra were observed (Figure 4b and 4c). Changes of emission properties in deoxygenated atmosphere are an indication that processes including triplet excited states are involved in these spectral shifts. To gain insight in the underlying mechanism for the appearance of the structured emission profile, time-resolved emission and luminescence decay measurements were obtained (Figure 4d and 4e) for complex **1**. The results show an emergence of long-lived structured emission under anaerobic conditions attributed to the ^{3}LE phosphorescence of the carbazolide ligand. The lifetime of the structured emission could be estimated at several hundred microseconds. A relatively weaker structureless CT emission band overlaps with the carbazolide phosphorescence. The ^{3}LE phosphorescence is effectively quenched in aerobic conditions with only the short-lived CT emission remaining. A small hypsochromic shift (11 nm) was observed for emission maxima for complex **2** in anaerobic conditions. A dual TADF mechanism for the CT emission similar to complexes **3-6** could be proposed. In this case emission originating from two distinct TADF processes (faster $TADF_1$ and slower $TADF_2$) takes place. It can be argued that the slower $TADF_2$ could be more susceptible to oxygen quenching than faster $TADF_1$. Thus, the blue shifted emission band originating in deoxygenated atmosphere could be attributed to the slower $TADF_2$ process. The origin of the dual TADF processes was attributed to the existence of two distinctive conformations in excited state for complexes **3-6**. A more comprehensive study of this phenomenon is given in our previous report.[11]
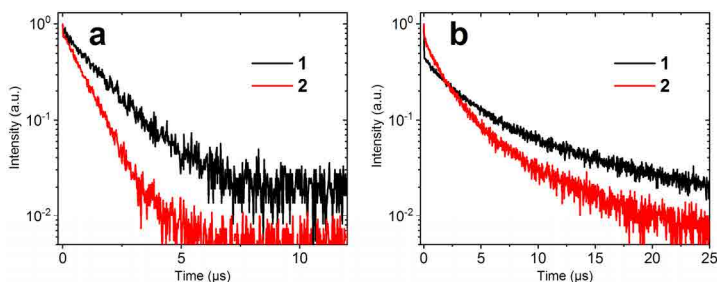

Figure 5. (a) Photoluminescence decay of complexes **1** and **2** in deoxygenated toluene solution (10^{-4} M). (b) Photoluminescence decay of complexes **1** and **2** doped in PMMA (5% emitter concentration).

Triexponential functions could be fitted to the PL decay curves of complexes doped in PMMA (Figure 5b, Table 1). However, it must be noted that the presence of an underlying long-lived ^{3}LE phosphorescence obstructs a precise estimation of the individual decay component contributions for complex **1**. The PL proceeds with a prompt fluorescence (τ_{prompt} = 19-37 ns). The contribution of the prompt fluorescence to the overall photoluminescence intensity is small (0.7% for complex **2**). The delayed fluorescence consists of two components. The lifetime of the faster component (τ_{TADF^1}= 1.38-2.27 µs) is approximately four times smaller than the lifetime of slower component (τ_{TADF^2}= 5.38-9.86 µs). The contributions of $TADF_1$ and $TADF_2$ to the overall photoluminescence intensity are almost identical for complex **2** (44.3% and 55.0%, accordingly). The lifetimes of the individual components of the delayed fluorescence decrease two times by the substitution of carbazolide ligand in **1** with 1,8-dimethylcarbazolide ligand in **2**. A similar observation was concluded for complexes **3-6**. The effect was attributed to a more favorable face-to-face alignment of donor and acceptor fragments in complexes **4** and **6** containing a 1,8-dimethylcarbazolide ligand compared to complexes **3** and **5** containing a carbazolide ligand. The overall weighed average radiative emission rate for **2** (k_r =2.21×10^5 s^{-1}) is comparable to complexes **4** and **6** (k_r =2.89-3.32×10^5 s^{-1}) indicating that an effective TADF still takes place in the presence of only one phenylsulphonyl- acceptor group.

Table 1. Emissive properties of complexes **1** and **2**. [a]Estimated contributions of individual decay components. [b]Weighted average of all PL decay components.

Complex	λ_{max} (nm)	Φ_{pl}	τ_{prompt} (ns)	τ_{TADF} (µs)	τ_{TADF}^{1} (µs)	τ_{TADF}^{2} (µs)	τ_{Avg}^{b} (µs)	k_r^{b} (×10⁵ s⁻¹)	k_{nr}^{b} (×10⁵ s⁻¹)
				Toluene solution (10⁻⁴M)					
1	519	0.38	8.3 (0.1%)[a]	1.47 (99,9%)[a]	-	-	1.47	2.59	4.22
2	521	0.39	-	0.87 (100%)[a]	-	-	0.87	4.48	7.01
				PMMA film (5%)					
1	464	0.80	19.4	-	2.27	9.86	-	-	-
2	476	0.79	37.2 (0.7%)[a]	-	1.38 (44.3%)[a]	5.38 (55.0%)[a]	3.57	2.21	0.59

The PL spectra of emitters in PMMA matrix undergo pronounced changes upon cooling to 77K (Figure 6a and 6b). Time-resolved PL measurements display almost a complete loss of CT emission band and preeminent ³LE phosphorescence of carbazolide ligand for **1**. For complex **2** the intensity of the ³LE phosphorescence is comparable to the slightly blueshifted emission from the CT state. It has been previously demonstrated that the hypsochromic shift is caused by the destabilization of the CT excited state in the rigid frozen host matrix.[6] The TD-DFT calculations (Figure 2) show that energy of the ¹CT state is only slightly (0.03 eV) lower compared to the ³LE state of **2** and even a small destabilizing effect provided by the freezing of the host matrix is enough to raise ¹CT state above the ³LE state.
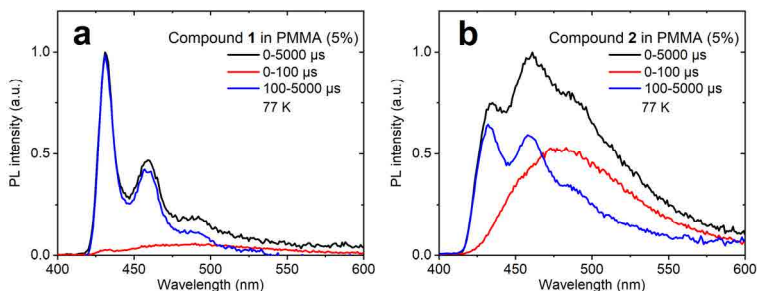

Figure 6. Time-resolved emission of complex **1** (a) and complex **2** (b) in PMMA matrix (5% emitter concentration) at 77 K temperature.

PL kinetics for emitters doped in PMMA were studied in the temperature interval 50-300 K (Figure 7). Complex **2** was chosen for the temperature dependent emission measurements due to the presence of a distinguishable CT emission band in the whole temperature range. In order to avoid possible contribution of ³LE phosphorescence of the 1,8-dimethylcarbazolide, the PL measurements were in performed in time-resolved mode (Figure 7a). The overall intensity of the CT emission band diminishes with cooling indicating a behavior similar to other TADF emitters.[20] As a result the Φ_{pl} of CT emission decreases from 0.79 at 300 K to 0.43 at 50 K. A retention of triexponential nature of PL decay curves was observed throughout the cooling process. However, the radiative emission rates for both the TADF₁ and the TADF₂ components decrease with cooling, indicating a thermal activation of the emissive process (Figure 7b). The fits to the Arrhenius plots of experimentally determined k_{rTADF1} and k_{rTADF2} values (Figure 7c and 7d) yielded ΔE_{ST1} = 0.0110 eV (for TADF₁) and ΔE_{ST2} = 0.0072 eV (for TADF₂). These results are in good agreement with the value provided by TD-DFT calculations and are comparable to the ΔE_{ST} values determined for the symmetrical complexes **4** and **6** (0.0062 eV - 0.0075 eV).
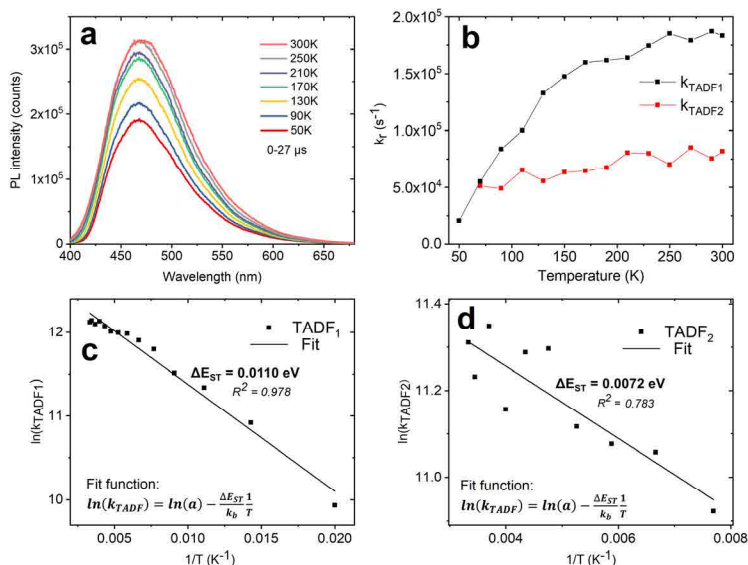
Figure 7. Temperature dependent emission measurements for complex **2** in PMMA matrix (5% emitter concentration): (a) Temperature induced changes in CT emission band intensity, PL spectra obtained in time-resolved mode (0-27 μs). (b) Temperature dependence of individual delayed fluorescence component radiative rates. (c) and (d) Arrhenius plots showing the correlation between k_{rTADF1} and k_{rTADF2} of **2** and temperature, accordingly. Fit function, fit lines and estimated ΔE_{ST} values are shown.

4. CONCLUSIONS

The synthetic approach to the novel asymmetrically substituted imidazolidine NHC copper (I) complexes has been elaborated. The asymmetrical phenylsulfonyl- acceptor group bearing ligand has been successfully integrated in the design of highly luminescent CMA complexes. We have demonstrated that the asymmetrical complexes exhibit similar photophysical properties compared to the previously reported symmetrical molecular design. By utilizing metal promoted through-space charge transfer process fast ($k_r = 2.21 \times 10^5$ s^{-1}) and highly efficient TADF could be realized. Additionally, the improved solubility and reduced luminescence concentration quenching extends the possibilities for the use of the asymmetrical complexes in applications like solution processed OLED's.

ACKNOWLEDGMENTS

REFERENCES

[1] Nakanotani, H., Tsuchiya, Y. and Adachi, C., "Thermally-activated delayed fluorescence for light-emitting devices," Chem. Lett. 50(5), 938–948 (2021).

[2] Gibson, J., Monkman, A. P. and Penfold, T. J., "The Importance of Vibronic Coupling for Efficient Reverse Intersystem Crossing in Thermally Activated Delayed Fluorescence Molecules," ChemPhysChem 17(19), 2956–2961 (2016).

[3] Eng, J. and Penfold, T. J., "Open questions on the photophysics of thermally activated delayed fluorescence,"

Commun. Chem. 4(1), 21–24 (2021).

[4]   Samanta, P. K., Kim, D., Coropceanu, V. and Brédas, J. L., "Up-Conversion Intersystem Crossing Rates in Organic Emitters for Thermally Activated Delayed Fluorescence: Impact of the Nature of Singlet vs Triplet Excited States," J. Am. Chem. Soc. 139(11), 4042–4051 (2017).

[5]   Di, D., Romanov, A. S., Yang, L., Richter, J. M., Rivett, J. P. H., Jones, S., Thomas, T. H., Abdi Jalebi, M., Friend, R. H., Linnolahti, M., Bochmann, M. and Credgington, D., "High-performance light-emitting diodes based on carbene-metal-amides," Science. 356(6334), 159–163 (2017).

[6]   Hamze, R., Peltier, J. L., Sylvinson, D., Jung, M., Cardenas, J., Haiges, R., Soleilhavoup, M., Jazzar, R., Djurovich, P. I., Bertrand, G. and Thompson, M. E., "Eliminating nonradiative decay in Cu(I) emitters: 99% quantum efficiency and microsecond lifetime," Science. 363(6427), 601–606 (2019).

[7]   Hamze, R., Shi, S., Kapper, S. C., Ravinson, D. S. M., Estergreen, L., Jung, M. C., Tadle, A. C., Haiges, R., Djurovich, P. I., Peltier, J. L., Jazzar, R., Bertrand, G., Bradforth, S. E. and Thompson, M. E., "'Quick-Silver' from a Systematic Study of Highly Luminescent, Two-Coordinate, d10 Coinage Metal Complexes," J. Am. Chem. Soc. 141(21), 8616–8626 (2019).

[8]   Shi, S., Jung, M. C., Coburn, C., Tadle, A., Sylvinson, D. M. R., Djurovich, P. I., Forrest, S. R. and Thompson, M. E., "Highly Efficient Photo- and Electroluminescence from Two-Coordinate Cu(I) Complexes Featuring Nonconventional N-Heterocyclic Carbenes," J. Am. Chem. Soc. 141(8), 3576–3588 (2019).

[9]   Romanov, A. S., Jones, S. T. E., Gu, Q., Conaghan, P. J., Drummond, B. H., Feng, J., Chotard, F., Buizza, L., Foley, M., Linnolahti, M., Credgington, D. and Bochmann, M., "Carbene metal amide photoemitters: Tailoring conformationally flexible amides for full color range emissions including white-emitting OLED," Chem. Sci. 11(2), 435–446 (2020).

[10]   Hamze, R., Idris, M., Daniel Sylvinson, M. R., Chul Jung, M., Haiges, R., Djurovich, P. I. and Thompson, M. E., "Highly Efficient Deep Blue Luminescence of 2-Coordinate Coinage Metal Complexes Bearing Bulky NHC Benzimidazolyl Carbene," Front. Chem. 8(May), 1–9 (2020).

[11]   Ruduss, A., Turovska, B., Belyakov, S., Stucere, K. A., Vembris, A. and Traskovskis, K., "Carbene–Metal Complexes As Molecular Scaffolds for Construction of through-Space Thermally Activated Delayed Fluorescence Emitters," Inorg. Chem. 61(4), 2174–2185 (2022).

[12]   Zhang, M., Xu, Z. and Shi, D., "Cu(I)–N-heterocyclic carbene-catalyzed base free C–N bond formation of arylboronic acids with amines and azoles," Tetrahedron 79, 131861 (2021).

[13]   Bedford, R. B. and Betham, M., "N-H carbazole synthesis from 2-chloroanilines via consecutive amination and C-H activation," J. Org. Chem. 71(25), 9403–9410 (2006).

[14]   Bochevarov, A. D., Harder, E., Hughes, T. F., Greenwood, J. R., Braden, D. A., Philipp, D. M., Rinaldo, D., Halls, M. D., Zhang, J. and Friesner, R. A., "Jaguar: A high-performance quantum chemistry software program with strengths in life and materials sciences," Int. J. Quantum Chem. 113(18), 2110–2142 (2013).

[15]   Kim, K.-H., Yoo, S.-J. and Kim, J.-J., "Boosting Triplet Harvest by Reducing Nonradiative Transition of Exciplex toward Fluorescent Organic Light-Emitting Diodes with 100% Internal Quantum Efficiency," Chem. Mater. 28(6), 1936–1941 (2016).

[16]   Santoro, O., Collado, A., Slawin, A. M. Z., Nolan, S. P. and Cazin, C. S. J., "A general synthetic route to [Cu(X)(NHC)] (NHC = N-heterocyclic carbene, X = Cl, Br, I) complexes," Chem. Commun. 49(89), 10483–10485 (2013).

[17]   Nobuyasu, R. S., Ward, J. S., Gibson, J., Laidlaw, B. A., Ren, Z., Data, P., Batsanov, A. S., Penfold, T. J., Bryce, M. R. and Dias, F. B., "The influence of molecular geometry on the efficiency of thermally activated delayed fluorescence," J. Mater. Chem. C 7(22), 6672–6684 (2019).

[18]   Lüdtke, N., Föller, J. and Marian, C. M., "Understanding the luminescence properties of Cu (I) complexes: a quantum chemical perusal," Phys. Chem. Chem. Phys. 22(41), 23530–23544 (2020).

[19]   Li, T. Y., Muthiah Ravinson, D. S., Haiges, R., Djurovich, P. I. and Thompson, M. E., "Enhancement of the Luminescent Efficiency in Carbene-Au(I)-Aryl Complexes by the Restriction of Renner-Teller Distortion and Bond Rotation," J. Am. Chem. Soc. 142(13), 6158–6172 (2020).

[20]   Uoyama, H., Goushi, K., Shizu, K., Nomura, H. and Adachi, C., "Highly efficient organic light-emitting diodes from delayed fluorescence," Nature 492(7428), 234–238 (2012).

Jece, A.; **Ruduss, A.**; Štucere, K. A.; Vembris, A.; Traskovskis, K.
TADF Active Carbene-Metal-Amide Complexes Exhibiting Through-Space
Charge Transfer: An Impact of Metal Atom. *Organic Electronics and
Photonics: Fundamentals and Devices III.* **2022**, 1214909.

TADF active carbene-metal-amide complexes exhibiting through-space charge transfer: an impact of metal atom

Annija Jece[a], Armands Ruduss[a], Kitija A. Stucere[b], Aivars Vembris[b], Kaspars Traskovskis*[a]

[a]Institute of Applied Chemistry, Riga Technical University, 3/7 Paula Valdena Str., Riga, LV-1048, Latvia; [b]Institute of Solid State Physics, University of Latvia, 8 Kengaraga Str., Riga, LV-1064, Latvia

ABSTRACT

The impact of metal atom on the photophysical properties of luminescent organometallic carbene-metal-amide complexes exhibiting through-space charge transfer is investigated. The substitution of copper atom with gold alters the excited state energy level configuration of the emitter. While in the copper-based emitters the lowest triplet excited state (T_1) is related to a through-space charge transfer between the carbazolide donor and carbene-bound phenylsulphonyl acceptor, in the gold-bearing structural analogue T_1 level is accompanied by an additional closely situated triplet state T_2, which features a charge transfer between the carbazolide donor and imidazolidine carbene acceptor. Because of a significant spin-orbit coupling provided by Au atom T_2 state exhibits relatively fast phosphorescence rate of 8×10^4 s^{-1}. Consequently, the emissive process for the gold-functionalized compound can be characterized with a co-occurring thermally activated delayed fluorescence (TADF) and phosphorescence, in contrast to the copper-based structural analogues, where only TADF is observed.

Keywords: TADF, N-heterocyclic carbene, gold complex, through-space charge transfer, phosphorescence

1. INTRODUCTION

Organic molecules possessing the ability to emit light from the forbidden triplet state have found applications in a wide variety of directions, such as organic light emitting diodes (OLEDs),[1] luminescent sensors[2] and photocatalysts.[3] Compounds exhibiting thermally activated delayed fluorescence (TADF) can be classified as one of the main classes of triplet emitters.[4] In these materials the lowest energy triplet excited state (T_1) can undergo a reverse intersystem crossing (rISC) to the emissive singlet state (S_1) under thermal activation, granted that the energy gap between these two sates ΔE_{ST} is sufficiently low. Majority of the studied TADF active compounds are all-organic molecules in which the small ΔE_{ST} value is determined by the low overlap integral between the highest occupied molecular orbital (HOMO) and the lowest unoccupied molecular orbital (LUMO).[5] Conventional structural approach to such emitters involves synthesizing luminophores, which are composed of covalently bound structural fragment pairs with electron rich and electron deficient nature. A key requirement for such design is a structural twist between the electron donor and acceptor planes, limiting the conjugation between the involved π-electron systems. Further structural evolution of TADF materials allowed even lower ΔE_{ST} by taking advantage of through-space charge transfer process in exciplex forming bicomponent mixtures[6] or in so called intramolecular exciplexes.[7–9] While minimal HOMO-LUMO overlap integrals are achieved in these designs, such emitters suffer from low radiative rates, partly caused by insufficient spin-orbit coupling (SOC) between the involved T_1 and S_1 states.[10]

Recently we have demonstrated a novel structural concept for through-space TADF-active compounds. On the basis of two-coordinate metalloorganic complexes, composed of carbene and carbazolide ligands and copper metal, through-space charge transfer process was observed between the carbazolide donor and carbene-bound sulphonyl acceptor.[11] TADF process in the compounds was aided by small ΔE_{ST} in the range of 0.0062−0.0075 eV and non-zero SOC provided by the present Cu atom. In this study we examine the structural analogue (complex **1**) of the previously investigated carbene-metal-amide (CMA) complexes, where copper atom is substituted with more massive gold (Scheme 1). Extensive photophysical characterization of the compound has been performed, including temperature-dependent photoluminescence (PL) and PL kinetics measurements. Additionally, DFT calculations were performed to interpret the light emission mechanism of complex **1**. As the results show, the substitution of the metal has profound effects on the photophysical behavior for the examined emitter class.
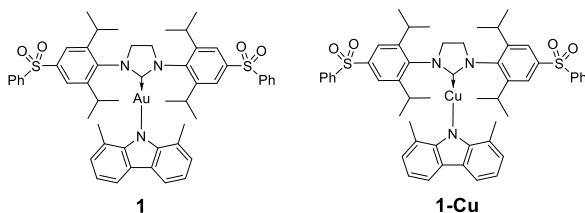
Scheme 1. Chemical structure of the investigated gold-based complex **1** and its previously studied copper-based structural analogue 1-**Cu**.[11]

2. EXPERIMENTAL

2.1 General methods

All synthetic procedures and purification of NHC derivatives were carried out using standard Schlenk techniques and using water and oxygen-free solvents. Starting materials and solvents were purchased from commercial suppliers. Compound **2**[11] and 1,8-dimethylcarbazole[12] were prepared by following the procedures described in the literature. NMR spectra were obtained on a Bruker Avance 300 MHz spectrometer using DMSO-d_6 residual signals as an internal reference (^{1}H, δ 2.50; ^{13}C, δ 39.52).

2.2 Synthesis and structural characterization of the asymmetrical CMA complexes
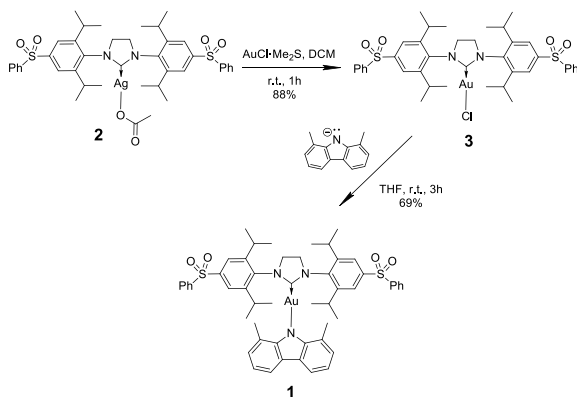
Scheme 2. Synthesis of complex **1**.

Compound (**3**): A mixture of **2** (0.818 g, 1.01 mmol) and AuCl·Me$_2$S (0.355 g, 1.206 mmol) was stirred in dry DCM (50 ml) for 1 h under inert atmosphere. Then reaction mixture was filtered into hexane (100 ml) through a pad of celite. The DCM was evaporated under reduced pressure, and additional hexane was added to precipitate the product. Mixture was filtered and washed with hexane to obtain product as grayish-white solid. Yield: 0.797 g (88%). **^{1}H NMR** δH (DMSO-d_6, 500 MHz): 8.08 (d, J = 7.4 Hz, 4H), 7.88 (s, 4H), 7.71 (t, J = 6.9 Hz, 2H), 7.65 (t, J = 7.3 Hz, 4H), 4.14 (s, 4H), 3.11 (hept, J = 6.1 Hz, 4H), 1.30 (d, J = 5.8 Hz, 12H), 1.24 (d, J = 6.1 Hz, 12H). **^{13}C NMR** δC (DMSO-d_6, 125.77 MHz): 149.07, 142.52, 140.75, 139.02, 134.00, 129.87, 127.62, 123.53, 53.78, 28.42, 24.70, 23.19.

Compound (**1**): A mixture of 1,8-dimethylcarbazole (0.032 g, 0.164 mmol) and KOtBu (0.031 g, 0.276 mmol) was stirred in dry, deoxygenated THF (10 ml) for 30 min. Then a solution of compound 3 (0.10 g, 0.111 mmol) in dry, deoxygenated THF (30 ml) was added to reaction flask and the resulting mixture stirred for 3 h. Finally, reaction mixture

was filtered through a pad of celite into degassed hexane (200 ml) to precipitate the product. The resulting mixture was filtered and washed with hexane to obtain grayish-white solid. Yield: 0.081 g (69%). **^{1}H NMR** δH (DMSO-d_6, 500 MHz): 8.25 (d, J = 7.3 Hz, 4H), 8.00 (s, 4H), 7.84 (t, J = 6.7 Hz, 2H), 7.75 (t, J = 7.0 Hz, 4H), 7.62 (t, J = 7.3 Hz, 2H), 6.62 (t, J = 7.0 Hz, 2H), 6.20 (d, J = 6.5 Hz, 2H), 4.20 (s, 4H), 3.21 (hept, J = 6.6 Hz, 4H), 1.36 (d, J = 5.7 Hz, 12H), 1.21 (d, J = 5.9 Hz, 12H), 1.13 (s, 6H). **^{13}C NMR** δC (DMSO-d_6, 125.77 MHz): 148.82, 147.93, 143.01, 140.86, 139.47, 134.16, 129.99, 127.96, 124.18, 123.88, 123.84, 120.36, 116.79, 114.66, 53.86, 28.57, 24.52, 23.38, 17.10.

2.3 Photo physical measurements

For UV-Vis absorption and PL measurements solutions with material concentration of $1 \cdot 10^{-5}$ mol L^{-1} were used. Solutions for Φ_{PL} and emission decay measurements were prepared under Ar atmosphere in glovebox using previously deoxygenated solvents. PMMA films for PL measurements were prepared from chlorobenzene solutions using drop-casting method. The UV-Vis spectra were recorded with a Perkin Elmer Lambda 35 spectrometer. Emission spectra, Φ_{PL} and PL lifetimes for solution and thin films at room temperature and at 77 K (in liquid nitrogen filled quartz Dewar) were measured employing QuantaMaster 40 spectrofluorometer (Photon Technology International, Inc.). The 375 nm laser with 60 ps pulse width and tunable repetition rate (between 1Mh and 50 kHz) was used for the fast (nanosecond - microsecond range) kinetics measurements. Steady state and pulsed (3µs pulse width) xenon lamp was used for steady state and millisecond kinetics measurements. The excitation source for temperature-dependent (50–300 K, He cryostat) PL measurements was a tunable Ekspla laser NT 342/3UV with the repetition rate 10 Hz and 5 ns pulse width. Photoluminescence spectra and PL decays were obtained with PMT attached to Andor monochromator. Analysis of PL kinetics and rate constant acquisition were performed following procedures and formulas described in our previous work.[11]

2.4 DFT calculations

Density functional theory (DFT) calculations, including geometry optimization and time-dependent DFT (TD-DFT) were performed using Schrödinger Jaguar[13] software package (release 2020–2). Geometry optimization and TD-DFT calculations used MN15[14] functional and LACVP** basis. Ground state geometry and Tamm–Dancoff approximation (TDA) was used for TD-DFT calculations. For solvation effects conductor-like polarizable continuum model (CPCM) was used. SOC-TD-DFT calculations were performed at MN06/ ZORA-DEF2-TZVP level using Orca 5.0.1 software.[15]

3. RESULTS AND DISCUSSION

3.1 Synthesis

The synthetic path to complex **1** is outlined in Scheme 2. The synthesis of the starting compound imidazolidine carbene – silver acetate complex **2** is described in our previous paper.[11] The gold atom was introduced in the molecule through the transmetalation reaction in the presence of AuCl·Me$_2$S. The target compound **1** was acquired in the following reaction with deprotonated 1,8-dimethylcarbazole as a light-gray solid. In the crystalline form the compound is stable and can be indefinitely stored under air exposure.

3.2 Photophysical characterization

UV-Vis spectra of complex **1** can be seen in Figure 1a. Like in its structural analogue **1-Cu**, UV-Vis absorption band consists of the structured region (300–370 nm), which is attributed to π–π* transitions of the carbazolide donor fragment. Region at 370-420 nm features the shoulder of CT transition. This is indicated by the characteristic negative solvatochromism of the band, observed in the solvent series toluene–chlorobenzene–acetonitrile.[16] In toluene solution the compound exhibits bluish-green luminescence characterized with a broad PL band (Figure 1b) with maximum at 521 nm (Table 1). The corresponding PL decay (Figure 2a) can be approximated with two-exponential decay function, composed of prompt fluorescence (3 ns) and delayed component (0.43 µs). As a consequence of heavy metal presence, only 0.5 % of the total emission originates from the singlet sate due to rapid excitation transfer to the triplet state. Similarly to Cu-based emitters, in solution PL quantum yield (Φ_{PL}) of complex **1** is relatively low and amounts to 0.27.
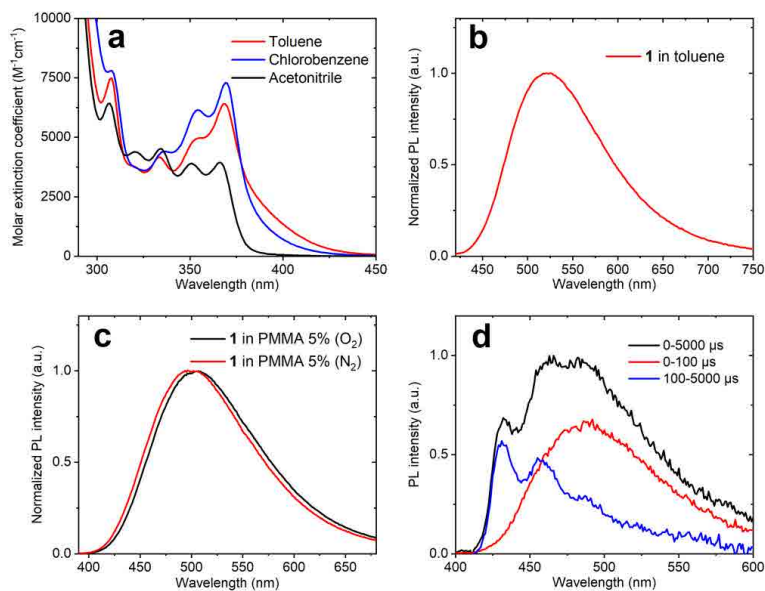
Figure 1. UV-Vis absorption spectra of complex **1** in different polarity solvents (a). PL spectra of complex **1** in toluene solution (b). PL spectra of complex **1** in doped PMMA film (5 wt%) taken in air and under N_2 (c). Time-resolved PL spectra of complex **1** in doped PMMA film (5 wt%) measured at 77 K temperature (d).

PL efficiency of compound **1** significantly increases in PMMA films. At 5 wt% emitter mass fraction Φ_{PL} reaches value 0.69. In analogy to **1-Cu**, such observation is explained by through-space CT nature of the emissive excited state, which is susceptible to several PL efficiency-reducing torsional motions, namely the rotation around Au–carbazolide and imidazolidine–phenylsulphonyl bonds. In solid state these motions are suppressed, increasing Φ_{PL} value of the compound. PL intensity substantially drops, by 32 %, if the PMMA film is exposed to air oxygen, providing evidence for triplet state involvement in the emissive process. Additionally, in oxygen free environment PL band experiences a sight blueshift (Figure 1c). In contrast to the previously examined toluene solution, PL kinetics in PMMA film can be characterized with triexponential decay function, consisting of prompt fluorescence and two delayed emission components (Table 1). Like in the solution, the contribution of prompt emission is small, as it accounts only for 0.2 % of the total emission. The delayed emission features a faster (1.36 μs, 31.8 %) and slower (4.73 μs, 68 %) component. The overall radiative rate (k_r) of **1** is 1.89×10^5 s^{-1}, which is notably slower than in the case of **1-Cu**, for which this parameter was estimated at 2.89×10^5 s^{-1}.
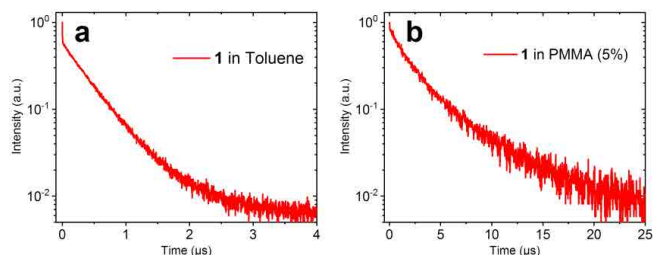

Figure 2. PL decays of complex 1, measured in toluene solution (a) or in doped PMMA film (5 wt%) (b).

At 77 K temperature PL band of complex **1** transforms, assuming a structured shape. Time resolved PL measurements (Figure 1d) relate this observation to simultaneous emission from the CT state (time interval 0–100 μs) and phosphorescence from the local triplet excited state (^{3}LE) of the carbazolide donor (time interval 100–5000 μs). Such behavior is characteristic for the investigated emitter class[11] and is attributed to the rigidochromic blueshift of the CT emission band which arises due to the destabilizing effects of the frozen host solvation shell around the emitter molecules.[17]

Table 1. PL characteristics of complex **1**.

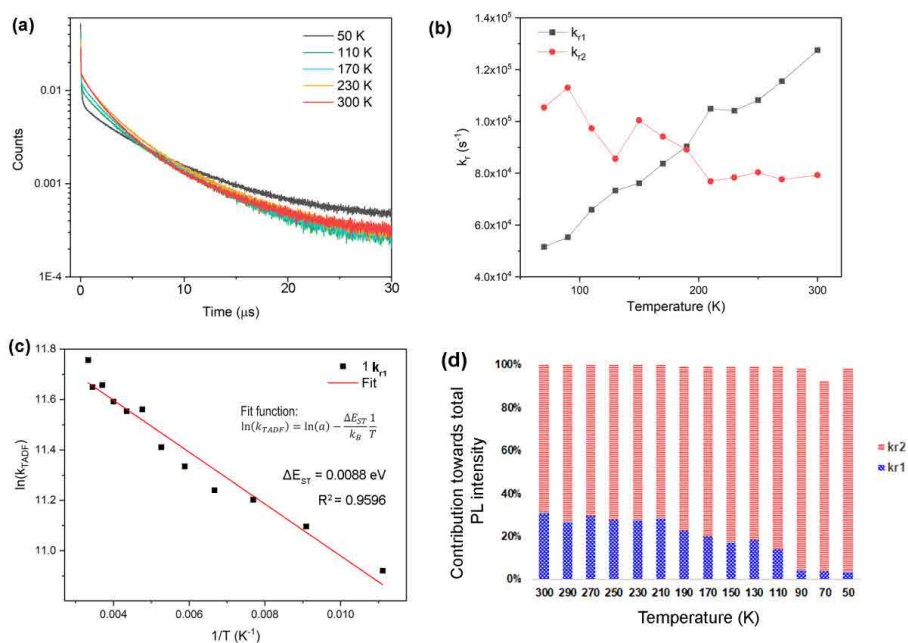| Medium	λ_{max} (nm)	Φ_{pl}	τ_{prompt} (ns)	τ_2 (μs)	τ_3 (μs)	τ_{avg} (μs)	k_r (×10^5 s^{-1})	k_{nr} (×10^5 s^{-1})
Toluene solution (10^{-5} M)	521	0.27	3 (0.5%)	0.43 (99.5%)	-	0.43	6.31	17.07
PMMA film (5%)	502	0.69	1 (0.2%)	1.36 (31.8%)	4.73 (68.0%)	3.65	1.89	0.85

Figure 3. PL decays of complex **1** at selected temperatures measured in PMMA films (5 wt%) (a). Radiative rates of the delayed emission components (k_{r1} and k_{r2}) in response to temperature changes (b). Arrhenius plot (squares) showing the correlation between k_{r1} and temperature (c). Fit function formula, corresponding fit (line) and obtained ΔE_{ST} value is shown. Contribution of individual PL decay components towards total PL intensity (d).

In order to closer examine the light emission mechanism of complex **1** temperature-dependent PL measurements were conducted in the range 300–50 K. PL decays measured at selected temperatures are given in Figure 3a. Throughout the examined cooling range the sample retained three-exponential PL decay featuring a prompt fluorescence and two delayed emission components. On the surface this behavior is identical to that previously observed for complex **1-Cu**, which also exhibited similar PL decay profile. However, the deeper analysis reveals notable differences between the

compounds. First, in the examined temperature interval the intensity of CT emission remains almost identical for compound **1**, whereas for copper-based structural analogues a gradual intensity decline was observed, as the excitation was presumably transferred to the dark triplet ^{3}CT state, which is not able to emit due to the insufficient SOC.[11] The calculated k_r values for the delayed emission components at different temperatures reveal another discrepancy (Figure 3b). In the case of complex **1** it can be seen that the fastest delayed emission component (k_{r1}) exhibits a well-resolved thermal activation, indicating TADF mechanism of the corresponding emissive process. In the case of k_2, however, no thermal activation can be seen and the emissive rate remains almost unchanged throughout the cooling range. This is a contrasting behavior to **1-Cu**, where both delayed emission components were attributed to TADF process due to an apparent thermal activation. Arrhenius plot for the thermally activated PL component of complex **1** (Figure 3c), relating k_{r1} value with the temperature,[18] indicates ΔE_{ST} gap of 0.0088 eV. This value is in line with the singlet-triplet energy gaps seen in copper-based structural analogues of **1** and is consistent with the presumed through-space CT nature of the emissive state. With the cooling the PL intensity transfer takes place between the delayed emission components (Figure 3d). While at the room temperature conditions the emissive process characterized with rate constant k_{r1} accounts for around 30 % of the total PL intensity, at 50 K the PL intensity almost exclusively originates from emissive process k_{r2}, which now accounts for 95 %. Such intensity transfer is an indication of a significant energy barrier between the geometries of the two respective emissive states, as no thermal equilibration takes place through the examined temperature range.
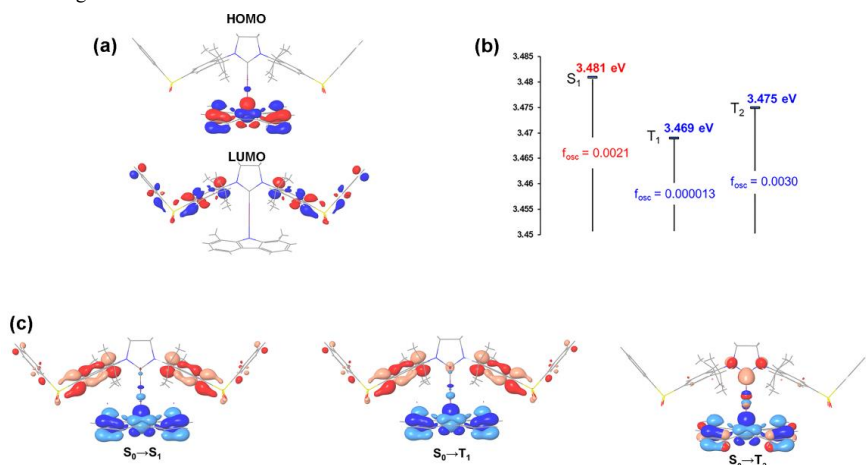

Figure 4. Calculated HOMO and LUMO orbitals of complex **1** (a). Diagram showing the lowest energy excited states of complex **1** (b). Oscillator strength values (f_{osc}) for transitions are given. Natural transition orbitals (NTOs) for the lowest energy transitions (c). Blue color illustrates the hole, while red the particle.

To better interpret the experimental observations, DFT calculations were performed for complex **1**. The optimized geometry of the compound predicts a molecular geometry, where the carbazolide plane is pushed out of the coplanar position with the carbene. This is consistent with the X-ray crystallography data acquired for Cu-based structural analogues, where a similar structural deformation was observed due to the sterical repulsion between the methyls of 1,8-dimethylcarbazole and carbene-bound diisopropylphenyl groups. Frontier molecular orbital configuration of **1** is similar to that of **1-Cu**, as HOMO is placed on carbazolide fragment, while LUMO resides on the peripheral phenylsulfonyl groups (Figure 4a). TD-DFT calculations were performed to analyze the excited state energy level configuration of the complex (Figure 4b,c). Predictably, the lowest energy excited singlet state possesses CT nature with electron transfer between the carbazolide and phenylsulfonyl groups. T_1 level corresponds to the triplet transition with the identical electron transfer configuration and is placed only 0.012 eV below the S_1 state. While similar level placement was observed for **1-Cu**, a notable difference can be resolved in the case of **1**. An additional closely placed triplet state (T_2) is predicted, which resides in-between the S_1 and T_1 levels, only 0.006 eV above T_1 and 0.006 eV below S_1. This transition features the electron transfer between carbazolide and carbene ring systems. Similar carbazolide-carbene CT states determines emissive processes in the classical CMA emitters.[18–20] In contrast to our structural design featuring through-

space CT process, carbazolide-carbene electronic transitions can be characterized with significantly higher HOMO-LUMO overlap integrals, as the metal atom is effectively shared between the both frontier orbitals. This results in larger ΔE_{ST}, but at the same time stronger oscillator strength values. Consequently, such CMAs possess highly favorable photophysical properties in the form of large Φ_{PL} and low PL lifetimes, in some cases below 1 μs.[21,22] For complex **1** the corresponding carbazolide-carbene CT singlet sate (S_3) is situated 0.19 eV above T_2 level. It can be reasoned that rISC process $T_2 \rightarrow S_3$ in this case cannot result in a viable emissive pathway due to the low laying S_1 state, to which rapid internal conversion $S_3 \rightarrow S_1$ would take place. On the other hand, CMA emitters with carbazolide-carbene CT transitions often exhibit reasonably fast phosphorescence from the corresponding ^{3}CT state due to sufficiently large SOC values, as metal atom d orbitals are significantly involved in the emissive charge transfer process. Indeed, the performed SOC-TD-DFT calculations predict that transition $T_2 \rightarrow S_0$ is reasonably bright, with oscillator strength (f_{osc}) value of 0.003. In fact, the transition is stronger than the through-space CT process $S_1 \rightarrow S_0$, where $f_{osc} = 0.0021$. Due to a minimal involvement of gold d-orbitals f_{osc} for $T_1 \rightarrow S_0$ is only 0.000013.

Based on the previously discussed theoretical calculations a following emissive mechanism can be proposed for complex **1**. At room temperature conditions the emission originates from two co-occurring pathways. The first is a TADF process, characterized with rate constant k_{r1}, which is associated with rISC from the closely placed T_1 and T_2 states to the emissive S_1 level. The second emissive process is attributed to phosphorescence from T_2 level (k_{r2}), which is aided by the strong SOC provided by the gold atom. This can be reasoned by the apparent thermal activation seen in the case of k_{r1} process, while for k_{r2} the rate constant is not affected by temperature. Second, no cooling-induced PL intensity drop is seen for complex **1**, in stark contrast to **1-Cu**, which lacks the efficient emissive pathway from the ^{3}CT state.

4. CONCLUSIONS

We have shown that the photophysical properties of metal assisted through-space TADF emitters, featuring carbene-metal-amide molecular architecture can be substantially modified by altering the complex-forming metal. The substitution of copper with gold in imidazolidine-based CMA **1**, transforms the emissive mechanism from strictly TADF to the combination of TADF and phosphorescence. Such transformation is not strictly related to the introduction of heavier metal, but by the excited state energy level shift that places the bright carbazolide-to-carbene ^{3}CT state in a close proximity to the T_1 level. In such way the investigated molecular design can be considered as a hybrid case between the through-space TADF emitters and conventional strongly luminescent CMAs.

ACKNOWLEDGMENTS

REFERENCES

[1] Yersin, H., Rausch, A. F., Czerwieniec, R., Hofbeck, T. and Fischer, T., "The triplet state of organo-transition metal compounds. Triplet harvesting and singlet harvesting for efficient OLEDs," Coord. Chem. Rev. 255(21–22), 2622–2652 (2011).

[2] Ni, F., Li, N., Zhan, L. and Yang, C., "Organic Thermally Activated Delayed Fluorescence Materials for Time-Resolved Luminescence Imaging and Sensing," Adv. Opt. Mater. 8(14), 1902187 (2020).

[3] Bryden, M. A. and Zysman-Colman, E., "Organic thermally activated delayed fluorescence (TADF) compounds used in photocatalysis," Chem. Soc. Rev. 50(13), 7587–7680 (2021).

[4] [Uoyama, H., Goushi, K., Shizu, K., Nomura, H. and Adachi, C., "Highly efficient organic light-emitting diodes from delayed fluorescence," Nature 492(7428), 234–238 (2012).

[5] Köhler, A. and Beljonne, D., "The Singlet–Triplet Exchange Energy in Conjugated Polymers," Adv. Funct. Mater. 14(1), 11–18 (2004).

[6] Goushi, K. and Adachi, C., "Efficient organic light-emitting diodes through up-conversion from triplet to singlet excited states of exciplexes," Appl. Phys. Lett. 101(2), 023306 (2012).

[7] Shao, S., Hu, J., Wang, X., Wang, L., Jing, X. and Wang, F., "Blue Thermally Activated Delayed Fluorescence Polymers with Nonconjugated Backbone and Through-Space Charge Transfer Effect," J. Am. Chem. Soc. 139(49), 17739–17742 (2017).

[8] Tsujimoto, H., Ha, D.-G., Markopoulos, G., Chae, H. S., Baldo, M. A. and Swager, T. M., "Thermally Activated Delayed Fluorescence and Aggregation Induced Emission with Through-Space Charge Transfer," J. Am. Chem. Soc. 139(13), 4894–4900 (2017).

[9] Traskovskis, K., Sebris, A., Novosjolova, I., Turks, M., Guzauskas, M., Volyniuk, D., Bezvikonnyi, O., Grazulevicius, J. V., Mishnev, A., Grzibovskis, R. and Vembris, A., "All-organic fast intersystem crossing assisted exciplexes exhibiting sub-microsecond thermally activated delayed fluorescence," J. Mater. Chem. C 9(13), 4532–4543 (2021).

[10] Wang, Y., Huang, C., Ye, H., Zhong, C., Khan, A., Yang, S., Fung, M., Jiang, Z., Adachi, C. and Liao, L., "Through Space Charge Transfer for Efficient Sky-Blue Thermally Activated Delayed Fluorescence (TADF) Emitter with Unconjugated Connection," Adv. Opt. Mater. 8(2), 1901150 (2020).

[11] Ruduss, A., Turovska, B., Belyakov, S., Stucere, K. A., Vembris, A. and Traskovskis, K., "Carbene–Metal Complexes As Molecular Scaffolds for Construction of through-Space Thermally Activated Delayed Fluorescence Emitters," Inorg. Chem. 61(4), 2174–2185 (2022).

[12] Bedford, R. B. and Betham, M., "N -H Carbazole Synthesis from 2-Chloroanilines via Consecutive Amination and C−H Activation," J. Org. Chem. 71(25), 9403–9410 (2006).

[13] Bochevarov, A. D., Harder, E., Hughes, T. F., Greenwood, J. R., Braden, D. A., Philipp, D. M., Rinaldo, D., Halls, M. D., Zhang, J. and Friesner, R. A., "Jaguar: A high-performance quantum chemistry software program with strengths in life and materials sciences," Int. J. Quantum Chem. 113(18), 2110–2142 (2013).

[14] Yu, H. S., He, X., Li, S. L. and Truhlar, D. G., "MN15: A Kohn–Sham global-hybrid exchange–correlation density functional with broad accuracy for multi-reference and single-reference systems and noncovalent interactions," Chem. Sci. 7(8), 5032–5051 (2016).

[15] Neese, F., "The ORCA program system," WIREs Comput. Mol. Sci. 2(1), 73–78 (2012).

[16] Lüdtke, N., Föller, J. and Marian, C. M., "Understanding the luminescence properties of Cu(I) complexes: a quantum chemical perusal," Phys. Chem. Chem. Phys. 22(41), 23530–23544 (2020).

[17] Romanov, A. S., Jones, S. T. E., Gu, Q., Conaghan, P. J., Drummond, B. H., Feng, J., Chotard, F., Buizza, L., Foley, M., Linnolahti, M., Credgington, D. and Bochmann, M., "Carbene metal amide photoemitters: tailoring conformationally flexible amides for full color range emissions including white-emitting OLED," Chem. Sci. 11(2), 435–446 (2020).

[18] Hamze, R., Shi, S., Kapper, S. C., Muthiah Ravinson, D. S., Estergreen, L., Jung, M.-C., Tadle, A. C., Haiges, R., Djurovich, P. I., Peltier, J. L., Jazzar, R., Bertrand, G., Bradforth, S. E. and Thompson, M. E., "'Quick-Silver' from a Systematic Study of Highly Luminescent, Two-Coordinate, d 10 Coinage Metal Complexes," J. Am. Chem. Soc. 141(21), 8616–8626 (2019).

[19] Di, D., Romanov, A. S., Yang, L., Richter, J. M., Rivett, J. P. H., Jones, S., Thomas, T. H., Abdi Jalebi, M., Friend, R. H., Linnolahti, M., Bochmann, M. and Credgington, D., "High-performance light-emitting diodes based on carbene-metal-amides," Science (80-.). 356(6334), 159–163 (2017).

[20] Chotard, F., Sivchik, V., Linnolahti, M., Bochmann, M. and Romanov, A. S., "Mono- versus Bicyclic Carbene Metal Amide Photoemitters: Which Design Leads to the Best Performance?," Chem. Mater. 32(14), 6114–6122 (2020).

[21] Thompson, M. E., Li, T. Y., Djurovich, P. and Shlian, D., "A Luminescent Two-Coordinate Au(I) Bimetallic Complex with a Tandem-Carbene Structure: A Molecular Design for the Enhancement of TADF Radiative Decay Rate," Chem. – A Eur. J., chem.202100512 (2021).

[22] Romanov, A. S., Jones, S. T. E., Yang, L., Conaghan, P. J., Di, D., Linnolahti, M., Credgington, D. and Bochmann, M., "Mononuclear Silver Complexes for Efficient Solution and Vacuum-Processed OLEDs," Adv. Opt. Mater. 6(24), 1801347 (2018).